

UCLA

UCLA Electronic Theses and Dissertations

Title

Glaciologic and hydrologic processes in the Arctic

Permalink

<https://escholarship.org/uc/item/3hg8m3wg>

Author

Pitcher, Lincoln H

Publication Date

2019

Peer reviewed|Thesis/dissertation

UNIVERSITY OF CALIFORNIA

Los Angeles

Glaciologic and hydrologic processes in the Arctic

A dissertation submitted in partial satisfaction of the
requirements for the degree Doctor of Philosophy
in Geography

by

Lincoln H Pitcher

2019

© Copyright by

Lincoln H Pitcher

2019

ABSTRACT OF THE DISSERTATION

Glaciologic and hydrologic processes in the Arctic

by

Lincoln H Pitcher

Doctor of Philosophy in Geography

University of California, Los Angeles, 2019

Professor Laurence C. Smith, Chair

Land surface temperatures have increased since the end of the 19th C., with warming in the Arctic outpacing the rest of the globe. This “Arctic amplification” has fueled an acceleration in both glaciologic and hydrologic processes. My dissertation seeks to enhance understanding of these processes. To achieve this, I use exhaustive in situ surveys in combination with terrestrial, airborne and spaceborne remote sensing and spatial data science analytical methods. My dissertation is subdivided into three themes, namely: **(Theme 1)** Greenland Ice Sheet hydrologic processes; **(Theme 2)** surface water storage, dynamics and transport in heterogeneous Arctic lake-river-wetland-floodplain systems; and **(Theme 3)** development and application of novel geospatial technologies for measuring surface water systems.

The dissertation of Lincoln H Pitcher is approved.

Kurt Cuffey

Gregory S. Okin

Yongwei Sheng

Laurence C. Smith, Committee Chair

University of California, Los Angeles

2019

TABLE OF CONTENTS

Introduction	1
Chapter 1	8
1.1 Abstract	8
1.2 Introduction.....	9
1.3 Definitions and Spatial Distribution	13
<i>1.3.1 Definitions</i>	13
<i>1.3.2 Spatial Distribution</i>	14
1.4. Formation, Evolution, Morphology, and Sediment Transport.....	17
<i>1.4.1. Formation and Evolution</i>	17
<i>1.4.2. Morphology</i>	20
1.4.2.1 Meandering	21
1.4.2.2 Incision.....	23
<i>1.4.3. Sediment Transport</i>	27
1.5. Hydrographs, Hydraulic Geometry, Flow Resistance, and Open- Channel Flow.....	29
<i>1.5.1. Hydrographs</i>	29
<i>1.5.2. Hydraulic Geometry and Flow Resistance</i>	31
<i>1.5.3. Open-Channel Flow</i>	34

1.6. Surface energy balance, heat exchange, subglacial connectivity in Greenland, and Ice Sheet/Shelf Stability in Antarctica	36
1.6.1. <i>Surface Energy Balance</i>	37
1.6.2. <i>Heat Exchange</i>	39
1.6.3. <i>Subglacial Connectivity in Greenland</i>	41
1.6.4. <i>Stability of Antarctic Ice Sheet and Shelves</i>	43
1.7. Research Frontiers.....	44
1.7.1. <i>What Is the Geographical Distribution of Supraglacial Rivers Globally, and How Might It Change in the Future?</i>	44
1.7.2. <i>How Accurate Are Ice Sheet Runoff Models?</i>	46
1.7.3. <i>Do Supraglacial Rivers Influence Ice Dynamics?</i>	47
1.7.4. <i>Does Meltwater Transport on Ice Shelves Inhibit or Accelerate Ice Shelf Collapse?</i>	48
1.8. Conclusions	49
1.9 Acknowledgements	50
1.10 Figures	51
Figure 1-1: Examples of supraglacial river research and process.	52
Figure 1-2: Supraglacial networks in Northern and Southern Hemispheres.....	54
Figure 1-3: Schematic of supraglacial stream and river processes.	56

1.11 Tables	58
Table 1-1: Summary of discharge measurements.	60
Table 1-2: Summary of channel incision rates.	61
1.12 References.....	62
Chapter 2	91
2.1 Abstract	91
2.2 Introduction.....	92
2.3 Discovery of GrIS wintertime water export	95
2.3.1 <i>Mapping and measuring wintertime flux</i>	95
2.3.2 <i>Isortoq River water geochemistry</i>	97
2.4. Mechanisms enabling GrIS wintertime meltwater drainage	99
2.5 Implications of GrIS wintertime surface melt, retention, refreezing and drainage	102
2.6 Conclusion.....	104
2.7 Acknowledgments, Samples, and Data	105
2.8 Figures.....	107
Figure 2-1: study area map	107
Figure 2-2: discovery of wintertime residual meltwater drainage	109
Figure 2-3: K-Transect wintertime ice surface melt.....	111

Figure 2-4: Greenland Ice Sheet wintertime surface melt	112
2.9 References	114
2.10 Supporting Information	123
<i>2.10.1 Fraction of runoff from the Southwest GrIS compared to total GrIS runoff</i>	123
<i>2.10.2 Ground-penetrating radar (GPR) data collection, processing and interpretation</i>	124
2.10.2.1 Overview of ground-penetrating radar (GPR) surveys and data processing	124
2.10.2.2 GPR conduit height and width estimates for the Isortoq River	126
2.10.3. <i>Description of MODIS wintertime surface melt analysis</i>	127
2.10.4 <i>Description of MEaSUREs passive microwave surface melt analysis</i>	127
2.10.5 <i>Description of theoretical subglacial routing analysis</i>	128
2.10.6 <i>Explanation of geochemical interpretations</i>	129
2.10.7 Comparison of wintertime and annual average ice surface temperature 1979-2017 at five Greenland Ice Sheet outlet glaciers ...	130
Figure S2-1: fraction of runoff from southwest Greenland Ice Sheet ..	132
Figure S2-2: geochemical analysis	134

Figure S2-3: Distribution of Chu et al. (2016) storage locations	135
Figure S2-4: Isortoq River under-ice conduit geometry from GPR echogram	136
Figure S2-5: average annual and winter ice surface temperature increase	137
Table S2-1: Summary of conduit velocity (V) from February 12, 2015 Isortoq River field data.....	138
Table S2-2: summary conduit geometries	139
Table S2-3: Summary of conduit flux (Q) from February 12, 2015 Isortoq River field data.....	140
Table S2-4: summary of geochemical analysis of river water and snow samples	142
Table S2-5: K-Transect wintertime surface melt.....	143
Table S2-6: summary of proglacial river ice boreholes in the Watson river, beneath the Kanglerussuaq bridge.	144
Table S2-7: summary of proglacial river ice boreholes in the Watson river, east of Kanglerussuaq runway.	145
Table S2-8: summary of proglacial river ice boreholes in the Sandflugtdalen river, upstream of Watson river confluence.	146

Table S2-9: summary of proglacial river ice boreholes in the Ørkendalen river, upstream of Watson river confluence.....	147
Table S2-10: summary of proglacial river ice boreholes in the Ørkendalen river, near outlet glacier termini.....	148
Table S2-11: summary of proglacial river ice boreholes in the Isortoq river, near outlet glacier terminus.....	149
Table S2-12: summary of MAR grid cells used for ice surface temperature analysis.....	150
Table S2-13: linear regression model results for wintertime and annual temperatures.....	151
<i>2.10.3 References:</i>	152
Chapter 3	169
3.1 Abstract	169
3.2 Introduction.....	170
3.3. Data and Methods	176
<i>3.3.1. AirSWOT Data Collection and Processing</i>	176
<i>3.3.2. AirSWOT Open Water Mask</i>	182
<i>3.3.3. In Situ Lake and River GPS Surveys Lake</i>	184
<i>3.3.4. Permafrost and Topographic Control on Spatial Variability of WSE</i>	187

3.4 Results.....	188
3.4.1 <i>AirSWOT Lake WSE Validation</i>	188
3.4.2. <i>AirSWOT River WSE and WSS Validation</i>	189
3.4.3. <i>AirSWOT Precision and Spatial Averaging</i>	190
3.4.4. <i>Hydraulic Gradients</i>	191
3.4.5. <i>Mapping Longitudinal River Profiles and WSS</i>	191
3.5 Discussion	192
3.5.1. <i>AirSWOT Precision, Calibration, and Experiment Design</i>	192
3.5.2. <i>Scientific Applications of AirSWOT Slope and WSE Measurements Over Rivers and Lakes</i>	195
3.5.2.1. <i>WSS and Rates-of-Change for Investigating River Hydraulics, Reaeration, and Fluvial Geomorphology</i>	196
3.5.2.2. <i>Longitudinal Profiles, Catchment Geomorphology, and Discharge Retrieval</i>	198
3.5.2.3. <i>Topographic and Permafrost Control on WSE Variability in the YFB</i>	199
3.5.2.4. <i>Detecting Changes in Lake Volume Not Currently Observable from Space</i>	200
3.6 Conclusions	202
3.7 Acknowledgements	203

3.8 Figures.....	204
Figure 3-1: AirSOWT mapping extent, data filtering, and field validation.	204
Figure 3-2: comparison of AirSWOT and GPS water surface elevations.	206
Figure 3-3: Yukon River water surface slopes (WSS).....	208
Figure 3-4: AirSWOT WSE, spatial averaging, and channel width.	210
Figure 3-5: Yukon Flats Basin (YFB) lake WSE as mapped by AirSWOT.	212
Figure 3-6: AirSWOT longitudinal river mappings.....	213
Figure 3-7: controls on water surface elevation (WSE) variability.	214
3.9 Tables.....	215
Table 3-1: Summary of data used.	216
Table 3-2: Summary of field surveyed lakes.	217
3.10 References.....	218
3.11 Supporting Information	227
3.11.1 <i>Introduction to supporting information</i>	228
3.11.2 <i>AirSWOT radar geolocation</i>	228
Figure S3-1: AirSWOT geolocation uncertainty.	229

Figure S3-2: AirSWOT aircraft horizontal and vertical locations.	231
3.11.3 AirSWOT layover	232
Figure S3-3: AirSWOT layover simulations.....	232
3.11.4 Lake water surface elevation (WSE).....	233
Figure S3-4: Lake water surface elevation (WSE).	233
3.11.5 water mask validation	234
Figure S3-5: CIR water mask validation.	234
3.11.6 manual pressure transducer corrections	235
Figure S3-6: manual pressure transducer corrections.....	235
3.11.7 spatial averaging	236
Figure S3-7: downstream spatial averaging in the Yukon River, AK, USA.	236
Table S3-1: pixel count to spatial averaging area conversions.....	237
3.11.8 Yukon Flats Basins (YFB) channel characteristics	238
Table S3-2: Yukon Flats Basins (YFB) channel characteristics.....	238
3.11.8 Yukon River GPS water surface elevation (WSE) data.....	239
Data Set S3-1.....	239
Chapter 4	2
4.1 Abstract	2

4.2 Introduction.....	3
4.3 Methods	7
4.3.1 <i>WaSP Description</i>	7
4.3.1.1 <i>GNSS receiver and antenna</i>	8
4.3.1.2 <i>Power system</i>	9
4.3.1.3 <i>Enclosure</i>	10
4.3.1.4 <i>WaSP float</i>	11
4.3.2 <i>WaSP Deployment</i>	13
4.3.3 <i>WaSP Data Processing</i>	15
4.3.4 <i>AirSWOT radar processing</i>	19
4.3.5 <i>North Saskatchewan River motorboat GNSS surveys</i>	21
4.3.6 <i>North Saskatchewan River in situ water level sensor arrays</i>	22
4.5 Results.....	23
4.5.1 <i>WaSP and near-shore static surveys in Prairie Pothole ponds</i>	23
4.5.2 <i>North Saskatchewan River</i>	25
4.6 Discussion	30
4.6.1 <i>Overall WaSP performance</i>	30
4.6.2 <i>WaSP for NASA SWOT validation</i>	31

4.6.3 <i>WaSP lake surveys for the NASA Arctic Boreal Vulnerability Experiment (ABoVE)</i>	32
4.6.4 <i>Future WaSP improvements</i>	33
4.7 Conclusions	35
4.8 Acknowledgements	36
4.9 Figures.....	38
Figure 4-1: the Water Surface Profiler (WaSP) system	38
Figure 4-2: illustration of WaSP components.....	40
Figure 4-3: WaSP set up steps	42
Figure 4-4: WaSP lake/pond data processing	43
Figure 4-6: prairie pothole ponds, Saskatchewan, Canada	46
Figure 4-7: map of North Saskatchewan River study reach	47
Figure 4-8: North Saskatchewan River study reach WSE	48
Figure 4-9: WaSP versus AirSWOT in the North Saskatchewan River....	50
Figure 4-10: water level drawdown.....	51
Figure 4-11: water surface slope	52
Figure 4-12: 2017 WaSP lake deployments in support of NASA ABoVE .	54
4.10 Tables	56
Table 4-1: WaSP uncertainty	56

Table 4-2: summary of water surface slope	57
Table 4-3: 2017 WaSP lake surveys during NASA ABoVE campaign.	59
4.11 References.....	60
4.12 Supporting Information	66
Figure S4-1: ECCC pressure transducer record.....	66
Figure S4-2: PT WSE difference.....	67
Table S4-1: pressure transducer locations	69
Table S4-2: corrected pressure transducer data	71
Table S4-3: pond shoreline areas	72

ACKNOWLEDGEMENTS

This work was supported by NASA Cryosphere Program Grants NNX14AH93G and 80NSSC19K0942 managed by Thomas P. Wagner, Colene Haffke, and Thorsten Markus; NASA Terrestrial Hydrology Program Grant NNX13AD05G managed by Jared Entin; NASA Terrestrial Ecology Program Arctic-Boreal Vulnerability Experiment (ABOVE) Grant NNX17AC60A managed by Hank Margolis; NASA Surface Water and Ocean Topography mission Grant NNX16AH83G managed by Eric Lindstrom; and NASA Earth and Space Sciences Fellowship Program Grant NNX14AP57H managed by Lin Chambers. Additional support was provided by a UCLA Graduate Division Graduate Research Mentorship (GRM) fellowship, the UCLA Department of Geography, and an Exploration Fund Grant from The Explorers Club.

Chapter 1 and Chapter 3 are both published in peer-reviewed journals. Citations for these chapters, including co-authors, are as follows: **Chapter 1.** Pitcher, L.H, and Smith, L.C. (2019). Supraglacial streams and rivers. *Annual Review of Earth and Planetary Sciences* 47, 421–452. doi: doi.org/10.1146/annurev-earth-053018-060212. **Chapter 3.** Pitcher, L.H, Pavelsky, T.M., Smith, L.C., Moller, D.K., Altenau, E H., Allen, G.H., Lion, C., Butman, D., Cooley, S.W., Fayne, J., Bertram, M. (2019). AirSWOT InSAR mapping of surface water elevations and hydraulic gradients across the Yukon Flats Basin, Alaska. *Water Resources Research* doi: <https://doi.org/10.1029/2018WR023274>. Chapter 2 and Chapter 4 have

been submitted for publication and are currently in-review. The in-review citation for these chapters, including co-authors, are as follows: **Chapter 2.** Pitcher, L.H, Smith, L.C., Gleason, C.J., Miège, C., Ryan, J.C., Hagedorn, B., van As, D., Chu, W., Forster, R.R. (in review). Direct observation of wintertime meltwater drainage from the Greenland Ice Sheet. **Chapter 4.** Pitcher, L.H, Smith, L.C., Cooley, S.W., Zaino, A., Carlson, R., Pettit, J., Gleason, C.J., Minear, T., Fayne, J.V., Harlan, M., Langhorst, T., Topp, S.N., Dolan, W., Kyzivat, E., Pietroniro, A., Yang, D., Carter, T., Onclin, C., Hosseini, N., Moreira, D., Berge-Nguyen, M., Cretaux, J.-F., Pavelsky, T.M. (in review). Advancing field-based GNSS surveying for validation of remotely sensed water surface elevation products.

First and foremost, I thank my advisor Larry Smith for over a decade of mentorship, guidance, and unwavering support during my time as an undergraduate student, staff researcher, master's student and PhD student at UCLA. Thank you for teaching me to ask big questions, for pushing me intellectually, for destroying every piece of writing I ever sent you, and for empowering me to lead expeditions to the most remote corners of our planet. Thank you for introducing me to the Arctic - which now, inescapably, pulses through me.

I am also grateful for my committee members. Greg Okin - thank you for being a counterbalance, and a voice of reason during this journey. Yongwei Sheng - thank you for teaching me how to break-down and solve

data problems. Kurt Cuffey – thank you for enabling my scholarship at UC Berkely; for teaching me how glaciers, ice sheets and ice shelves work; and for challenging me to ask big questions (don't worry, the exorbitant use of “;” is, of course, intentional). I have also significantly benefited from the mentorship, tutelage, and friendship of Tamlin Pavelsky. Thank you for showing me interior Alaska, and for your constant support.

After spending over a year of my PhD in the Arctic, I have learned that the best field team is the one in which I am the weakest link. Brandon Overstreet and Adam LeWinter - thank you for teaching me this, and for always being willing to get stuck in remote corners of the world with me. To the late Alberto Behar, thank you for showing me that it is possible to build the impossible, even in the harshest environments.

To the ambassadors of the Arctic, thank you for showing me your home, teaching me how to navigate in it, and for (mostly) answering the phone when I call. In Greenland, thank you to Karsten and Nini for always making Kanger feel like home. Thank you to Casper for making Thule work, for showing me meteorites and for teaching me how to smoke salmon in a machine shop. In Alaska, thank you to Alex and Raelene for letting me sleep on your runway; to Birch for showing me what of-the-land craftsmanship is; and to Jerry for reliably getting me through Fort Yukon, each-and-every time. In Canada, thank you to Cuyler for teaching me to do fieldwork the right way. And to all the fixed-wing and rotorcraft pilots I have worked with,

thank you for always coming back to me up. At Polar Field Services, thank you Kathy Young, Kyli Cospers, Colleen Hardiman and Jessy Jenkins for making our projects work, for being the embodiment of selflessness and for teaching me how to manage a project.

For their collaboration and support, I thank Vena Chu, Colin Gleason, Asa Rennermalm, and Kang Yang. For letting me spend a winter with you, and for showing me why the W(b)est coast eclipses New England, I thank Sarah Cooley and Johnny Ryan. For their camaraderie in graduate school, I thank my cohort: Heather Agnew, Dimitar Anguelov, Lauren Brown, Dylan Connor, Ashley Fent, Sarah Halterman, Tyler Harlan, Sarah Hughes, and Taylor McCleery. For their professional feedback and friendship, I thank the Smith lab namely: Mia Bennett, Scott Stephenson, Matthew Cooper, Jessica Fayne and Ethan Kyzivat. I also thank: Kasi McMurray, Brian Won, and Matt Zebrowski for their support during my time at UCLA; Joanne Yung for teaching me how to manage a budget; Marilyn Hart for shipping our equipment all over the world; and Charles Kim for always processing my pay check.

I am also tremendously grateful to the Berkeley community that I am a part of. Thank you to Katie and Dan for always providing a welcome distraction from my PhD. Thank you to Isaac and Jacob for reminding me that there is a bigger world out there, with lots of good in it. And thank you to Maggi Kelly for hosting me at UC Berkeley.

I am also eternally grateful to the Travis, Mott, Huston/Dewitt, McClure/Easterday and Pitcher families. To Joan Travis, thank you for hosting me during my weekly commute from Berkeley to UCLA, I will always remember my times at Holmby with fondness and gratitude. To the late Sam Mott, thank you for selflessly tackling everyone else's problems, and for making the untouchable attainable. Jan and Boo, thank you for all the craft service meals, late-night trips to the Intercontinental pool, and for the countless Los Angeles adventures that offered reprieve from my studies. To Libby and Phil, thank you for unconditionally supporting this journey. To my mom, thank you for your resilience. To my dad, growing up you always told me two that today was the first day of the rest of my life – thank you for teaching me what this means.

Importantly, thank you to my partner Kelly. Thank you for teaching me what hard work means. For supporting more than a year away as I traveled to remote corners of the Arctic. For countless Monday morning airport rides in the dark and pickups in the rain. For being the embodiment of relentless perseverance and support. For helping to keep me sane, and on track. For forcing me to go the beach every weekend, for justifying spontaneous mid-week happy hours, and for teaching me that the journey is just as important as the result.

VITA

EDUCATION

- **C.Phil. (2017)** Geography, U.C., Los Angeles
- **M.A. (2015)** Geography, U.C., Los Angeles
- **B.A. (2011)** Geography & Political Science, U.C., Los Angeles

AWARDS AND HONORS

- Association of American Geographers R.S. Tarr Student Paper Award
- The Explorers Club Exploration Fund Grant
- NASA Earth and Space Sciences Fellowship
- UCLA Graduate Division Research Mentorship Fellowship

PEER REVIEWED JOURNAL PUBLICATIONS

- J.C. Ryan, L.C. Smith, D. Van As, S.W. Cooley, M.G. Cooper, **L.H. Pitcher**, A. Hubbard, "Greenland Ice Sheet surface melt amplified by snowline migration and bare ice exposure," *Science Advances*. 2019.
- E.D. Kyzivat, L.C. Smith, **L.H. Pitcher**, J.V. Fayne, S.W. Cooley, M.G. Cooper, S.N. Topp, T. Langhorst, M.E. Harlan, C. Horvat, C.J. Gleason, T.M. Pavelsky, "High-resolution water mask from NASA ABoVE AirSWOT flight campaign reveals variable size distributions of Arctic-Boreal lakes," *Remote Sensing*, 2019.
- E.H. Altenau, T.M. Pavelsky, D. Moller, **L.H. Pitcher**, P.D. Bates, M.T. Durand, L.C. Smith, "Temporal variations in river water surface elevation and slope captured by AirSWOT," *Remote Sensing of Environment*. 2019.
- **L.H. Pitcher**, L.C. Smith, "Supraglacial streams and rivers," *Annual Reviews of Earth and Planetary Sciences*. 2019.
- **L.H. Pitcher**, T.M. Pavelsky, L.C. Smith, D.K. Moller, E.H. Altenau, G.H. Allen, C. Lion, D. Butman, S.W. Cooley, J.V. Fayne, M. Bertram, "AirSWOT InSAR mapping of surface water elevations and hydraulic gradients across the Yukon Flats Basin, Alaska," *Water Resources Research*. 2019.
- S.W. Cooley, L.C. Smith, J.C. Ryan, **L.H. Pitcher**, T.M. Pavelsky, "Arctic Boreal lake dynamics revealed using CubeSat imagery," *Geophysical Research Letters*. 2019.
- M.G. Cooper, L.C. Smith, Å.K. Rennermalm, C. Miège, **L.H. Pitcher**, J.C. Ryan, K. Yang, S.W. Cooley, "Near surface meltwater storage in low-density bare ice of the Greenland ice sheet ablation zone," *The Cryosphere*. 2018.
- L.C. Kelley, **L.H. Pitcher**, C. Bacon, "Using google earth engine to map complex shade-grown coffee landscapes in northern Nicaragua," *Remote Sensing*. 2018.
- D. van As, A.B. Mikkelsen, M.H. Nielsen, J.E. Box, L.C. Liljedahl, K. Lindback, **L.H. Pitcher**, B. Hasholt, "Hypsometric amplification and routing moderation of Greenland ice sheet meltwater release," *The Cryosphere*. 2017.

- L.C. Smith, K. Yang, **L.H Pitcher**, B.T. Overstreet, V.W. Chu, Å.K. Rennermalm, J.C. Ryan, M.G. Cooper, C.J. Gleason, M. Tedesco, J. Jeyaratnam, D. Van as, M.R. van den Broeke, W.J. van den Berg, B. Noël, P.L. Langen, R.I. Cullather, B. Zhao, M.J. Willis, A. Hubbard, J.E. Box, B.A. Jenner, A.E. Behar, "Direct measurements of meltwater runoff on the Greenland Ice Sheet surface," *Proceedings of the National Academy of Sciences*. 2017.
- J.C. Ryan A. Hubbard, J.E. Box, S. Brough, K. Cameron, J.M. Cook, M.G. Cooper, S.H. Doyle, A. Edwards, T. Holt, T. Irvine-Fynn, C. Jones, **L.H Pitcher**, Å.K. Rennermalm, L.C. Smith, M. Stibal, N. Snooke, "Derivation of High Spatial Resolution Albedo from UAV Digital Imagery: Application over the Greenland Ice Sheet," *Frontiers in Earth Science*. 2017.
- E. H. Altenau, T.M. Pavelsky, D. Moller, C. Lion, **L.H Pitcher**, G.H. Allen, P.D. Bates, S. Calmant, M. Durand, L.C. Smith, "AirSWOT measurements of river water surface elevation and slope: Tanana River, AK," *Geophysical Research Letters*. 2017.
- K. Yang, L.C. Smith, V.W. Chu, **L.H Pitcher**, C.J. Gleason, Å.K. Rennermalm, M. Li, "Fluvial morphometry of supraglacial river networks on the southwest Greenland Ice Sheet," *GIScience Remote Sensing*. 2016.
- **L.H Pitcher**, L.C. Smith, C.J. Gleason, K. Yang, "CryoSheds: a GIS modeling framework for delineating land-ice watersheds for the Greenland Ice Sheet," *GIScience Remote Sensing*. 2016.
- C.J. Gleason, L.C. Smith, V.W. Chu, C.J. Legleiter, **L.H Pitcher**, B.T. Overstreet, Å.K. Rennermalm, R.R. Forster, K. Yang, "Characterizing supraglacial meltwater channel hydraulics on the Greenland Ice Sheet from in situ observations," *Earth Surface Processes and Landforms*. 2016.
- L.C. Smith, V.W. Chu, K. Yang, C.J. Gleason, **L.H Pitcher**, Å.K. Rennermalm, C.J. Legleiter, A.E. Behar, B.T. Overstreet, S.E. Moustafa, M. Tedesco, R.R. Forster, A.L. LeWinter, D.C. Finnegan, Y. Sheng, J. Balog, "Efficient meltwater drainage through supraglacial streams and rivers on the southwest Greenland Ice Sheet," *Proceedings of the National Academy of Sciences*. 2015.
- C.J. Gleason, L.C. Smith, D.C. Finnegan, A.L. LeWinter, **L.H Pitcher**, V.W. Chu, "Technical Note: Semi-automated effective width extraction from time-lapse RGB imagery of a remote, braided Greenlandic river," *Hydrology and Earth System Sciences*. 2015.
- E.C. Riordan, T.W. Gillespie, **L.H Pitcher**, S.S. Pincetl, G.D. Jenerette, D.E. Pataki, "Threats of future climate change and land use to vulnerable tree species native to Southern California," *Environmental Conservation*. 2014

INTRODUCTION

Global surface temperatures have increased since the end of the 19th century (Hartmann et al., 2013), with warming in the Arctic outpacing the rest of the globe (Masson-Delmotte et al., 2013). This “Arctic amplification” (e.g. Arrhenius, 1896; Serreze et al., 2009) has fueled an acceleration in both glaciologic (Vaughan et al., 2013) and hydrologic (Hartmann et al., 2013) processes. My dissertation research seeks to enhance scientific understanding of these processes. To achieve this, I use exhaustive in situ surveys complimented by terrestrial, airborne and spaceborne remote sensing and spatial data science analytics. My dissertation research is subdivided into three sections:

Chapters 1 and 2: *Greenland Ice Sheet hydrology*

Warming temperatures accelerate melting of the Greenland Ice Sheet (GrIS), resulting in sea level rise (slr) (Nerem et al., 2018). Currently, the GrIS contributes $\sim 0.6 \text{ mm yr}^{-1}$ to slr (Church et al., 2013), up two two-thirds of which occurs via meltwater runoff (van den Broeke et al., 2009, 2016). Such increases in meltwater production magnifies the importance of glacier hydrology both for mass loss and slr, but also to enhance understanding of glacier processes and feedbacks between meltwater production and ice sheet stability (e.g. Banwell et al., 2013; Bell et al.,

2017; Kingslake et al., 2017; Pitcher and Smith, 2019). Despite heightened importance, GrIS meltwater production, transport and export remains poorly studied (Smith et al., 2015). To that end, I use in situ hydrological and geophysical field surveys, remote sensing and climatology forced ice sheet melt models to assess spatial and temporal trends in meltwater export from the GrIS. Specifically, in *Chapter 1*, I summarize relevant research on this topic. In *Chapter 2*, I investigate residual wintertime subglacial drainage from the GrIS and the potential for GrIS surface melt during winter.

Chapter 3: *surface water in Arctic Boreal lake-river-wetland systems*

Hydrologic processes rely on freshwater availability, yet knowledge of surface water storage, transport and dynamics is deficient, especially in the Arctic (Alsdorf and Lettenmaier, 2003). Furthermore, surface water dynamics in non-channelized, heterogeneous wetland complexes that typify the Arctic remain difficult to measure and are poorly understood (Alsdorf et al., 2007). To that end, I use experimental Ka-band radar derived mappings of water surface elevation (WSE) and water surface slope (WSS) over the Yukon Flats Basin, Alaska, USA validated with in situ GPS surveys to assess lake-wetland-river hydrologic processes.

Chapter 4: *novel technologies for measuring surface water systems*

Novel remote sensing technologies, including the forthcoming Surface Water and Ocean Topography (SWOT) satellite (launch 2021) (Biancamaria et al., 2016; Durand et al., 2010) and its experimental airborne prototype, AirSWOT (Altenau et al., 2017, 2019; Pitcher et al., 2019; Tuozzolo et al., 2019) are being developed to map WSE and WSS of the world's rivers, lakes, and reservoirs. However, the vertical accuracies of these novel technologies are largely unverified while standard and repeatable field methods to validate remotely sensed WSE and WSS retrievals are needed. To that end, I developed and oversaw construction of 10 custom water surface profiler (WaSP) units, which use ruggedized Global Navigation Satellite Systems (GNSS) technologies and precise point positioning (PPP) corrections to accurately and directly survey WSE and WSS. In 2017, WaSP was successfully deployed in lakes and rivers across Canada and Alaska, spanning $\sim 17^\circ$ of latitude, in support of the NASA Arctic Boreal Vulnerability Experiment (ABoVE). Given these successful deployments, WaSP is now being considered by the SWOT mission for operational calibration/validation activities upon launch. *Chapter 4* presents this instrument, including hardware development, deployment/data processing and current use case applications.

References

Alsdorf, D. E., and Lettenmaier, D. P. (2003). Tracking Fresh Water from

- Space. *Science* (80-.). 301, 1491–1494. doi:10.1126/science.1089802.
- Alsdorf, D. E., Rodríguez, E., and Lettenmaier, D. P. (2007). Measuring surface water from space. *Rev. Geophys.* 45. doi:10.1029/2006RG000197.
- Altenau, E. H., Pavelsky, T. M., Moller, D., Lion, C., Pitcher, L. ., Allen, G. H., et al. (2017). AirSWOT measurements of river water surface elevation and slope: Tanana River, AK. *Geophys. Res. Lett.* 44, 181–189. doi:10.1002/2016GL071577.
- Altenau, E. H., Pavelsky, T. M., Moller, D., Pitcher, L. H., Bates, P. D., Durand, M. T., et al. (2019). Temporal variations in river water surface elevation and slope captured by AirSWOT. *Remote Sens. Environ.* 224, 304–316. doi:10.1016/j.rse.2019.02.002.
- Arrhenius, S. (1896). On the influence of carbonic acid in the air upon the temperature of the ground. *Philos. Mag. J. Sci.* 41, 237–276. doi:10.1080/14786449608620846.
- Banwell, A. F., MacAyeal, D. R., and Sergienko, O. V. (2013). Breakup of the Larsen B Ice Shelf triggered by chain reaction drainage of supraglacial lakes. *Geophys. Res. Lett.* 40, 5872–5876. doi:10.1002/2013GL057694.
- Bell, R. E., Chu, W., Kingslake, J., Das, I., Tedesco, M., Tinto, K. J., et al. (2017). Antarctic ice shelf potentially stabilized by export of meltwater in surface river. *Nature* 544, 344–348. doi:10.1038/nature22048.
- Biancamaria, S., Lettenmaier, D. P., and Pavelsky, T. M. (2016). The SWOT

Mission and Its Capabilities for Land Hydrology. *Surv. Geophys.* 37, 307–337. doi:10.1007/s10712-015-9346-y.

Church, J. a., Clark, P. U., Cazenave, a., Gregory, J. M., Jevrejeva, S., Levermann, a., et al. (2013). Sea level change. *Clim. Chang. 2013 Phys. Sci. Basis. Contrib. Work. Gr. I to Fifth Assess. Rep. Intergov. Panel Clim. Chang.*, 1137–1216. doi:10.1017/CB09781107415315.026.

Durand, M., Lee-Lueng, F., Lettenmaier, D. P., Alsdord, D. E., Rodriguez, E., and Esteban-Fernandez, D. (2010). The surface water and ocean topography mission: Observing terrestrial surface water and oceanic submesoscale eddies. *Proc. IEEE* 98, 766–779. doi:10.1109/JPROC.2010.2043031.

Hartmann, D. J., Klein Tank, A. M. G., Rusticucci, M., Alexander, L. V., Brönnimann, S., Charabi, Y. A. R., et al. (2013). Observations: Atmosphere and Surface. *Clim. Chang. 2013 Phys. Sci. Basis. Contrib. Work. Gr. I to Fifth Assess. Rep. Intergov. Panel Clim. Chang.*, 159–254. doi:10.1017/CB09781107415324.008.

Kingslake, J., Ely, J. C., Das, I., and Bell, R. E. (2017). Widespread movement of meltwater onto and across Antarctic ice shelves. *Nature* 544, 349–352. doi:10.1038/nature22049.

Masson-Delmotte, V., Schulz, M., Abe-Ouchi, A., Beer, J., Ganopolski, A., González Rouco, J. F., et al. (2013). Information from Paleoclimate Archives. *Clim. Chang. 2013 Phys. Sci. Basis. Contrib. Work. Gr. I to*

Fifth Assess. Rep. Intergov. Panel Clim. Chang., 383–464.

doi:10.1017/CBO9781107415324.

Nerem, R. S., Beckley, B. D., Fasullo, J. T., Hamlington, B. D., Masters, D., and Mitchum, G. T. (2018). Climate-change-driven accelerated sea-level rise detected in the altimeter era. *Proc. Natl. Acad. Sci.* 0, 201717312. doi:10.1073/pnas.1717312115.

Pitcher, L. H., Pavelsky, T. M., Smith, L. C., Moller, D. K., Altenau, E. H., Allen, G. H., et al. (2019). AirSWOT InSAR mapping of surface water elevations and hydraulic gradients across the Yukon Flats Basin, Alaska. *Water Resour. Res.* doi:https://doi.org/10.1029/2018WR023274.

Pitcher, L. H., and Smith, L. C. (2019). Supraglacial streams and rivers. *Annu. Rev. Earth Planet. Sci.* 47, 421–452. doi:doi.org/10.1146/annurev-earth-053018-060212.

Serreze, M. C., Barrett, A. P., Stroeve, J. C., Kindig, D. N., and Holland, M. M. (2009). The emergence of surface-based Arctic amplification. *Cryosphere* 3, 11–19. doi:10.5194/tc-3-11-2009.

Smith, L. C., Chu, V. W., Yang, K., Gleason, C. J., Pitcher, L. H., Rennermalm, A. K., et al. (2015). Efficient meltwater drainage through supraglacial streams and rivers on the southwest Greenland Ice Sheet. *Proc. Natl. Acad. Sci.*

Tuozzolo, S., Lind, G., Overstreet, B., Mangano, J., Fonstad, M., Hagemann, M., et al. (2019). Estimating River Discharge With Swath Altimetry: A

Proof of Concept Using AirSWOT Observations. *Geophys. Res. Lett.* 46, 1459–1466. doi:10.1029/2018GL080771.

van den Broeke, M. R., Bamber, J., Ettema, J., Rignot, E., Schrama, E., van de Berg, W. J., et al. (2009). Partitioning recent Greenland mass loss. *Science* (80-.). 326, 984–6. doi:10.1126/science.1178176.

van den Broeke, M. R., Enderlin, E. M., Howat, I. M., Kuipers Munneke, P., Noël, B. P. Y., van de Berg, W. J., et al. (2016). On the recent contribution of the Greenland ice sheet to sea level change. *Cryosphere* 10, 1933–1946. doi:10.5194/tc-10-1933-2016.

Vaughan, D. G., Comiso, J. C., Allison, I., Carrasco, J., Kaser, G., Kwok, R., et al. (2013). Observations: Cryosphere. doi:10.1017/CBO9781107415324.012.

CHAPTER 1

Supraglacial streams and rivers

1.1 Abstract

Supraglacial meltwater channels that flow on the surfaces of glaciers, ice sheets, and ice shelves connect ice surface climatology with subglacial processes, ice dynamics, and eustatic sea level changes. Their important role in transferring water and heat across and into ice is currently absent from models of surface mass balance and runoff contributions to global sea level rise. Furthermore, relatively little is known about the genesis, evolution, hydrology, hydraulics, and morphology of supraglacial rivers, and a first synthesis and review of published research on these unusual features is lacking. To that end, we review their (a) known geographical distribution; (b) formation, morphology, and sediment transport processes; (c) hydrology and hydraulics; and (d) impact on ice sheet surface energy balance, heat exchange, basal conditions, and ice shelf stability. We conclude with a synthesis of key knowledge gaps and provide recommendations for future research.

1.2 Introduction

Glaciers and ice sheets lose mass via calving and meltwater runoff, which reflect a larger suite of dynamic and hydrologic processes (Rignot et al. 2011, van den Broeke et al. 2009). Appreciation for the importance of hydrological processes continues to grow, owing to climate warming and associated increases in meltwater production across the cryosphere.

Furthermore, because the penetration of meltwater can both warm glaciers and alter their basal properties, there are complex feedbacks between meltwater production and long-term stability (e.g., Banwell et al. 2013a; Bell et al. 2017; Colgan et al. 2011; Kingslake et al. 2017; Palmer et al. 2011; Scambos et al. 2004, 2009). Despite this recognition, supraglacial production, storage, and transport on ice masses “remains one of the least-studied hydrologic processes on Earth” (Smith et al. 2015, p. 1001).

The historical record of meltwater transport in supraglacial channels on ice sheets dates to the 1800s. During an early traverse of Greenland, Fridtjof Nansen (1906) recounted crossing channels with depths submerging explorers’ ankles. Reports from the British Antarctic Expedition of 1907–1909 led by Sir E.H. Shackleton similarly noted the presence of channelized meltwater in Antarctica (David & Priestley 1914) (Figure 1-1a). In 1909 a Swiss team led by Alfred de Quervain investigated outlet glaciers in Greenland and noted that meltwater streams made travel difficult. Three years later, Quervain led an eastward traverse across Greenland and

recounted that a team member slipped into a meltwater channel upstream of a terminal moulin, regained his footing using crampons, and safely escaped, losing only an ice axe (Barr 2015). In 1930–1931 the British Arctic Air-Route Expedition noted navigating channels in southwest Greenland (Chapman 1932), while a separate 1934 British-led traverse also encountered a handful of rapidly flowing meltwater channels (Lindsay 1935). There are similar reports of supraglacial meltwater channels in Svalbard (Ahlmann & Rosenbaum 1933, Glen 1941, KSS 1934), Scandinavia (Ahlmann 1922, 1923; Lindskog 1928), and the Yukon, Canada (Sharp 1947). Aerial photography enabled surveying ice masses from above, including photointerpretation of meltwater channels in Antarctica (Roscoe 1952).

In the nineteenth century, the US armed forces grew interested in supraglacial channels in the context of aircraft operations and engineering projects on ice. In 1947 the US Army Corps of Engineers initiated Project Snowman, in which a team was deployed to southwest Greenland to study the feasibility of landing aircraft on ice and subsequently identified a complex network of meltwater lakes and channels as an obstacle (USACE 1947) (Figure 1-1*b*). In 1951 the United States launched Operation Skyline to develop helicopter search and rescue operations in Greenland and similarly noted an abundance of meltwater-filled lakes and channels emanating inland from the ice edge (Locker 1951) (Figure 1-1*b*). The first known discharge measurements in Greenland meltwater channels were

made in 1953 as part of the US Army Corps' Project Mint Julep (Holmes 1955, USACE 1953) (Figure 1-1d). Between 1953 and 1955, the US Army also investigated ice conditions near Thule Air Base in northwest Greenland (Figure 1-1c). This work further characterized supraglacial meltwater channels, making note of diurnal flow variations, multiyear stability, morphometry, and lateral spacing (Nobles 1960).

Observations by early explorers, coupled with military-led research, set the stage for targeted field investigations, primarily of small channels along the periphery of alpine glaciers. These included examinations of channel morphology, hydraulics, meandering or sinuosity, longitudinal profiles, and analogs with the morphology and processes of terrestrially based bedrock rivers (Dozier 1974, 1976; Ferguson 1973; Knighton 1972, 1981, 1985; Marston 1983; Parker 1975; Sharp 1947; Zeller 1967). Collectively these process-based studies dominated the course of study through the late 1980s (Gleason et al. 2016).

More recently, a heightened awareness of accelerating mass loss trends from glaciers and ice sheets (e.g., Vaughan et al. 2013) has motivated new research on supraglacial meltwater channels, primarily due to their occurrence as visible and integral elements of the hydrological system governing surface mass balance (SMB) (e.g., Smith et al. 2015, 2017), ice dynamics (e.g., Karlstrom et al. 2014), and ice shelf stability (Bell et al. 2017, Kingslake et al. 2017, Macdonald et al. 2018). This has been

facilitated by advances in remote sensing that enable manual and automated detection of supraglacial meltwater channels in visible and near-infrared airborne and spaceborne imagery (e.g., Bell et al. 2017; Brykala 1998a; Ewing 1970; Holmes 1955; Kingslake et al. 2017; Lampkin & VanderBerg 2014; Legleiter et al. 2014; Orheim & Lucchitta 1987; Ryan et al. 2016, 2017a,b; Smith et al. 2015; Swithinbank 1988; USACE 1953; Yang & Smith 2013, 2016; Yang et al. 2016a,b) as well as radar data (Munneke et al. 2018, Phillips 1998). Yet the location of meltwater channels in cold, harsh, remote, costly, and logistically difficult-to-study areas has resulted in limited field observations, particularly of large channels on the interiors of ice sheets (Gleason et al. 2016).

There are several reviews of glacier hydrology research that discuss surface meltwater transport. Lawson (1993) focused on meltwater and sediment supply to downstream lake and river systems. Fountain & Walder (1998) proposed a framework for meltwater transport on, in, under, and from glaciers. Irvine-Fynn et al. (2011) detailed hydrologic processes in temperate glaciers with a specific focus on valley glaciers in the Arctic. Greenwood et al. (2016) linked contemporary research with paleo-reconstructions of ice sheet hydrology. Rennermalm et al. (2013a), Chu (2014), Yang & Li (2014), and Flowers (2018) provided overviews of the hydrology of the Greenland Ice Sheet, while Liestøl (1993), Hagen et al. (1993), and Hodgkins (1997) reviewed hydrologic and glaciologic research in

Svalbard. There are also reviews that focused on englacial and/or subglacial hydrology (e.g., Hooke 1989, Hubbard & Nienow 1997), while Cuffey & Paterson (2010) covered the role of meltwater in mass balance, ice dynamics, and ice shelf processes more broadly. However, at the time of writing, a review specific to supraglacial meltwater channels is lacking. To that end, this article reviews their (a) known spatial distribution; (b) formation, evolution, morphology, and sediment transport processes; (c) hydrology, hydraulic geometry, hydraulics, and open-channel flow characteristics; and (d) impact on surface energy balance, heat transfer, significance for ice sheet basal conditions in Greenland, and ice shelf stability in Antarctica. It concludes with a discussion of knowledge gaps and recommends future research directions.

1.3 Definitions and Spatial Distribution

1.3.1 Definitions

A channel transporting meltwater on the surface of an ice mass can be categorized as a supraglacial river or a supraglacial stream (Smith et al. 2015). Channels is also used as a generic term for supraglacial streams and rivers collectively. Supraglacial rivers are primarily main-stem channels with high stream orders that are perennially occupied. They are regularly spaced, form parallel to ice flow directions, have elongated patterns, and often

terminate in moulins. In contrast, supraglacial streams are low order with shallow depths, are annual or transient on multiyear timescales, and are often tributary to larger rivers (Ewing 1970, Smith et al. 2015). For example, Figure 1-2e shows supraglacial streams emanating from a slush field in Novaya Zemlya, Russia, while Figure 1-2d features a small reach of perhaps the longest (Pelto 2018) supraglacial river in Greenland on Nioghalvsfjerdsfjorden Glacier. This review emphasizes larger, perennially active supraglacial rivers because they remain understudied despite their importance for surface energy balance, thermal heat transfer, and meltwater distribution, especially in comparison to supraglacial streams.

Supraglacial channels can terminate in moulins, crevasses, or meltwater lakes/ponds or can drain directly off the ice into terrestrial hydrologic systems or the ocean (Figure 1-3). Figure 1-2a shows a network of supraglacial streams that flow tributary to a supraglacial river terminating in a moulin. This network provides an example of an internally drained catchment (IDC), which delimits the ice surface source area for meltwater delivered to a terminal outlet moulin or endorheic lake (Yang & Smith 2016).

1.3.2 Spatial Distribution

Supraglacial streams and rivers activate during the summer melt season across the cryosphere. A large fraction of supraglacial river research has been conducted on the west coast of Greenland where the ablation zone

is dominated by supraglacial channels. In this region, these features have been surveyed in situ (Cowton et al. 2013; Gleason et al. 2016; Holmes 1955; Locker 1951; Smith et al. 2015, 2017; USACE 1947, 1953), observed using remote sensing (Charalampidis et al. 2016; King et al. 2016; Legleiter et al. 2014; Machguth et al. 2016; Ryan et al. 2016, 2017a, 2018; Yang & Smith 2013, 2016; Yang et al. 2015, 2016a,b, 2018), and inferred with models (Clason et al. 2015, de Fleurian et al. 2016, Karlstrom & Yang 2016, Palmer et al. 2011). Further south, near Nuuk, supraglacial rivers have been mapped with remote sensing (Thomsen 1986). Further north, in proximity to Ilulissat, supraglacial rivers have also been studied in situ (Echelmeyer & Harrison 1990, McGrath et al. 2011, Tedesco et al. 2013), with remote sensing (Colgan et al. 2011; Lampkin & VanderBerg 2014; Thomsen 1986; Thomsen et al. 1988, 1989), and using model-based approaches (Arnold et al. 2014; Banwell et al. 2012, 2013b, 2016; Kingslake et al. 2015; Phillips et al. 2011). A handful of studies investigated supraglacial rivers in other regions of Greenland (Bell et al. 2017, Bøggild et al. 2010, Carver et al. 1994, Cathles et al. 2011, Colgan et al. 2015, Macdonald et al. 2018, Nobles 1960, Pelto 2018) and surrounding glaciers and ice caps (Mernild et al. 2006, Sugiyama et al. 2014). Supraglacial streams and rivers have also been studied in Antarctica (Bell et al. 2017; Birnie & Gordon 1980; Fortner et al. 2005; Kingslake et al. 2015, 2017; Orheim & Lucchitta 1987; Phillips 1998; Rack & Rott 2004; Roscoe 1952; SanClements et al. 2017;

Swithinbank 1988; Winther et al. 1996), yet in comparison to Greenland, Antarctica has received considerably less attention.

In Europe supraglacial channels have been studied in Austria (Behrens et al. 1971, Burkimsher 1983), Iceland (Dowdeswell 1982, Flett et al. 2017, Jarosch & Gudmundsson 2012, MacDonald et al. 2016), Italy (Mantelli et al. 2015), Norway (Hambrey 1977; Knighton 1972, 1981, 1985; Lindskog 1928; Willis et al. 1990), Svalbard (Brykala 1998a,b, 1999; Hagen et al. 1993; Hodgkins 2001; Hodson et al. 2007; Jarosch & Gudmundsson 2012; Kostrzewski & Zwolinski 1995; Rippin et al. 2015), Sweden (Kohler 1995; Seaberg et al. 1988; Stenborg 1968, 1969), and Switzerland (Arnold et al. 1998, Ferguson 1973, Hock et al. 1999, Iken & Bindschadler 1986, Willis et al. 2002, Zeller 1967). There are sparser accounts of supraglacial rivers in Asia (Jarosch & Gudmundsson 2012, Xiao-bo 2018), South America (Isenko et al. 2005), and Russia (Isenko & Mavlyudov 2002, Isenko et al. 2005).

In the United States supraglacial channels have been studied in Alaska (Dozier 1974, 1976; Karlstrom et al. 2013; Marston 1983; Raymond & Nolan 2000; Scott et al. 2010; Sturm & Cosgrove 1990), Washington (Krimmel et al. 1972), and Wyoming (Leopold & Wolman 1960). In Canada supraglacial channels have been studied in Alberta (Hammer & Smith 1983; Mantelli et al. 2015; Munro 2010, 2011), British Columbia (Karlstrom et al. 2014), Nunavut (Bingham et al. 2005, Germain & Moorman 2016, Müller & Iken 1973, Parker 1975, Whitehead et al. 2013), the Northwest Territories (Iken

1972), and the Yukon (Dewart 1966, Ewing 1970, Jarvis & Clarke 1974, Sharp 1947, Stanley 1972).

There is also a lengthy history of injecting moulin-terminating supraglacial channels with tracers to monitor transport times and chemical concentrations exported at a glacier portal. This helps infer the configuration, geometry, and efficiency of en-/subglacial hydrologic networks. Examples of tracer studies that note the presence of supraglacial channels include those conducted in Austria (Behrens et al. 1971, Burkimsher 1983), Canada (Bingham et al. 2005), Greenland (Cowton et al. 2013), Norway (Willis et al. 1990), Sweden (Kohler 1995, Seaberg et al. 1988, Stenborg 1969), Switzerland (Hock et al. 1999), and the United States (Krimmel et al. 1972).

This overview is conservative because it does not review investigations into glacier hydrology written in languages other than English. Similarly, many conference proceedings and master and doctoral theses are not included.

1.4. Formation, Evolution, Morphology, and Sediment Transport

1.4.1. Formation and Evolution

During the transition from winter accumulation to the early melt season, ablation zones remain snow covered. As days grow longer, solar

heating warms the ice/snow surface and produces meltwater (Kingslake et al. 2015, 2017; Phillips 1998). Meltwater then percolates through underlying snow and ice, refreezes, and establishes impermeable superimposed ice lenses (Benson 1960, Hambrey 1977, Irvine-Fynn et al. 2011). As production increases, inefficient surface drainage with transport rates of $<3 \text{ mm h}^{-1}$ ensue (Cuffey & Paterson 2010, Fountain & Walder 1998, Irvine-Fynn et al. 2011). When surface snow and ice reach saturation, drainage begins to mobilize the transport of snow and firn, creating slush flow through topographic lows (e.g., Irvine-Fynn et al. 2011, Onesti 1985, Onesti & Hestnes 1989). Fountain & Walder (1998) suggested that supraglacial meltwater channels indicate that near-surface glacier ice is impermeable. Therefore, runoff begins when the near-surface ice becomes saturated, which is similar to hillslope processes for terrestrial systems (Cuffey & Paterson 2010).

The genesis of supraglacial channels remains poorly understood (Irvine-Fynn et al. 2011, Mantelli et al. 2015), but it is thought to be influenced by the rate of channel incision relative to surface ablation (Marston 1983), weathering crust hydrology, meltwater production, and surface topography (Irvine-Fynn et al. 2011). At the beginning of the melt season, rills develop tributary to larger channels, which often form parallel to ice flow directions (Hambrey 1977, Knighton 1972). Supraglacial channels form along the path of the steepest flow direction (Mantelli et al. 2015), and

streamflow is maintained by both runoff from contributing icescapes (e.g., Munro 2010, 2011) and melting along channel walls (e.g., Knighton 1972).

Supraglacial rivers are an important erosional agent for the ice surface (Birnie & Gordon 1980). Many channels are occupied perennially (Ferguson 1973, Glen 1941, Hambrey 1977) and can adjust rapidly (Dozier 1974, 1976; Ferguson 1973; Karlstrom et al. 2014) in response to internal and external forcing. Internal adjustments are caused by thermal erosion and result in geometric modifications such as changes in channel width or depth. External adjustments are forced by glacier flow (Dozier 1974) or by interactions of glacier flow with bedrock topography (Karlstrom & Yang 2016). In general, as the melt season progresses, supraglacial rivers evolve into dynamic, complex, sinuous, dendritic, incised systems (Irvine-Fynn et al. 2011). Kostrzewski & Zwolinski (1995) proposed that channel evolution follows three stages. First, channels incise, resulting in large changes in depth relative to width. Second, ablation along channel walls results in lateral expansion, increasing width relative to depth. Third, meandering (Section 1.4.2.1) initiates as flow velocity responds to modifications in channel roughness.

This conceptual model is based on internal forcing, but supraglacial rivers are also affected by external processes. Transport of preexisting channels by ice flow and modification of ice topography as it reacts to bedrock topography can alter gradients, realign drainage patterns, elongate

channel networks, and set the location of supraglacial rivers at length scales approximately equal to ice thickness (Ewing 1970, Karlstrom & Yang 2016). Dozier (1974) suggested that, like their bedrock counterparts, supraglacial channels evolve toward an equilibrium state and that sinuous systems (Section 1.4.2.1) are closest to achieving it. Fountain & Walder (1998) disputed this, arguing that an equilibrium state is unattainable due to variations in meltwater supply. Karlstrom & Yang (2016) hypothesized that an equilibrium state is possible if channel incision rates equal surface ablation rates but also hypothesized that such conditions are likely rare. Prevailing theory concludes that at length scales much smaller than one ice thickness, internal thermal adjustments control fluvial channel topography. But at scales approximately equal to ice thickness or more, ablation zone fluvial landscapes are controlled by subglacial topography (Karlstrom & Yang 2016).

1.4.2. Morphology

The primary erosional process influencing supraglacial channel morphology is the melting of channels as driven by two energetic sources: frictional dissipation of heat as flowing water loses potential energy and energy input to the surface of the channel boundary. The latter is enhanced by lower albedos relative to glacier ice (Section 1.6.1), topographic shading resulting in variable melt rates, and tributary in- and outflows that modify

flow conditions (Karlstrom et al. 2013). Additionally, morphology is influenced by extensional and compressional ice flow (e.g., Karlstrom et al. 2013, Marston 1983). Collectively, these processes govern the morphology of supraglacial channels.

1.4.2.1 Meandering

It is widely observed that supraglacial channels can meander (Dozier 1974, 1976; Ferguson 1973; Hambrey 1977; Karlstrom et al. 2013; Knighton 1972; Leopold & Wolman 1960; Marston 1983; Parker 1975; Rippin et al. 2015; Zeller 1967) (e.g., Figures 1-1a,i and 1-2c,d,f). It is also understood that curvature in terrestrial and supraglacial systems is amplified by both flow against channel boundaries and channel curvature itself, wherein flow either mechanically or thermally erodes the bank. Prevailing theories attribute meandering in alluvial rivers to sediment erosion and deposition (e.g., Braudrick et al. 2009, Church 2006). But meandering in supraglacial channels that lack similar sediment processes yet exhibit similar meander geometries (Leopold & Wolman 1960) suggests that sediment transport is not a requirement for meandering.

There are numerical models that simulate supraglacial channel meandering based on thermal forcing. For example, Parker (1975) proposed that meandering can be explained by thermal erosion due to differential frictional heating around bends. He found that to initiate meandering, inertial

forces must be sufficiently large relative to resisting forces (specifically flow must be supercritical; Section 1.5.3), and that meanders do not migrate downstream. Marston (1983) agreed that differential frictional heating promotes meandering yet disagreed that meander formation requires supercritical flow and that meanders do not migrate downstream. Karlstrom et al. (2013) built upon the Parker (1975) framework by coupling a streamflow model with an ice melt model that accounted for spatially varying frictional heating. Their simulations revealed that meanders can form in subcritical flows when Froude numbers (Section 1.5.3) exceed ~ 0.4 and when channel width-to-depth ratios are 2.5 to 5. They concluded that meandering is initiated by channel curvature, which establishes a flow instability triggering differential heat transfer and therefore uneven melt rates along channel walls.

Knowledge of meandering processes in supraglacial channels has progressed since the behavior was first observed. While Karlstrom et al.'s (2013) coupling of a flow model with an ice melt model was a significant advance, their framework assumed a constant channel geometry and did not account for surface melt or non-channelized flow that drives meltwater supply. Model parameters (e.g., ice/water temperatures) were tuned to reproduce field-observed meander geometries and thereby made inferences about natural form and process. To further advance understanding of supraglacial channel meandering, the coupled hydrologic flow and ice melt

modeling framework of Karlstrom et al. (2013) should be integrated with temporally evolving channel geometry and realistic discharge and temperature fluctuations constrained by field measurements.

1.4.2.2 Incision.

Supraglacial channels erode laterally and incise vertically (Figure 1-1h,i). Vertical channel incision rates of ~2–4 cm per day and ~4–6 cm per day have been measured in Greenland (McGrath et al. 2011) and Alaska (Marston 1983), respectively, while rates of >10 cm per day have been measured on mountain glaciers in Switzerland, Patagonia, and Russia (Ferguson 1973, Isenko et al. 2005). Examples of modeled and field-measured incision rates are given in Table 1-2. Supraglacial channel incision is thermally driven (Ferguson 1973, Fountain & Walder 1998, Isenko & Mavlyudov 2002, Isenko et al. 2005, Kingslake et al. 2015, Marston 1983). Potentially, suspended ice particles (Figure 1-1h) cause mechanical abrasion (Knighton 1981, 1985), but this remains untested.

Researchers have measured in situ and numerically simulated incision (e.g., Ferguson 1973, Fountain & Walder 1998, Holmes 1955, Isenko & Mavlyudov 2002, Isenko et al. 2005, Jarosch & Gudmundsson 2012, Karlstrom & Yang 2016, Karlstrom et al. 2013, Kingslake et al. 2015, Marston 1983, McGrath et al. 2011, Willis et al. 2002). Models assume that, as in the case of meander bend growth, the primary mechanism of vertical

incision is the melting of channel boundaries. Again, melting is driven by the sum of frictional heat dissipation and positive net energy flux. Some models include both energy sources as drivers of incision while others include only one. Some models quantify lowering for a channel cross section, and others do so for a point.

Fountain & Walder (1998) proposed a model that assumes all melt is driven by frictional heat dissipation and did not consider energy fluxes at the water surface. They quantified channel incision (\dot{d}) for a theoretical semicircle-shaped open conduit that incises without widening as

$$\dot{d} = \frac{1}{2} \left(\frac{\pi}{2n} \right)^{\frac{3}{8}} \left(\frac{\rho_w}{\rho_i} \right) \left(\frac{g}{L} \right) S^{\frac{19}{16}} Q^{\frac{5}{8}},$$

where n is Manning's roughness (Section 1.5.3), approximated as $0.1 \text{ s m}^{-1/3}$ for a smooth channel, ρ_w is water density ($1,000 \text{ kg m}^{-3}$), ρ_i is ice density ($\sim 900 \text{ kg m}^{-3}$), g is acceleration due to gravity, L is the latent heat of melting (335 kJ kg^{-1}), S is the water surface slope, and Q is discharge ($\text{m}^3 \text{ s}^{-1}$). This model is presented in the context of stream capture in which supraglacial channels become en-/subglacial conduits via thermal and dynamical processes (e.g., Fountain & Walder 1998, Irvine-Fynn et al. 2011) (en-/subglacial drainage constitutes its own subfield and is not covered here). In this model, \dot{d} is the same for open and closed channels given that

the conduit maintains a free surface. Note that \dot{d}_c calculates the channel lowering for the bottom of a semicircle conduit, not the conduit sides.

Jarosch & Gudmundsson (2012) proposed a more complicated framework for simulating incision in which they coupled a nonlinear viscous ice dynamics model with an open-channel flow model and a thermal transfer model. They found that incision is most sensitive to heat transfer from turbulent mixing, which varies with discharge. The primary purpose of this framework is similar to Fountain & Walder's (1998) and is to explain englacial conduit formation; therefore, Jarosch & Gudmundsson (2012) considered only the contribution of heat dissipation to channel melting, not surface energy fluxes.

To enhance understanding of lateral supraglacial lake drainages through meltwater channels (e.g., Raymond & Nolan 2000, Sturm & Cosgrove 1990, Winther et al. 1996), Kingslake et al. (2015) modeled incision for supraglacial channels that drain lakes. Change (Δ) in the outlet channel bottom elevation (d_c) over time (t) is calculated as

$$\frac{\Delta d_c}{\Delta t} = -\frac{f_f \rho_w}{8L\rho_i} v_z^3,$$

where f_f is the channel hydraulic roughness [Darcy-Weisbach roughness from Clarke (2003)] and v_z is the surface velocity. For simulations, Kingslake et al. (2015) assumed that $f_f = 0.25$ based on calculations of Manning's

roughness coefficient (n) in supraglacial streams as measured by Mernild et al. (2006) and that

$$f_f = \frac{8gn^2}{R_h},$$

where R_h is the hydraulic radius or the ratio of a cross-sectional area and wetted perimeter (Clarke 2003). This model assumes that incision occurs only vertically and that melting along channel sides is negligible. Similar to Fountain & Walder (1998) and Jarosch & Gudmundsson (2012), Kingslake et al. (2015) assumed that all incision is due to frictional heat dissipation without consideration of surface energy fluxes.

Karlstrom & Yang (2016) built upon previous frameworks by considering the sum of surface energy fluxes and frictional heat dissipation. They modeled the average rate of incision (\dot{d}) along a channel boundary as

$$\dot{d} = -\frac{\theta + \tau_d \bar{v}}{\rho_i L},$$

where θ is the energy balance at the free water surface (W m^{-2}), \bar{v} is average velocity (m s^{-1}), and τ_d is the shear stress on the channel bottom calculated as $\tau_d = \rho_i g d S$. This framework assumes uniform flow and that any additional thermal heating due to channel meandering is negligible. The addition of the

surface energy flux term with heat dissipation represents a significant departure from previous models and should similarly be considered in future investigations into incision. There are limited field observations for validation of these models, but a comparison of simulations forced with realistic field observations would help determine optimal applications for each of the proposed frameworks.

1.4.3. *Sediment Transport*

Sediment in supraglacial rivers can be organic [e.g., mobilized or deposited cryoconite that is grain-like in form and composed of biologically active algae, bacteria, and other particulates (Irvine-Fynn et al. 2011, Takeuchi 2002)] or inorganic (e.g., minerals, aeolian deposits, rockfall debris, volcanic ash, suspended ice crystals). Sediment concentrations are typically low, and direct measurements are limited. That said, sediment accumulation on channel beds can reduce ice albedo, thereby increasing the proportion of absorbed to reflected shortwave radiation and promoting channel melt. This positive feedback remains poorly quantified (Mantelli et al. 2015, Stibal et al. 2012), and further research is needed. Gleason et al. (2016) hypothesized that cryoconite pitting, which is widely observed in supraglacial channels (e.g., Hodson et al. 2007), can increase flow roughness, particularly in a cross-stream direction, consequently impacting stream velocity and hydraulics (Section 1.5.2). There is also tangential

literature about geochemical and isotopic flux through supraglacial channels (Fortner et al. 2005, MacDonald et al. 2016, SanClements et al. 2017, Scott et al. 2010, Tranter et al. 1993, Xiao-bo 2018) and connected downstream watersheds that is not reviewed here.

Lawson (1993) noted that while suspended loads in supraglacial channels can be 0 g L⁻¹, typical concentrations range from 0.05 to 0.4 g L⁻¹ and can exceed 60 g L⁻¹, with the highest concentrations found in channels that drain moraines. In >40 samples from two supraglacial streams on Hilda Glacier in Canada, Hammer & Smith (1983) found suspended loads of <0.5 g L⁻¹, with most samples having loads of <0.25 g L⁻¹. Supraglacial streams near volcanoes are also observed to have high sediment loads. During volcanic activity, ash can be deposited on a glacier surface in the accumulation zone, buried by snowfall over subsequent winters, and transferred to the ablation zone, where it is reexposed as sediment veins that can be mobilized and transported (Dowdeswell 1982). Over a 5-day study of nine supraglacial rivers on Sylgjujökull, west Vatnajökull, Iceland, Dowdeswell (1982) observed sediment concentrations ranging from 0.06 to 0.43 g L⁻¹ and loads ranging from 0.2 to 32.7 g s⁻¹ that were ultimately deposited at lower elevations.

Suspended ice crystals (also referred to as slush) (see Figure 1-1h) in supraglacial channels are widely observed (e.g., Chu 2014; Gleason et al. 2016; Holmes 1955; Knighton 1981, 1985; Marston 1983) but have received

little specific study. Marston (1983) found that slush load is mostly sourced from the non-channelized surface compared to channel boundaries and that loads vary from ~ 2.5 to $\sim 25 \text{ g s}^{-1}$, which is consistent with the inorganic loads observed by Dowdeswell (1982). Furthermore, for his field site(s) in Alaska, Marston (1983) observed that slush roughly varies with discharge, that loads pulsate, and that channels are supply rather than transport limited. In general, understanding of the effect of slush transport on channel morphology and hydraulics remains preliminary.

1.5. Hydrographs, Hydraulic Geometry, Flow Resistance, and Open-Channel Flow

1.5.1. Hydrographs

Given the challenges in glacier field research, supraglacial hydrographs are rare (e.g., Marston 1983, Smith et al. 2017) (Table 1-1). Reconstructing hydrographs from a stage-discharge rating curve should be approached carefully (McGrath et al. 2011) due to rapid changes in channel geometry (Holmes 1955, USACE 1953) and may be unsuitable (Smith et al. 2017). Supraglacial hydrographs have been inferred from climatology forced-runoff models (e.g., Banwell et al. 2013b, de Fleurian et al. 2016, Willis et al. 2002), yet one study found that models overpredict discharge by 21–58% and do not reproduce the timing of peak discharge (Smith et al. 2017).

The supraglacial river hydrograph is characterized by large diurnal and seasonal variability. Depending on the size and shape of the catchment, peak discharge lags behind peak melt, which tracks peak solar radiation (Dozier 1974; McGrath et al. 2011; Munro 2010, 2011; Smith et al. 2017; Willis et al. 2002). This lag is due to catchment shape and area, with large, elongated catchments having longer delays than short, compact ones (Munro 2010, Smith et al. 2017); residual drainage from weathering crust, a low-density surface that modulates the timing of hillslope processes and meltwater delivery to channels (Cooper et al. 2018, Irvine-Fynn et al. 2011, Karlstrom et al. 2014, Munro 2011, Smith et al. 2017, Willis et al. 2002); and drainage density of the channel network, with high density associated with faster routing (Yang et al. 2018).

A motivation for studying the supraglacial river hydrograph is to constrain the timing and volume of meltwater delivery to moulins, which modulate subglacial water pressure and sometimes basal sliding (e.g., Andrews et al. 2014, Bartholomew et al. 2011a, Chandler et al. 2013, Chu et al. 2016a, Cowton et al. 2013, de Fleurian et al. 2016, McGrath et al. 2011). However, it is unrealistic to monitor discharge in situ for numerous or even one channel for more than a few days. Therefore, routing the output of climatology-based melt/runoff models through a watershed routing model (e.g., Arnold et al. 1998, 2014; Banwell et al. 2012, 2013b, 2016; Clason et al. 2015; de Fleurian et al. 2016; Leeson et al. 2015; Willis et al. 2002)

remains the most realistic mechanism for estimating discharge delivered to moulins. To that end, Smith et al. (2017) applied synthetic unit hydrograph (SUH) theory to convert modeled melt into hydrographs at a terminal outlet moulin. The empirical SUH coefficients were derived using 72 continuous hours of in situ discharge measurements collected in Greenland in July 2015. They demonstrated that IDC area, shape, and river length dictate the timing and magnitude of peak meltwater delivery to moulins. Building on this and using the same hydrograph, Yang et al. (2018) partitioned meltwater routing into non-channelized surface (or interfluvial) flow and channelized flow. They found that representative interfluvial flow distances are 0–100 m compared to 10 km for channelized flow. Smith et al.'s (2017) and Yang et al.'s (2018) findings were calibrated for one IDC and one 3-day snapshot, yet the studies provided a first set of empirical measurements that enabled modeling of moulin hydrographs using classical unit hydrograph and hillslope transport theory.

1.5.2. Hydraulic Geometry and Flow Resistance

Hydraulic geometry (HG) is an empirically derived set of equations that relates changes in channel width (w), depth (d), and velocity (v) to changing discharge (Q), both at a given cross section [at-a-station hydraulic geometry (AHG)] and in a downstream flow direction [downstream hydraulic geometry (DHG)]. HG was introduced by Leopold & Maddock (1953) and has

since been widely applied to supraglacial systems (e.g., Brykala 1999, Gleason et al. 2016, Kostrzewski & Zwolinski 1995, Marston 1983). The HG theorem states that for a given cross section, w , d and v vary as a power function of Q (Leopold & Maddock 1953). The equations governing HG are

$$w = aQ^b, d = cQ^f, \text{ and } v = kQ^m,$$

where a , b , c , f , k and m are empirically derived constants. It follows that

$$b + f + m = a \times c \times k = 1,$$

where b , f and m are calculated as the slope of the linear regression when w , d , or v is plotted against Q in logarithmic form. While a , c , and k are the intercepts of the same logarithmic regressions and are therefore equivalent to respective values of w , d , and v when $Q = 1$ (Leopold & Maddock 1953), Gleason & Smith (2014) and Gleason & Wang (2015) revealed empirical correlations between AHG intercepts and coefficients for w , d , and v when averaged over long reaches of terrestrial rivers, a phenomenon they term at-many-stations hydraulic geometry (AMHG). While AMHG has been successfully inverted to estimate terrestrial river discharge from remote sensing (Bonnema et al. 2016, Durand et al. 2016, Gleason & Smith 2014,

Gleason et al. 2014, Hagemann et al. 2017), this approach has yet to be applied to supraglacial channels.

Gleason et al. (2016) summarized AHG and DHG coefficients for supraglacial research. A primary takeaway of this summary is that at a given cross section, higher Q is accommodated by larger increases in v relative to w and d (Gleason et al. 2016, Knighton 1981, Marston 1983). Similarly, with higher Q , d increases faster than w (Brykala 1998a, Gleason et al. 2016, Kostrzewski & Zwolinski 1995, Marston 1983), which is consistent with observations of vertical channel incision rates exceeding those of lateral channel melting (Marston 1983). In Greenland, Smith et al. (2015) aggregated in situ measurements of w , d and v from 54 small supraglacial streams and 24 cross sections across three large supraglacial rivers to calibrate an interchannel AHG power-law function relating Q to w ($w = 3.84Q^{0.54}$, $r^2 = 0.89$, with a root mean square error of $3.11 \text{ m}^3 \text{ s}^{-1}$). The stability of this empirical relationship among the 78 measured cross sections was attributed to incision of similar channel geometries. DHG investigations suggest that supraglacial Q increases downstream, resulting in subsequent increases in w , d and v (Gleason et al. 2016, Knighton 1981, Marston 1983), which is consistent with DHG in terrestrial rivers (Leopold & Maddock 1953).

1.5.3. Open-Channel Flow

Open-channel or free-surface flow conditions are dictated by gravity, channel slope, and friction or channel roughness (Knighton 1998). Flow conditions can be categorized as subcritical, critical, or supercritical. With subcritical flow, gravity and friction are in balance and flow depth/velocity remains consistent over short time intervals. In contrast, critical and supercritical flows are characterized by abrupt changes in flow depth/velocity over short time intervals, akin to downstream flood wave propagation (Chow 1959, Knighton 1972). Flow conditions can be numerically defined by thresholding the instantaneously derived Froude number (F_r), a dimensionless quantity calculated as the ratio between channel velocity, gravity, and depth:

$$F_r = \frac{\bar{v}}{\sqrt{gd}}$$

Flows with $F_r < 1$ are subcritical, $F_r = 1$ are critical, and $F_r > 1$ are supercritical (e.g., Hugget 2007).

Flows in supraglacial channels are often subcritical but can be supercritical (e.g., Ferguson 1973; Gleason et al. 2016; Knighton 1981, 1985; Marston 1983; Parker 1975). For example, Leopold & Wolman (1960) calculated $F_r = 1.9$ on Dinwoody Glacier, Wyoming. Carver et al. (1994) found evidence of supercritical flow with $F_r > 2$ on Harlech Gletscher, Greenland,

when they observed roll waves with 6- to 7-second lags between pulses propagating downstream. This is consistent with Knighton's (1981) observations on Austre Okstindbreen Glacier, Norway, and Germain & Moorman's (2016) observations on Bylot Island, Nunavut. Gleason et al. (2016) calculated supercritical flows in small ($Q < 0.5 \text{ m}^3 \text{ s}^{-1}$), steep (slopes $> 0.7\%$) streams with maximum $F_r = 3.11$ in Greenland, while the rivers ($Q = 4.58$ to $23.12 \text{ m}^3 \text{ s}^{-1}$) were subcritical (minimum $F_r = 0.45$). In general, supraglacial channels display both subcritical and supercritical flow.

An important hydraulic parameter for open-channel flow is resistance, which modulates and inversely correlates with velocity. Flow resistance is approximated as channel roughness using Chezy, Manning's, or Darcy-Weisbach equations [refer to chapter 4 of Knighton (1998) for a review of resistance and roughness calculations]. The most commonly used resistance metric in supraglacial hydrology is Manning's n , which is calculated as

$$n = \frac{1}{\bar{v}} R_h^{2/3} S^{1/2},$$

where \bar{v} is the average velocity, R_h is the hydraulic radius, and S is the channel slope. Flow resistance is composed of boundary resistance including substrate and form friction, channel resistance including irregularities that disturb flow, and free surface resistance caused by unsteady flow and potentially slush at the water surface (Knighton 1998). Morphologically,

meander bends disturb flow and increase roughness, which suggests that variations in roughness might be reflected by variations in sinuosity. From field measurements, supraglacial channels are observed to have a large range in roughness despite having a uniform substrate and limited sediment and being free of alluvial bedforms. Gleason et al. (2016) hypothesized that such variations may be due to extensional and compressional fractures in channels and bank scalloping, cryoconite pitting, slush, and low water temperatures associated with high viscosity. However, Yang et al. (2018) suggested a mean n value of 0.03–0.05 when averaged across the scale of an entire supraglacial stream/river catchment. In situ characterizations of open-channel flow conditions in supraglacial channels of varying sizes, planforms, and discharges are needed for remote estimation (e.g., Kingslake et al. 2017, Smith et al. 2015) of discharge.

1.6. Surface energy balance, heat exchange, subglacial connectivity in Greenland, and Ice Sheet/Shelf Stability in Antarctica

Supraglacial channels influence surface melt by modulating surface reflectance (albedo) and topographic roughness. They also impact the thermal regime of ice by descending into a glacier, freezing, and releasing latent heat. Most recently, supraglacial rivers are being investigated for their role in ice shelf stability. These processes of surface energy balance, heat

exchange, subglacial connectivity, and ice shelf stability are reviewed in the following subsections.

1.6.1. Surface Energy Balance

Supraglacial channel initiation and maintenance require surface melt and runoff. Melt is driven by the surface energy balance, particularly net shortwave radiation, which is the difference between downward and reflected shortwave radiation (van den Broeke et al. 2008). Net shortwave radiation is modulated by surface albedo, which is the total reflected shortwave radiation across all wavelengths. Albedos can range from >0.8 for snow to <0.4 for ice (Cuffey & Paterson 2010). Low albedos enhance melt because a higher proportion of downward shortwave radiation is absorbed rather than reflected. Importantly, the albedo of surfaces wetted by meltwater is less than half that of clean ice (Ryan et al. 2018). For example, in Greenland the field-measured albedo of a melt pond at depths of <5 m ranges from ~ 0.15 to 0.3 (Tedesco & Steiner 2011). Remotely sensed albedo in supraglacial channels ranges from 0.16 to 0.26 (Ryan et al. 2016, 2017a), while average clean ice albedo is ~ 0.55 (Ryan et al. 2018). Furthermore, low albedos correlate with high melt (e.g., Greuell 2000), while 15% of albedo variability in west Greenland can be explained by the presence of supraglacial meltwater (Ryan et al. 2018). Cryoconite deposition and pitting are also present in many streams and rivers, which will further

reduce albedo (Gleason et al. 2016). Collectively, this suggests that supraglacial channels help modulate the spatial distribution of albedo as they transport sediment (Section 3.3) and meltwater from saturated ice to slush and to ponds and eventually excavate it from the surface.

Supraglacial channels also alter the topography of the ice surface via vertical and lateral channel incision (Section 3.2). Local surface topography modulates the spatial variability of melt, especially in the cross-glacier direction (Arnold et al. 2006). That is, deviation from a flat surface and the subsequent introduction of variable topography establish a rougher surface that can intersect and absorb incoming and reflected radiation. Cathles et al. (2011) modeled the feedback between surface roughness, albedo, and ablation, finding that topographic features, simulated as circular and V-shaped canyons, enhance melt at local scales and therefore influence surface meltwater transport (Cathles et al. 2011). Rippin et al. (2015) investigated linkages between channel presence and surface reflectance (as a proxy for albedo), finding that high channel densities correlate with low reflectance—confirming an important feedback between channel-induced topography, albedo, and melt.

The presence and evolution of supraglacial channels also affect non-channelized icescapes. Vertical channel incision creates relief that propagates as non-channelized flow and small slush-filled rills, and tributary streams develop on ablating slopes tributary to valley floor channels. This

channel propagation alters surface topography and albedo. The importance of fluvially eroded icescapes due to channel evolution for surface energy balance has received little study.

Collectively, this suggests that the future expansion of meltwater under a warming climate (e.g., Howat et al. 2013, Ignéczi et al. 2016, Leeson et al. 2015) will further lower ice surface albedos, reducing the fraction of reflected shortwave radiation and promoting melt. It is likely that such an albedo reduction will be attributable to both the expansion of surface meltwater and related propagation of meltwater channels that dissect the ice surface and produce localized topographic features. This also suggests a self-reinforcing feedback between positive net shortwave radiation, melt production, and supraglacial channel evolution.

1.6.2. Heat Exchange

Supraglacial channels deliver meltwater to internal and subglacial hydrological networks that convey it through, beneath, and beyond a glacier (Fountain & Walder 1998). A large portion of this meltwater is rapidly exported via subglacial meltwater portals (van As et al. 2017). However, some fraction (Chu et al. 2016b, Hodgkins 2001, Rennermalm et al. 2013b, Smith et al. 2015) is retained within the ice, where, if it refreezes, it releases latent heat, thus warming the ice. Such warming is in addition to heat transfer from through-flowing water with initial temperatures warmer than

the internal temperature of the glacier (Lüthi et al. 2015, Phillips et al. 2010). The warming produced by these processes, often focused at stable moulins and crevasses (Catania & Neumann 2010, Colgan et al. 2011, McGrath et al. 2011), is collectively termed cryo-hydrologic warming (Phillips et al. 2010). This process was investigated as a mechanism for the thermal response of ice masses to surface melt and has been documented in both Greenland (Charalampidis et al. 2016; Harrington et al. 2015; Lüthi et al. 2015; Phillips et al. 2010, 2013) and the Steele Glacier, Yukon, Canada (Jarvis & Clarke 1974).

Cryo-hydrologic warming can explain differences between field-measured and modeled ice temperature profiles (Harrington et al. 2015, Lüthi et al. 2015). Phillips et al. (2010) found that cryo-hydrologic warming can occur on timescales of years to decades and is modulated by the horizontal spacing of the hydrologic system. This suggests that supraglacial meltwater volume and channel spacing influence cryo-hydrologic warming. It was also proposed that cryo-hydrologic warming enhances ice velocity by warming basal temperatures and reducing viscosity (Phillips et al. 2013). Furthermore, models simulate that the onset of abundant surface melt reaching the bed near the interior of the Greenland Ice Sheet would cryo-hydrologically warm the ice, reduce its viscosity, and promote a thermal-viscous collapse over several thousand years (Colgan et al. 2015). This

stresses the importance of water and heat transfer delivered by supraglacial channels to en-/subglacial networks.

1.6.3. Subglacial Connectivity in Greenland

In Greenland, particularly along the western land terminating flank of the ice sheet, a complex network of supraglacial rivers transports large volumes of surface meltwater to moulins, lakes, and crevasses (Colgan et al. 2011, Smith et al. 2015). Surface melting, discharge, and the spatial location of supraglacial rivers positively correlate with ice velocity (Bartholomew et al. 2011b, Palmer et al. 2011) as well as broadscale bedrock topography (Yang et al. 2015). The mechanisms by which meltwater transported by supraglacial rivers affect dynamical processes differ if the river is terminated by a moulin, crevasse, or lake.

Moulin-terminating rivers inject meltwater directly into en-/subglacial drainage systems. The timing of meltwater delivery to the moulin is determined by its contributing supraglacial river transport capacity, surface climatology, and IDC properties (Smith et al. 2015, 2017; Yang & Smith 2016; Yang et al. 2018). If moulin discharge exceeds the subglacial drainage system capacity, then subglacial water pressures increase and basal sliding may ensue. It is hypothesized that eventually the subglacial drainage system adapts to moulin discharge and basal sliding ceases, while if the moulin discharge is less than the subglacial drainage system capacity, there is little

change in water pressure or basal sliding (e.g., Colgan et al. 2011, Schoof 2010).

Crevasse-terminating channels often deliver meltwater to a distributed englacial system. If moulins form from water-filled crevasses, the same subglacial water pressure and ice velocity feedback is invoked. Alternatively, crevasses can diffuse flow, resulting in low-amplitude hydrograph delivery to the subglacial system, a minimal change in subglacial water pressure, and sliding (Colgan et al. 2011).

Supraglacial river discharge entering lakes can be temporarily impounded before escaping at a lake outlet (e.g., Smith et al. 2015) or draining directly into the ice via a hydrofractured moulin that opens at the lake bottom (e.g., Das et al. 2008, Selmes et al. 2011, Tedesco et al. 2013). Therefore, rapid lake drainage events might overwhelm the subglacial drainage system capacity and enhance sliding, while slowly draining lakes and those having river outlets may result in a lower amplitude injection to the bed having minimal impact on sliding (e.g., Das et al. 2008, Tedesco et al. 2013). Meltwater can also be retained in lakes, with their surfaces freezing over during winter (Koenig et al. 2015). Such lakes should have no significant impact on basal water pressures and sliding.

1.6.4. Stability of Antarctic Ice Sheet and Shelves

The deformation of ice shelves past embayment walls and over basal islands provides a drag force that restrains the seaward flow of marine-terminating glaciers and ice streams. Thus, ice shelf disintegration can cause large increases in ice velocity, upstream ice thinning, and sea level rise. Meltwater on ice shelves is linked with ice shelf stability (Rack & Rott 2004, Scambos et al. 2000), while supraglacial rivers may strengthen (Bell et al. 2017) and weaken (Kingslake et al. 2017) shelf integrity.

Kingslake et al. (2017) outlined a weakening mechanism in which supraglacial rivers can promote ice shelf collapse by filling lakes, which increases the load on an ice shelf and can result in bulging and fracturing (Banwell et al. 2013a, Scambos et al. 2009) (Figure 1-3). Lakes also ablate faster than surrounding ice due to lower albedos (Section 1.6.1) and can hydrofracture or drain, resulting in shelf rebound. This cycle of loading, fracture, drainage, and rebound induces structural weakness that can cause widespread lake drainage and “a fracture system capable of driving explosive [ice shelf] breakup” (Banwell et al. 2013a, p. 5872). In contrast, Bell et al. (2017) proposed that supraglacial rivers may buffer ice shelves from collapse by efficiently transporting mass off ice shelves into the ocean without impoundment/loading (Figure 1-3). The differing impacts that supraglacial rivers may have on ice shelf stability underscore the need for further study.

1.7. Research Frontiers

There remain gaps in understanding of supraglacial processes. For example, supraglacial channels are well studied in Greenland, yet those in Antarctica have received less attention. Morphologically, vertical channel incision is noted in the field and complex modeling frameworks have been developed, yet a comparison of incision models forced with field observations is lacking. Ice crystal transport in channels is well documented, yet understanding of the effect of slush on channel morphology and hydraulics remains preliminary. Additionally, four outstanding research questions with relevance to climate variability and global sea level rise are highlighted in the following sections.

1.7.1. What Is the Geographical Distribution of Supraglacial Rivers Globally, and How Might It Change in the Future?

The global distribution of supraglacial rivers remains unmapped, which is expected given that they are seasonally ephemeral and generally located in cold, harsh, inaccessible places. Also, most supraglacial rivers are narrow, which makes them challenging to map using historically available satellite imagery such as ASTER, Landsat, and MODIS with 15-m, 30-m, and 250-m pixel sizes, respectively. However, advances in cloud-based computing power coupled with improved satellite resolutions and novel automated

image classification software packages now enable repeat mappings of surface water bodies (Pekel et al. 2016) as well as bedrock and alluvial rivers at continental (Allen & Pavelsky 2015) to global scales (Allen & Pavelsky 2018). Furthermore, high-resolution satellite data (e.g., Sentinel-2/-3 and WorldView-1/-2/-3/-4) have been used to map supraglacial streams and rivers in Greenland (e.g., Karlstrom & Yang 2016; King et al. 2016; Poinar et al. 2015; Yang & Smith 2013, 2016; Yang et al. 2015, 2016a,b) and Antarctica (e.g., Bell et al. 2017, Kingslake et al. 2017), while the recent advent of CubeSats, such as the Planet cluster (e.g., Cooley et al. 2017, 2019), which now images the entire Earth each day, offers the exciting possibility of the high spatial and temporal resolutions needed to capture these fine-scale, dynamic, and often short-lived features. Collectively, this suggests that global supraglacial river mapping is now feasible.

Supraglacial rivers create fluvial fingerprints indicating active meltwater production and transport across the ice surface, and their termination points reveal moulin locations (Smith et al. 2015, Yang & Smith 2016) and surface-to-bed connections. Therefore, the widescale mapping of supraglacial rivers informs not only the presence of melting ice but also where surface climatology interacts with subglacial water pressures and therefore ice dynamics (de Fleurian et al. 2016). In contrast, supraglacial rivers that drain directly off the terminus of an ice mass may indicate cold-

based glaciers and locations where ice dynamics receive little or no surface meltwater. A global supraglacial river map is needed to discern where ice masses receive inputs of heat and water from surface meltwater and where they do not. Coupled with topographic information and climate model outputs, such a map could be used to assess future distributions of supraglacial rivers using climate model simulations. This could help inform which regions of the Greenland and Antarctic Ice Sheets and associated ice shelves are most vulnerable to positive feedbacks between climate warming, supraglacial meltwater transport, and potential linkages to the bed.

1.7.2. How Accurate Are Ice Sheet Runoff Models?

The primary method for forecasting sea level rise contributions from glaciers and ice sheets uses regional or global climate models to estimate SMB and runoff (e.g., van den Broeke et al. 2009). SMB runoff is often validated via comparisons with measured subglacial outflow or discharge in proglacial rivers (e.g., Mernild et al. 2008, 2012; Overeem et al. 2015; Rennermalm et al. 2013b; Smith et al. 2015; van As et al. 2014, 2017). However, surface meltwater expelled via subglacial conduits into proglacial rivers has been routed through a host of en-/subglacial processes and is therefore removed from the SMB process of meltwater production and runoff. Such comparisons of simulated runoff and observed proglacial river discharge have identified dissimilarities of at least 38% (Overeem et al.

2015, Smith et al. 2015). There are also discrepancies between satellite-based gravimetric observations of mass change and SMB models in melt-prone areas of Greenland (Sasgen et al. 2012, Xu et al. 2015). At the IDC scale (Figure 1-2a), SMB models oversimulate runoff by at least 21% (Smith et al. 2017). Discrepancies between satellite/field observations and models emphasize the need for validation, interrogation, and refinement of SMB modeling. A promising strategy for such research is direct monitoring of supraglacial river flows across space and time. This has implicit societal relevance given that SMB models are used to forecast sea level rise.

1.7.3. Do Supraglacial Rivers Influence Ice Dynamics?

Current ice sheet models do not consider hydrologic flow paths through channelized or non-channelized ice, nor do they account for point source locations of surface-to-bed hydrologic connections (e.g., moulins). This is noteworthy because ice surface hydrology preconditions the magnitude and timing of meltwater delivery to the bed (Smith et al. 2017) and is therefore an important control on subglacial hydrologic flow gradients, water pressures, and ice sliding (Schoof 2010). Consequently, the lack of coupled hydrologic and ice dynamics models impedes accurate coupling of SMB with ice flow, especially at short (i.e., diurnal) timescales. Therefore, coupling a surface hydrology-routing model with an ice dynamics model that accurately simulates the volume, magnitude, and location of meltwater

injection to the bed will improve our understanding of the future response of glaciers and ice sheets to increased meltwater production.

1.7.4. Does Meltwater Transport on Ice Shelves Inhibit or Accelerate Ice Shelf Collapse?

Geological records indicate that during the Last Interglacial and the Pliocene (~130,000 and ~3 million years ago, respectively), global mean sea levels were >6 m higher than today (Dutton et al. 2015). DeConto & Pollard (2016) explained that most of this historical difference is attributed to a smaller Antarctic Ice Sheet, which motivates the use of coupled ice-ocean-atmosphere models to reconstruct past conditions and assess the vulnerability of the Antarctic Ice Sheet to the current climate. DeConto & Pollard (2016) found that simulating ancient Antarctic Ice Sheet retreat on scales commensurate with geological sea level rise records requires the retreat and collapse of major ice shelves, which currently stabilize and buttress grounded ice. To mimic historical ice shelf retreat and collapse, models require ocean warming, resulting in subsurface melt and shelf thinning, and/or surface meltwater production, resulting in thinning, crevassing, calving, and hydrofracturing. This suggests that ice shelves are vulnerable to meltwater production, which is amplified by low hypsometry whereby small temperature increases yield disproportionately large melt area increases (DeConto & Pollard 2016). As reviewed in this article, the

impact of meltwater transport on ice shelf stability has been interpreted as both a stabilizing (Bell et al. 2017, Macdonald et al. 2018) and a destabilizing (Kingslake et al. 2017) process. Further research is needed to enhance understanding of pathways and processes of ice shelf meltwater production, transport, and export to determine how supraglacial channels impact ice shelf stability and therefore global sea level rise.

1.8. Conclusions

This work reviews and synthesizes published English-language studies of supraglacial streams and rivers on glaciers, ice sheets, and ice shelves. Supraglacial rivers link surface climatology with ice dynamics and are an important component of how glaciers and ice sheets respond to climate variability. Despite this, relatively little is known about their geographical distribution, their transport capacity, or how they might respond to increased meltwater production on the ice surface. Logistical challenges render field research difficult, but advances in remote sensing enhance the ability to monitor dynamics across space and time. Accelerated climate warming increases suitable areas for supraglacial river formation and underscores the importance of coupling supraglacial river hydrology with ice dynamics to improve estimates and projections of eustatic sea level rise.

1.9 Acknowledgements

This work was supported by a grant from the NASA Cryosphere Program managed by Dr. Thomas P. Wagner and a graduate fellowship from the NASA Earth and Space Sciences Fellowship Program managed by Dr. Lin Chambers. WorldView Imagery © 2018 DigitalGlobe, Inc. Geospatial support for this work was provided by the Polar Geospatial Center under NSF-OPP awards 1043681 and 1559691. Matt Zebrowski, a cartographer in the UCLA Department of Geography, kindly illustrated Figure 1-3. Conversations with Brandon Overstreet about supraglacial river morphology and hydraulics helped motivate topics of this synthesis. Kang Yang helped locate historical primary source documents. Grant Macdonald shared photos from a recent field expedition to Antarctica for use in Figure 1-1*f*. Lucy Martin at the Scott Polar Research Institute, University of Cambridge, provided access to the historical photograph of Antarctica used in Figure 1-1*a*. Maria Jankowska and Martin Brennan at the Young Research Library, UCLA, assisted with image use rights for Figure 1-1*b,c,d*. We are especially grateful to Professor Kurt Cuffey, who significantly contributed to the wording, structure, and theoretical discussions in this review.

1.10 Figures

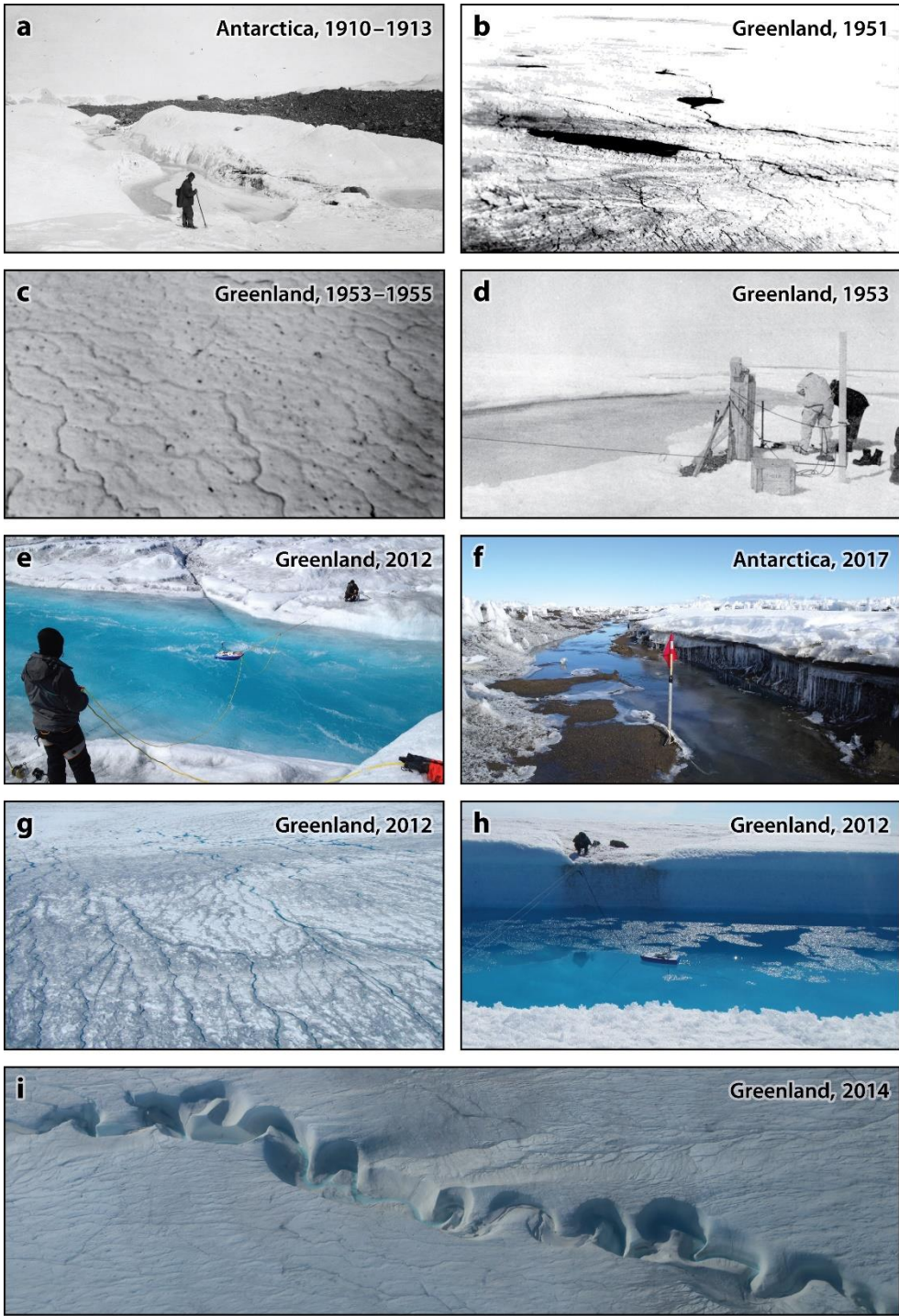


Figure 1-1: Examples of supraglacial river research and process.

(a) An early polar explorer, a member of the 1910–1913 British Antarctic Expedition, standing next to a supraglacial river in Antarctica. Photo by Frank Debenham from the Scott Polar Research Institute, University of Cambridge. **(b–d)** Aerial photographs from US armed forces investigations in the early to mid-1900s of supraglacial channels in the context of aircraft operations and engineering on ice. **(b)** A photograph collected by the Operation Skyline team (scale unknown) in southwest Greenland. Photo taken from Locker (1951). **(c)** A photograph collected as part of the US Army investigation into ice conditions (scale unknown) near Thule Air Base in northwest Greenland. Photo taken from Nobles (1960). **(d)** Members of the 1953 US Army's Project Mint Julep measuring streamflow in southwest Greenland. Photo taken from USACE (1953). **(e)** An example of a streamflow measurement in a supraglacial river in Greenland as part of ongoing research aimed at validating melt and runoff models. Photo provided by Laurence C. Smith. **(f)** An example of a supraglacial river meandering across the McMurdo Ice Shelf. These rivers have been studied in Antarctica for their role in ice shelf stability. Photo provided by Grant Macdonald. **(g)** A dendritic network of supraglacial channels in Greenland (scale unknown). Photo by Lincoln H Pitcher and Laurence C. Smith. **(h)** Vertical channel incision and floating ice crystals or slush (researcher on far bank for scale). Photo by

Lincoln H Pitcher. (i) A sinuous and incised supraglacial river in Greenland (scale unknown). Photo by Lincoln H Pitcher.

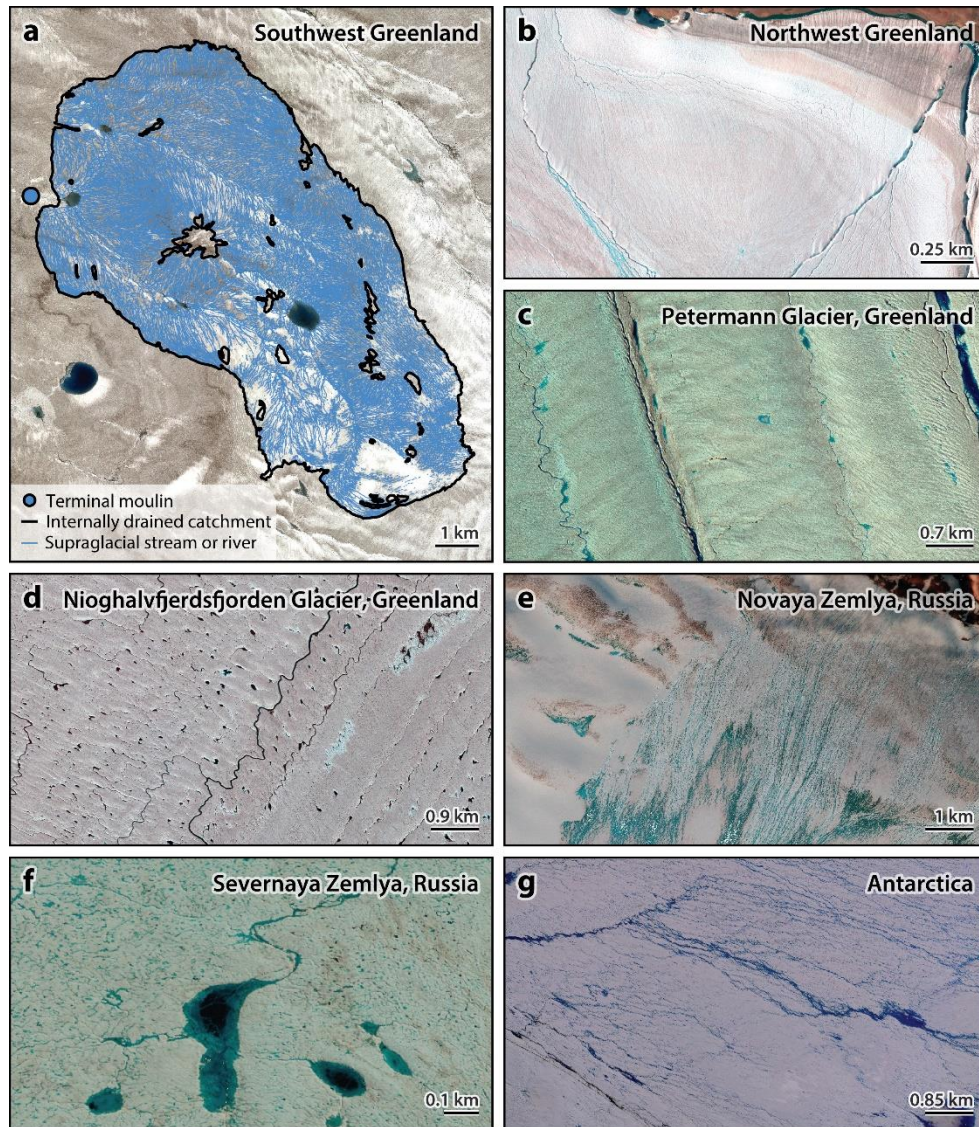


Figure 1-2: Supraglacial networks in Northern and Southern Hemispheres. **(a)** An internally drained catchment (black) and supraglacial stream/river network (blue). The internally drained catchment boundary and channel networks are from Smith et al. (2017). The image is from WorldView-3, collected July 17, 2015. **(b)** Two incised, land-terminating supraglacial rivers in northwest Greenland. The image is from WorldView-2, collected July 28, 2017. **(c,d)** Supraglacial streams and rivers on ice shelves in Greenland.

Both images are from WorldView-2, collected July 9, 2015, and July 26, 2013, respectively. **(e,f)** Supraglacial streams and rivers on grounded and floating ice in Novaya Zemlya and Severnaya Zemlya, Russia, respectively. Both images are from WorldView-2/-3, collected July 12, 2016, and July 12, 2013, respectively. **(g)** A dendritic supraglacial stream and river network on grounded ice in Antarctica. The image is from QuickBird2, collected January 23, 2011. All images © 2018 DigitalGlobe, Inc.

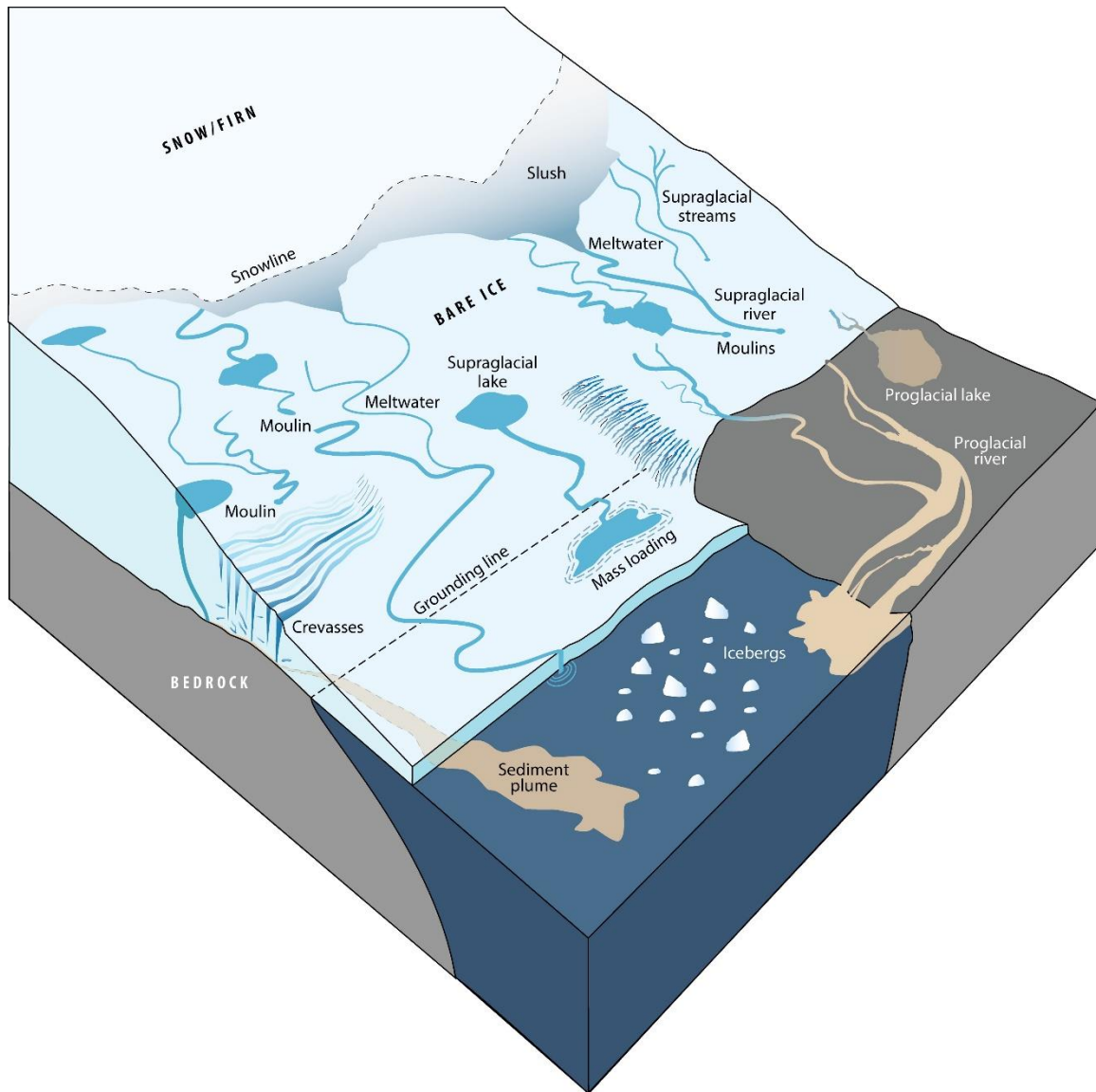


Figure 1-3: Schematic of supraglacial stream and river processes.

Meltwater from ablating snow, firn, and bare ice is transported through supraglacial stream/river channels across bare ice and ice shelves. Their thermally incised channels may terminate directly into moulins, in supraglacial lakes that in turn drain into moulins or outlet streams, or in crevasses. Lake drainages, moulins, and crevasses connect surface climatology and meltwater runoff with en-/subglacial conduits and can

modulate a glacier's internal thermal properties, subglacial water pressure, and sometimes sliding velocity. Alternatively, supraglacial streams/ rivers may drain directly off the ice into a proglacial lake, river, or fjord with no modification from en-/subglacial processes or remain stored in supraglacial lakes through the winter. In temperate glaciers, moulins commonly supply water to sediment-rich proglacial rivers that emerge where subglacial eskers arrive at the ice edge. In marine environments, esker flows commonly produce turbid sediment plumes in coastal waters near the ice front. Supraglacial streams and rivers can terminate in lakes on ice shelves, which may stress ice shelf integrity via mass loading, or drain directly into the ocean with no impoundment or ice shelf weakening. Illustration by Matt Zebrowski, UCLA Department of Geography.

1.11 Tables

Source	Location	Time	Minimum discharge ($\text{m}^3 \text{s}^{-1}$)	Maximum discharge ($\text{m}^3 \text{s}^{-1}$)	Number of streams	Method and/or notes
Holmes (1955)	Alpha River, Project Mint Julep, southwest Greenland	July 21 – August 15, 1953	0.14	5.11	1	Evidence of wading measurements with mechanical flow meter (inferred from Holmes (1955, Photo 5, Pg. 28)).
Leopold & Wolman (1960)	Dinwoody Glacier, Wind River Range, Wyoming, USA	NA	0.07	0.07	>1	NA
Knighton (1972)	Østerdalsisen Glacier, Svartisen ice cap, Norway	July–August, year NA	0.005	0.02	1	NA
Ferguson (1973)	Lower Arolla Glacier, Switzerland	1967	<0.01	>0.08	3	Surveys of channel geometry at 20 stations on three streams plus salt-dilution discharge measurements Range in discharge not specified Approximated from Ferguson (1973, figure 2)
Müller & Iken (1973)	White Glacier, Axel Heiberg Island, Canada	1959–1969	~0	>0.15	NA	Approximated from Müller & Iken (1973, figure 2 and figure 3)
Dozier (1974)	Capps Glacier, Chitistone Pass, Wrangell Mountains, Alaska, USA	1969	0.0076	0.30	2	Manual measurements of stream width and depth Velocity measured with Price-type current meter
Knighton (1981)	Austre Okstindbreen, Norway	NA	0.002	0.052	3	NA
Dowdeswell (1982)	Sylgjujökull, west Vatnajökull, Iceland	July 1979	0.003–0.107 (mean peak discharge, 3-h records for 5 days)	0.003–0.107 (mean peak discharge, 3-h records for 5 days)	9	Product of cross-sectional area and velocity
Echelmeyer & Harrison (1990)	Jakobshavn Isbræ, west Greenland	1985–1986	50–80	50–80	1	Discharge range given for large river flowing along center of glacier that terminates above ~900-m elevation
Carver et al. (1994)	Harlech Gletscher, east Greenland	August 1989	0	1.0	1	Observe of pulsating discharge with 6-7 s lags between pulses
Kostrzewski & Zwolinski (1995)	Ragnarbreen, west Spitsbergen, Norway	July 1985	0.003	0.016	1	Width and depth manually measured Surface velocity measured with float

						method and correction applied for depth integrated velocity
Kohler (1995)	Storglaciaren, Sweden	1988	~0.25	~1.5	5	Discharge inferred from Kohler (1995, figure 3)
Brykala (1999)	Waldemar Glacier, northwest Spitsbergen, Norway	July–August 1997	0.00005	0.0947	1	NA
Hock et al. (1999)	Aletschgletscher, Switzerland	1990, 1991	0.0005	0.002	Several	NA
Willis et al. (2002)	Haut Glacier d’Arolla, Switzerland	August 1993	$\sim 0 \pm 0.014$	$> 0.25 \pm 0.014$	1	Stage-discharge rating curve established using detrended pressure transducer data and six discharge measurements Error given as root mean square error
Mernild et al. (2006)	Mittivakkat Glacier, Ammassalik Island, southeast Greenland	August 2004, May 2005	0.012	0.034	5	Hydraulic radius (product of width and depth) manually measured at cross sections Velocity calculated using Manning’s formula
Bingham et al. (2005)	John Evans Glacier, Ellesmere Island, Canada	2000–2001	> 0	< 2	1	Stage-discharge rating curve
Scott et al. (2010)	Mendenhall Glacier, Alaska, USA	NA	0.01	0.02	1	NA
McGrath et al. (2011)	69.554°N, 49.899°W, west Greenland	August 3–17, 2009	0.18 ± 0.05 (daily average)	0.18 ± 0.05 (daily average)	1	Manual survey of cross-sectional area Stage recordings with noncontact sonic level sensor Velocity measurements of in-channel propeller
Karlstrom et al. (2014)	Llewellyn Glacier, Juneau Ice Field, British Columbia, Canada	August 2010	0.01 (daytime average)	0.01 (daytime average)	> 1	Manual measurements of width and depth Velocity measurements with acoustic Doppler velocimeter
Smith et al. (2015)	Southwest Greenland Ice Sheet	July 2012	0.36 ± 3.6	17.72 ± 3.6	523	Width retrieval from high-resolution WorldView-1/-2 satellite imagery Depth retrieval from WorldView-1/-2 using field-calibrated spectral relationship between depth and reflectance (Legleiter et al. 2014) Velocity determined from field-calibrated hydraulic-geometry relationships
Germain & Moorman (2016)	Fountain Glacier, Bylot Island, Nunavut,	2014	0.01	1	1	Stage-discharge rating curve established with 13 manual

	Canada					measurements
Gleason et al. (2016)	Southwest Greenland Ice Sheet	2012	Small: 0.006 Large: 4.58	Small: 0.402 Large: 23.12	9	Small streams surveyed with manual mechanical instruments Large streams surveyed with acoustic doppler current profiler
Smith et al. (2017)	Southwest Greenland Ice Sheet	July 2015	4.61	26.73	1	Acoustic doppler current profiler
Bell et al. (2017)	Nansen Ice Shelf, Antarctica	2006–2015	259	806	1	Width calculated from Landsat-8 Depth retrieval using reflectance-depth optical band ratios Velocity estimates using Manning's equation
San Clements et al. (2017)	Cotton Glacier, McMurdo Dry Valleys, Antarctica	2011	0.11 (one measurement)	0.11 (one measurement)	1	Width calculated manually Depth from pressure transducer Hydroacoustic velocity

Table 1-1: Summary of discharge measurements.

TABLE 1-2			
Source	Location	Rate (cm d⁻¹)	Method
Holmes (1955); USACE (1953)	Greenland Ice Sheet	~6.5	Measured
Ferguson (1973)	Lower Arolla Glacier, Switzerland	2.6–11.2	Modeled
Marston (1983)	Juneau Icefield	4–8	Measured
Fountain & Walder (1998)	Theoretical channel, where $n = 0.1 \text{ s m}^{-1/3}$, $\rho_w = 1000 \text{ kg m}^{-3}$, $\rho_i = 900 \text{ kg m}^{-3}$, $g = 9.8 \text{ m s}^{-2}$, $h_{iw} = 335 \text{ kJ kg}^{-1}$, $S = .1$, $Q = 1\text{--}100 \text{ m}^3 \text{ s}^{-1}$	7.95 (if $Q = 1 \text{ m}^3 \text{ s}^{-1}$) 22.19 (if $Q = 5 \text{ m}^3 \text{ s}^{-1}$) 27.40 (if $Q = 10 \text{ m}^3 \text{ s}^{-1}$) 142.47 (if $Q = 100 \text{ m}^3 \text{ s}^{-1}$)	Modeled
Isenko & Mavlyudov (2002)	Fisht Flacier, West Caucasus, Russia	4–7	Measured
Willis et al. (2002)	Haut Glacier d’Arolla, Switzerland	7	Inferred from detrended pressure transducer time series shown in Willis et al. (2002, figure 6)
Isenko et al. (2005)	Fisht Flacier, West Caucasus, Russia Perito Moreno Glacier, Patagonia	3–4 (morning) 7–10 (afternoon)	Measured
McGrath et al. (2011)	Greenland Ice Sheet	3.3 ± 0.47	Measured
Jarosch & Gudmundsson (2012)		1.66–29.08 (if $Q = 1 \text{ m}^3 \text{ s}^{-1}$) 8.89–838.78 (if $Q = 10 \text{ m}^3 \text{ s}^{-1}$) 37.96–143.97 (if $Q = 100 \text{ m}^3 \text{ s}^{-1}$)	Modeled
Karlstrom & Yang (2016)	Greenland Ice Sheet	1–4	Modeled

Table 1-2: Summary of channel incision rates.

1.12 References

- Ahlmann HW. **1922**. Glaciers in Jotunheim and their physiography. *Geogr. Ann.* 4: 1–57
- Ahlmann HW. **1923**. Physico-geographical researches in the Horung Massive, Jotunheim: the recrystallization of snow into firn and the glaciation of the latter. *Geogr. Ann.* 5: 51–58
- Ahlmann HW, Rosenbaum L. **1933**. Scientific results of the Swedish-Norwegian Arctic Expedition in the summer of 1931, Parts I–III. *Geogr. Ann.* 15: 1–68
- Allen GH, Pavelsky TM. **2015**. Patterns of river width and surface area newly revealed by the satellite-derived North American River Width (NARWidth) dataset. *Geophys. Res. Lett.* 42: 395–402
- Allen GH, Pavelsky TM. **2018**. Global extent of rivers and streams. *Science* 361: 585–88
- Andrews LC, Catania GA, Hoffman MJ, Gulley JD, Lüthi MP, et al. **2014**. Direct observations of evolving subglacial drainage beneath the Greenland Ice Sheet. *Nature* 514: 80–83
- Arnold NS, Banwell AF, Willis IC. **2014**. High-resolution modelling of the seasonal evolution of surface water storage on the Greenland Ice Sheet. *Cryosphere* 8(4): 1149–60

- Arnold NS, Rees WG, Hodson AJ, Kohler J. **2006**. Topographic controls on the surface energy balance of a high Arctic valley glacier. *J. Geophys. Res.* 111: F02011
- Arnold NS, Richards K, Willis I, Sharp M. **1998**. Initial results from a distributed, physically based model of glacier hydrology. *Hydrol. Process.* 12(2): 191–219
- Banwell AF, Arnold NS, Willis IC, Tedesco M, Ahlstrøm AP. **2012**. Modeling supraglacial water routing and lake filling on the Greenland Ice Sheet. *J. Geophys. Res.* 117: F04012
- Banwell AF, Hewitt I, Willis I, Arnold N. **2016**. Moulin density controls drainage development beneath the Greenland ice sheet. *J. Geophys. Res. Earth Surf.* 121(12): 2248–69
- Banwell AF, MacAyeal DR, Sergienko OV. **2013a**. Breakup of the Larsen B Ice Shelf triggered by chain reaction drainage of supraglacial lakes. *Geophys. Res. Lett.* 40(22): 5872–76
- Banwell AF, Willis IC, Arnold NS. **2013b**. Modeling subglacial water routing at Paakitsoq, W Greenland. *J. Geophys. Res. Earth Surf.* 118(3): 1282–95
- Barr W. **2015**. Alfred de Quervain's Swiss Greenland expeditions, 1909 and 1912. *Polar Rec.* 51(4): 366–85

- Bartholomew ID, Nienow P, Sole A, Douglas M, Cowton T, et al. **2011a**.
Supraglacial forcing of subglacial drainage in the ablation zone of the
Greenland ice sheet. *Geophys. Res. Lett.* 38: L08502
- Bartholomew ID, Nienow P, Sole A, Mair D, Cowton T, et al. **2011b**.
Seasonal variations in Greenland Ice Sheet motion: inland extent and
behaviour at higher elevations. *Earth Planet. Sci. Lett.* 307(3–4): 271–78
- Behrens H, Bergmann H, Moser H, Ambach W, Jochum O. **1971**. On the
water channels of the internal drainage system of the Hintereisferner,
Ötztal Alps, Austria. *J. Glaciol.* 14(72): 375–82
- Bell RE, Chu W, Kingslake J, Das I, Tedesco M, et al. **2017**. Antarctic ice
shelf potentially stabilized by export of meltwater in surface river. *Nature*
544(7650): 344–48
- Benson CS. **1960**. *Stratigraphic studies in the snow and firn of the
Greenland ice sheet*. PhD Diss., Calif. Inst. Technol., Pasadena
- Bingham RG, Nienow PW, Sharp MJ, Boon S. **2005**. Subglacial drainage
processes at a High Arctic polythermal valley glacier. *J. Glaciol.* 51(172):
15–24
- Birnie RV, Gordon JE. **1980**. Drainage systems associated with snow melt,
South Shetland Islands, Antarctica. *Geogr. Ann. Ser. A Phys. Geogr.*
62(1–2): 57–62

Bøggild CE, Brandt RE, Brown KJ, Warren SG. **2010**. The ablation zone in northeast Greenland: ice types, albedos and impurities. *J. Glaciol.* 56(195): 101–13

Bonnema MG, Sikder S, Hossain F, Durand M, Gleason CJ, Bjerklie DM. **2016**. Benchmarking wide swath altimetry-based river discharge estimation algorithms for the Ganges river system. *Water Resour. Res.* 52(4): 2439–61

Braudrick CA, Dietrich WE, Leverich GT, Sklar LS. **2009**. Experimental evidence for the conditions necessary to sustain meandering in coarse-bedded rivers. *PNAS* 106(40): 16936–41

Brykala D. **1998a**. Evolution of supraglacial drainage on Waldemar Glacier (Spitsbergen) in the period 1936–1998. In *Polish Polar Studies: 25th International Polar Symposium*, pp. 247–61. Warsaw: Inst. Geofiz. Polskiej Akad. Nauk

Brykala D. **1998b**. Short-term changes of flow intensity and hydraulic geometry of the supraglacial stream on the Waldemar Glacier (NW Spitsbergen). In *Quaternary Paleogeography and Changes of the Polar Environment: Polar Session. IV Conference of Polish Geomorphologists, Lublin, 3–6 June 1998*, pp. 25–39. Lublin, Pol.: Maria Curie-Skłodowska Univ. Press

- Brykala D. **1999**. Hydraulic geometry of a supraglacial stream on the Waldemar Glacier (Spitsbergen) in the summer of 1997. *Pol. Polar Stud.* 26: 51–64
- Burkimsher M. **1983**. Investigations of glacier hydrological systems using dye tracer techniques: observations at Pasterzengletscher, Austria. *J. Glaciol.* 29(103): 403–16
- Carver S, Sear D, Valentine E. **1994**. An observation of roll waves in a supraglacial meltwater channel, Harlech Gletscher, East Greenland. *J. Glaciol.* 40(134): 75–78
- Catania GA, Neumann TA. **2010**. Persistent englacial drainage features in the Greenland Ice Sheet. *Geophys. Res. Lett.* 37: L02501
- Cathles LM, Abbot DS, Bassis JN, MacAyeal DR. **2011**. Modeling surface-roughness/solar-ablation feedback: application to small-scale surface channels and crevasses of the Greenland ice sheet. *Ann. Glaciol.* 52(59): 99–108
- Chandler DM, Wadham JL, Lis GP, Cowton T, Sole A, et al. **2013**. Evolution of the subglacial drainage system beneath the Greenland Ice Sheet revealed by tracers. *Nat. Geosci.* 6(3): 195–98
- Chapman FS. **1932**. *Northern Lights: The Official Account of the British Arctic Air-Route Expedition*. London: Chatto and Windus
- Charalampidis C, van As D, Colgan WT, Fausto RS, Macferrin M, Machguth H. **2016**. Thermal tracing of retained meltwater in the lower accumulation

- area of the Southwestern Greenland ice sheet. *Ann. Glaciol.* 57(72): 1–10
- Chow VTE. **1959**. *Open-Channel Hydraulics*. New York: McGraw-Hill
- Chu VW. **2014**. Greenland ice sheet hydrology: a review. *Prog. Phys. Geogr.* 38(1): 19–54
- Chu W, Creyts TT, Bell RE. **2016a**. Rerouting of subglacial water flow between neighboring glaciers in West Greenland. *J. Geophys. Res. Earth Surf.* 121: 925–38
- Chu W, Schroeder DM, Seroussi H, Creyts TT, Palmer SJ, Bell RE. **2016b**. Extensive winter subglacial water storage beneath the Greenland Ice Sheet. *Geophys. Res. Lett.* 43(24): 12484–92
- Church M. **2006**. Bed material transport and the morphology of alluvial river channels. *Annu. Rev. Earth Planet. Sci.* 34: 325–54
- Clarke GKC. **2003**. Hydraulics of subglacial outburst floods: new insights from the Spring-Hutter formulation. *J. Glaciol.* 49(165): 299–313
- Clason CC, Mair DWF, Nienow PW, Bartholomew ID, Sole A, et al. **2015**. Modelling the transfer of supraglacial meltwater to the bed of Leverett Glacier, Southwest Greenland. *Cryosphere* 9(1): 123–38
- Colgan W, Sommers A, Rajaram H, Abdalati W, Frahm J. **2015**. Considering thermal-viscous collapse of the Greenland ice sheet. *Earth's Future* 3: 252–67

- Colgan W, Steffen K, McLamb WS, Abdalati W, Rajaram H, et al. **2011**. An increase in crevasse extent, West Greenland: hydrologic implications. *Geophys. Res. Lett.* 38: L18502
- Cooley SW, Smith LC, Ryan JC, Pitcher LH, Pavelsky TM. **2019**. Arctic-Boreal lake dynamics revealed using CubeSat imagery. *Geophys. Res. Lett.* In press. <https://doi.org/10.1029/2018GL081584>
- Cooley SW, Smith LC, Stepan L, Mascaro J. **2017**. Tracking dynamic northern surface water changes with high-frequency planet CubeSat imagery. *Remote Sens.* 9(12): 1306
- Cooper MG, Smith LC, Rennermalm AK, Miège C, Pitcher LH, et al. **2018**. Near surface meltwater storage in low-density bare ice of the Greenland ice sheet ablation zone. *Cryosphere* 12: 955–70
- Cowton T, Nienow P, Sole A, Wadham J, Lis G, et al. **2013**. Evolution of drainage system morphology at a land-terminating Greenlandic outlet glacier. *J. Geophys. Res. Earth Surf.* 118(1): 29–41
- Cuffey K, Paterson WSB. **2010**. *The Physics of Glaciers*. Burlington, MA: Elsevier. 4th ed.
- Das SB, Joughin I, Behn MD, Howat IM, King MA, et al. **2008**. Fracture propagation to the base of the Greenland Ice Sheet during supraglacial lake drainage. *Science* 320(5877): 778–81
- David TW, Priestley E. **1914**. *British Antarctic Expedition, 1907–9, Under the Command of Sir E.H. Shackleton, c.v.o. Reports on the Scientific*

Investigations, Geology Vol. 1: Glaciology, Physiography, Stratigraphy and Tectonic Geology of South Victoria Land. London: William Heinemann

de Fleurian B, Morlighem M, Seroussi H, Rignot E, van den Broeke MR, et al.

2016. A modeling study of the effect of runoff variability on the effective pressure beneath Russell Glacier, West Greenland. *J. Geophys. Res. Earth Surf.* 121(10): 1834–48

DeConto RM, Pollard D. **2016.** Contribution of Antarctica to past and future sea-level rise. *Nature* 531(7596): 591–97

Dewart G. **1966.** Moulins on Kaskawulsh Glacier, Yukon Territory. *J. Glaciol.* 6(44): 320–21

Dowdeswell JA. **1982.** Supraglacial re-sedimentation from melt-water streams on to snow overlying glacier ice, Sylgjujökull, West Vatnajökull, Iceland. *J. Glaciol.* 28(99): 365–75

Dozier J. **1974.** Channel adjustment in supraglacial streams. In *Icefield Ranges Research Project Scientific Results*, ed. VC Bushnell, MG Marcus, Vol. 4, pp. 189–205. New York: Am. Geogr. Soc.

Dozier J. **1976.** An examination of the variance minimization tendencies of a supraglacial stream. *J. Hydrol.* 31(3–4): 359–80

Durand M, Gleason CJ, Garambois PA, Bjerklie D, Smith LC, et al. **2016.** An intercomparison of remote sensing river discharge estimation algorithms

- from measurements of river height, width, and slope. *Water Resour. Res.* 52(6): 4527–49
- Dutton A, Carlson AE, Long AJ, Milne GA, Clark PU, et al. **2015**. Sea-level rise due to polar ice-sheet mass loss during past warm periods. *Science* 349(6244): aaa4019
- Echelmeyer K, Harrison WD. **1990**. Jakobshavns Isbræ, West Greenland: seasonal variations in velocity—or lack thereof. *J. Glaciol.* 36(122): 82–88
- Ewing KJ. **1970**. Supraglacial streams of the Kaskawulsh Glacier. In *Icefield Ranges Research Project, Scientific Results*, ed. VC Bushnell, RH Ragle, Vol. 3, pp. 153–62. New York: Am. Geogr. Soc.
- Ferguson RI. **1973**. Sinuosity of supraglacial streams. *Geol. Soc. Am. Bull.* 84(1): 251–56
- Flett V, Maurice L, Finlayson A, Black AR, MacDonald AM, et al. **2017**. Meltwater flow through a rapidly deglaciating glacier and foreland catchment system: Virkisjökull, SE Iceland. *Hydrol. Res.* 48(6): 1666–81
- Flowers GE. **2018**. Hydrology and the future of the Greenland Ice Sheet. *Nat. Commun.* 9(1): 2729
- Fortner SK, Tranter M, Fountain A, Lyons WB, Welch KA. **2005**. The geochemistry of supraglacial streams of Canada Glacier, Taylor Valley (Antarctica), and their evolution into proglacial waters. *Aquat. Geochem.* 11(4): 391–412

- Fountain AG, Walder JS. **1998**. Water flow through temperate glaciers. *Rev. Geophys.* 36(3): 299–328
- Germain SLS, Moorman BJ. **2016**. The development of a pulsating supraglacial stream. *Ann. Glaciol.* 57(72): 31–38
- Gleason CJ, Smith LC. **2014**. Toward global mapping of river discharge using satellite images and at-many-stations hydraulic geometry. *PNAS* 111(13): 4788–91
- Gleason CJ, Smith LC, Chu VW, Legleiter CJ, Pitcher LH, et al. **2016**. Characterizing supraglacial meltwater channel hydraulics on the Greenland Ice Sheet from in situ observations. *Earth Surf. Process. Landf.* 41(14): 2111–22
- Gleason CJ, Smith LC, Lee J. **2014**. Retrieval of river discharge solely from satellite imagery and at-many-stations hydraulic geometry: sensitivity to river form and optimization parameters. *Water Resour. Res.* 50(12): 9604–19
- Gleason CJ, Wang J. **2015**. Theoretical basis for at-many-stations hydraulic geometry. *Geophys. Res. Lett.* 42(17): 7107–14
- Glen AR. **1941**. A Sub-Arctic glacier cap: the West Ice of North East Land. *Geogr. J.* 98(2): 65–76
- Greenwood SL, Clason CC, Helanow C, Margold M. **2016**. Theoretical, contemporary observational and palaeo-perspectives on ice sheet hydrology: processes and products. *Earth-Sci. Rev.* 155: 1–27

- Greuell W. **2000**. Melt-water accumulation on the surface of the Greenland ice sheet: effect on albedo and mass balance. *Geogr. Ann. Ser. A Phys. Geogr.* 82(4): 489–98
- Hagemann MW, Gleason CJ, Durand MT. **2017**. BAM: Bayesian AMHG-Manning inference of discharge using remotely sensed stream width, slope, and height. *Water Resour. Res.* 53(11): 9692–707
- Hagen JO, Liestøl O, Roland E, Jørgensen T. **1993**. *Glacier Atlas of Svalbard and Jan Mayen*. Oslo: Norsk Polarinstitut
- Hambrey MJ. **1977**. Supraglacial drainage and its relationship to structure, with particular reference to Charles Rabots Bre, Okstindan, Norway. *Nor. Geogr. Tidsskr.–Nor. J. Geogr.* 31(2): 69–77
- Hammer KM, Smith ND. **1983**. Sediment production and transport in a proglacial stream: Hilda Glacier, Alberta, Canada. *Boreas* 12(2): 91–106
- Harrington JA, Humphrey NF, Harper JT. **2015**. Temperature distribution and thermal anomalies along a flowline of the Greenland ice sheet. *Ann. Glaciol.* 56(70): 98–104
- Hock R, Iken A, Wangler A. **1999**. Tracer experiments and borehole observations in the overdeepening of Aletschgletscher, Switzerland. *Ann. Glaciol.* 28: 253–60
- Hodgkins R. **1997**. Glacier hydrology in Svalbard, Norwegian High Arctic. *Quat. Sci. Rev.* 16(9): 957–73

- Hodgkins R. **2001**. Seasonal evolution of meltwater generation, storage and discharge at a non-temperate glacier in Svalbard. *Hydrol. Process.* 15(3): 441–60
- Hodson A, Anesio AM, Ng F, Watson R, Quirk J, et al. **2007**. A glacier respire: quantifying the distribution and respiration CO₂ flux of cryoconite across an entire arctic supraglacial ecosystem. *J. Geophys. Res.* 112: G04S36
- Holmes G. **1955**. Morphology and hydrology of the Mint Julep area, southwest Greenland. In *Project Mint Julep: Investigation of Smooth Ice Areas of the Greenland Ice Cap, 1953; Part II: Special Scientific Reports*. Maxwell Air Force Base, AL: Arct. Desert Tropic Inf. Cent., Res. Stud. Inst., Air Univ.
- Hooke RL. **1989**. Englacial and subglacial hydrology: a qualitative review. *Arct. Alp. Res.* 21(3): 221–33
- Howat IM, de la Peña S, van Angelen JH, Lenaerts JTM, van den Broeke MR. **2013**. Brief communication “expansion of meltwater lakes on the Greenland Ice Sheet.” *Cryosphere* 7: 201–4
- Hubbard B, Nienow P. **1997**. Alpine subglacial hydrology. *Quat. Sci. Rev.* 16(9): 939–55
- Hugget RJ. **2007**. *Fundamentals of Geomorphology*, Vol. 11. London: Routledge Taylor & Francis Group. 2nd ed.

- Ignéczi Á, Sole AJ, Livingstone SJ, Leeson AA, Fettweis X, et al. **2016**. Northeast sector of the Greenland Ice Sheet to undergo the greatest inland expansion of supraglacial lakes during the 21st century. *Geophys. Res. Lett.* 43(18): 9729–38
- Iken A. **1972**. Measurements of water pressure in moulins as part of a movement study of the White Glacier, Axel Heiberg Island, Northwest Territories, Canada. *J. Glaciol.* 11(61): 53–58
- Iken A, Bindschadler RA. **1986**. Combined measurements of subglacial water pressure and surface velocity of Findelengletscher, Switzerland: conclusions about drainage system and sliding mechanism. *J. Glaciol.* 32(110): 101–19
- Irvine-Fynn TDL, Hodson AJ, Moorman BJ, Vatne G, Hubbard AL. **2011**. Polythermal glacier hydrology: a review. *Rev. Geophys.* 49(4): RG4002
- Isenko E, Mavlyudov B. **2002**. On the intensity of ice melting in supraglacial and englacial channels. *Bull. Glaciol. Res.* 19: 93–99
- Isenko E, Naruse R, Mavlyudov B. **2005**. Water temperature in englacial and supraglacial channels: change along the flow and contribution to ice melting on the channel wall. *Cold Reg. Sci. Technol.* 42(1): 53–62
- Jarosch AH, Gudmundsson MT. **2012**. A numerical model for meltwater channel evolution in glaciers. *Cryosphere* 6(2): 493–503
- Jarvis GT, Clarke GK. **1974**. Thermal effects of crevassing on Steele Glacier, Yukon Territory, Canada. *J. Glaciol.* 13(68): 243–54

- Karlstrom L, Gajjar P, Manga M. **2013**. Meander formation in supraglacial streams. *J. Geophys. Res. Earth Surf.* 118(3): 1897–907
- Karlstrom L, Yang K. **2016**. Fluvial supraglacial landscape evolution on the Greenland Ice Sheet. *Geophys. Res. Lett.* 43(6): 2683–92
- Karlstrom L, Zok A, Manga M. **2014**. Near-surface permeability in a supraglacial drainage basin on the Llewellyn Glacier, Juneau Icefield, British Columbia. *Cryosphere* 8(2): 537–46
- King L, Hassan MA, Yang K, Flowers G. **2016**. Flow routing for delineating supraglacial meltwater channel networks. *Remote Sens.* 8(12): 988
- Kingslake J, Ely JC, Das I, Bell RE. **2017**. Widespread movement of meltwater onto and across Antarctic ice shelves. *Nature* 544(7650): 349–52
- Kingslake J, Ng F, Sole A. **2015**. Modelling channelized surface drainage of supraglacial lakes. *J. Glaciol.* 61(225): 185–99
- Knighton AD. **1972**. Meandering habit of supraglacial streams. *Bull. Geol. Soc. Am.* 83(1): 201–4
- Knighton AD. **1981**. Channel form and flow characteristics of supraglacial streams, Austre Okstindbreen, Norway. *Arct. Alp. Res.* 13(3): 295–306
- Knighton AD. **1985**. Channel form adjustment in supraglacial streams, Austre Okstindbreen, Norway. *Arct. Alp. Res.* 17(4): 451–66
- Knighton D. **1998**. *Fluvial Forms and Processes: A New Perspective*. London: Arnold

- Koenig LS, Lampkin DJ, Montgomery LN, Hamilton SL, Turrin JB, et al. **2015**. Wintertime storage of water in buried supraglacial lakes across the Greenland Ice Sheet. *Cryosphere* 9(4): 1333–42
- Kohler J. **1995**. Determining the extent of pressurized flow beneath Storglaciaren, Sweden, using results of tracer experiments and measurements of input and output discharge. *J. Glaciol.* 41(138): 217–31
- Kostrzewski A, Zwolinski Z. **1995**. Hydraulic geometry of a supraglacial stream, Ragnarbreen, Spitsbergen. *Quaest. Geogr.* (4): 165–76
- Krimmel RM, Tangborn WV, Meier MF. **1972**. Water flow through a temperate glacier. In *The Role of Snow and Ice in Hydrology Symposium, Proceedings*, Vol. 1, pp. 401–16. Banff: UNESCO-WMO-IASH/UNESCO-OMM-AISH
- KSS. **1934**. Review: the Swedish-Norwegian arctic expedition, 1931. *Geogr. J.* 83(5): 420–25
- Lampkin DJ, VanderBerg J. **2014**. Supraglacial melt channel networks in the Jakobshavn Isbræ region during the 2007 melt season. *Hydrol. Process.* 28(25): 6038–53
- Lawson DE. **1993**. *Glaciohydrologic and Glaciohydraulic Effects on Runoff and Sediment Yield in Glacierized Basins*. Hanover: NH: US Army Corps Eng. Cold Reg. Res. Eng. Lab.

- Leeson AA, Shepherd A, Briggs K, Howat I, Fettweis X, et al. **2015**.
Supraglacial lakes on the Greenland ice sheet advance inland under
warming climate. *Nat. Clim. Change* 5(1): 51–55
- Legleiter CJ, Tedesco M, Smith LC, Behar AE, Overstreet BT. **2014**. Mapping
the bathymetry of supraglacial lakes and streams on the Greenland ice
sheet using field measurements and high-resolution satellite images.
Cryosphere 8: 215–28
- Leopold LB, Maddock TJ. **1953**. *The hydraulic geometry of stream channels
and some physiographic implications*. US Geol. Surv. Prof. Pap. 252,
Dep. Interior, Washington, DC
- Leopold LB, Wolman MG. **1960**. River meanders. *Bull. Geol. Soc. Am.* 71(6):
769–93
- Liestøl O. **1993**. Glaciers of Europe—Glaciers of Svalbard, Norway. In
Satellite Image Atlas of Glaciers of the World, ed. RS Williams Jr., JG
Ferrigno, pp. E127–51. Washington, DC: US Gov. Print. Off.
- Lindsay M. **1935**. The British Trans-Greenland Expedition, 1934. *Geogr. J.*
85(5): 393–408
- Lindskog E. **1928**. The drainage, especially that of the Styggedal Glacier.
Geogr. Ann. 10: 308–39
- Locker AR. **1951**. *Operation Skyline*. Rep., 6th Air Rescue Squadron,
Northeast Air Command, US Air Force

- Lüthi MP, Ryser C, Andrews LC, Catania GA, Funk M, et al. **2015**. Heat sources within the Greenland Ice Sheet: dissipation, temperate paleo-firn and cryo-hydrologic warming. *Cryosphere* 9(1): 245–53
- MacDonald AM, Black AR, Ó Dochartaigh BE, Everest J, Darling WG, et al. **2016**. Using stable isotopes and continuous meltwater river monitoring to investigate the hydrology of a rapidly retreating Icelandic outlet glacier. *Ann. Glaciol.* 57(72): 151–58
- Macdonald GJ, Banwell AF, Macayeal DR. **2018**. Seasonal evolution of supraglacial lakes on a floating ice tongue, Petermann Glacier, Greenland. *Ann. Glaciol.* 59(76): 56–65
- Machguth H, MacFerrin M, van As D, Box JE, Charalampidis C, et al. **2016**. Greenland meltwater storage in firn limited by near-surface ice formation. *Nat. Clim. Change* 6(4): 390–95
- Mantelli E, Camporeale C, Ridolfi L. **2015**. Supraglacial channel inception: modeling and processes. *Water Resour. Res.* 51(9): 7044–63
- Marston RA. **1983**. Supraglacial stream dynamics on the Juneau Icefield. *Ann. Assoc. Am. Geogr.* 73(4): 597–608
- McGrath D, Colgan W, Steffen K, Lauffenburger P, Balog J. **2011**. Assessing the summer water budget of a moulin basin in the Sermeq Avannarleq ablation region, Greenland ice sheet. *J. Glaciol.* 57(205): 954–64
- Mernild SH, Hasholt B, Liston GE. **2006**. Water flow through Mittivakkat Glacier, Ammassalik Island, SE Greenland. *J. Geog.* 106(1): 25–44

- Mernild SH, Hasholt B, Liston GE. **2008**. Climatic control on river discharge simulations, Zackenberg River drainage basin, northeast Greenland. *Hydrol. Process.* 22(12): 1932–48
- Mernild SH, Liston GE, van den Broeke M. **2012**. Simulated internal storage buildup, release, and runoff from Greenland Ice Sheet at Kangerlussuaq, West Greenland. *Arct. Antarct. Alp. Res.* 44(1): 83–94
- Müller F, Iken A. **1973**. Velocity fluctuations and water regime of Arctic valley glaciers. In *Symposium on the Hydrology of Glaciers*, pp. 165–82. London: Int. Assoc. Sci. Hydrol.
- Munneke PK, Luckman AJ, Bevan SL, Smeets CJPP, Gilbert E, et al. **2018**. Intense winter surface melt on an Antarctic ice shelf. *Geophys. Res. Lett.* 45: 7615–23
- Munro SD. **2010**. Runoff response time of a loosely defined supraglacial microbasin. *Hydrol. Earth Syst. Sci. Discuss.* 7: 1569–87
- Munro SD. **2011**. Delays of supraglacial runoff from differently defined microbasin areas on the Peyto Glacier. *Hydrol. Process.* 25(19): 2983–94
- Nansen F. **1906**. *The First Crossing of Greenland*. London: Longmans Green & Co.
- Nobles LH. **1960**. *Glaciological investigations, Nunatarssuaq ice ramp, northwestern Greenland*. Tech. Rep. 66, US Army Snow, Ice Permafr. Res. Establ., Corps Eng., Wilmette, IL

- Onesti LJ. **1985**. Meteorological conditions that initiate slushflows in the Central Brooks Range, Alaska. *Ann. Glaciol.* 6: 23–25
- Onesti LJ, Hestnes E. **1989**. Slush-flow questionnaire. *Ann. Glaciol.* 13: 226–30
- Orheim O, Lucchitta BK. **1987**. Snow and ice studies by Thematic Mapper and Multispectral Scanner Landsat images. *Ann. Glaciol.* 9: 109–18
- Overeem I, Hudson B, Welty E, Mikkelsen A, Bamber J, et al. **2015**. River inundation suggests ice-sheet runoff retention. *J. Glaciol.* 61(228): 776–88
- Palmer S, Shepherd A, Nienow P, Joughin I. **2011**. Seasonal speedup of the Greenland ice sheet linked to routing of surface water. *Earth Planet. Sci. Lett.* 302(3–4): 423–28
- Parker G. **1975**. Meandering of supraglacial melt streams. *Water Resour. Res.* 11(4): 551–52
- Pekel J-F, Cottam A, Gorelick N, Belward AS. **2016**. High-resolution mapping of global surface water and its long-term changes. *Nature* 540(7633): 418–22
- Pelto M. **2018**. Nioghalvfjærdsbræ 70 km+ long supraglacial stream, Greenland's longest? *AGU Blogosphere, From a Glacier's Perspective*, June 27.
<https://blogs.agu.org/fromaglaciersperspective/2018/06/27/ni>

oghalvfjerdingsbrae-70-km-long-supraglacial-stream-greenlands-longest/

- Phillips HA. **1998**. Surface meltstreams on the Amery Ice Shelf, East Antarctica. *Ann. Glaciol.* 27: 177–81
- Phillips T, Leyk S, Rajaram H, Colgan W, Abdalati W, et al. **2011**. Modeling moulin distribution on Sermeq Avannarleq glacier using ASTER and WorldView imagery and fuzzy set theory. *Remote Sens. Environ.* 115(9): 2292–301
- Phillips T, Rajaram H, Colgan W, Steffen K, Abdalati W. **2013**. Evaluation of cryo-hydrologic warming as an explanation for increased ice velocities in the wet snow zone, Sermeq Avannarleq, West Greenland. *J. Geophys. Res. Earth Surf.* 118(3): 1241–56
- Phillips T, Rajaram H, Steffen K. **2010**. Cryo-hydrologic warming: a potential mechanism for rapid thermal response of ice sheets. *Geophys. Res. Lett.* 37(20): L20503
- Poinar K, Joughin I, Das SB, Behn MD, Lenaerts JTM, van den Broeke MR. **2015**. Limits to future expansion of surface-melt-enhanced ice flow into the interior of western Greenland. *Geophys. Res. Lett.* 42(6): 1800–7
- Rack W, Rott H. **2004**. Pattern of retreat and disintegration of the Larsen B Ice Shelf, Antarctic Peninsula. *Ann. Glaciol.* 39: 505–10
- Raymond CF, Nolan M. **2000**. Drainage of a glacial lake through an ice spillway. In *Debris-Covered Glaciers: Proceedings of an International*

- Workshop Held in Seattle, WA, USA, September 13–15, 2000*, ed. M Nakawo, A Fountain, CF Raymond, pp. 199–210. Oxfordshire, UK: IAHS Press
- Rennermalm AK, Moustafa SE, Mioduszewski J, Chu VW, Forster RR, et al. **2013a**. Understanding Greenland ice sheet hydrology using an integrated multi-scale approach. *Environ. Res. Lett.* 8: 015017
- Rennermalm AK, Smith LC, Chu VW, Forster RR, van den Broeke M, et al. **2013b**. Evidence of meltwater retention within the Greenland ice sheet. *Cryosphere* 7: 1443–45
- Rignot E, Velicogna I, van den Broeke MR, Monaghan A, Lenaerts JTM. **2011**. Acceleration of the contribution of the Greenland and Antarctic ice sheets to sea level rise. *Geophys. Res. Lett.* 38: L05503
- Rippin DM, Pomfret A, King N. **2015**. High resolution mapping of supra-glacial drainage pathways reveals link between micro-channel drainage density, surface roughness and surface reflectance. *Earth Surf. Process. Landf.* 40(10): 1279–90
- Roscoe JH. **1952**. *Contributions to the study of Antarctic surface features by photogeographical methods*. PhD Diss., Univ. Maryland, College Park
- Ryan JC, Hubbard A, Box JE, Brough S, Cameron K, et al. **2017a**. Derivation of high spatial resolution albedo from UAV digital imagery: application over the Greenland Ice Sheet. *Front. Earth Sci.* 5: 40

Ryan JC, Hubbard A, Irvine-Fynn TD, Doyle SH, Cook JM, et al. **2017b**. How robust are in situ observations for validating satellite-derived albedo over the dark zone of the Greenland Ice Sheet? *Geophys. Res. Lett.* 44(12): 6218–25

Ryan JC, Hubbard A, Stibal M, Box JE, Dark Snow Proj. Team. **2016**. Attribution of Greenland's ablating ice surfaces on ice sheet albedo using unmanned aerial systems. *Cryosphere Discuss.*
<https://doi.org/10.5194/tc-2016-204>

Ryan JC, Hubbard A, Stibal M, Irvine-Fynn TD, Cook J, et al. **2018**. Dark zone of the Greenland Ice Sheet controlled by distributed biologically-active impurities. *Nat. Commun.* 9: 1065

SanClements MD, Smith HJ, Foreman CM, Tedesco M, Chin YP, et al. **2017**. Biogeophysical properties of an expansive Antarctic supraglacial stream. *Antarct. Sci.* 29(1): 33–44

Sasgen I, van den Broeke M, Bamber JL, Rignot E, Sørensen LS, et al. **2012**. Timing and origin of recent regional ice-mass loss in Greenland. *Earth Planet. Sci. Lett.* 333–34: 293–303

Scambos TA, Bohlander JA, Shuman CA, Skvarca P. **2004**. Glacier acceleration and thinning after ice shelf collapse in the Larsen B embayment, Antarctica. *Geophys. Res. Lett.* 31(18): 2001–4

Scambos TA, Fricker HA, Liu CC, Bohlander J, Fastook J, et al. **2009**. Ice shelf disintegration by plate bending and hydro-fracture: satellite

- observations and model results of the 2008 Wilkins ice shelf break-ups. *Earth Planet. Sci. Lett.* 280(1–4): 51–60
- Scambos TA, Hulbe CL, Fahnestock M, Bohlander J. **2000**. The link between climate warming and ice shelf breakups in the Antarctic Peninsula. *J. Glaciol.* 46(154): 516–30
- Schoof C. **2010**. Ice-sheet acceleration driven by melt supply variability. *Nature* 468(7325): 803–6
- Scott D, Hood E, Nassry M. **2010**. In-stream uptake and retention of C, N, and P in a supraglacial stream. *Ann. Glaciol.* 51(56): 80–86
- Seaberg SZ, Seaberg JZ, Hooke RL, Wiberg DW. **1988**. Character of the englacial and subglacial drainage system in the lower part of the ablation area of Storglaciären, Sweden, as revealed by dye-trace studies. *J. Glaciol.* 34(117): 228–31
- Selmes N, Murray T, James TD. **2011**. Fast draining lakes on the Greenland Ice Sheet. *Geophys. Res. Lett.* 38: L15501
- Sharp RP. **1947**. The Wolf Creek Glaciers, St. Elias Range, Yukon Territory. *Geogr. Rev.* 37(1): 26–52
- Smith LC, Chu VW, Yang K, Gleason CJ, Pitcher LH, et al. **2015**. Efficient meltwater drainage through supraglacial streams and rivers on the southwest Greenland Ice Sheet. *PNAS* 112(4): 1001–6

- Smith LC, Yang K, Pitcher LH, Overstreet BT, Chu VW, et al. **2017**. Direct measurements of meltwater runoff on the Greenland Ice Sheet surface. *PNAS* 114(50): 201707743
- Stanley AD. **1972**. Observations of the surge of Steele Glacier. In *Icefield Ranges Research Project Scientific Results*, Vol. 3, ed. VC Bushnell, RH Ragle, pp. 61–69. New York: Am. Geogr. Soc. Arct. Inst. N. Am.
- Stenborg T. **1968**. Glacier drainage connected with ice structures. *Geogr. Ann. Ser. A Phys. Geogr.* 50(1): 25–53
- Stenborg T. **1969**. Studies of the internal drainage of glaciers. *Geogr. Ann. Ser. A Phys. Geogr.* 51(1/2): 13–41
- Stibal M, Šabacká M, Žárský J. **2012**. Biological processes on glacier and ice sheet surfaces. *Nat. Geosci.* 5(11): 771–74
- Sturm M, Cosgrove DM. **1990**. An unusual jökulhlaup involving potholes on Black Rapids Glacier, Alaska Range, Alaska, U.S.A. *J. Glaciol.* 36(122): 125–26
- Sugiyama S, Sakakibara D, Matsuno S, Yamaguchi S, Matoba S, Aoki T. **2014**. Initial field observations on Qaanaaq ice cap, northwestern Greenland. *Ann. Glaciol.* 55(66): 25–33
- Swithinbank C. **1988**. *Satellite image atlas of glaciers of the world: Antarctica*. US Geol. Surv. Prof. Pap. 1386-B, US Dep. Interior, Washington, DC

- Takeuchi N. **2002**. Optical characteristics of cryoconite (surface dust) on glaciers: the relationships between light absorbency and the property of organic matter contained in the cryoconite. *Ann. Glaciol.* 34: 409–14
- Tedesco M, Steiner N. **2011**. In-situ multispectral and bathymetric measurements over a supraglacial lake in western Greenland using a remotely controlled watercraft. *Cryosphere* 5(2): 445–52
- Tedesco M, Willis IC, Hoffman MJ, Banwell AF, Alexander P, Arnold NS. **2013**. Ice dynamic response to two modes of surface lake drainage on the Greenland ice sheet. *Environ. Res. Lett.* 8(3): 034007
- Thomsen HH. **1986**. Photogrammetric and satellite mapping of the margin of the inland ice, West Greenland. *Ann. Glaciol.* 8: 164–67
- Thomsen HH, Thorning L, Braithwaite RJ. **1988**. *Glacier-hydrological conditions on the Inland Ice north-east of Jakobshavn/Ilulissat, West Greenland*. Rep. 138, Grønlands Geol. Unders., Denmark
- Thomsen HH, Thorning L, Olesen OB. **1989**. Applied glacier research for planning hydro-electric power, Ilulissat/Jakobshavn, West Greenland. *Ann. Glaciol.* 13: 257–61
- Tranter M, Brown G, Raiswell R, Sharp M, Gurnell A. **1993**. A conceptual model of solute acquisition by Alpine glacial meltwaters. *J. Glaciol.* 39(133): 573–81
- US Army Corps Eng. (USACE). **1947**. *Investigation of construction and maintenance of airdromes on ice, 1947–1948: report of Corps of*

- Engineers observers on Project Snowman of Atlantic Division, ATC. Tech. Rep. 15, US Army Corps Eng. N. Engl. Div., Boston, MA*
- US Army Corps Eng. (USACE). **1953**. *Project Mint Julep: Investigation of a Smooth Ice Area of the Greenland Ice Cap*. Arct. Constr. Frost Eff. Lab., US Eng. Res. Dev. Cent., Boston, MA
- van As D, Andersen ML, Petersen D, Fettweis X, van Angelen JH, et al. **2014**. Increasing meltwater discharge from the Nuuk region of the Greenland ice sheet and implications for mass balance (1960–2012). *J. Glaciol.* 60(220): 314–22
- van As D, Mikkelsen AB, Nielsen MH, Box JE, Liljedahl LC, et al. **2017**. Hypsometric amplification and routing moderation of Greenland ice sheet meltwater release. *Cryosphere* 11(3): 1371–86
- van den Broeke M, Bamber J, Ettema J, Rignot E, Schrama E, et al. **2009**. Partitioning recent Greenland mass loss. *Science* 326(5955): 984–86
- van den Broeke M, Smeets P, Ettema J, van der Veen C, van de Wal R, Oerlemans J. **2008**. Partitioning of melt energy and meltwater fluxes in the ablation zone of the west Greenland ice sheet. *Cryosphere* 2(2): 179–89
- Vaughan DG, Comiso JC, Allison I, Carrasco J, Kaser G, et al. **2013**. Observations: cryosphere. In *Climate Change 2013: The Physical Science Basis. Contribution of Working Group I to the Fifth Assessment Report of the Intergovernmental Panel on Climate Change*, ed. TF Stocker, D Qin,

- G-K Plattner, M Tignor, SK Allen, et al., pp. 317–82. Cambridge, UK: Cambridge Univ. Press
- Whitehead K, Moorman BJ, Hugenholtz CH. **2013**. Brief communication: low-cost, on-demand aerial photogrammetry for glaciological measurement. *Cryosphere* 7(6): 1879–84
- Willis IC, Arnold NS, Brock BW. **2002**. Effect of snowpack removal on energy balance, melt and runoff in a small supraglacial catchment. *Hydrol. Process.* 16(14): 2721–49
- Willis IC, Sharp MJ, Richards KS. **1990**. Configuration of the drainage system of Midtdalsbreen, Norway, as indicated by dye-tracing experiments. *J. Glaciol.* 36(122): 89–101
- Winther J-G, Elvehøy H, Bøggild CE, Sand K, Liston G. **1996**. Melting, runoff and the formation of frozen lakes in a mixed snow and blue-ice field in Dronning Maud Land, Antarctica. *J. Glaciol.* 42(141): 271–78
- Xiao-bo W. **2018**. Diurnal and seasonal variation of glacier meltwater hydrochemistry in Qiyi glacierized catchment in Qilian Mountains, Northwest China: implication for chemical weathering. *J. Mt. Sci.* 15(5): 1035–45
- Xu Z, Schrama E, van der Wal W, van den Broeke M, Enderlin EM. **2015**. Improved GRACE regional mass balance estimates of the Greenland Ice Sheet cross-validated with the input-output method. *Cryosphere Discuss.* 9(5): 4661–99

- Yang K, Karlstrom L, Smith LC, Li M. **2016a**. Automated high-resolution satellite image registration using supraglacial rivers on the Greenland Ice Sheet. *IEEE J. Sel. Top. Appl. Earth Obs. Remote Sens.* 10(3): 845–56
- Yang K, Li M. **2014**. Greenland Ice Sheet surface melt: a review. *Sci. Cold Arid Reg.* 6(2): 99–106
- Yang K, Smith LC. **2013**. Supraglacial streams on the Greenland Ice Sheet delineated from combined spectral-shape information in high-resolution satellite imagery. *IEEE Geosci. Remote Sens. Lett.* 10(4): 801–5
- Yang K, Smith LC. **2016**. Internally drained catchments dominate supraglacial hydrology of the southwest Greenland Ice Sheet. *J. Geophys. Res. Earth Surf.* 121(10): 1891–910
- Yang K, Smith LC, Chu VW, Gleason CJ, Li M. **2015**. A caution on the use of surface digital elevation models to simulate supraglacial hydrology of the Greenland ice sheet. *IEEE J. Sel. Top. Appl. Earth Obs. Remote Sens.* 8(11): 5212–24
- Yang K, Smith LC, Chu VW, Pitcher LH, Gleason CJ, et al. **2016b**. Fluvial morphometry of supraglacial river networks on the southwest Greenland Ice Sheet. *GIScience Remote Sens.* 53(4): 459–82
- Yang K, Smith LC, Karlstrom L, Cooper MG, Tedesco M, et al. **2018**. Supraglacial meltwater routing through internally drained catchments on the Greenland Ice Sheet surface. *Cryosphere* 12: 3791–811

Zeller J. **1967**. Meandering channels in Switzerland. In *Symposium on River Morphology*, pp. 174–86. London: Int. Assoc. Sci. Hydrol.

CHAPTER 2

Direct observation of wintertime meltwater drainage from the Greenland Ice Sheet

2.1 Abstract

Meltwater runoff from the Greenland Ice Sheet (GrIS) significantly contributes to sea level rise and is the dominant driver of enhanced mass loss. While most melt occurs during summer, little is known about its seasonal and/or inter-annual retention within the GrIS. Here, we document evidence of runoff during winter, ~4 months after summertime melt. Ground-penetrating radar and borehole surveys in the proglacial Isortoq River reveal slowly flowing water beneath >0.5 m of river ice. Geochemical analysis of this water indicates previous contact with the ice sheet bed. Comparable surveys in proglacial rivers draining four neighboring catchments found no wintertime drainage, despite a brief surface melt event ~10 days prior. We attribute the observed runoff to residual meltwater storage and release enabled by a >600 m deep trough beneath Isunguata Sermia, but not neighboring glaciers. We conclude that the GrIS bed can stay wet and drain small amounts of meltwater year-round.

2.2 Introduction

The Greenland Ice Sheet (GrIS) is losing mass at an accelerating rate (Nerem et al., 2018; Rignot et al., 2011; Shepherd et al., 2012), primarily due to increases in surface meltwater runoff (van den Broeke et al., 2009, 2016). This is important, because GrIS runoff significantly contributes to global sea level rise (van den Broeke et al., 2016) and thus the vulnerability of coastal population centers (Hauer et al., 2016). Despite recent increases in surface melt and runoff, process-level understanding of GrIS hydrology remains deficient, especially outside of the summer melt season. In particular, the temporal and volumetric partitioning between supraglacial meltwater production, en/subglacial retention, and ocean-going runoff remains poorly understood (e.g. Chu, 2014; Rennermalm, et al., 2013).

Virtually all runoff from the ablation zone of the GrIS occurs during the summer melt season. Such estimates are derived from regional climate models (RCMs), which assume that meltwater at the ice surface runs off to the ocean, without impoundment or delay (Smith et al., 2017). However, volumetric mismatches between RCM runoff and field-measured proglacial meltwater outflow suggest that meltwater can be retained within the ice sheet, and that the hydrologic routing of meltwater from the ice surface, through the ice sheet, to the ocean is complex and poorly constrained (Rennermalm et al., 2013; Smith et al., 2015).

RCM simulations find that approximately one-third of total GrIS runoff derives from southwestern Greenland (Section 2.10.1), where supraglacial meltwater is routed into moulins (Smith et al., 2015; Yang & Smith, 2016) and a seasonally evolving subglacial hydrologic network (e.g. Andrews et al., 2014). The volume of surface meltwater penetration to the ice-sheet bed modulates subglacial water pressures, drainage efficiency and ice dynamics on seasonal timescales (e.g. Catania & Neumann, 2010; Colgan et al., 2011; Cowton et al., 2013; Joughin et al., 2008; Tedesco et al., 2013). An unknown fraction of this meltwater is seasonally retained (e.g. Chu et al., 2016; Lindbäck et al., 2015; Overeem et al., 2015), while the rest is subglacially exported into proglacial rivers and the ocean (e.g. Ahlstrøm et al., 2017; van As et al., 2017, 2018). Despite GrIS surface melt being predominantly a summertime phenomenon, wintertime temperatures around Greenland are increasing faster than the annual average (Section 2.10.7, Figure S2-5 and Table S2-13), and pan-Arctic wintertime melt events are increasingly common (Graham et al., 2017; Moore, 2016). In Greenland, anomalously high wintertime temperatures made international headlines in 2018 (Samenow, 2018), while wintertime surface melt has been detected using both satellite data and climate models (Oltmanns et al., 2019).

Subglacial meltwater flows through cavities, channels, in thin films, and/or as groundwater through sediment/bedrock (Ravier & Buoncristiani, 2017). Channelized flow requires sufficient meltwater supply to the basal

drainage system to maintain melt rates along conduit walls that exceed closure (Meierbachtol et al., 2013). During winter, surface runoff input to the bed ceases and conduits close via deformation and creep (Schoof, 2010). In theory, a cessation of meltwater runoff and closure of conduits during the following weeks should preclude ocean-going meltwater export. However, evidence of supraglacial, englacial, and subglacial meltwater storage at seasonal and interannual timescales raises questions about the validity of this assumption (Chu et al., 2016; Forster et al., 2014; Kendrick et al., 2018; Koenig et al., 2015; Rennermalm et al., 2013). To our knowledge, it is currently unknown whether residual GrIS meltwater drainage into proglacial rivers occurs during winter.

To test the assumption of a shutdown of subglacial hydrologic processes during winter, we deployed to southwest Greenland in February 2015 to investigate four proglacial rivers draining the Greenland Ice Sheet through five outlet glaciers, namely: (1) Isunguata Sermia, (2) Russell, (3) Leverette, (4) Ørkendalen, and (5) Isorlersuup (Figure 2-1). These five adjoining glaciers develop complex summertime supraglacial stream networks that drain meltwater via moulins to the bed and ultimately the proglacial Isortoq, Sandflugtdalen, Ørkendalen, and Watson Rivers (Figure 2-1A). Flowing liquid water was discovered beneath the seasonal ice cover in the Isortoq River, but not the others. Here, we document the discovery of this modest wintertime (December, January and February or DJF) proglacial

outflow, including its estimated flux, spatial distribution, and geochemistry, and discuss plausible explanations for its presence as well as broader scientific implications.

2.3 Discovery of GrIS wintertime water export

2.3.1 Mapping and measuring wintertime flux

On February 12, 2015, we discovered slowly flowing water beneath proglacial Isortoq River ice ~1 km downstream from the Isunguata Sermia glacier terminus (Figure 2-2d). A transect was established orthogonal to the channel direction and a sled-mounted 400-MHz ground-penetrating radar (GPR) was dragged across the frozen river surface (Figure 2-2a). Resultant GPR profiles reveal four significant bright reflectors (Figure S2-4) indicative of meltwater filled conduits. Three bright reflectors were located at stations 84-92 m along the transect and one was located at stations 126-128 m along the transect (Figure 2-2c).

To aid interpretation of GPR data, eleven boreholes (see Table S2-11) were mechanically drilled through the river ice using a 5 cm diameter Kovacs ice auger (Figure 2-2d-e). Meltwater was discovered beneath approximately 53 cm of river ice in one borehole (location: 67.1914 °N, -50.3699 °W), that coincided with a bright reflector (88-90 m along orthogonal transect, Figure 2-2c). A gas-powered Jiffy Model 30 Ice Drill was then used to excavate a

larger (~25 cm diameter) borehole (Figure 2-2b) and the under-ice water velocity was approximated using a USGS Type AAMH Ice Current Meter (see note in Table S2-1 about low flow instrument limits). The slowly moving flow produced at least one rotation per two minutes, enabling rough estimation of a flow velocity of at least 1 to 3 cm s⁻¹ (see Table S2-1). The GPR data were then used to estimate the height and width of these conduits (see Section 2.10.2). The individual under-ice conduit cross-sectional areas of the four conduits were 684 - 1533 cm², 969 - 1720 cm², 6468 - 8995 cm², 7260 - 7689 cm², with a cumulative cross-sectional area in the range of 1.54 to 1.99 m² (see Section 2.10.2, Figure S2-4 and Table S2-2). Given these areas, and assuming a constant flow velocity in all conduits, we estimate an approximate instantaneous water flux of 20 to 60 l s⁻¹ (see Table S2-3).

To confirm the presence of an elongated water filled conduit, we collected nine 25 m long GPR transects at distances of approximately 6 m, 14 m, 20 m and 26 m upstream and 18 m, 28 m, 41 m, 64 m and 101 m downstream from the wet borehole (Figure 2-2e, see Section 2.10.2 for discussion of geolocation uncertainty). These GPR surveys also reveal bright reflectors (teal diamonds, Figure 2-2e) indicative of meltwater-filled under-ice conduits persisting at least 90 m downstream (Figure 2-2d-e). To our knowledge, this is the first documentation of wintertime flow of a Greenlandic proglacial river.

Borehole and GPR transect surveys were similarly conducted at five other locations during February 2015 (Figure 2-1a), namely, (1) beneath the Watson River bridge in Kangerlussuaq (Table S2-6), (2) along a single-channel reach of the Watson River (Table S2-7), (3) along the Sandflugtdalen tributary ~350 m upstream of its confluence into the Watson River (Table S2-8), (4) along the Ørkendalen tributary both ~1.9 km upstream of its confluence with the Watson River (Table S2-9) and (5) at the Ørkendalen, and Isorlersuup outlet glacier termini (Table S2-10). These six surveys, all within the Watson River watershed (Figure 2-1), revealed no liquid water. This suggests subglacial drainage of seasonally retained meltwater beneath Isunguata Sermia, but not its neighboring outlet glaciers to the south, at least at the time of the field visit.

2.3.2 Isortoq River water geochemistry

Isortoq River wintertime water samples were collected by lowering a 1 L polyethylene bottle on a line into the Isortoq River borehole. The water was supercooled, with a temperature of -2 °C. Bulk water samples were split into 8 x 125 ml unfiltered samples, and 4 x 30 ml filtered samples using a 0.45 µm syringe filter. Prior to filling, the collector and sample bottles were rinsed with river water. Samples of snow atop the river ice were collected at four locations surrounding the borehole, which were later melted and transferred into 16 x 30 ml sample bottles. All samples were refrigerated

including during transport from Greenland to the U.S. for laboratory analysis. Opportunistic grab samples of Isortoq River water and Watson River water were also collected during previous summertime melt seasons, when both rivers were ice and snow free (Figure S2-2 and Table S2-4).

Geochemical analysis of these wintertime Isortoq River water samples reveals high total dissolved solute (TDS) concentration and deviation from local snow samples. TDS concentrations and deviation from meteoric composition indicates that the Isortoq River water had been in contact with sediments or rocks and solutes derived partly from dissolution of minerals, signifying contact with glacial bedrock/sediment. Two of four snow samples had higher TDS concentrations than river water (Figure S2-2), which might be impacted by recrystallization and refreezing of older river water, yet cannot be traced to a specific source or process with available data (Section 2.10.6). Stable isotope composition of δD and $\delta O-18$ (Figure S2-2), indicate high isotopic ratios for snow compared to river water, suggesting that the Isortoq River water samples were not sourced from local snow melt on the frozen river. Collectively, this geochemical evidence suggests that the under-ice proglacial river water has a unique chemical signature different from both wintertime snow samples and summer melt season proglacial Isortoq River water and has also been in contact with glacial bedrock/sediment (see Table S2-4 for full geochemistry laboratory results).

2.4. Mechanisms enabling GrIS wintertime meltwater drainage

We hypothesize that the discovery of residual wintertime drainage in the Isortoq River is enabled by a >600 m deep subglacial trough which extends >20 km inland from the terminus of Isunguata Sermia (Figure 2-1b) (Jezek et al., 2013). Comparison of both subglacial topography and potential subglacial drainage networks modelled using hydrostatic pressure grids (see Section 2.10.5) beneath Isunguata Sermia, with those for Russell, Leverette, Ørkendalen, and Isorlersuup glaciers confirms that comparable troughs and spatially pervasive subglacial drainage areas are not present beneath these other four glaciers (Figure 2-1b). Isunguata Sermia's potential subglacial drainage network also coincides with IceBridge airborne radar springtime (May 2010 and April 2011) mappings of bright subglacial reflectors, interpreted as likely locations of subglacial storage (Chu et al., 2016), plotted as green dots in Figure 2-1b (also, see Figure S2-3 for summary of reflectors by ice surface elevation and thickness).

Discovery of residual wintertime drainage from Isunguata Sermia is consistent with the possibility of seasonal and/or inter-annual retention of summer meltwater runoff and with previously observed mismatches between observed and modeled proglacial outflow (Lindbäck et al., 2015; Rennermalm et al., 2013; Smith et al., 2015). A similar mismatch is not present for the Watson River (which integrates all meltwater outflow from the Russell, Leverette, Ørkendalen, and Isorlersuup glaciers) (Lindbäck et

al., 2015). Lag times between summertime GrIS surface melt and proglacial runoff in the Watson River range from <24 h to ~10 d, with no evidence suggesting significant (wintertime) storage or retention (van As et al., 2017). This suggests that previously reported mismatches between simulated runoff and observed outflow in the region may be unique to Isunguata Sermia.

Our finding of residual drainage from Isunguata Sermia is also consistent with regional contrasts in ice velocity. Subglacial hydrologic connectivity partially modulates ice velocity, with high connectivity associated with high basal traction and low flow speeds (Andrews et al., 2014). Unlike Isunguata Sermia, outlet glaciers draining into the Watson River watershed accelerate rapidly at the onset of the summer melt season (Lindbäck et al., 2015). Similarly, our finding of a wet bed and residual wintertime drainage only from Isunguata Sermia suggests higher subglacial hydrologic connectivity, which should reduce associated velocity accelerations.

An alternate source of the residual outflow observed draining Isunguata Sermia could be the result of a brief wintertime surface melt event that occurred ~10 days prior to our borehole and GPR surveys (Figure 2-3). On February 2-3, 2015 a ~21 h period of above freezing conditions was recorded at the nearby KAN-L PROMICE meteorological station, with air temperatures briefly exceeding 4 °C (Figure 2-3a; data available at <https://www.promice.dk/>). An observation-fed surface energy balance (SEB)

model (van As et al., 2017) simulates ~ 12 h of surface melt with rates > 29 mm d⁻¹ at ice surface elevations up to 700 m during this period (Figure 2-3a). The occurrence of this melt event prior to our field study raises the possibility that surface melting might enable modest proglacial meltwater drainage during winter.

Surface melting along the K-Transect (Figure 2-4a) occurred on average 4.5 days per year (i.e. 36 melt days over 8 winters) from 2009-2017 (Figure 2-3b). The intensity of the February 2-3, 2015 surface melt preceding our field study was above average, but not a statistical outlier (i.e. total melt $< \mu \pm \sigma$, see Table S2-5). When analyzing the PROMICE record for all stations on the GrIS, only 4 of 20 stations did not have DJF positive degree-days (PDD) (Figure 2-4a). Similarly, surface temperature/emissivity observations from the MODIS satellite record reveals surface melt conditions during all winters over the period 2000-19 (Figure 2-4b,d, and Section 2.10.3). The MEaSUREs passive microwave satellite record (Mote, 2014) further reveals that the occurrence of GrIS wintertime surface melt increased (p-value < 0.05 ; $r^2 = 0.27$) between 1979-2012 (Figure 2-4c,d and Section 2.10.4). Collectively, these datasets suggest that brief episodes of wintertime surface melt are relatively common, both within our study area and across the margins of the GrIS.

2.5 Implications of GrIS wintertime surface melt, retention, refreezing and drainage

Regardless of the causal mechanism, our finding of mineral-rich liquid water draining from Isunguata Sermia during winter confirms that this outlet glacier maintains a wet bed year-round. This finding, which is consistent with Chu et al (2016) IceBridge airborne radar reflector mappings (Figure 2-1b), supports the idea of subglacial water retention in some parts of the ice sheet but not others, and consequent alteration of the overlying GrIS thermal structure. As retained meltwater refreezes, it releases latent heat and warms surrounding ice, raising basal temperatures, reducing ice viscosity, and promoting basal sliding (Phillips et al., 2013; Pitcher & Smith, 2019). This process, termed cryo-hydrologic warming (Phillips et al., 2010) may influence the long-term stability of the GrIS (Colgan et al., 2015). Field observations identify temperate basal ice at least 45 km from the Isunguata Sermia terminus, which can be partially explained by heat from refreezing, particularly within basal crevasses, which softens ice and enhances deformation (Harrington et al., 2015). The temporal and spatial pervasiveness of wintertime subglacial water, refreezing, and associated cryo-hydrologic warming is an important yet poorly constrained forcing on ice deformation, flow and long-term ice sheet stability.

It is also important to consider the implication of potential wintertime subglacial drainage from marine terminating glaciers. During the summer

melt season, subglacial drainage from marine terminating glaciers fuels submarine melting (Fried et al., 2015), which is a key control on ice dynamics (Cowton et al., 2019). The other process enhancing mass loss in marine terminating glaciers is the circulation of warm ocean waters to glacier termini (Holland et al., 2008), which similarly intensifies submarine melting (Rignot et al., 2010). Simulations suggest that ocean-fjord circulation in Greenland can result in wintertime melting in at least some outlet glaciers (Fraser et al., 2018). However, during the summer melt season, oceanographic and subglacial hydrologic forcing's in unison result in submarine melting at rates an order of magnitude larger than during winter (Sciascia et al., 2013), implying that subglacial hydrologic drainage during wintertime would be similarly important. Collectively, this suggests that subglacial hydrology may be an important control on the stability of marine terminating glaciers, not just during the summer melt-season, but year-round.

Recognition of wintertime retention and runoff is also important for regional climate model (RCM) simulations of the GrIS contribution to global sea level rise. Currently, RCMs make the assumption that surface runoff flows into the ocean without impoundment, retention or long-term delay (Smith et al., 2017). Recent work finds that bare ice hydrological routing and retention processes (e.g. Cooper et al., 2018; Yang et al., *in review*) result in incorrect RCM simulation of meltwater delivery to moulins during

the melt season (Smith et al., 2017). At a seasonal time scale, this may be unimportant for systems like the Watson River, where simulated annual runoff from tributary outlet glaciers closely matches annual Watson River discharge (van As et al., 2017; Lindbäck et al., 2015). However, the mismatch between simulated runoff and proglacial discharge for Isunguata Sermia (Lindbäck et al., 2015; Rennermalm et al., 2013; Smith et al., 2015) suggests that current assumptions of instantaneous runoff transfer can yield inaccurate simulation of sea level rise contributions from some glaciers. Our discovery of residual wintertime drainage supports the idea that seasonal retention is an important yet poorly constrained term in RCM's (e.g. Rennermalm, Smith, et al., 2013; Smith et al., 2015), suggesting that field-based validations of RCM runoff using measurements of proglacial river discharge should avoid glaciers (such as Isunguata Sermia) having large over deepened troughs, thawed beds, and active subglacial hydrologic systems.

2.6 Conclusion

Our wintertime field study of four proglacial rivers draining the southwestern Greenland Ice Sheet confirms that a wet glacial bed and residual subglacial drainage can occur even in February, at least when located downstream of a large, well-integrated, over deepened subglacial trough. We conclude that some fast-flowing land-terminating areas of the

GrIS bed can experience basal cryo-hydrological warming and drain residual meltwater during winter. This supports the overall notion of ice sheet retention and/or delayed release of summer meltwater for at least several months after cessation of melt. Further studies are needed to document whether wintertime surface melt events are sufficient to activate GrIS subglacial hydrological processes in winter, but AWS and satellite observations do confirm the ubiquity of such events. This is consistent with an overall pan-Arctic trend of increasing melt events in winter (Graham et al., 2017; Moore, 2016), and highlights a growing need for Arctic hydrologic investigations to be conducted during the cold season as well as summer.

2.7 Acknowledgments, Samples, and Data

This work was supported NASA Cryosphere Program Grants NNX14AH93G and 80NSSC19K0942 managed by Thomas P. Wagner, Colene Haffke, and Thorsten Markus; and by a NASA Earth and Space Sciences Fellowship award # NNX14AP57H managed by Lin Chambers. Field and logistics support was provided by Kathy Young, Jessy Jenkins and Kyli Cospers. Automated Weather Station (AWS) data from the Program for Monitoring of the Greenland Ice Sheet (PROMICE) and the Greenland Analogue Project (GAP) were provided by the Geological Survey of Denmark and Greenland (GEUS) at <http://www.promice.dk>. ArcticDEM was provided by the Polar Geospatial Center under NSF-OPP awards 1043681, 1559691,

and 1542736. Geospatial support for this work provided by the Polar Geospatial Center under NSF-OPP awards 1043681 and 1559691. Data supporting results and conclusions can be obtained via in text references and Supporting Information.

2.8 Figures

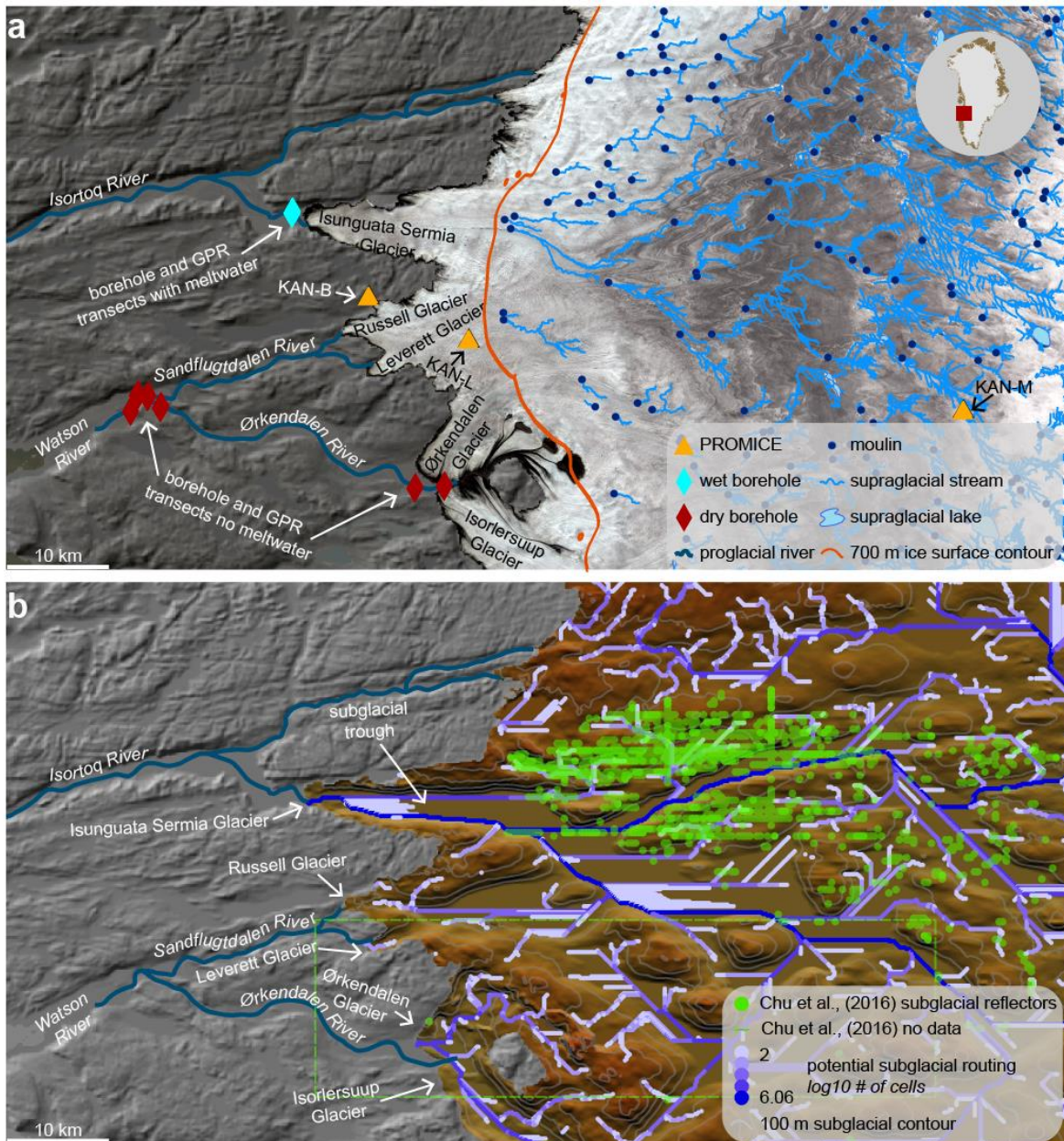


Figure 2-1: study area map

Field surveys (diamonds) were conducted in four frozen proglacial rivers during February 2015. Each river drains subglacial meltwater from the Greenland Ice Sheet to the ocean. **(a)** During the summer melt season, a

supraglacial hydrologic network develops on the ice surface ablation zone and delivers meltwater via moulines (navy dots) to en/subglacial conduits (mapped by Yang et al., (2018)). Cyan-colored diamond indicates where water was discovered in the proglacial Isortoq River on February 12, 2015. Red diamonds indicate in situ location where no meltwater was found. Panel **(b)** shows the basal topography beneath the ice sheet (Morlighem et al., 2017), with green dots showing locations of subglacial meltwater storage as mapped using IceBridge Multichannel Coherent Radar Depth Sounder data and green dashed-line denoting the no data area (Chu et al., 2016). Proglacial land surface topography, shown as shaded relief, is from the 100 m resolution ArcticDEM Mosaic (Porter et al., 2018).

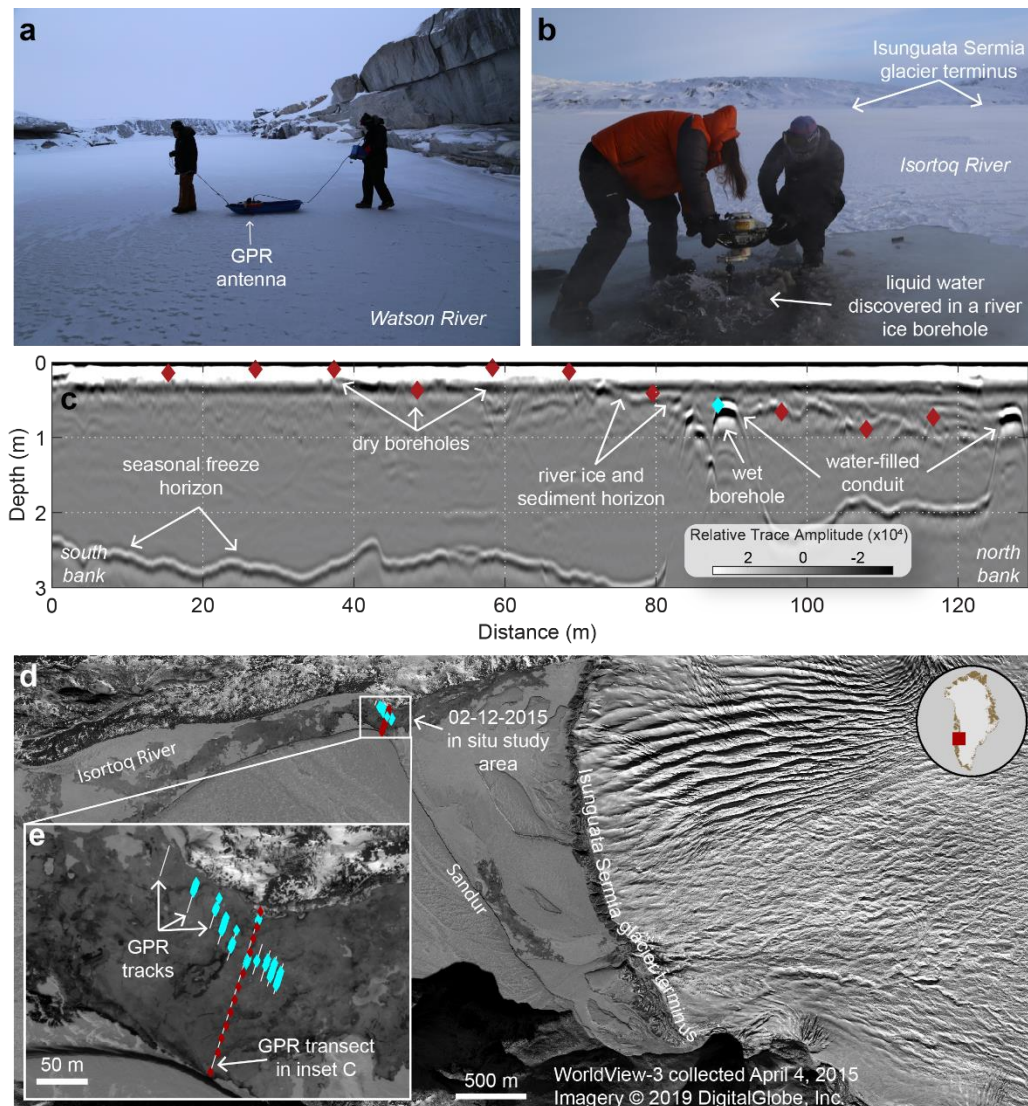


Figure 2-2: discovery of wintertime residual meltwater drainage

Ground penetrating radar (GPR) transect (a) and boreholes across the Watson River near Kangerlussuaq indicate this proglacial river to be frozen to the bed. (b) On February 12, 2015 slowly flowing liquid water was discovered beneath the seasonal ice cover of the proglacial Isortoq River draining the Isinguata Sermia outlet glacier. (c) Long GPR transect across the frozen proglacial Isortoq River identifies four bright reflectors interpreted as water-filled conduits, one 126-128 m and the other three 84-92 m from

the south bank. The latter was validated via an in-situ borehole (cyan diamond, **b**) and its longitudinal continuity confirmed through short GPR transects upstream and downstream of the water-filled borehole (**d**, **e**). Red diamonds indicate river ice thickness measured in-situ as the distance from the river ice surface to dry proglacial channel bed in the boreholes. Other cyan diamonds (**d**, **e**) signify liquid water, as interpreted from bright radar reflectors in GPR transects.

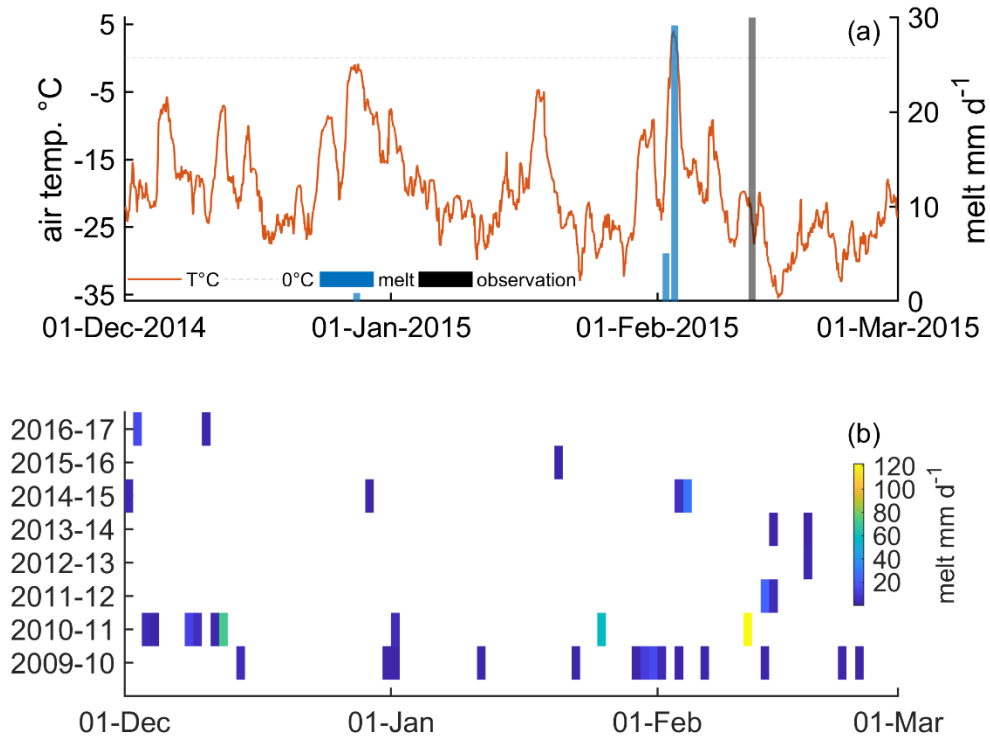


Figure 2-3: K-Transect wintertime ice surface melt

The glaciated region of our west Greenland study area experienced (a) above freezing temperatures (orange line) and surface melt (modelled, blue bars) on February 2-3, 2015, ~10 days prior to our field study (black bars). (b) Interrogation of a surface energy balance (SEB) melt model established for the K-Transect, representative of our study region of the Greenland ice sheet, finds that this February 2015 melt event was neither rare nor anomalously intense.

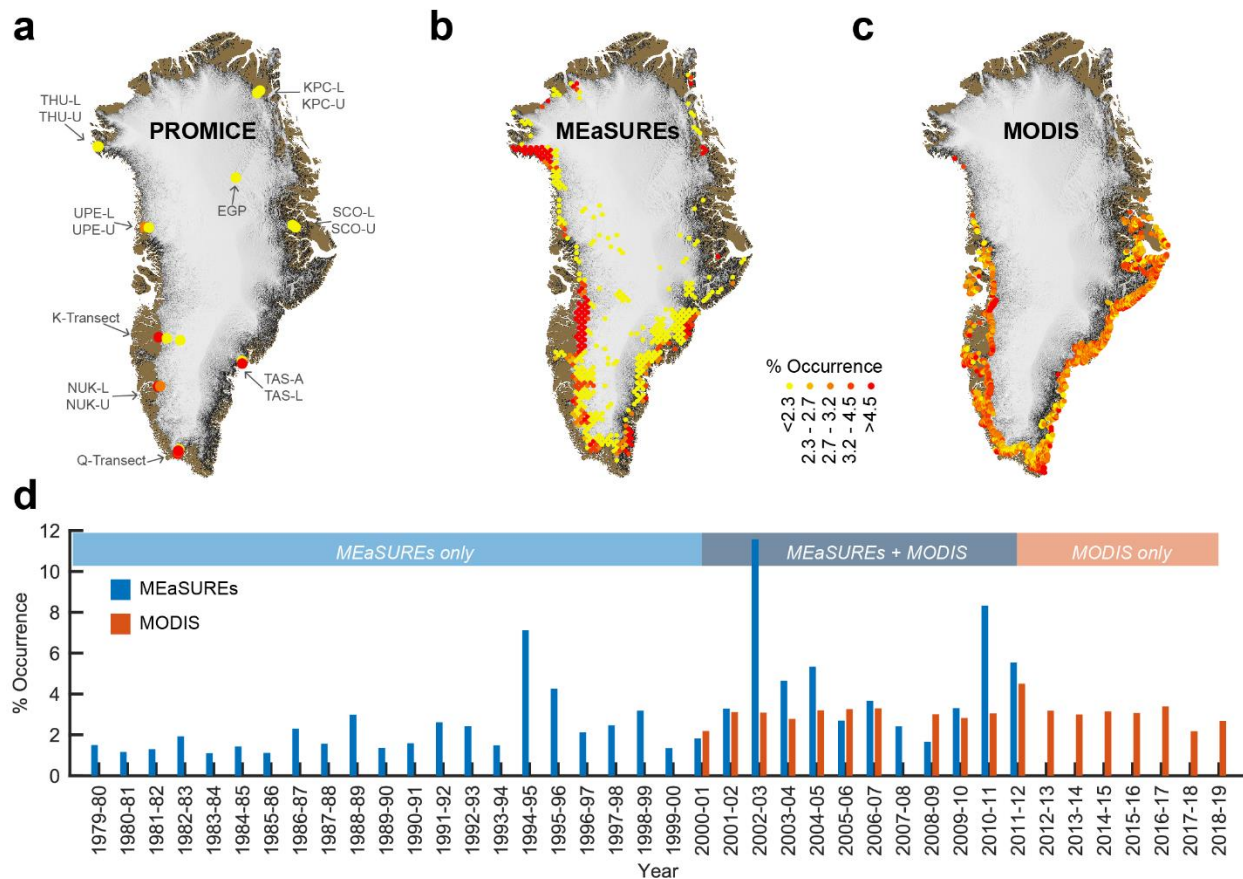


Figure 2-4: Greenland Ice Sheet wintertime surface melt

Wintertime surface melt on the Greenland Ice Sheet (GrIS) is relatively common, as determined from **(a)** PROMICE meteorological stations (2007-2018, record length is station dependent); **(b)** MEaSURES brightness temperatures derived from microwave radiometer satellite data (1979-2012); and **(c)** MODIS Terra MOD11A1 land surface temperature/emissivity data (2000-2019). The **(d)** MODIS and MEaSURES records indicate at least 1.1% occurrence (frequency of wintertime melt divided by the number of wintertime observations) of wintertime melt over their respective observation periods (orange tones in **(a)**, **(b)**, and **(c)**). The **(d)** percent

occurrence of wintertime melt events also increased (p-value < 0.05; $r^2 = 0.27$) across the 1979-2012 MEaSURES record.

2.9 References

- Ahlstrøm, A. P., Petersen, D., Langen, P. L., Citterio, M., & Box, J. E. (2017). Abrupt shift in the observed runoff from the southwestern Greenland ice sheet. *Science Advances*, *3*(12), 1–8.
<https://doi.org/10.1126/sciadv.1701169>
- Andrews, L. C., Catania, G. A., Hoffman, M. J., Gulley, J. D., Lüthi, M. P., Ryser, C., et al. (2014). Direct observations of evolving subglacial drainage beneath the Greenland Ice Sheet. *Nature*, *514*, 80–83.
<https://doi.org/10.1038/nature13796>
- van As, D., Mikkelsen, A. B., Nielsen, M. H., Box, J. E., Liljedahl, L. C., Lindbäck, K., et al. (2017). Hypsometric amplification and routing moderation of Greenland ice sheet meltwater release. *The Cryosphere*, *11*(3), 1371–1386. <https://doi.org/10.5194/tc-11-1371-2017>
- van As, D., Hasholt, B., Ahlstrøm, A. P., Box, J. E., Cappelen, J., Colgan, W., et al. (2018). Reconstructing Greenland Ice Sheet meltwater discharge through the Watson River (1949–2017). *Arctic, Antarctic, and Alpine Research*, *50*(1), 10. <https://doi.org/10.1080/15230430.2018.1433799>
- van den Broeke, M. R., Bamber, J., Ettema, J., Rignot, E., Schrama, E., van de Berg, W. J., et al. (2009). Partitioning recent Greenland mass loss. *Science*, *326*(5955), 984–6. <https://doi.org/10.1126/science.1178176>
- van den Broeke, M. R., Enderlin, E. M., Howat, I. M., Kuipers Munneke, P., Noël, B. P. Y., van de Berg, W. J., et al. (2016). On the recent

- contribution of the Greenland ice sheet to sea level change. *Cryosphere*, 10(5), 1933–1946. <https://doi.org/10.5194/tc-10-1933-2016>
- Catania, G. A., & Neumann, T. A. (2010). Persistent englacial drainage features in the Greenland Ice Sheet. *Geophysical Research Letters*, 37, 1–5. <https://doi.org/10.1029/2009GL041108>
- Chu, V. W. (2014). Greenland ice sheet hydrology A review. *Progress in Physical Geography*, 38(1), 19–54. <https://doi.org/10.1177/0309133313507075>
- Chu, W., Schroeder, D. M., Seroussi, H., Creyts, T. T., Palmer, S. J., & Bell, R. E. (2016). Extensive winter subglacial water storage beneath the Greenland Ice Sheet. *Geophysical Research Letters*, 43(24), 12,484–12,492. <https://doi.org/10.1002/2016GL071538>
- Colgan, W., Steffen, K., McLamb, W. S., Abdalati, W., Rajaram, H., Motyka, R., et al. (2011). An increase in crevasse extent, West Greenland: Hydrologic implications. *Geophysical Research Letters*, 38(18), L18502. <https://doi.org/10.1029/2011GL048491>
- Colgan, W., Sommers, A., Rajaram, H., Abdalati, W., & Frahm, J. (2015). Considering thermal-viscous collapse of the Greenland ice sheet. *Earth's Future*, 3, 252–267. <https://doi.org/10.1002/2015EF000301>.Abstract
- Cooper, M. G., Smith, L. C., Rennermalm, A. K., Miège, C., Pitcher, L. H., Ryan, J. C., et al. (2018). Near surface meltwater storage in low-density bare ice of the Greenland ice sheet ablation zone. *The Cryosphere*, 12,

955–970. <https://doi.org/https://doi.org/10.5194/tc-2017-107>

Cowton, T., Nienow, P., Sole, A., Wadham, J., Lis, G., Bartholomew, I., et al.

(2013). Evolution of drainage system morphology at a land-terminating Greenlandic outlet glacier. *Journal of Geophysical Research: Earth Surface*, *118*(1), 29–41. <https://doi.org/10.1029/2012JF002540>

Cowton, T. R., Todd, J. A., & Benn, D. I. (2019). Sensitivity of tidewater glaciers to submarine melting governed by plume locations. *Geophysical Research Letters*, 1–9. <https://doi.org/10.1029/2019gl084215>

Forster, R. R., Box, J. E., van den Broeke, M. R., Miede, C., Burgess, E. W., van Angelen, J. H., et al. (2014). Extensive liquid meltwater storage in firn within the Greenland ice sheet. *Nature Geoscience*, *7*(2), 95–98. Retrieved from <http://dx.doi.org/10.1038/ngeo2043>

Fraser, N. J., Inall, M. E., Jones, S. C., Magaldi, M. G., Haine, T. W. N., & Jones, S. C. (2018). Wintertime Fjord-Shelf Interaction and Ice Sheet Melting in Southeast Greenland. *Journal of Geophysical Research: Oceans*, *123*, 9156–9177. <https://doi.org/10.1029/2018JC014435>

Fried, M. J., Catania, G. A., Bartholomew, T. C., Duncan, D., Davis, M., Stearns, L. A., et al. (2015). Distributed subglacial discharge drives significant submarine melt at a Greenland tidewater glacier. *Geophysical Research Letters*, *42*(21), 9328–9336. <https://doi.org/10.1002/2015GL065806>

Graham, R. M., Cohen, L., Petty, A. A., Boisvert, L. N., Rinke, A., Hudson, S.

- R., et al. (2017). Increasing frequency and duration of Arctic winter warming events. *Geophysical Research Letters*, 44(13), 6974–6983. <https://doi.org/10.1002/2017GL073395>
- Harrington, J. A., Humphrey, N. F., & Harper, J. T. (2015). Temperature distribution and thermal anomalies along a flowline of the Greenland ice sheet. *Annals of Glaciology*, 56(70), 98–104. <https://doi.org/10.3189/2015AoG70A945>
- Hauer, M. E., Evans, J. M., & Mishra, D. R. (2016). Millions projected to be at risk from sea-level rise in the continental United States. *Nature Climate Change*, 6, 691–695. <https://doi.org/10.1038/NCLIMATE2961>
- Holland, D. M., Thomas, R. H., De Young, B., Ribergaard, M. H., & Lyberth, B. (2008). Acceleration of Jakobshavn Isbr triggered by warm subsurface ocean waters. *Nature Geoscience*, 1(10), 659–664. <https://doi.org/10.1038/ngeo316>
- Jezek, K., Wu, X., Paden, J., & Leuschen, C. (2013). Radar mapping of Isunnguata Sermia, Greenland. *Journal of Glaciology*, 59(218), 1135–1146. <https://doi.org/10.3189/2013JoG12J248>
- Joughin, I., Das, S. B., King, M. A., Smith, B. E., & Howat, I. M. (2008). Seasonal Speedup Along the Western Flank of the Greenland Ice Sheet. *Science*.
- Kendrick, A. K., Schroeder, D. M., Chu, W., Young, T. J., Christoffersen, P., Todd, J., et al. (2018). Surface Meltwater Impounded by Seasonal

- Englacial Storage in West Greenland. *Geophysical Research Letters*, 1–8.
<https://doi.org/10.1029/2018GL079787>
- Koenig, L. S., Lampkin, D. J., Montgomery, L. N., Hamilton, S. L., Turrin, J. B., Joseph, C. A., et al. (2015). Wintertime storage of water in buried supraglacial lakes across the Greenland Ice Sheet. *The Cryosphere*, 9(4), 1333–1342. <https://doi.org/10.5194/tc-9-1333-2015>
- Lindbäck, K., Pettersson, R., Hubbard, A. L., Doyle, S. H., van As, D., Mikkelsen, A. B., & Fitzpatrick, A. A. (2015). Subglacial water drainage, storage, and piracy beneath the Greenland Ice Sheet. *Geophysical Research Letters*, n/a-n/a. <https://doi.org/10.1002/2015GL065393>
- Meierbachtol, T., Harper, J., & Humphrey, N. (2013). Basal Drainage System Response to Increasing Surface Melt on the Greenland Ice Sheet. *Science*, 341(6147), 777–779. <https://doi.org/10.1126/science.1235905>
- Moore, G. W. K. (2016). The December 2015 North Pole Warming Event and the Increasing Occurrence of Such Events. *Scientific Reports*.
<https://doi.org/10.1038/srep39084>
- Morlighem, M., Williams, C. N., Rignot, E., An, L., Arndt, J. E., Bamber, J. L., et al. (2017). BedMachine v3: Complete Bed Topography and Ocean Bathymetry Mapping of Greenland From Multibeam Echo Sounding Combined With Mass Conservation. *Geophysical Research Letters*, 44(21), 11,051–11,061. <https://doi.org/10.1002/2017GL074954>
- Mote, T. L. (2014). MEaSURES Greenland Surface Melt Daily 25km EASE-Grid

2.0, Version 1. NASA National Snow and Ice Data Center Distributed Active Archive Center.

<https://doi.org/https://doi.org/10.5067/MEASURES/CRYOSPHERE/nsidc-0533.001>

- Nerem, R. S., Beckley, B. D., Fasullo, J. T., Hamlington, B. D., Masters, D., & Mitchum, G. T. (2018). Climate-change-driven accelerated sea-level rise detected in the altimeter era. *Proceedings of the National Academy of Sciences*, *0*, 201717312. <https://doi.org/10.1073/pnas.1717312115>
- Oltmanns, M., Straneo, F., & Tedesco, M. (2019). Increased Greenland melt triggered by large-scale , year-round cyclonic moisture intrusions. *The Cryosphere*, *13*, 815–825. <https://doi.org/https://doi.org/10.5194/tc-13-815-2019>
- Overeem, I., Hudson, B., Welty, E., Mikkelsen, A., Bamber, J., Petersen, D., et al. (2015). River inundation suggests ice-sheet runoff retention. *Journal of Glaciology*, *61*(228), 776–788. <https://doi.org/10.3189/2015JoG15J012>
- Phillips, T., Rajaram, H., & Steffen, K. (2010). Cryo-hydrologic warming: A potential mechanism for rapid thermal response of ice sheets. *Geophysical Research Letters*, *37*(20), 1–5. <https://doi.org/10.1029/2010GL044397>
- Phillips, T., Rajaram, H., Colgan, W., Steffen, K., & Abdalati, W. (2013). Evaluation of cryo-hydrologic warming as an explanation for increased

- ice velocities in the wet snow zone, Sermeq Avannarleq, West Greenland. *Journal of Geophysical Research: Earth Surface*, 118(3), 1241–1256. <https://doi.org/10.1002/jgrf.20079>
- Pitcher, L. H., & Smith, L. C. (2019). Supraglacial streams and rivers. *Annual Review of Earth and Planetary Sciences*, 47, 421–452. <https://doi.org/doi.org/10.1146/annurev-earth-053018-060212>
- Porter, C., Morin, P., Howat, I., Noh, M.-J., Bates, B., Peterman, K., et al. (2018). ArcticDEM. Harvard Dataverse. <https://doi.org/doi:10.7910/DVN/OHHUKH>
- Ravier, E., & Buoncristiani, J.-F. (2017). Glaciohydrogeology. In *Past Glacial Environments* (Second Edi, pp. 431–466). Elsevier Ltd. <https://doi.org/10.1016/B978-0-08-100524-8.00013-0>
- Rennermalm, A. K., Smith, L. C., Chu, V. W., Forster, R. R., van den Broeke, M., van As, D., & Moustafa, S. E. (2013). Evidence of meltwater retention within the Greenland ice sheet. *The Cryosphere*, 7, 1443–1445. <https://doi.org/10.5194/tc-7-1433-2013>
- Rennermalm, A. K., Moustafa, S. E., Mioduszewski, J., Chu, V. W., Forster, R. R., Hagerdorn, B., et al. (2013). Understanding Greenland ice sheet hydrology using an integrated multi-scale approach. *Environmental Research Letters*, 8, 14pp. <https://doi.org/10.1088/1748-9326/8/1/015017>
- Rignot, E., Koppes, M., & Velicogna, I. (2010). Rapid submarine melting of

- the calving faces of West Greenland glaciers. *Nature Geoscience*, 3(3), 187–191. <https://doi.org/10.1038/ngeo765>
- Rignot, E., Velicogna, I., van den Broeke, M. R., Monaghan, A., & Lenaerts, J. T. M. (2011). Acceleration of the contribution of the Greenland and Antarctic ice sheets to sea level rise. *Geophysical Research Letters*, 38(5). <https://doi.org/10.1029/2011GL046583>
- Samenow, J. (2018, February 26). North Pole surges above freezing in the dead of winter, stunning scientists. *The Washington Post*. Retrieved from <https://www.washingtonpost.com/news/capital-weather-gang/wp/2018/02/26/north-pole-surges-above-freezing-in-the-dead-of-winter-stunning-scientists/?noredirect=on>
- Schoof, C. (2010). Ice-sheet acceleration driven by melt supply variability. *Nature*, 468(7325), 803. <https://doi.org/10.1038/nature09618>
- Sciascia, R., Straneo, F., Cenedese, C., & Heimbach, P. (2013). Seasonal variability of submarine melt rate and circulation in an East Greenland fjord. *Journal of Geophysical Research: Oceans*, 118(5), 2492–2506. <https://doi.org/10.1002/jgrc.20142>
- Shepherd, A., Ivins, E. R., A, G., Barletta, V. R., Bentley, M. J., Bettadpur, S., et al. (2012). A Reconciled Estimate of Ice-Sheet Mass Balance. *Science*, 338(1183). <https://doi.org/10.1126/science.1228102>
- Smith, L. C., Chu, V. W., Yang, K., Gleason, C. J., Pitcher, L. H., Rennermalm, A. K., et al. (2015). Efficient meltwater drainage through

supraglacial streams and rivers on the southwest Greenland Ice Sheet. *Proceedings of the National Academy of Sciences*.

Smith, L. C., Yank, K., Pitcher, L. H., Overstreet, B. T., CHu, V. W., Rennermalm, Å. K., et al. (2017). Direct measurements of meltwater runoff on the Greenland Ice Sheet surface. *Proceedings of the National Academy of Sciences*, 114(50).

<https://doi.org/10.1073/pnas.1707743114>

Tedesco, M., Willis, I. C., Hoffman, M. J., Banwell, A. F., Alexander, P., & Arnold, N. S. (2013). Ice dynamic response to two modes of surface lake drainage on the Greenland ice sheet. *Environmental Research Letters*, 8(3), 34007. Retrieved from <http://stacks.iop.org/1748-9326/8/i=3/a=034007>

Yang, K., Smith, L. C., Cooper, M. G., Pitcher, L. ., van As, D., Lu, Y., & Li, M. (n.d.). Seasonal evolution of supraglacial lakes and rivers on the southwestern Greenland Ice Sheet. *Journal of Geophysical Research - Earth Surface*.

Yang, K., Smith, L. C., Karlstrom, L., Cooper, M. G., Tedesco, M., van As, D., et al. (2018). Supraglacial meltwater routing through internally drained catchments on the Greenland Ice Sheet surface. *The Cryosphere Discussions*. <https://doi.org/https://doi.org/10.5194/tc-2018-145>

Yang, Kang, & Smith, L. C. (2016). Internally drained catchments dominate supraglacial hydrology of the southwest Greenland Ice Sheet. *Journal of*

Geophysical Research: Earth Surface, 1891–1910.

<https://doi.org/10.1002/2016JF003927>.Received

2.10 Supporting Information

2.10.1 Fraction of runoff from the Southwest GrIS compared to total GrIS runoff

The fraction of total GrIS runoff sourced from the southwest GrIS (SW, Figure S2-1b) was calculated using Modèle Atmosphérique Régional (MAR) version 3.8 regional climate model (RCM) outputs acquired from: <ftp://ftp.climato.be/fettweis/>. To delimit the spatial extent of the southwest GrIS, drainage basins and an ice mask (Rignot and Mouginot, 2012), available as part of the ice sheet mass balance inter-comparison exercise (imbie) were used (Figure S2-1a-b). These data were acquired from: <http://imbie.org/imbie-2016/drainage-basins/>.

To extract runoff data from MAR, first a polygon grid .shp file was created from the unique latitude and longitude pairs specified by the “LAT” and “LON” variables in MAR netcdf outputs. These coordinates were read into ArcMap as points and assigned a polar stereographic projection. Next, Thiessen polygons were created for MAR grid cell points and the area of each polygon was calculated (Figure S2-1c). Thiessen polygons were then clipped to the ice mask (Figure S2-1a) and the SW basin (Figure S2-1b), both reprojected into polar stereographic projection. The fractional area of each

grid cell contained within the GrIS ice mask and southwest basin was then calculated.

The Thiessen polygons clipped to the ice mask and the SW basin were then read into MATLAB R2017a and the 1 km topography corrected runoff (MAR variable name in netcdf files: "RUcorr") for each intersecting grid cell on every day with MAR data (January 1, 1979 through July 23, 2017, 14,084 days). The runoff in each grid cell was then multiplied by the grid cell area, weighted by the fractional area of each grid cell contained within the ice mask or SW basin and then summed. The result is a daily cumulative runoff value for the GrIS and the SW basin. Finally, daily cumulative runoff was summarized and the percent of total runoff from the SW basin as a fraction of total GrIS runoff between January 1, 1979 and July 23, 2017 was calculated to be 30.97%.

2.10.2 Ground-penetrating radar (GPR) data collection, processing and interpretation

2.10.2.1 Overview of ground-penetrating radar (GPR) surveys and data processing

Ground-based radar surveys were performed using a SIR-3000 Geophysical Survey Systems, Inc. (GSSI©) ground-penetrating radar (GPR) controller and a 400-MHz antenna installed and towed on a 0.6 cm thick

plastic Siglin© sled. Surveys were conducted on foot (Figure 2a) by establishing cross sections orthogonal to flow direction spanning each of the surveyed frozen proglacial channels. Data collection was designed vertically with 2048 samples per trace for a 100 ns window range resulting in a 0.05 ns sample interval. Horizontally, 10 traces were collected per second which correspond to a 7-cm mean trace spacing interval at an average speed of 0.7 m/s. Each trace sample is stored as a 16-bit integer (2^{16}), which when centered on zero, allows the relative amplitude to range between -32768 and 32768. During post processing, time zero is set using the first positive amplitude peak of each radar trace (corresponding to the first 85 samples of each trace). A linear time-dependent gain was added to compensate for radar-wave attenuation within the heterogeneous media and to accentuate internal reflectors in the processed echogram. Two-way-travel times are converted to depth assuming a homogeneous permittivity of ice at 3.15 from the ice surface to the river bed.

For the main GPR echogram (Figure 2c) where boreholes were drilled, the GPS coordinates taken at each borehole were used to geolocate the GPR traces, assuming a constant travel speed between boreholes.

Given limited ground time and helicopter resources, the shorter GPR cross sections (~40 m long on average, mapped in Figure 2e) were not validated with in situ boreholes nor were GPS coordinates recorded. Therefore, the geolocation of these shorter radar echograms, are best

approximated from field notes, satellite imagery and assuming a constant 0.7 m/s travel speed.

2.10.2.2 GPR conduit height and width estimates for the Isortoq River

The cross section resulting in the GPR echogram plotted in Figure 2c was surveyed twice, from south to north (GPR File ID 065) and from north to south (GPR File ID 066). The size of the four conduits observed in the two GPR echograms were estimated based on the size of the bright reflectors observed (Figure S4, sizes are summarized in Table S2-2). Conduit C3 geometry (Figure S4b) is validated with an in-situ borehole, enabling independent validation of the distance between the river ice surface and the under-ice conduit water surface. Conduit heights in the other three conduits were estimated from the GPR echogram alone. Conduit widths are estimated using both lateral ends of each bright reflector. First, each conduit is selected based on a visual inspection and identification of bright reflector, which is defined as having: (1) lateral continuity over at least 15 traces and (2) the relative amplitude of the bright reflector (from negative peak to positive peak) is equal to the full amplitude (2^{16}). Estimating conduit geometries from both GPS echograms provides a range of conduit widths and heights from which a minimum and maximum cross-sectional area is calculated (Table S2-2).

2.10.3. Description of MODIS wintertime surface melt analysis

Surface melt is inferred using the MOD11A1 Moderate Resolution Imaging Spectroradiometer (MODIS) daily Land Surface Temperature/Emissivity product in Google Earth Engine. First, the MOD11A1 collection is filtered to winter months (December, January and February or DJF) for each winter spanning the MODIS data archive (2000 – 2019). Next, pixel values are converted to °C. and the collection is binarized as pixels with temperature ≥ -1 °C indicative of melt and < -1 °C indicative of no melt (following Hall et al., 2018). The binarized collection is then summed. Finally, the % occurrence of wintertime melts is calculated as the number of grid cells with wintertime melt divided by the number of wintertime observations for grid cells with melt. MOD11A1 wintertime surface melt record should be conservative because melt events during cloudy conditions are not imaged.

2.10.4 Description of MEaSURES passive microwave surface melt analysis

Wintertime surface melt is also identified using the MEaSURES Greenland Surface Melt Daily 25 km EASE-Grid 2.0, Version 1 dataset acquired from the National Snow & Ice Data Center (NSIDC) at: <https://nsidc.org/data/nsidc-0533/versions/1> (Mote, 2014). These data identify the presence of GrIS surface melt at daily time intervals for 25 km

grids using brightness temperature data from three satellite microwave radiometers. The MEaSURES record spans 1979-2012 and finds evidence of surface melt during all winters on record. Melt is identified as far north as 80.77 °N and >3000 m on the ice surface. The % occurrence of wintertime melts is calculated as the number of grid cells with wintertime melt divided by the number of wintertime observations for grid cells experiencing melt.

2.10.5 Description of theoretical subglacial routing analysis

Theoretical subglacial flow paths are simulated using the Hydrology toolbox in ArcMap following the assumption that water at the bed of a glacier flows along a pressure gradient from areas of high to low pressure (Cuffey and Paterson, 2010; Shreve, 1972). To map this, a hydrostatic pressure grid is calculated using the form of the equation given by Lindbäck et al., (2015), where hydraulic head h , in meters, is:

$$h = k \frac{\rho_i}{\rho_w} H + (Z_i - H)$$

where k is the ratio of subglacial water pressure to ice overburden pressure, ρ_i is ice density, ρ_w is water density, H is ice thickness, and Z_i is ice surface elevation. For simulations presented here, $k = 1$ is used, which is a steady state approximation assuming subglacial water pressure is equivalent to ice overburden pressure (Lindbäck et al., 2015). To generate the hydrostatic pressure grid, BedMachine v. 3 data is used (Morlighem et al., 2017).

2.10.6 Explanation of geochemical interpretations

The Na/Cl ratios of snow from bag 1 and 2 deviate from bag 3 and 4 (Figure S2-2). That is, snow from bag 1 and 2 have low solute concentrations and Na/Cl ratios close to seawater composition, indicating meteoric signature of this snow. Snow samples collected in bag 3 and 4 have higher solute concentrations with Na/Cl ratio higher than seawater. Snow sample in bag 3 has even higher total dissolved solute (TDS) and Na/Cl ratios than river water but lower Ca concentrations. The difference in chemical composition between snow collected in bag 3 and Isortoq river water may suggest that the high solute concentrations in the snow may not simply be related to contamination (mixing) with river water. Snow samples from bag 4 have higher TDS, Ca and Na/Cl ratios than snow from bag 1 and 2, but lower than snow in bag 3 and river water collected in February. Snow from bag 3 has a composition similar to Isortoq river water collected in August 2014.

The Isortoq river water collected in August has lower concentrations and Na/Cl ratios compared to Isortoq river water collected in February. The lower concentration in August samples may be due to dilution of a baseflow due to meltwater, while the February samples may indicate chemical and isotopic composition of the baseflow of the river. The Watson river sample has distinguished chemical composition with higher concentration in Ca and TDS, but considerably lower Na/Cl ratios.

Stable isotope composition of the water and snow samples assemble along a line with river water from Isortoq samples collected in February have the lowest (lightest) isotope ratios and snow samples 1 and 2 have higher (heavier) isotope ratios. This may suggest that water source from Isortoq river outflow in February is not related to melting of local snow on the frozen river.

Overall the chemical composition of the Isortoq river water suggest an independent source from snow and from river water in August. Its high solute content, deviation from seawater composition and distinguished isotope composition suggests that this water has been in contact with rock and derived from a water (or ice) source different from local snow. The high solute concentration in the snow from bag 3 and 4 cannot be attributed to any specific processes or sources without further investigation.

2.10.7 Comparison of wintertime and annual average ice surface temperature 1979-2017 at five Greenland Ice Sheet outlet glaciers

The rate of average annual and average wintertime (DJF) ice surface temperature increase was calculated using Modèle Atmosphérique Régional (MAR) version 3.8 regional climate model (RCM) topography corrected ice surface temperature data (variable name = 'STcorr'), acquired from: <ftp://ftp.climato.be/fettweis/>. First, daily temperature data was extracted for five grid cells located near the terminus of five GrIS outlet glaciers, bounding the entire ice sheet (see Table S2-12). Next, the average annual and

average winter ice surface temperature was calculated from the daily data series for each year of available data (1979 – 2017) and for each glacier. Finally, linear regression models were calculated with year as the independent variable (x-axis) and average annual or average winter temperatures as the dependent variable (y-axis). Linear regression results are summarized in Table S2-13. The trends in average annual and average wintertime temperature over time are not all statistically significant (i.e. p-value is > 0.05 for some models). However, Figure S5 suggests that, for all 5 outlet glaciers tested, average wintertime temperatures increased faster than average annual temperatures.

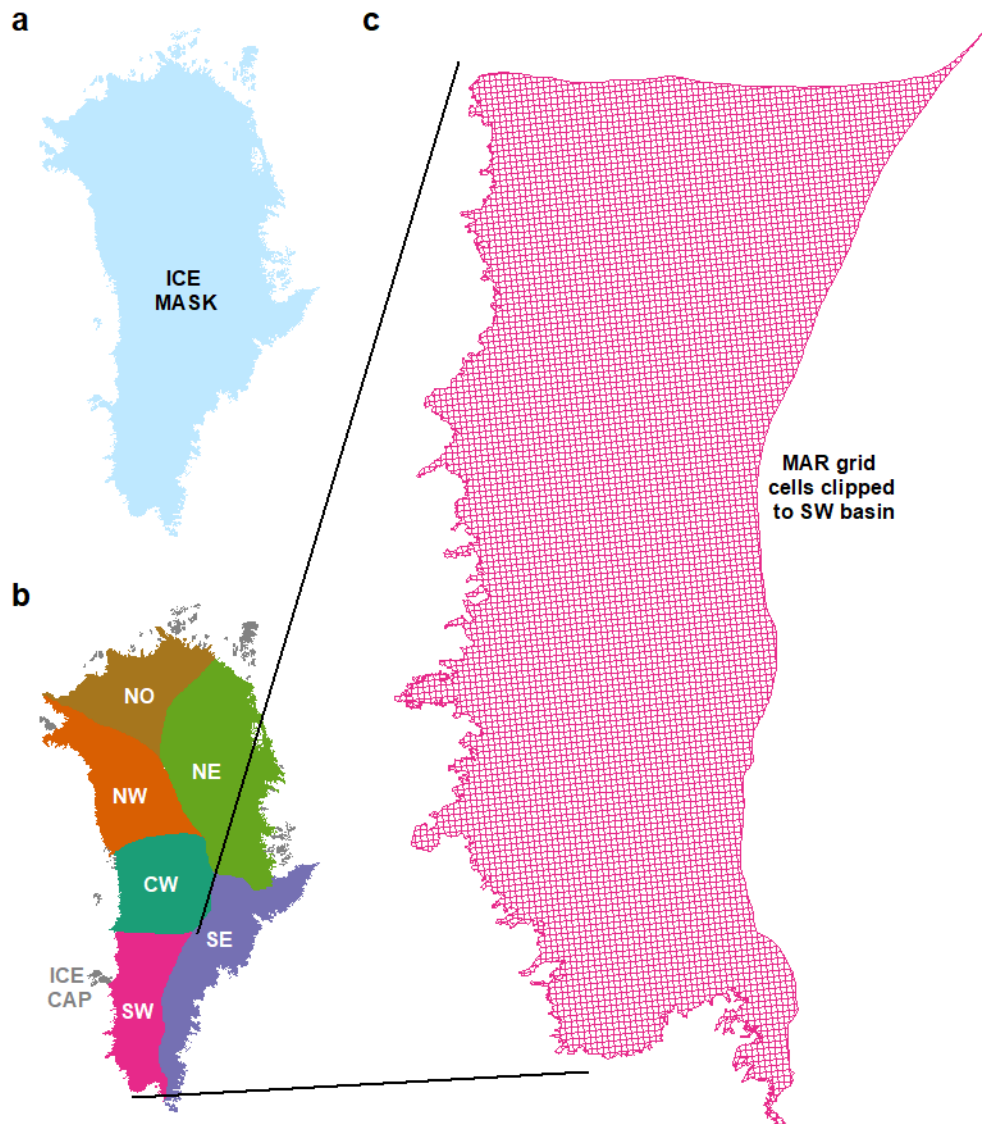


Figure S2-1: fraction of runoff from southwest Greenland Ice Sheet

An (a) ice and (b) basin mask (Rignot and Mouginot, 2012), available as part of the ice sheet mass balance inter-comparison exercise (imbie; link: <http://imbie.org/imbie-2016/drainage-basins/>) were used to extract runoff from MAR outputs. (c) shows thiesen polygons grid cells, in polar stereographic projection, generated from MAR coordinate pairs clipped to the southwest (SW) region. This analysis estimates that ~31% of cumulative

Greenland Ice Sheet runoff between January 1, 1979 and July 23, 2017 comes from the SW region.

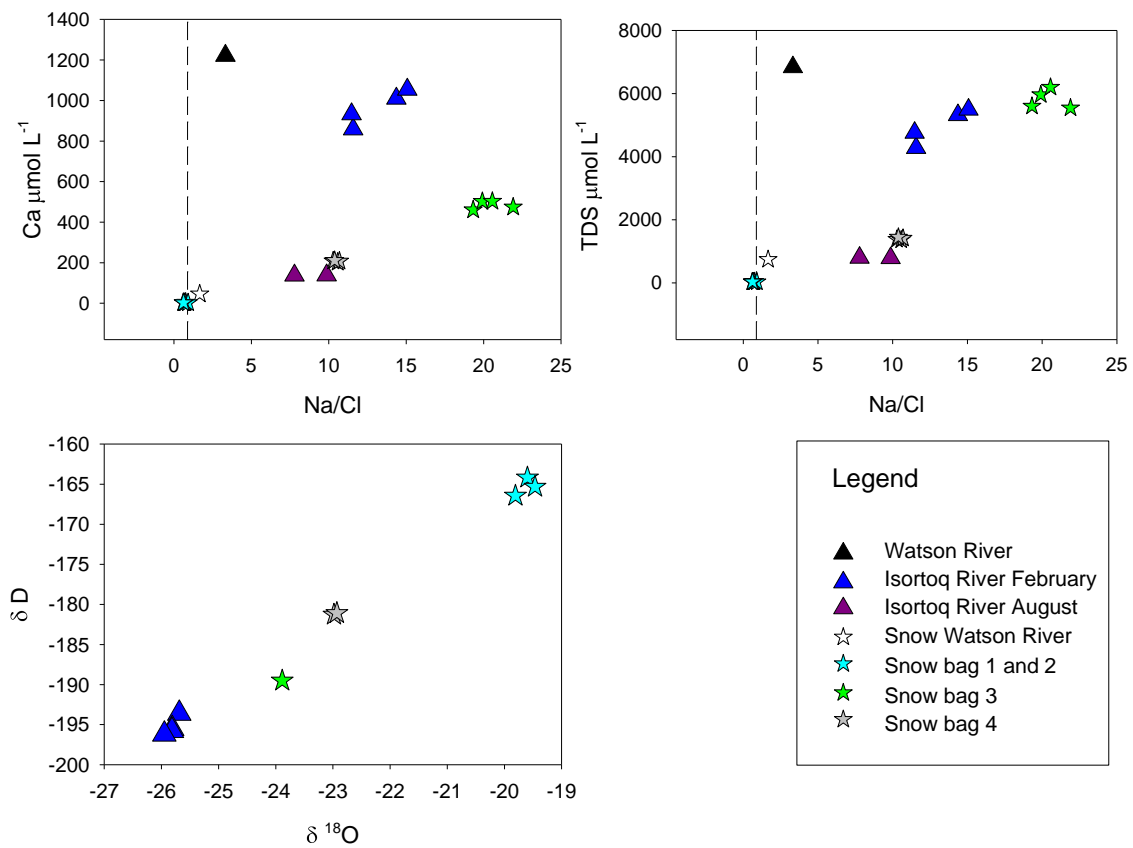


Figure S2-2: geochemical analysis

Geochemical concentrations of snow, and river water in $\mu\text{mol L}^{-1}$ and mol ratio. Na/Cl molar ratio for seawater is displayed as reference.

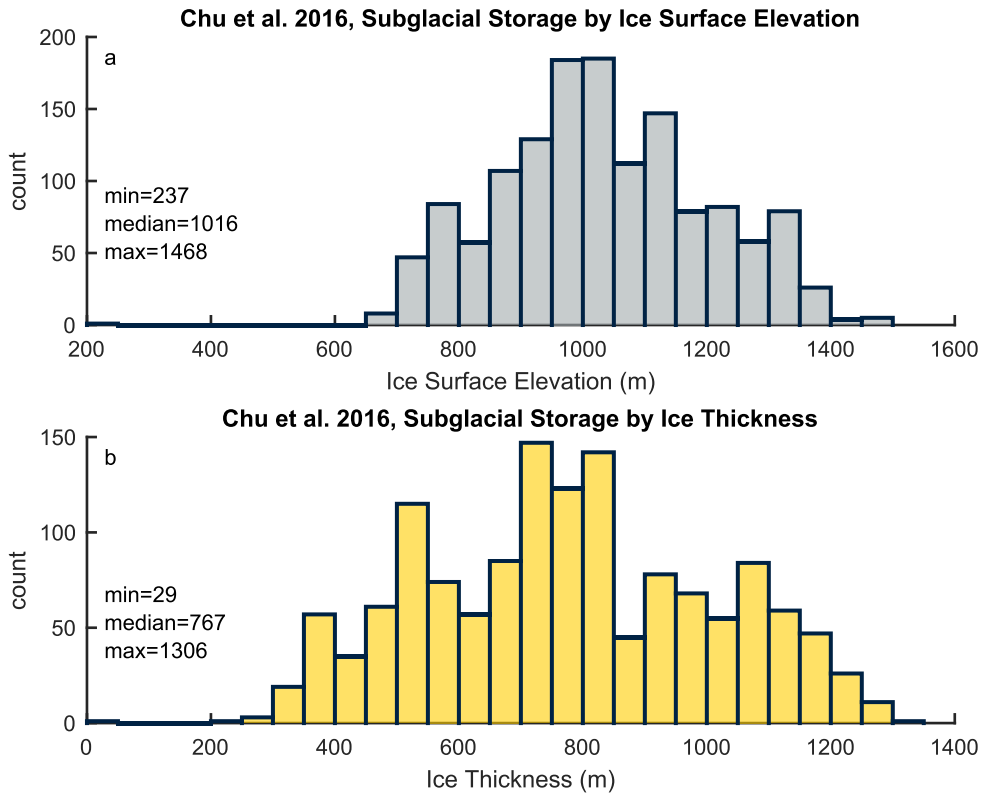


Figure S2-3: Distribution of Chu et al. (2016) storage locations Potential winter/spring subglacial storage locations by (a) ice surface elevation and (b) ice thickness. Subglacial storage location data are from Chu et al. (2016), ice surface elevation and ice thickness data are from BedMachine v. 3 (Morlighem et al., 2017).

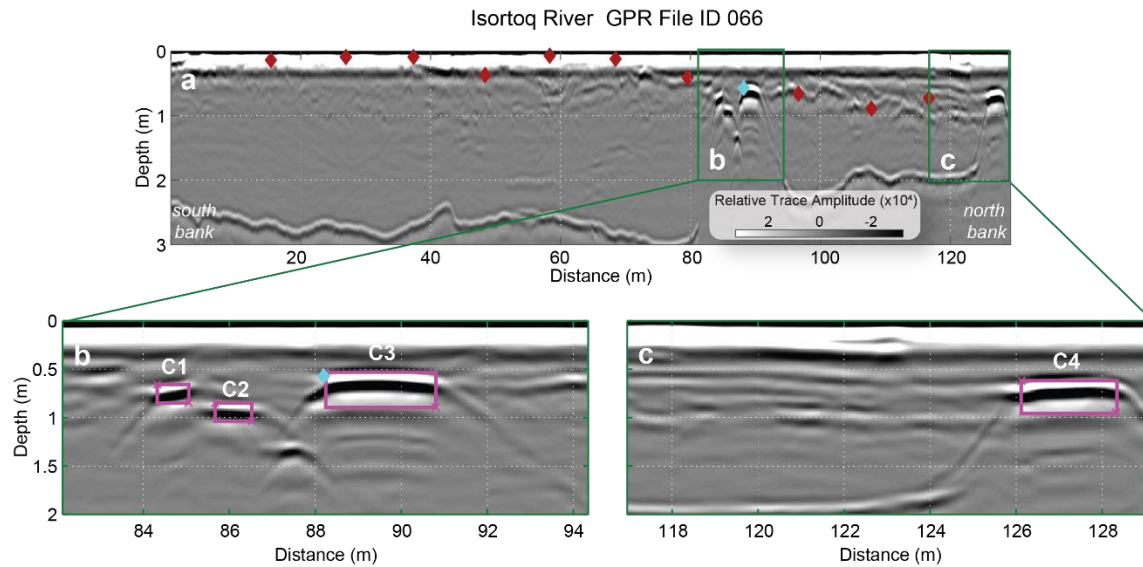


Figure S2-4: Isortoq River under-ice conduit geometry from GPR echogram. The (a) Isortoq River GPR echogram cross-section collected on February 12, 2015. This is the same cross-section shown in Figure 2c, GPR travels from the north bank (right side of GPR echogram) to south (left side of GPR echogram). 11 boreholes were mechanically drilled through the river ice, dry boreholes are shown in red, wet boreholes are shown in cyan. (b) Shows the three bright reflectors closest to the south bank, which is interpreted as conduits #s1-3 (C1, C2 and C3, respectively). Magenta rectangles show estimated conduit width and depth. C3 was validated in-situ with a borehole (Figure 2b). (c) shows conduit #4 (c4), which is closest to the north bank of the Isortoq river.

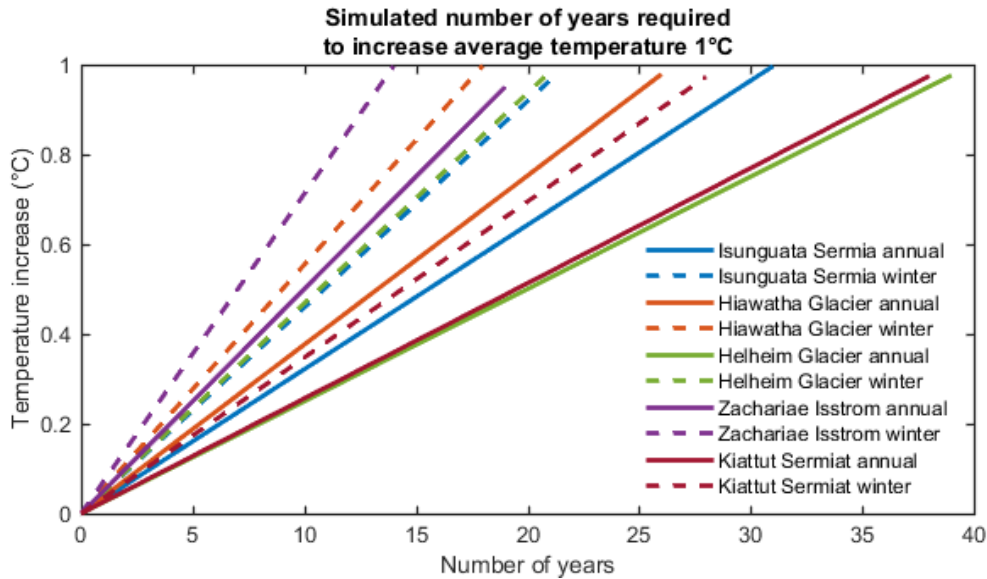


Figure S2-5: average annual and winter ice surface temperature increase. Simulation of the number of years required for average annual (solid lines) and average wintertime (DJF, dashed lines) ice surface temperature to increase 1 °C. These simulations assume a linear fit and are based on the trend in average annual and average wintertime surface temperatures between 1979-2017, as simulated MAR v.3.8. Note that the increase in temperature is not statistically significant across all glaciers. Refer to Table S2-13 for summary of regression results. Simulations are performed for 5 GrIS outlet glaciers that span both east and west coasts of the GrIS from north to south (Table S2-12).

Table S2-1 February 12, 2015 Isortoq River under-ice conduit velocity (V) estimated using mechanical flow meter			
Describing of under-ice velocity measurement			
Instrument Type	Mechanical flow meter		
Model	USGS Type AAMH Ice Current Meter with Poly Buckets. Manufactured by Rickly Hydrological Co.		
Information for converting number of rotations to flow-speed or velocity			
Equation	$V = 2.45R + 0.020$ V = velocity in feet per second (ft s^{-1}) R = revolutions per second (R s^{-1})		
Source	United States Department of the Interior Geological Survey Water Resource Division Standard Rating Table for Type PAA Current Meter (cat's whisker head, polymer bucket wheel)		
Limitations	Instrument rated limits as stated on Standard Rating Table are 0.16 to 12.0 ft s^{-1} or 0.05 to 3.66 m s^{-1} . The field observation presented here falls beneath the minimum instrument rating. Therefore, the resultant discharge measurement is presented as a best approximation. This large uncertainty is further reflected in the ranges in both cross-sectional area (Table S-22) and flow-speeds used to calculate discharge.		
Velocity (V) Calculations			
		number of revolutions (R)	
		1	2
Time (seconds)	60	$V = 2.45 * (1/60) + 0.020$ $V = 0.06 \text{ ft s}^{-1}$ or 0.02 m s^{-1}	$V = 2.45 * (2/60) + 0.020$ $V = 0.10 \text{ ft s}^{-1}$ or 0.03 m s^{-1}
	90	$V = 2.45 * (1/90) + 0.020$ $V = 0.05 \text{ ft s}^{-1}$ or 0.02 m s^{-1}	$V = 2.45 * (2/90) + 0.020$ $V = 0.07 \text{ ft s}^{-1}$ or 0.02 m s^{-1}
	120	$V = 2.45 * (1/120) + 0.020$ $V = 0.04 \text{ ft s}^{-1}$ or 0.01 m s^{-1}	$V = 2.45 * (2/120) + 0.020$ $V = 0.06 \text{ ft s}^{-1}$ or 0.02 m s^{-1}
	150	$V = 2.45 * (1/150) + 0.020$ $V = 0.04 \text{ ft s}^{-1}$ or 0.01 m s^{-1}	$V = 2.45 * (2/150) + 0.020$ $V = 0.05 \text{ ft s}^{-1}$ or 0.02 m s^{-1}
Minimum Velocity (V)	$V = 0.04 \text{ ft s}^{-1}$ $V = 0.01 \text{ m s}^{-1}$		
Maximum Velocity (V)	$V = 0.10 \text{ ft s}^{-1}$ $V = 0.03 \text{ m s}^{-1}$		

Table S2-1: Summary of conduit velocity (V) from February 12, 2015

Isortoq River field data

Table S2-2 February 12, 2015 Isortoq River under-ice conduit cross-sectional areas (A) estimated from GPR transects				
GPR File ID	Conduit ID	Height (cm)	Width (cm)	Area (cm ²)
65	1	21	36	756
65	2	20	51	1020
65	3	33	196	6468
65	4	33	233	7689
66	1	19	73	1387
66	2	19	86	1634
66	3	35	257	8995
66	4	33	220	7260
Summary of Minimum A Values				
	Conduit ID	Height (cm)	Width (cm)	Area (cm ²)
	1	19	36	684
	2	19	51	969
	3	33	196	6468
	4	33	220	7260
sum cm ²			15381	
sum m ²			1.5381	
Summary of Maximum A Values				
	Conduit ID	Height (cm)	Width (cm)	Area (cm ²)
	1	21	73	1533
	2	20	86	1720
	3	35	257	8995
	4	33	233	7689
sum cm ²			19937	
sum m ²			1.9937	
Summary for Discharge (Q) calculations (see Table S2-3)				
Minimum A	1.54 m ²			
Maximum A	1.99 m ²			

Table S2-2: summary conduit geometries

Summary of conduit cross-sectional areas (A = cross-sectional area = width × height). Cross-sectional areas of meltwater conduits are measured in processed GPR data. Results are for the Isortoq River from field measurements collected February 12, 2015

Table S2-3	
Discharge (Q) or Flux Calculations	
Equation	$Q = A * V$ A = Cross-Sectional Area in m^2 (see Table S2-1) V = Velocity in $m s^{-1}$ (see Table S2-2)
Minimum Q	$Q = 1.54 m^2 * 0.01 m s^{-1} = 0.02 m^3 s^{-1}$
Maximum Q	$Q = 1.99 m^2 * 0.03 m s^{-1} = 0.06 m^3 s^{-1}$
Minimum Q per day	$Q = 0.02 m^3 s^{-1} * 60 s m^{-1} * 60 m h^{-1} * 24 h d^{-1}$ $Q = 1639.13 m^3 d^{-1}$
Maximum Q per day	$Q = 0.06 m^3 s^{-1} * 60 s m^{-1} * 60 m h^{-1} * 24 h d^{-1}$ $Q = 5348.38 m^3 d^{-1}$

Table S2-3: Summary of conduit flux (Q) from February 12, 2015 Isortoq

River field data

Table S2-4									
Summary of geochemical analysis of river water and snow samples									
Info		River water				Isortoq River		Watson River	
sample id		LS 5	LS 6	LS 7	LS 8	IST 3B	IST 3A	WS	WB1
Na	umol/L	628.53	707.44	810.39	820.86	92.46	92.61	143.99	642.62
Mg	umol/L	195.83	221.08	245.26	249.75	29.37	28.09	87.61	459.61
Al	nmol/L	567.46	445.14	492.22	473.31	988.14	1032.99	1134.54	1073.39
K	umol/L	152.66	167.67	190.43	194.55	72.20	67.07	42.63	358.11
Ca	umol/L	858.55	932.39	1009.98	1053.74	136.99	137.61	45.83	1221.21
Sr	nmol/L	1166.06	1215.59	1301.99	1307.69	232.82	218.90	82.86	1503.99
Ba	nmol/L	92.33	95.75	98.88	96.77	36.48	34.22	11.29	188.66
Cl	umol/L	54.34	61.70	56.41	54.47	11.88	9.39	86.63	193.35
SO4	umol/L	448.98	450.63	446.95	447.74	29.49	27.53	29.19	204.20
Br	umol/L	<LOD	<LOD	<LOD	<LOD	<LOD	<LOD	<LOD	<LOD
NO3	umol/L	1.39	<LOD	1.02	1.18	<LOD	4.05	14.63	56.01
HCO3*	umol/L	1937.66	2219.08	2560.98	2672.43	426.51	426.65	308.50	3760.59
δ18O	permil	-25.69	-25.81	-25.82	-25.95				
δD	permil	-193.61	-195.52	-195.75	-196.21				
Info		snow bag 1				snow bag 2			
sample id		LS 13	LS 14	LS 15	LS 16	LS 17	LS 18	LS 19	LS 20
Na	umol/L	10.60	12.08	10.57	11.14	10.87	10.21	10.40	10.04
Mg	umol/L	1.88	2.22	1.82	1.85	1.82	1.69	1.72	1.62
Al	nmol/L	151.22	87.47	322.83	88.21	97.11	244.26	251.30	68.57
K	umol/L	0.84	1.25	0.89	0.82	0.75	0.71	0.74	0.68
Ca	umol/L	3.15	4.51	2.98	2.79	2.13	3.25	2.51	2.29
Sr	nmol/L	5.02	7.65	4.91	5.59	4.68	5.02	4.57	4.79
Ba	nmol/L	<LOD	<LOD	<LOD	<LOD	<LOD	<LOD	<LOD	<LOD
Cl	umol/L	14.86	15.92	16.78	15.41	11.95	17.05	15.80	16.18
SO4	umol/L	2.63	2.42	2.59	2.22	<LOD	2.33	2.60	2.52
Br	umol/L	<LOD	<LOD	<LOD	<LOD	<LOD	<LOD	<LOD	<LOD
NO3	umol/L	<LOD	<LOD	<LOD	<LOD	<LOD	<LOD	<LOD	<LOD
HCO3*	umol/L	1.38	6.02	0.00	1.36	7.57	0.00	0.00	0.00
δ18O	permil	-19.60	-19.47						-19.81
δD	permil	-164.18	-165.32						-166.43
Info		snow bag 3				snow bag 4			
sample id		LS 21	LS 22	LS 23	LS 24	LS 25	LS 26	LS 27	LS 28
Na	umol/L	1378.39	1400.93	1474.48	1539.27	247.46	245.37	258.83	267.66
Mg	umol/L	489.18	497.83	526.02	547.62	91.80	91.40	93.58	94.43
Al	nmol/L	57.45	51.89	54.11	47.44	198.30	286.14	216.83	241.66

K	umol/L	249.80	260.06	267.31	285.77	45.95	47.22	49.85	50.47
Ca	umol/L	474.39	460.65	502.18	502.68	208.00	202.26	207.33	210.84
Sr	nmol/L	781.21	781.21	797.76	830.75	251.43	262.38	260.79	273.11
Ba	nmol/L	16.02	15.07	15.36	15.22	8.96	8.96	10.12	8.59
Cl	umol/L	62.93	72.52	74.05	74.87	24.07	23.22	24.22	25.80
SO4	umol/L	599.20	593.56	600.14	598.67	102.06	101.35	101.58	101.39
Br	umol/L	4.09	<LOD	<LOD	<LOD	<LOD	<LOD	<LOD	<LOD
NO3	umol/L	<LOD	2.63	2.42	2.36	<LOD	<LOD	<LOD	<LOD
HCO3*	umol/L	2293.99	2318.33	2523.85	2653.41	664.80	654.02	683.14	700.10
δ18O	permil	-23.89				-22.98	-22.93		
δD	permil	-189.50				-181.27	-181.07		

Info	Hagedorn 2012, GrIS snow/slush	
Na	umol/L	109.02
Mg	umol/L	19.58
Al	nmol/L	2466.54
K	umol/L	7.08
Ca	umol/L	37.94
Sr	nmol/L	108.42
Ba	nmol/L	48.06
Cl	umol/L	112.33
SO4	umol/L	48.14
Br	umol/L	<LOD
NO3	umol/L	92.19
HCO3*	umol/L	22.55
δ18O	permil	
δD	permil	

Table S2-4: summary of geochemical analysis of river water and snow samples

Table S2-5					
West Greenland Daily Surface Energy Balance Winter Melt Events					
Count	Date (yyyy-mm-dd)	Melt mm d⁻¹	Count	Date (yyyy-mm-dd)	Melt mm d⁻¹
1	2009-12-14	3.29	19	2010-12-11	1.24
2	2009-12-31	0.41	20	2010-12-12	72.73
3	2010-01-01	0.05	21	2011-01-01	2.61
4	2010-01-11	0.65	22	2011-01-25	58.5
5	2010-01-22	0.11	23	2011-02-11	121.82
6	2010-01-29	0.1	24	2012-02-13	24.19
7	2010-01-30	9.8	25	2012-02-14	3.24
8	2010-01-31	14.44	26	2013-02-17	1.37
9	2010-02-01	2.3	27	2014-02-13	0.07
10	2010-02-03	0.09	28	2014-02-17	0.16
11	2010-02-06	0.39	29	2014-02-28	1.47
12	2010-02-13	0.21	30	2014-12-28	0.9
13	2010-02-22	0.31	31	2015-02-02	5.09
14	2010-02-24	0.43	32	2015-02-03	29.17
15	2010-12-03	2.63	33	2016-01-19	0.02
16	2010-12-04	0.43	34	2016-02-29	14.61
17	2010-12-08	12.29	35	2016-12-08	0.56
18	2010-12-09	4.13	36	2017-02-27	13.73
Statistical Summary (melt mm d ⁻¹)					
	Minimum		0.02		
	Mean		11.21		
	median		1.42		
	Maximum		121.82		
	Standard Deviation		24.73		

Table S2-5: K-Transect wintertime surface melt

Summary of wintertime (DJF) surface melt events as calculated using surface energy balance (SEB) model outputs (van As et al., 2017) for the K-Transect in southwest Greenland from 2009-17

Table S2-6					
<i>River name: Watson River</i>					
<i>Tributary outlet glaciers: Russell, Leverette, Ørkendalen, Isorlersuup</i>					
<i>Site description: Kangerlussuaq bridge</i>					
Date	ID	Notes	Depth (m)	Latitude	Longitude
Feb. 9, 2015	TN	Transect End - north	-	67.00546	-50.68718
	H1	Borehole #1	1.11	67.00539	-50.68711
	H2	Borehole #2	0.94	67.00535	-50.68707
	TS	Transect end - south	-	67.00530	-50.68701
Depth = thickness of proglacial river ice.					

Table S2-6: summary of proglacial river ice boreholes in the Watson river, beneath the Kangerlussuaq bridge.

Table S2-7					
<i>River name: Watson River</i>					
<i>Tributary outlet glaciers: Russell, Leverette, Ørkendalen, Isorlersuup</i>					
<i>Site description: main channel, east of Kanglerssuaq International Airport</i>					
Date	ID	Notes	Depth (m)	Latitude	Longitude
February 11, 2015	TN	Transect end - north	-	67.02029	-50.67550
	H10	Borehole #10	0.02	67.02017	-50.67540
	H9	Borehole #9	0.45	67.02012	-50.67537
	H8	Borehole #8	0.42	67.02007	-50.67534
	H7	Borehole #7	0.61	67.02004	-50.67531
	H6	Borehole #6	0.58	67.01998	-50.67529
	H5	Borehole #5	0.66	67.01993	-50.67525
	H4	Borehole #4	0.55	67.01987	-50.67522
	H3	Borehole #3	1	67.01978	-50.67520
	H2	Borehole #2	0.82	67.01969	-50.67515
	H1	Borehole #1	0.22	67.01957	-50.67505
TS	Transect end - south	-	67.01948	-50.67493	
Depth = thickness of proglacial river ice.					

Table S2-7: summary of proglacial river ice boreholes in the Watson river, east of Kanglerussuaq runway.

Table S2-8					
<i>River name: Sandflugtdalen River</i>					
<i>Tributary outlet glaciers: Russell, Leverette</i>					
<i>Site description: upstream of Watson river confluence</i>					
Date	ID	Notes	Depth (m)	Latitude	Longitude
February 11, 2015	TN	Transect end - north	-	67.01993	-50.65291
	H10	Borehole #10	0.02	67.01990	-50.65283
	H9	Borehole #9	0.01	67.01988	-50.65278
	H8	Borehole #8	0.03	67.01985	-50.65276
	H7	Borehole #7	0.02	67.01980	-50.65273
	H6	Borehole #6	0.02	67.01977	-50.65267
	H5	Borehole #5	0.06	67.01973	-50.65263
	H4	Borehole #4 - channel bar	0	67.01970	-50.65259
	H3	Borehole #3 - channel bar	0	67.01966	-50.65254
	H2	Borehole #2	0.04	67.01963	-50.65250
	H1	Borehole #1	0.11	67.01961	-50.65243
TS	Transect end - south	-	67.01951	-50.65231	
Depth = thickness of proglacial river ice.					

Table S2-8: summary of proglacial river ice boreholes in the Sandflugtdalen river, upstream of Watson river confluence.

Table S2-9					
<i>River name: Ørkendalen River</i>					
<i>Tributary outlet glaciers: Ørkendalen, Isorlersuup</i>					
<i>Site description: upstream of Watson river confluence</i>					
Date	ID	Notes	Depth (m)	Latitude	Longitude
February 13, 2015	TN	Transect end - north	-	67.01186	-50.62106
	H10	Borehole #10	0.56	67.01180	-50.62105
	CR	Crack in river ice	0.70	67.01176	-50.62107
	H9	Borehole #9	0.37	67.01170	-50.62115
	H8	Borehole #8	0.24	67.01162	-50.62117
	H7	Borehole #7	0.13	67.01154	-50.62124
	H6	Borehole #6	0.10	67.01148	-50.62130
	H5	Borehole #5	0.11	67.01141	-50.62136
	H4	Borehole #4	0.26	67.01127	-50.62147
	H3	Borehole #3	0.05	67.01119	-50.62152
	H2	Borehole #2	0.33	67.01101	-50.62168
	H1	Borehole #1	0.38	67.01113	-50.6216
TS	Transect end - south	-	67.01094	-50.62177	
Depth = thickness of proglacial river ice.					

Table S2-9: summary of proglacial river ice boreholes in the Ørkendalen river, upstream of Watson river confluence.

Table S2-10					
<i>River name: Ørkendalen River</i>					
<i>Tributary outlet glaciers: Ørkendalen, Isorlersuup</i>					
<i>Site description: near glacier termini</i>					
Date	ID	Notes	Depth (m)	Latitude	Longitude
Februa ry 9, 2015	TN	Transect end - north	-	66.96605	-49.97620
	H2	Borehole #2	2.03	66.96598	-49.97624
	H1	Borehole #1	2.07	66.96584	-49.97624
	TS	Transect end - south	-	66.96569	-49.97622
Depth = thickness of proglacial river ice.					

Table S2-10: summary of proglacial river ice boreholes in the Ørkendalen river, near outlet glacier termini.

Table S2-11					
<i>River name: Isortoq River</i>					
<i>Tributary outlet glaciers: Isinguata Sermia</i>					
<i>Site description: near glacier terminus</i>					
Date	ID	Notes	Depth (m)	Latitude	Longitude
February 12, 2015	TN	Transect end - north	-	67.19179	-50.36975
	H11	Borehole #11	0.73	67.19168	-50.36979
	H10	Borehole #10	0.89	67.19160	-50.36982
	H9	Borehole #9	0.66	67.19150	-50.36987
	H8	Borehole #8 - water	<i>*water*</i>	67.19143	-50.36991
	H7	Borehole #7	0.41	67.19135	-50.36995
	H6	Borehole #6	0.12	67.19125	-50.37001
	H5	Borehole #5	0.07	67.19116	-50.37006
	H4	Borehole #4	0.37	67.19108	-50.37011
	H3	Borehole #3	0.09	67.19098	-50.37016
	H2	Borehole #2	0.09	67.19089	-50.37023
	H1	Borehole #1	0.14	67.19079	-50.37028
TS	Transect end - south	-	67.19081	-50.37037	
Depth = thickness of proglacial river ice.					

Table S2-11: summary of proglacial river ice boreholes in the Isortoq river, near outlet glacier terminus.

Table S2-12					
MAR v3.8 grid cell locations for four outlet glacier daily temperature data extractions for years 1979-2017					
Glacier Name	MAR v3.8 grid cell				
	Latitude	Longitude	linear index	row	column
Isunguata Sermia	67.1726	-50.1310	56351	64	188
Hiawatha Glacier	78.7950	-66.8241	139711	47	465
Helheim Glacier	66.3950	-38.3389	48327	167	161
Zachariae Isstrom	78.9287	-21.3910	135684	234	451
Kiattut Sermiat	61.2898	-45.2210	14239	92	48

Table S2-12: summary of MAR grid cells used for ice surface temperature analysis

Table S2-13					
Linear regression model fits from five Greenland Ice Sheet (GrIS) outlet glaciers. Average annual temperature by year and average wintertime (DJF) temperature by year for all years 1979-2017. Temperature data is topography corrected surface temperature from MAR v.3.8.					
Glacier name	Time	Coefficient	SE	p-value	r²
Isinguata	annual	0.03	0.02	0.16	0.05
Sermia	winter	0.05	0.05	0.32	0.03
Hiawatha	annual	0.04	0.01	0.01	0.17
Glacier	winter	0.06	0.02	0.03	0.12
Helheim	annual	0.03	0.01	<0.00	0.30
Glacier	winter	0.05	0.02	0.01	0.16
Zachariae	annual	0.05	0.01	<0.00	0.38
Isstrom	winter	0.07	0.02	<0.00	0.21
Kiattut	annual	0.03	0.02	0.14	0.06
Sermiat	winter	0.03	0.04	0.36	0.02

Table S2-13: linear regression model results for wintertime and annual temperatures

2.10.3 References:

- Ahlstrøm, A. P., Petersen, D., Langen, P. L., Citterio, M., and Box, J. E. (2017). Abrupt shift in the observed runoff from the southwestern Greenland ice sheet. *Sci. Adv.* 3, 1–8. doi:10.1126/sciadv.1701169.
- Alsdorf, D. E., and Lettenmaier, D. P. (2003). Tracking Fresh Water from Space. *Science (80-.)*. 301, 1491–1494. doi:10.1126/science.1089802.
- Alsdorf, D. E., Lettenmaier, D. P., and Vörösmarty, C. J. (2003). The need for global, satellite-based observations of terrestrial surface waters. *EOS, Trans. Am. Geophys. Union Trans. Am. Geophys. Union* 84, 269–276. doi:10.1029/2003EO290001.
- Alsdorf, D. E., Rodríguez, E., and Lettenmaier, D. P. (2007). Measuring surface water from space. *Rev. Geophys.* 45. doi:10.1029/2006RG000197.
- Altenau, E. H., Pavelsky, T. M., Moller, D., Lion, C., Pitcher, L. ., Allen, G. H., et al. (2017). AirSWOT measurements of river water surface elevation and slope: Tanana River, AK. *Geophys. Res. Lett.* 44, 181–189. doi:10.1002/2016GL071577.
- Altenau, E. H., Pavelsky, T. M., Moller, D., Pitcher, L. H., Bates, P. D., Durand, M. T., et al. (2019). Temporal variations in river water surface elevation and slope captured by AirSWOT. *Remote Sens. Environ.* 224, 304–316. doi:10.1016/j.rse.2019.02.002.
- Andrews, L. C., Catania, G. A., Hoffman, M. J., Gulley, J. D., Lüthi, M. P.,

- Ryser, C., et al. (2014). Direct observations of evolving subglacial drainage beneath the Greenland Ice Sheet. *Nature* 514, 80–83. doi:10.1038/nature13796.
- Arrhenius, S. (1896). On the influence of carbonic acid in the air upon the temperature of the ground. *Philos. Mag. J. Sci.* 41, 237–276. doi:10.1080/14786449608620846.
- Banwell, A. F., MacAyeal, D. R., and Sergienko, O. V. (2013). Breakup of the Larsen B Ice Shelf triggered by chain reaction drainage of supraglacial lakes. *Geophys. Res. Lett.* 40, 5872–5876. doi:10.1002/2013GL057694.
- Bates, P. D., Wilson, M. D., Horritt, M. S., Mason, D. C., Holden, N., and Currie, A. (2006). Reach scale floodplain inundation dynamics observed using airborne synthetic aperture radar imagery: Data analysis and modelling. *J. Hydrol.* 328, 306–318. doi:10.1016/j.jhydrol.2005.12.028.
- Bell, R. E., Chu, W., Kingslake, J., Das, I., Tedesco, M., Tinto, K. J., et al. (2017). Antarctic ice shelf potentially stabilized by export of meltwater in surface river. *Nature* 544, 344–348. doi:10.1038/nature22048.
- Biancamaria, S., Lettenmaier, D. P., and Pavelsky, T. M. (2016). The SWOT Mission and Its Capabilities for Land Hydrology. *Surv. Geophys.* 37, 307–337. doi:10.1007/s10712-015-9346-y.
- Catania, G. A., and Neumann, T. A. (2010). Persistent englacial drainage features in the Greenland Ice Sheet. *Geophys. Res. Lett.* 37, 1–5. doi:10.1029/2009GL041108.

- Chu, V. W. (2014). Greenland ice sheet hydrology A review. *Prog. Phys. Geogr.* 38, 19–54. doi:10.1177/0309133313507075.
- Chu, W., Schroeder, D. M., Seroussi, H., Creyts, T. T., Palmer, S. J., and Bell, R. E. (2016). Extensive winter subglacial water storage beneath the Greenland Ice Sheet. *Geophys. Res. Lett.* 43, 12,484–12,492. doi:10.1002/2016GL071538.
- Church, J. a., Clark, P. U., Cazenave, a., Gregory, J. M., Jevrejeva, S., Levermann, a., et al. (2013). Sea level change. *Clim. Chang. 2013 Phys. Sci. Basis. Contrib. Work. Gr. I to Fifth Assess. Rep. Intergov. Panel Clim. Chang.*, 1137–1216. doi:10.1017/CB09781107415315.026.
- Colgan, W., Sommers, A., Rajaram, H., Abdalati, W., and Frahm, J. (2015). Considering thermal-viscous collapse of the Greenland ice sheet. *Earth's Futur.* 3, 252–267. doi:10.1002/2015EF000301.Abstract.
- Colgan, W., Steffen, K., McLamb, W. S., Abdalati, W., Rajaram, H., Motyka, R., et al. (2011). An increase in crevasse extent, West Greenland: Hydrologic implications. *Geophys. Res. Lett.* 38, L18502. doi:10.1029/2011GL048491.
- Cooper, M. G., Smith, L. C., Rennermalm, A. K., Miège, C., Pitcher, L. H., Ryan, J. C., et al. (2018). Near surface meltwater storage in low-density bare ice of the Greenland ice sheet ablation zone. *Cryosph.* 12, 955–970. doi:https://doi.org/10.5194/tc-2017-107.
- Cowton, T., Nienow, P., Sole, A., Wadham, J., Lis, G., Bartholomew, I., et al.

- (2013). Evolution of drainage system morphology at a land-terminating Greenlandic outlet glacier. *J. Geophys. Res. Earth Surf.* 118, 29–41. doi:10.1029/2012JF002540.
- Cowton, T. R., Todd, J. A., and Benn, D. I. (2019). Sensitivity of tidewater glaciers to submarine melting governed by plume locations. *Geophys. Res. Lett.*, 1–9. doi:10.1029/2019gl084215.
- Cuffey, K., and Paterson, W. S. B. (2010). *The Physics of Glacier*. 4th ed. Academic Press.
- Dietrich, W. E., Smith, J. D., and Dunne, T. (1979). Flow and Sediment Transport in a Sand Bedded Meander. *J. Geol.* 87, 305–315. Available at: <https://www.jstor.org/stable/30060821>%0D.
- Durand, M., Lee-Lueng, F., Lettenmaier, D. P., Alsdord, D. E., Rodriguez, E., and Esteban-Fernandez, D. (2010). The surface water and ocean topography mission: Observing terrestrial surface water and oceanic submesoscale eddies. *Proc. IEEE* 98, 766–779. doi:10.1109/JPROC.2010.2043031.
- Fayne, J. V., Smith, L. C., Pitcher, L. H., and Pavelsky, T. M. (2019). ABoVE: AirSWOT Ka-band Radar over Surface Waters of Alaska and Canada, 2017. *ORNL DAAC, Oak Ridge, Tennessee, USA*. doi:<https://doi.org/10.3334/ORNLDAAC/1646>.
- Ferguson, R. I. (1973). Sinuosity of Supraglacial Streams. *Geol. Soc. Am. Bull.* 84, 251–256. doi:10.1130/0016-7606(1973)84<251.

- Forster, R. R., Box, J. E., van den Broeke, M. R., Miede, C., Burgess, E. W., van Angelen, J. H., et al. (2014). Extensive liquid meltwater storage in firn within the Greenland ice sheet. *Nat. Geosci.* 7, 95–98. Available at: <http://dx.doi.org/10.1038/ngeo2043>.
- Fountain, A. G., and Walder, J. S. (1998). Water flow through temperate glaciers. *Rev. Geophys.* 36, 299–328. doi:10.1029/97RG03579.
- Fraser, N. J., Inall, M. E., Jones, S. C., Magaldi, M. G., Haine, T. W. N., and Jones, S. C. (2018). Wintertime Fjord-Shelf Interaction and Ice Sheet Melting in Southeast Greenland. *J. Geophys. Res. Ocean.* 123, 9156–9177. doi:10.1029/2018JC014435.
- Fried, M. J., Catania, G. A., Bartholomaeus, T. C., Duncan, D., Davis, M., Stearns, L. A., et al. (2015). Distributed subglacial discharge drives significant submarine melt at a Greenland tidewater glacier. *Geophys. Res. Lett.* 42, 9328–9336. doi:10.1002/2015GL065806.
- Graham, R. M., Cohen, L., Petty, A. A., Boisvert, L. N., Rinke, A., Hudson, S. R., et al. (2017). Increasing frequency and duration of Arctic winter warming events. *Geophys. Res. Lett.* 44, 6974–6983. doi:10.1002/2017GL073395.
- Hall, D. K., Cullather, R. I., Digirolamo, N. E., Comiso, J. C., Medley, B. C., and Nowicki, S. M. (2018). A Multilayer Surface Temperature , Surface Albedo , and Water Vapor Product of Greenland from MODIS. *Remote Sens.*, 1–17. doi:10.3390/rs10040555.

- Harrington, J. A., Humphrey, N. F., and Harper, J. T. (2015). Temperature distribution and thermal anomalies along a flowline of the Greenland ice sheet. *Ann. Glaciol.* 56, 98–104. doi:10.3189/2015AoG70A945.
- Hartmann, D. J., Klein Tank, A. M. G., Rusticucci, M., Alexander, L. V., Brönnimann, S., Charabi, Y. A. R., et al. (2013). Observations: Atmosphere and Surface. *Clim. Chang. 2013 Phys. Sci. Basis. Contrib. Work. Gr. I to Fifth Assess. Rep. Intergov. Panel Clim. Chang.*, 159–254. doi:10.1017/CBO9781107415324.008.
- Hauer, M. E., Evans, J. M., and Mishra, D. R. (2016). Millions projected to be at risk from sea-level rise in the continental United States. *Nat. Clim. Chang.* 6, 691–695. doi:10.1038/NCLIMATE2961.
- Holland, D. M., Thomas, R. H., De Young, B., Ribergaard, M. H., and Lyberth, B. (2008). Acceleration of Jakobshavn Isbr triggered by warm subsurface ocean waters. *Nat. Geosci.* 1, 659–664. doi:10.1038/ngeo316.
- Holmes, G. (1955). Morphology and hydrology of the Mint Julep area, southwest Greenland.
- Isenko, E., and Mavlyudov, B. (2002). On the intensity of ice melting in supraglacial and englacial channels. *Bull. Glaciol. Res.* 19, 93–99.
- Isenko, E., Naruse, R., and Mavlyudov, B. (2005). Water temperature in englacial and supraglacial channels: Change along the flow and contribution to ice melting on the channel wall. *Cold Reg. Sci. Technol.*

42, 53–62. doi:10.1016/j.coldregions.2004.12.003.

Jarosch, A. H., and Gudmundsson, M. T. (2012). A numerical model for meltwater channel evolution in glaciers. *Cryosphere* 6, 493–503. doi:10.5194/tc-6-493-2012.

Jezek, K., Wu, X., Paden, J., and Leuschen, C. (2013). Radar mapping of Isunnguata Sermia, Greenland. *J. Glaciol.* 59, 1135–1146. doi:10.3189/2013JoG12J248.

Joughin, I., Das, S. B., King, M. A., Smith, B. E., and Howat, I. M. (2008). Seasonal Speedup Along the Western Flank of the Greenland Ice Sheet. *Science* (80-.).

Jowett, I. G. (1993). A method for objectively identifying pool, run, and riffle habitats from physical measurements. *New Zeal. J. Mar. Freshw. Res.* 27, 241–248. doi:10.1080/00288330.1993.9516563.

Karlstrom, L., and Yang, K. (2016). Fluvial supraglacial landscape evolution on the Greenland Ice Sheet. *Geophys. Res. Lett.* 43, 2683–2692. doi:10.1002/2016GL067697.

Kendrick, A. K., Schroeder, D. M., Chu, W., Young, T. J., Christoffersen, P., Todd, J., et al. (2018). Surface Meltwater Impounded by Seasonal Englacial Storage in West Greenland. *Geophys. Res. Lett.*, 1–8. doi:10.1029/2018GL079787.

Kiel, B., Alsdorf, D., and LeFavour, G. (2006). Capability of SRTM C- and X-band DEM Data to Measure Water Elevations in Ohio and the Amazon.

Photogramm. Eng. Remote Sens. 72, 313–320.

doi:10.14358/PERS.72.3.313.

Kingslake, J., Ely, J. C., Das, I., and Bell, R. E. (2017). Widespread movement of meltwater onto and across Antarctic ice shelves. *Nature* 544, 349–352. doi:10.1038/nature22049.

Koenig, L. S., Lampkin, D. J., Montgomery, L. N., Hamilton, S. L., Turrin, J. B., Joseph, C. A., et al. (2015). Wintertime storage of water in buried supraglacial lakes across the Greenland Ice Sheet. *Cryosph.* 9, 1333–1342. doi:10.5194/tc-9-1333-2015.

Kyzivat, E. D., Smith, L. C., Pitcher, L. H., Fayne, J. V., Cooley, S. W., Cooper, M. G., et al. (2019). ABoVE: AirSWOT Water Masks from Color-Infrared Imagery over Alaska and Canada, 2017. *ORNL DAAC, Oak Ridge, Tennessee, USA*. doi:https://doi.org/10.3334/ORNLDAAC/1707.

Kyzivat, E. D., Smith, L. C., Pitcher, L. H., J., A., Pavelsky, T. M., Cooley, S. W., et al. (2018). ABoVE: AirSWOT Color-Infrared Imagery Over Alaska and Canada, 2017. *ORNL DAAC, Oak Ridge, Tennessee, USA*. doi:https://doi.org/10.3334/ORNLDAAC/1643.

Lee, H., Durand, M., Jung, H. C., Alsdorf, D., Shum, C. K., and Sheng, Y. (2010). Characterization of surface water storage changes in Arctic lakes using simulated SWOT measurements. *Int. J. Remote Sens.* 31, 3931–3953. doi:10.1080/01431161.2010.483494.

LeFavour, G., and Alsdorf, D. (2005). Water slope and discharge in the

Amazon River estimated using the shuttle radar topography mission digital elevation model. *Geophys. Res. Lett.* 32.

doi:10.1029/2005GL023491.

Lindbäck, K., Pettersson, R., Hubbard, A. L., Doyle, S. H., van As, D., Mikkelsen, A. B., et al. (2015). Subglacial water drainage, storage, and piracy beneath the Greenland Ice Sheet. *Geophys. Res. Lett.*, n/a-n/a.

doi:10.1002/2015GL065393.

Margulis, S. A. (2017). *Introduction to Hydrology*.

doi:10.5021/ad.2012.24.4.438.

Marston, R. A. (1983). Supraglacial Stream Dynamics on the Juneau Icefield.

Ann. Assoc. Am. Geogr. 73, 597–608. doi:10.1111/j.1467-

8306.1983.tb01861.x.

Masson-Delmotte, V., Schulz, M., Abe-Ouchi, A., Beer, J., Ganopolski, A., González Rouco, J. F., et al. (2013). Information from Paleoclimate Archives. *Clim. Chang. 2013 Phys. Sci. Basis. Contrib. Work. Gr. I to Fifth Assess. Rep. Intergov. Panel Clim. Chang.*, 383–464.

doi:10.1017/CBO9781107415324.

McGrath, D., Colgan, W., Steffen, K., Lauffenburger, P., and Balog, J.

(2011). Assessing the summer water budget of a moulin basin in the sermeq avannarleq ablation region, Greenland ice sheet. *J. Glaciol.* 57,

954–964. doi:10.3189/002214311798043735.

Meierbachtol, T., Harper, J., and Humphrey, N. (2013). Basal Drainage

- System Response to Increasing Surface Melt on the Greenland Ice Sheet. *Science* (80-.). 341, 777–779. doi:10.1126/science.1235905.
- Miller, C. E., Griffith, P. C., Goetz, S. J., Hoy, E. E., Pinto, N., McCubbin, I. B., et al. (2019). An overview of ABoVE airborne campaign data acquisitions and science opportunities. *Environ. Res. Lett.* 14, 080201. doi:10.1088/1748-9326/ab0d44.
- Montgomery, D. R., Beamer, E. M., Pess, G. R., and Quinn, T. P. (1999). Channel type and salmonid spawning distribution and abundance. *Can. J. Fish. Aquat. Sci.* 56, 377–387. doi:10.1139/f98-181.
- Moore, G. W. K. (2016). The December 2015 North Pole Warming Event and the Increasing Occurrence of Such Events. *Sci. Rep.* doi:10.1038/srep39084.
- Morlighem, M., Williams, C. N., Rignot, E., An, L., Arndt, J. E., Bamber, J. L., et al. (2017). BedMachine v3: Complete Bed Topography and Ocean Bathymetry Mapping of Greenland From Multibeam Echo Sounding Combined With Mass Conservation. *Geophys. Res. Lett.* 44, 11,051–11,061. doi:10.1002/2017GL074954.
- Mote, T. L. (2014). MEaSURES Greenland Surface Melt Daily 25km EASE-Grid 2.0, Version 1. *NASA Natl. Snow Ice Data Cent. Distrib. Act. Arch. Cent.* doi:https://doi.org/10.5067/MEASURES/CRYOSPHERE/nsidc-0533.001.
- Nerem, R. S., Beckley, B. D., Fasullo, J. T., Hamlington, B. D., Masters, D., and Mitchum, G. T. (2018). Climate-change-driven accelerated sea-level

rise detected in the altimeter era. *Proc. Natl. Acad. Sci.* 0, 201717312.
doi:10.1073/pnas.1717312115.

Oltmanns, M., Straneo, F., and Tedesco, M. (2019). Increased Greenland melt triggered by large-scale , year-round cyclonic moisture intrusions. *Cryosph.* 13, 815–825. doi:https://doi.org/10.5194/tc-13-815-2019.

Ostrovsky, I., Yacobi, Y. Z., Walline, P., and Kalikhman, I. (1996). Seiche-induced mixing: Its impact on lake productivity. *Limnol. Oceanogr.* 41, 323–332. doi:10.4319/lo.1996.41.2.0323.

Overeem, I., Hudson, B., Welty, E., Mikkelsen, A., Bamber, J., Petersen, D., et al. (2015). River inundation suggests ice-sheet runoff retention. *J. Glaciol.* 61, 776–788. doi:10.3189/2015JoG15J012.

Papa, F., Durand, F., Rossow, W. B., Rahman, A., and Bala, S. K. (2010). Satellite altimeter-derived monthly discharge of the Ganga-Brahmaputra River and its seasonal to interannual variations from 1993 to 2008. *J. Geophys. Res. Ocean.* 115, C12013. doi:10.1029/2009JC006075.

Phillips, T., Rajaram, H., Colgan, W., Steffen, K., and Abdalati, W. (2013). Evaluation of cryo-hydrologic warming as an explanation for increased ice velocities in the wet snow zone, Sermeq Avannarleq, West Greenland. *J. Geophys. Res. Earth Surf.* 118, 1241–1256.
doi:10.1002/jgrf.20079.

Phillips, T., Rajaram, H., and Steffen, K. (2010). Cryo-hydrologic warming: A potential mechanism for rapid thermal response of ice sheets. *Geophys.*

- Res. Lett.* 37, 1–5. doi:10.1029/2010GL044397.
- Pitcher, L. H., Pavelsky, T. M., Smith, L. C., Moller, D. K., Altenau, E. H., Allen, G. H., et al. (2019). AirSWOT InSAR mapping of surface water elevations and hydraulic gradients across the Yukon Flats Basin, Alaska. *Water Resour. Res.* doi:https://doi.org/10.1029/2018WR023274.
- Pitcher, L. H., and Smith, L. C. (2019). Supraglacial streams and rivers. *Annu. Rev. Earth Planet. Sci.* 47, 421–452. doi:doi.org/10.1146/annurev-earth-053018-060212.
- Porter, C., Morin, P., Howat, I., Noh, M.-J., Bates, B., Peterman, K., et al. (2018). ArcticDEM. doi:doi:10.7910/DVN/OHHUKH.
- Prowse, T. D., Beltaos, S., Gardner, J. T., Gibson, J. J., Granger, R. J., Leconte, R., et al. (2006). Climate change, flow regulation and land-use effects on the hydrology of the Peace-Athabasca-Slave system; Findings from the Northern Rivers Ecosystem Initiative. *Environ. Monit. Assess.* 113, 167–197. doi:10.1007/s10661-005-9080-x.
- Ravier, E., and Buoncristiani, J.-F. (2017). “Glaciohydrogeology,” in *Past Glacial Environments* (Elsevier Ltd), 431–466. doi:10.1016/B978-0-08-100524-8.00013-0.
- Rennermalm, A. K., Moustafa, S. E., Mioduszewski, J., Chu, V. W., Forster, R. R., Hagerdorn, B., et al. (2013a). Understanding Greenland ice sheet hydrology using an integrated multi-scale approach. *Environ. Res. Lett.* 8, 14pp. doi:10.1088/1748-9326/8/1/015017.

- Rennermalm, A. K., Smith, L. C., Chu, V. W., Forster, R. R., van den Broeke, M., van As, D., et al. (2013b). Evidence of meltwater retention within the Greenland ice sheet. *Cryosph.* 7, 1443–1445. doi:10.5194/tc-7-1433-2013.
- Rignot, E., Koppes, M., and Velicogna, I. (2010). Rapid submarine melting of the calving faces of West Greenland glaciers. *Nat. Geosci.* 3, 187–191. doi:10.1038/ngeo765.
- Rignot, E., and Mouginot, J. (2012). Ice flow in Greenland for the International Polar Year 2008–2009. *Geophys. Res. Lett.* 39. doi:10.1029/2012GL051634.
- Rignot, E., Velicogna, I., van den Broeke, M. R., Monaghan, A., and Lenaerts, J. T. M. (2011). Acceleration of the contribution of the Greenland and Antarctic ice sheets to sea level rise. *Geophys. Res. Lett.* 38. doi:10.1029/2011GL046583.
- Rodriguez, E. (2016). Surface Water and Ocean Topography Mission (SWOT) Project: Science Requirements Document (Rev A). Available at: <https://pdms.jpl.nasa.gov>.
- Ryan, J. C., Smith, L. C., Van As, D., Cooley, S. W., Cooper, M. G., Pitcher, L. H., et al. (2019). Greenland Ice Sheet surface melt amplified by snowline migration and bare ice exposure. *Sci. Adv.* 5, 1–10. doi:10.1126/sciadv.aav3738.
- Samenow, J. (2018). North Pole surges above freezing in the dead of winter,

stunning scientists. *Washington Post*. Available at:
<https://www.washingtonpost.com/news/capital-weather-gang/wp/2018/02/26/north-pole-surges-above-freezing-in-the-dead-of-winter-stunning-scientists/?noredirect=on>.

Schoof, C. (2010). Ice-sheet acceleration driven by melt supply variability. *Nature* 468, 803. doi:10.1038/nature09618.

Sciascia, R., Straneo, F., Cenedese, C., and Heimbach, P. (2013). Seasonal variability of submarine melt rate and circulation in an East Greenland fjord. *J. Geophys. Res. Ocean.* 118, 2492–2506.
doi:10.1002/jgrc.20142.

Serreze, M. C., Barrett, A. P., Stroeve, J. C., Kindig, D. N., and Holland, M. M. (2009). The emergence of surface-based Arctic amplification. *Cryosphere* 3, 11–19. doi:10.5194/tc-3-11-2009.

Shepherd, A., Ivins, E. R., A, G., Barletta, V. R., Bentley, M. J., Bettadpur, S., et al. (2012). A Reconciled Estimate of Ice-Sheet Mass Balance. *Science* (80-.). 338. doi:10.1126/science.1228102.

Shreve, R. L. (1972). Movement of water in glaciers. *J. Glaciol.* 11, 205–214.

Smith, L. C. (1997). Satellite remote sensing of river inundation area, stage, and discharge: a review. *Hydrol. Process.* 11, 1427–1439.
doi:10.1002/(SICI)1099-1085(199708)11:10<1427::AID-HYP473>3.0.CO;2-S.

Smith, L. C., Chu, V. W., Yang, K., Gleason, C. J., Pitcher, L. H.,

- Rennermalm, A. K., et al. (2015). Efficient meltwater drainage through supraglacial streams and rivers on the southwest Greenland Ice Sheet. *Proc. Natl. Acad. Sci.*
- Smith, L. C., Yank, K., Pitcher, L. H., Overstreet, B. T., CHu, V. W., Rennermalm, Å. K., et al. (2017). Direct measurements of meltwater runoff on the Greenland Ice Sheet surface. *Proc. Natl. Acad. Sci.* 114. doi:10.1073/pnas.1707743114.
- Tedesco, M., Willis, I. C., Hoffman, M. J., Banwell, A. F., Alexander, P., and Arnold, N. S. (2013). Ice dynamic response to two modes of surface lake drainage on the Greenland ice sheet. *Environ. Res. Lett.* 8, 34007. Available at: <http://stacks.iop.org/1748-9326/8/i=3/a=034007>.
- Tuozzolo, S., Lind, G., Overstreet, B., Mangano, J., Fonstad, M., Hagemann, M., et al. (2019). Estimating River Discharge With Swath Altimetry: A Proof of Concept Using AirSWOT Observations. *Geophys. Res. Lett.* 46, 1459–1466. doi:10.1029/2018GL080771.
- USACE (1953). *Project Mint Julep: investigation of a smooth ice area of the Greenland ice cap*. Arctic Construction and Frost Effects Laboratory (U.S.) Engineer Research and Development Center (U.S.) Available at: http://acwc.sdp.sirsi.net/client/en_US/search/asset/1024681;jsessionid=1F3165DFEDEB03245AB301181DD6E5E8.enterprise-15000.
- van As, D., Hasholt, B., Ahlstrøm, A. P., Box, J. E., Cappelen, J., Colgan, W., et al. (2018). Reconstructing Greenland Ice Sheet meltwater discharge

- through the Watson River (1949–2017). *Arctic, Antarct. Alp. Res.* 50, 10. doi:10.1080/15230430.2018.1433799.
- van As, D., Mikkelsen, A. B., Nielsen, M. H., Box, J. E., Liljedahl, L. C., Lindbäck, K., et al. (2017). Hypsometric amplification and routing moderation of Greenland ice sheet meltwater release. *Cryosph.* 11, 1371–1386. doi:10.5194/tc-11-1371-2017.
- van den Broeke, M. R., Bamber, J., Ettema, J., Rignot, E., Schrama, E., van de Berg, W. J., et al. (2009). Partitioning recent Greenland mass loss. *Science (80-.)*. 326, 984–6. doi:10.1126/science.1178176.
- van den Broeke, M. R., Enderlin, E. M., Howat, I. M., Kuipers Munneke, P., Noël, B. P. Y., van de Berg, W. J., et al. (2016). On the recent contribution of the Greenland ice sheet to sea level change. *Cryosphere* 10, 1933–1946. doi:10.5194/tc-10-1933-2016.
- Vaughan, D. G., Comiso, J. C., Allison, I., Carrasco, J., Kaser, G., Kwok, R., et al. (2013). Observations: Cryosphere. doi:10.1017/CBO9781107415324.012.
- Willis, I. C., Arnold, N. S., and Brock, B. W. (2002). Effect of snowpack removal on energy balance, melt and runoff in a small supraglacial catchment. *Hydrol. Process.* 16, 2721–2749. doi:10.1002/hyp.1067.
- Yang, K., and Smith, L. C. (2016). Internally drained catchments dominate supraglacial hydrology of the southwest Greenland Ice Sheet. *J. Geophys. Res. Earth Surf.*, 1891–1910.

doi:10.1002/2016JF003927.Received.

Yang, K., Smith, L. C., Cooper, M. G., Pitcher, L. ., van As, D., Lu, Y., et al.

Seasonal evolution of supraglacial lakes and rivers on the southwestern Greenland Ice Sheet. *J. Geophys. Res. - Earth Surf.*

Yang, K., Smith, L. C., Karlstrom, L., Cooper, M. G., Tedesco, M., van As, D.,

et al. (2018). Supraglacial meltwater routing through internally drained catchments on the Greenland Ice Sheet surface. *Cryosph. Discuss.*

doi:<https://doi.org/10.5194/tc-2018-145>.

CHAPTER 3

AirSWOT InSAR mapping of surface water elevation and hydraulic gradients across the Yukon Flats Basin, Alaska

3.1 Abstract

AirSWOT, an experimental airborne Ka-band interferometric synthetic aperture radar, was developed for hydrologic research and validation of the forthcoming Surface Water and Ocean Topography (SWOT) satellite mission (to be launched in 2021). AirSWOT and SWOT aim to improve understanding of surface water processes by mapping water surface elevation (WSE) and water surface slope (WSS) in rivers, lakes, and wetlands. However, the utility of AirSWOT for these purposes remains largely unexamined. We present the first investigation of AirSWOT WSE and WSS surveys over complex, low-relief, wetland-river hydrologic environments, including (1) a field-validated assessment of AirSWOT WSE and WSS precisions for lakes and rivers in the Yukon Flats Basin, an Arctic-Boreal wetland complex in eastern interior Alaska; (2) improved scientific understanding of surface water flow gradients and the influence of subsurface permafrost; and (3) recommendations for improving AirSWOT precisions in future scientific and SWOT validation campaigns. AirSWOT quantifies WSE with an RMSE of 8 and 15 cm in 1 and 0.0625 km² river reaches, respectively, and 21 cm in lakes.

This indicates good utility for studying hydrologic flux, WSS, geomorphic processes, and coupled surface/subsurface hydrology in permafrost environments. This also suggests that AirSWOT supplies sufficient precision for validating SWOT WSE and WSS over rivers, but not lakes. However, improvements in sensor calibration and flight experiment design may improve precisions in future deployments as may modifications to data processing. We conclude that AirSWOT is a useful tool for bridging the gap between field observations and forthcoming global SWOT satellite products.

3.2 Introduction

Understanding surface water hydrological processes is critical for natural and engineered ecosystems (Cisneros et al., 2014; Gleason et al., 2017), yet empirical measurements of large-scale surface water storage, transport, and dynamics remain limited (Pekel et al., 2016). To that end, AirSWOT, an experimental airborne Ka-band radar interferometer uniquely engineered to map water surface elevation (hereafter called WSE), has been developed both to enhance scientific understanding of lake, wetland, and river floodplain hydrology and as a potential validation tool for the forthcoming Surface Water Ocean Topography (SWOT) satellite mission. SWOT is a joint international effort of the National Aeronautics and Space Administration (NASA), Centre National d'Etudes Spatiales, Canadian Space Agency, and United Kingdom Space Agency with anticipated launch in 2021.

Its nominal goal is to map global freshwater storage and transport in rivers and lakes every ~21 days (Biancamaria et al., 2016). For their core measurements, both AirSWOT and SWOT use 35-GHz Ka-band radar interferometers to produce swath-based mappings of WSE, which is used to derive water surface slope (hereafter called WSS), two hydrologic variables essential for quantifying storage and flux of terrestrial inland surface water.

This study deployed AirSWOT and a field team to eastern interior Alaska in June 2015 for testing over the Yukon Flats Basin (YFB), a protected wetland area within the Yukon Flats National Wildlife Refuge, which straddles the Arctic circle (Figure 3-1a). The YFB has complex, low-relief topography and is underlain by discontinuous permafrost (Gulbrandsen et al., 2016; Minsley et al., 2012; Pastick et al., 2013). It is characterized by hydrologically connected and disconnected lakes (Cooley et al., 2017), remnant oxbows (Brabets et al., 2000), and intermittently inundated lakes and wetlands (Jepsen et al., 2016). Our study area is crossed by a large anabranching reach of the Yukon River and a network of tributary channels, all referred to as rivers (Figure 3-1a). The global significance of Arctic-Boreal wetlands like the YFB is underscored by the key roles that lakes and rivers play in greenhouse gas exchanges with the atmosphere (Raymond et al., 2013) and the related impact of permafrost thaw on changing surface extent and groundwater fluxes (Smith et al., 2007; Walvoord et al., 2012). For these reasons, we directed AirSWOT deployments to the YFB as both a test

of instrument performance and to enhance scientific understanding of surface water interactions in a complex wetland environment underlain by discontinuous near-surface permafrost.

AirSWOT deploys a Ka-band SWOT Phenomenology Airborne Radar (KaSPAR) sensor, a digital camera system that collects high-resolution color infrared (CIR) imagery, and a precision internal motion unit (<https://swot.jpl.nasa.gov/airswot.htm>). KaSPAR has a 5-km swath width with incidence angles ranging from 2° to 25° (Neeck et al., 2012). The KaSPAR data are postprocessed using InSAR software at the NASA Jet Propulsion Laboratory to produce a uniformly gridded WSE data product, here processed to 3.6-m pixels. AirSWOT thus has a broader incidence angle range and considerably higher resolution than SWOT, which will have a native range resolution of 10–60 m, an azimuth resolution of 6–7 m, and an incidence angle range of 0.6–3.9° (Biancamaria et al., 2016; Fjørtoft et al., 2014). AirSWOT is thus not a direct analog for SWOT but yields similar types of measurements offering a unique opportunity to study Ka-band returns and assess the scientific value of WSE and WSS measurements in poorly understood wetland environments such as the YFB. Like all scientific satellite missions, SWOT is designed to meet predefined accuracy standards. The accuracy standards of SWOT relevant to this work include quantification of WSE to ± 10 -cm vertical accuracy per 1km² open water area, WSE to ± 25 -cm vertical accuracy per 0.0625 km² open water area, and WSS to an

accuracy of ± 1.7 cm/km when averaged over 10-km reaches that are at least 100 m wide (Rodriguez, 2016). Therefore, an important objective of this research is to examine whether AirSWOT measurements of WSE and WSS meet or exceed SWOT standards, which will help determine if AirSWOT is a suitable instrument platform to validate SWOT. Between 27 May and 15 June 2015, we collected in situ pressure transducer (PT) and global positioning system (GPS) field surveys of WSE in YFB lakes and rivers and then deployed AirSWOT over these same sites on 15 June 2015. These field and remotely sensed data sets are used to answer four questions: (1) Can AirSWOT measurements resolve WSE and WSS in lakes and rivers with sufficient precision to validate SWOT? (2) What factors contribute to variations in AirSWOT precision? (3) Can AirSWOT images be used to improve scientific understanding of surface water flow through complex Arctic-Boreal wetland systems? (4) How might AirSWOT precisions be improved in future campaigns? To address these questions, we first compare AirSWOT WSE with PT-corrected GPS surveys in 13 lakes (referred to as PT WSE) as well as a GPS survey along an ~ 82 -km reach of the Yukon River and a lateral distributary channel (referred to as GPS WSE). Second, we evaluate how spatial averaging of AirSWOT data impacts precision. Third, we assess the influence of permafrost on WSE variability across the YFB and examine longitudinal river profiles for fluvial geomorphological investigation. We also evaluate the utility of InSAR imaging as a demonstration of

AirSWOT's potential contributions to basic hydrologic research. Finally, we conclude with a discussion of the strengths and limitations of using AirSWOT to validate SWOT, how AirSWOT data precisions may be improved in the future, and the scientific potential for AirSWOT independent of the SWOT mission.

Water Resources Research 10.1029/2018WR023274

thus has a broader incidence angle range and considerably higher resolution than SWOT, which will have a native range resolution of 10–60 m, an azimuth resolution of 6–7 m, and an incidence angle range of 0.6–3.9° (Biancamaria et al., 2016; Fjørtoft et al., 2014). AirSWOT is thus not a direct analog for SWOT but yields similar types of measurements offering a unique opportunity to study Ka-band returns and assess the scientific value of WSE and WSS measurements in poorly understood wetland environments such as the YFB. Like all scientific satellite missions, SWOT is designed to meet predefined accuracy standards. The accuracy standards of SWOT relevant to this work include quantification of WSE to ± 10 -cm vertical accuracy per 1km² open water area, WSE to ± 25 -cm vertical accuracy per 0.0625 km² open water area, and WSS to an accuracy of ± 1.7 cm/km when averaged over 10-km reaches that are at least 100 m wide (Rodriguez, 2016).

Therefore, an important objective of this research is to examine whether AirSWOT measurements of WSE and WSS meet or exceed SWOT standards, which will help determine if AirSWOT is a suitable instrument platform to

validate SWOT. Between 27 May and 15 June 2015, we collected in situ pressure transducer (PT) and global positioning system (GPS) field surveys of WSE in YFB lakes and rivers and then deployed AirSWOT over these same sites on 15 June 2015. These field and remotely sensed data sets are used to answer four questions: (1) Can AirSWOT measurements resolve WSE and WSS in lakes and rivers with sufficient precision to validate SWOT? (2) What factors contribute to variations in AirSWOT precision? (3) Can AirSWOT images be used to improve scientific understanding of surface water flow through complex Arctic-Boreal wetland systems? (4) How might AirSWOT precisions be improved in future campaigns? To address these questions, we first compare AirSWOT WSE with PT-corrected GPS surveys in 13 lakes (referred to as PT WSE) as well as a GPS survey along an ~82-km reach of the Yukon River and a lateral distributary channel (referred to as GPS WSE). Second, we evaluate how spatial averaging of AirSWOT data impacts precision. Third, we assess the influence of permafrost on WSE variability across the YFB and examine longitudinal river profiles for fluvial geomorphological investigation. We also evaluate the utility of InSAR imaging as a demonstration of AirSWOT's potential contributions to basic hydrologic research. Finally, we conclude with a discussion of the strengths and limitations of using AirSWOT to validate SWOT, how AirSWOT data precisions may be improved in the future, and the scientific potential for AirSWOT independent of the SWOT mission.

3.3. Data and Methods

This research uses remotely sensed imagery collected with AirSWOT and other remote sensing platforms, in situ field measurements, and ancillary model data. These data sets are outlined in Table 3-1, and our processing procedures are detailed in the sections to follow.

3.3.1. AirSWOT Data Collection and Processing

On 15 June 2015, AirSWOT data were collected over a $\sim 3,300$ km² area of the YFB (Figure 3-1a). The surveyed area was ~ 30 km east-to-west and ~ 110 km north-to-south and was mapped using 10 overpasses or paths (Figure S3-2b in the supporting information). The CIR, internal motion unit, and KaSPAR instruments were mounted on a King Air B200 aircraft operated by NASA Armstrong (Dryden) Flight Research Center. The radar data were processed at Jet Propulsion Laboratory using custom, AirSWOT-specific InSAR software to yield standard data products of height in meters above the WGS84 ellipsoid, radar backscatter (dB), incidence angle ($^{\circ}$), and random height error (or precision, derived from the interferometric correlation; Rosen et al., (2000); m). Likewise, we derived signal to noise (SNR) as the difference between backscatter and noise equivalent backscatter. AirSWOT data layers are summarized in Table 3-1 and available

via the Oak Ridge National Laboratory Distributed Active Archive Center for Biogeochemical Dynamics (Pitcher et al., 2019).

Comparisons of AirSWOT to in situ WSE and WSS required data quality filtering of AirSWOT incidence angle, error, SNR, and height outliers (Figure 3-1b). First, we exclude all pixels with incidence angles $<5^\circ$ and $>20^\circ$. Near-nadir ($<5^\circ$) pixels were excluded because data processing limitations result in inconsistent height retrievals at these incidence angles. Data for angles $>20^\circ$ were excluded due to sensitivity of the antenna pattern roll off when coupled with aircraft roll. Next, we remove pixels with low SNR (<5 dB) and random height error >1 m.

Our data filtering does not explicitly remove pixels contaminated by topographic layover, which is an image distortion that is produced when incidence angles are smaller than a surface slope oriented toward the sensor (Jenson, 2000). However, due to minimal topographic relief across most of the YFB, we expect any layover to be driven primarily by vegetation, which is not reliably measured across our study area. Despite the small anticipated impacts, we simulate layover for one AirSWOT path (Figure S3-3a) using the approach developed by Sheng et al. (2016) and ArcticDEM as the input surface model. We find that $\sim 33\%$ of layover contaminated water pixels have incidence angles $<5^\circ$, which are eliminated by data quality filtering. Moreover, data quality filtering removes >12 times the number of pixels than those with layover (Figure S3-3b). We also recognize that ArcticDEM

does not reliably measure surface heights, particularly in forested areas (Glennie, 2018). Thus, we do not attempt additional corrections for layover. We consider AirSWOT WSE and WSS validation with other remotely sensed data sets (e.g., lidar) inappropriate because remotely sensed data that spatially and temporally overlap 15 June 2015 AirSWOT and accurately measure WSE and WSS are not available.

Our AirSWOT analysis is subdivided into rivers, streams, and channels (collectively referred to as rivers) and lakes, wetlands, remnant oxbows, and thermokarst ponds (collectively referred to as lakes). To calculate WSE in lakes, we first use an open water mask created from simultaneously collected AirSWOT CIR camera imagery (section 3.3.2) to select only water pixels from the radar data. Next, we apply a statistical outlier filter that removes AirSWOT WSE pixels >3 median absolute deviations from the median. Finally, the median value of remaining pixels in each lake is calculated. Individual lake masks vary in size from 55.9 m² (~ 4 AirSWOT pixels) to 3.26 km² ($\sim 251,543$ AirSWOT pixels). Refer to Figure S3-4 for histograms of filtered AirSWOT lake WSEs compared with in situ PT corrected GPS surveys.

We also use the AirSWOT CIR open water mask over rivers to extract only water pixels from the KaSPAR data. Next, we generate cross-section segments orthogonal to the river centerline and average AirSWOT WSE along each orthogonal cross section. The centerline is created using

ChanGeom v0.3 (Fisher et al., 2012, 2013). The output from ChanGeom is a raster file with pixel values corresponding to downstream distances starting from the upstream end of the water mask. We use a Polynomial Approximation with Exponential Kernel algorithm (<http://pro.arcgis.com/en/pro-app/tool-reference/cartography/smooth-line.htm>) to remove right angles in the raster-based centerline. Next, similar to Pavelsky and Smith (2008) and Fisher et al. (2013), we generate orthogonal polylines spanning the width of a river mask at 3.6 m downstream spacing along the river centerline by calculating the negative reciprocal of the slope between downstream centerline points and extending a polyline from a centerline pixel across the river. Lastly, we intersect the derived orthogonal cross sections with AirSWOT data for spatial averaging along the length of the cross section.

Our data filtering does not explicitly remove pixels contaminated by topographic layover, which is an image distortion that is produced when incidence angles are smaller than a surface slope oriented toward the sensor (Jenson, 2000). However, due to minimal topographic relief across most of the YFB, we expect any layover to be driven primarily by vegetation, which is not reliably measured across our study area. Despite the small anticipated impacts, we simulate layover for one AirSWOT path (Figure S3-3a) using the approach developed by Sheng et al. (2016) and ArcticDEM as the input surface model. We find that ~33% of layover- contaminated water pixels

have incidence angles $<5^\circ$, which are eliminated by data quality filtering. Moreover, data quality filtering removes >12 times the number of pixels than those with layover (Figure S3-3b). We also recognize that ArcticDEM does not reliably measure surface heights, particularly in forested areas (Glennie, 2018). Thus, we do not attempt additional corrections for layover. We consider AirSWOT WSE and WSS validation with other remotely sensed data sets (e.g., lidar) inappropriate because remotely sensed data that spatially and temporally overlap 15 June 2015 AirSWOT and accurately measure WSE and WSS are not available.

Our AirSWOT analysis is subdivided into rivers, streams, and channels (collectively referred to as rivers) and lakes, wetlands, remnant oxbows, and thermokarst ponds (collectively referred to as lakes). To calculate WSE in lakes, we first use an open water mask created from simultaneously collected AirSWOT CIR camera imagery (section 1.2) to select only water pixels from the radar data. Next, we apply a statistical outlier filter that removes AirSWOT WSE pixels >3 median absolute deviations from the median. Finally, the median value of remaining pixels in each lake is calculated. Individual lake masks vary in size from 55.9 m² (~ 4 AirSWOT pixels) to 3.26 km² ($\sim 251,543$ AirSWOT pixels). Refer to Figure S3-4 for histograms of filtered AirSWOT lake WSEs compared with in situ PT corrected GPS surveys.

We also use the AirSWOT CIR open water mask over rivers to extract only water pixels from the KaSPAR data. Next, we generate cross-section segments orthogonal to the river centerline and average AirSWOT WSE along each orthogonal cross section. The centerline is created using ChanGeom v0.3 (Fisher et al., 2012, 2013). The output from ChanGeom is a raster file with pixel values corresponding to downstream distances starting from the upstream end of the water mask. We use a Polynomial Approximation with Exponential Kernel algorithm (<http://pro.arcgis.com/en/pro-app/tool-reference/cartography/smooth-line.htm>) to remove right angles in the raster-based centerline. Next, similar to Pavelsky and Smith (2008) and Fisher et al. (2013), we generate orthogonal polylines spanning the width of a river mask at 3.6-m downstream spacing along the river centerline by calculating the negative reciprocal of the slope between downstream centerline points and extending a poly-line from a centerline pixel across the river. Lastly, we intersect the derived orthogonal cross sections with AirSWOT data for spatial averaging along the length of the cross section.

For comparison with SWOT accuracy standards, ~ 0.0625 - and ~ 1 -km² reaches were established by summing pixel areas in a downstream direction until the area threshold is exceeded. The average and standard deviation of orthogonal means contained within a reach were calculated, and the process was repeated for each centerline orthogonal. The reach start and end

downstream distances were used to subset GPS survey points, calculate the average GPS WSE value for each reach, and then compare with spatially averaged AirSWOT WSE. Similarly, slopes were calculated by first subsetting AirSWOT and GPS data according to start and end downstream distances for 10 km reaches established at each centerline orthogonal. Then, a linear model was fit between distance and AirSWOT/GPS WSE.

3.3.2. AirSWOT Open Water Mask

The AirSWOT instrument suite includes a Cirrus Digital Systems camera (<http://cirrus-designs.com/>), which collects 16-MP digital images using a Zeiss 60-mm focal length lens with a $34^\circ \times 34^\circ$ field of view. Each CIR digital image contained a near-infrared (nir), red (r), and green (g) band. A radially and relief-corrected orthomosaic was generated from 780 individual CIR images using a photogrammetrically generated digital surface model in Agisoft Photoscan Pro. The YFB has minimal topographic relief, and the flight altitude was $>8,770$ m (Figure S3-2); therefore, topographic distortion was minimal. The orthomosaic was exported as 16-bit GeoTiffs split into 33 quads, each containing $10,000 \times 10,000$ pixels with values given as raw digital numbers. To enable comparison with AirSWOT WSE data, the 33 CIR quads were combined into one orthomosaic, assigned a WGS-1984 UTM-6N projection, and resampled to a 3.6-m pixel size.

To limit extraction of AirSWOT WSE to open water pixels only, the CIR data were classified as water or non-water. To achieve this, a normalized difference water index (NDWI) was calculated as

$$NDWI = \frac{g - nir}{g + nir}$$

where g is the green band and nir is the near-infrared band in the CIR data (Mcfeeters, 1996). We then used an automated thresholding technique to classify water. As a first guess, we classified water for 1 km² cells in the NDWI using Otsu's threshold selection method (Otsu 1979), then visually inspected this preliminary water mask to remove clouds/shadows falsely identified as water and to separate rivers from lakes. To enhance classification accuracy, a localized NDWI threshold was then calculated for each lake and every 5-km down- stream channel reach. Similar to Li and Sheng (2012), localized search areas were defined with approximately twice the area of each lake and river reach in the preliminary water mask. Next, a threshold value was defined for each local search area (Otsu, 1979), and the NDWI was classified as water and non-water pixels, which were visually inspected for errors. In total, we identified 2,786 lakes across the study area, of which we manually edited 201 to improve classification accuracy.

To further assess water mask accuracy, we digitized boundaries of 50 lakes without manual edits and compared open water areas with those

automatically extracted. We find strong statistical agreement between auto extracted and manually digitized lake areas ($r^2 > 0.9$, RMSE = 0.01 km²; Figure S3-5). We manually modified all river masks to establish single-channel sections for generation of orthogonal cross sections to guide AirSWOT WSE extraction.

3.3.3. In Situ Lake and River GPS Surveys Lake

Lake water levels were monitored in situ using Solinst Levellogger PTs corrected with average Solinst Barologger barometric pressure readings logged along the shorelines of lake #19 (Canvasback Lake, Figure 3-1) and 9-Mile Lake (between lakes #5 and #15; Figure 3-1a). Solinst Levellogger uncertainty is 0.05% to 0.10% full-scale units (model dependent) and barologger uncertainty is 0.51 cm. We calculated WSE uncertainty due to logger error as the sum of 0.10% full scale meter applied to the maximum recorded depth, which yielded an uncertainty of 0.7 cm. Levellogger and barologgers were both set to record at 5-min intervals. We first removed outlier recordings from the original data series using a moving mean smoothing function and then calculated a daily average water level. The PTs in lakes #4 and #15 appear to move between installation, GPS survey date, and AirSWOT data collection. To correct for this, we calculate a constant depth offset at shifts in the time series and apply this offset to subsequent sections of the recorded water levels (see Figure S3-6).

Lake water levels were transformed to WSE in meter above the WGS-1984 ellipsoid by adjusting GPS lake WSE surveys performed between 27 May 2015 and 12 June 2015 with depth changes between in situ survey date and the AirSWOT collection. GPS surveys were completed using a custom-designed floating platform constructed by mounting a ruggedized watertight case on a high-density foam flotation ring and integrating a Trimble R5700 or R7 GPS receiver, a Trimble Zephyr Antenna, and a 12-volt power supply (Figure 3-1c). We refer to PT-corrected GPS surveys in lakes as PT WSE.

We first processed the lake GPS surveys using the Canadian Spatial Reference System Precise Point Positioning (PPP) web application (<https://webapp.geod.nrcan.gc.ca/geod/tools-outils/ppp.php>). We used the Canadian Spatial Reference System PPP solutions to clip the original data series to times when the GPS units were in the water. Next, surveys were subset using the UNAVCO TEQC tool (Estey and Meertens, 1999). The extracted data were then reprocessed with Geodésie par Intégrations Numériques Simultanées (GINS) software using the kinematic integer PPP method (Marty et al., 2011). Kinematic processing mode was selected because GPS lake drifters float on the lake surface and are locally influenced by wind and wave conditions, resulting in nonstationary surveys. A constant offset of 25.65 ± 1.95 cm was applied to each GPS survey to account for the distance from the GPS antenna to the water surface. Adapted from Hopkinson et al. (2011), PT WSE error is calculated as

$$\epsilon = \sqrt{(\epsilon_{lv} + \epsilon_{bl})^2 + (\epsilon_{gps} + \epsilon_{ant})^2}$$

where ϵ_{lv} is error from the levellogger, ϵ_{bl} is error from the barologger, ϵ_{gps} is maximum GPS uncertainty provided by the GINS kinematic solutions, and ϵ_{ant} is a 1.95 cm uncertainty in manual antenna offset measurement.

Average PT WSE ϵ was 8 cm with a range of 4 cm in lakes #2 and #11 to 29 cm in #15. PT WSEs are summarized in Table 3-2.

We also collected longitudinal profiles of WSE on the Yukon River and a lateral distributary channel (Figure 3-1a) using a custom engineered GPS system mounted on a SonTek/YSI Hydroboard II (Figure 3-1d). This custom GPS system consolidates a Trimble R5700 or R7 GPS receiver, a Trimble Zephyr Antenna, and a 12-volt power supply into a ruggedized waterproof housing with external cable and antenna ports. On 15 June 2015, coincident with the AirSWOT overflight, we escorted this GPS drifter down an ~82-km reach of the Yukon River behind a motorized river boat (Figure 3-1d). The GPS sampling interval results in ~1 GPS profile collection per ~100 m. The same postprocessing and differential corrections were applied. A constant 53.15 ± 2.15 cm vertical offset was subtracted from the processed data to account for the distance from the GPS antenna to the water surface. We refer to corrected and processed GPS surveys in rivers as GPS WSE. These data are provided in Data Set S3-1.

3.3.4. Permafrost and Topographic Control on Spatial Variability of WSE

Motivated by the impact of permafrost thaw on surface and groundwater fluxes (Smith et al., 2007; Walvoord et al., 2012) and the associated importance of Arctic and Boreal wetlands in greenhouse gas cycling (Wik et al., 2016), we use AirSWOT to demonstrate the possible impact of permafrost presence on spatial patterns in lake WSE across the YFB (see section 3.5.2.3). First, we grid our study domain into 5 km × 5 km cells and remove lakes from the land surface DEM. Next, we compare lake WSE variability (WSE_v), defined as the standard deviation of lake WSEs within each 5 km × 5 km cell, with surrounding topographic variability (DEM_v), defined as the standard deviation of land surface heights (Ascione et al., 2008) within the same 5 km × 5 km grid cell. To quantify the comparative magnitudes of WSE_v and surrounding landscape roughness, we define a dissimilarity ratio (d) as

$$d = \frac{\sqrt{WSE_v}}{\sqrt{DEM_v}} - 1$$

a $d < 0$ signifies that DEM_v exceeds WSE_v , which we interpret as the hydraulic gradient being influenced primarily by regional topography. A $d >$

0 suggests lake WSE_v exceeds DEM_v , which we interpret as the hydraulic gradient being influenced by factors additional to regional topography, in particular permafrost presence as modeled by (Pastick et al., 2013; Figure 3-7).

3.4 Results

3.4.1 AirSWOT Lake WSE Validation

AirSWOT and PT WSEs in 13 lakes are compared in Figures 3-2a and 3-2b. The absolute difference between PT and AirSWOT WSE ranges from 1 to 58 cm, with a mean difference of 25 cm, a standard deviation of 20 cm, and RMSE of 21 cm. Five of 13 lakes had open water areas of at least 1 km², and three of these five lakes had AirSWOT WSE within ± 10 cm of PT WSE. Three lakes had open water areas between 0.0625 and 1 km², and none of these lakes had AirSWOT WSE within ± 25 cm PT WSE. Two of the remaining five lakes smaller than 0.0625 km² had AirSWOT WSE within ± 10 cm PT WSE, which suggests that AirSWOT can map WSE in lakes smaller than SWOT will observe with precisions comparable to SWOT. Differences between AirSWOT and PT WSE for each lake are summarized in Table 3-2. Note that ground control points were not used for processing these data sets, yet we conservatively estimate that AirSWOT geolocation error is ~ 1 pixel (see 3.11.2 and Figure S3-1).

3.4.2. AirSWOT River WSE and WSS Validation

AirSWOT and GPS WSE are compared along the Yukon River and a lateral distributary channel for 1 km² reaches established at each centerline orthogonal (n = 16,332; Figures 3-2c and 3-2d). Seventy-two percent of reaches had AirSWOT absolute differences ± 10 cm and an RMSE of 8 cm. Similarly, 91% of 0.0625 km² (n = 16,472) downstream reaches had an AirSWOT absolute difference of ± 25 cm and an RMSE of 15 cm (Figure S3-7). In the context of the SWOT mission accuracy standards, these statistics suggest that AirSWOT can reliably validate SWOT WSE along 1 and 0.0625 km² reaches in >70% and >90% of samples, respectively. SWOT accuracy standards also state that for channels 100 m or wider, WSS should be accurate to ± 1.7 cm/km along 10-km reaches. To test AirSWOT precisions against this standard, we removed orthogonal channel cross sections with widths <100 m, established reaches at each centerline orthogonal, and then removed reaches with <80% data coverage (n = 2,411, Figure 3-3a). Sixty-four percent of 10-km reaches had AirSWOT WSS ± 1.7 cm/km of GPS WSS (Figure 3-3f), with an RMSE of 1.5 cm/km and r^2 of 0.8. Note that channel sections had varying braid intensities, tributary inputs, and hydraulic conditions, so some of the reaches in Figure 3-3 are not ideal for consistent WSS calculations and may contribute to larger uncertainties, particularly in comparison to AirSWOT WSE extractions.

3.4.3. AirSWOT Precision and Spatial Averaging

AirSWOT precision should improve nonlinearly with increasing spatial averaging area. To test this, we established reaches with variable pixel counts that simulate different sensor resolutions (i.e., for AirSWOT and SWOT) at 0.0625 and 1 km² spatial averaging (Table S3-1). As expected, the RMSE between GPS and AirSWOT decreased nonlinearly with increasing spatial averaging window size (Figure 3-4a). Similarly, the percent of reaches that met SWOT requirements for 1 km² (Figure 3-4b, red) and 0.0625 km² (Figure 3-4b, blue) area thresholds increased nonlinearly with increasing pixel counts. We do not present a parallel analysis for lakes because many open water lake areas are too small to test the full range of pixel counts.

We also compare the absolute median residual difference between river GPS measurements and nearest neighbor orthogonally averaged AirSWOT WSE by river mask width (Figure 3-4c). We find that narrow reaches had larger AirSWOT WSE errors. This is consistent with Figures 3-7a and 3-7b, suggesting that larger pixel counts increased overall AirSWOT precision. Holistically, these results imply that careful consideration of river widths in addition to spatial averaging area is important for future AirSWOT validations of SWOT.

3.4.4. Hydraulic Gradients

To assess the applicability of AirSWOT for surface water hydrology applications, we mapped hydraulic gradients across all YFB lakes with sufficient AirSWOT data for spatial averaging (see section 3.4.1) and WSE standard deviations <1 m (Figure 3-5). There was a dominant east to west hydraulic flow gradient near the Yukon River, which matches the flow direction of the river and its tributaries. North of the Yukon River the gradient trended from northeast to southwest, while south of the Yukon River it trended southeast to northwest. There was also a north-to-south gradient along the Teedriinjik River and east-to-west gradients along Birch Creek and Beaver Creek (Figure 3-5). These observed gradients were consistent with the prevailing physiography of the YFB. We present this result as a demonstration that despite poor lake WSE precisions, AirSWOT remains a useful tool for identifying hydrologic gradients in WSE independent of standard topography-based flow routing models.

3.4.5. Mapping Longitudinal River Profiles and WSS

We used AirSWOT to calculate and compare longitudinal WSE profiles and WSS (Figure 3-6) along six rivers (the Yukon River GPS WSE track, Yukon River-main channel, Teedriinjik River, Birch Creek-Upper, Birch Creek- Lower, and Beaver Creek) with varying widths, braid intensities, planforms, and orientations relative to the AirSWOT flight paths (Figure 3-

1a). The steepest river is the 24.6 km reach of the Teedriinjik River, which had an average 10 km reach length slope of 0.28 m/km and an overall slope of 0.29 m/km for the full longitudinal profile (Figure 3-6c). The Teedriinjik River through this reach is highly sinuous and threads into several distributary channels, as it approaches its confluence with the Yukon River. In contrast, Birch Creek-Upper, which was primarily single threaded and had a high degree of connectivity with neighboring lakes, had the most gradual average 10 km reach length slope of 0.11 m/km and an overall slope of 0.11 m/km for the full profile (Figure 3-6d). Table S3-2 summarizes the reach length and slope summary statistics for each of these six rivers.

3.5 Discussion

3.5.1. AirSWOT Precision, Calibration, and Experiment Design

This is the first empirical investigation of AirSWOT WSE and WSS precisions across a complex lake-river- wetland surface water system. We find that AirSWOT performs better over rivers (RMSE is 8 cm for 1 km² reaches and 15 cm for 0.0625 km² reaches) compared to lakes (RMSE = 21 cm), perhaps due to enhanced surface roughness resulting from a flow-induced turbulence in rivers that is absent in lakes. Furthermore, our results for rivers are similar to those in Altenau et al. (2017) who found RMSE = 9 cm on the Tanana River, Alaska, lending confidence that AirSWOT

reproducibly measures river WSE with RMSE <10 cm. Our WSS RMSE = 1.5 cm/km for 10 km reaches at least 100 m wide is similarly commensurate with Altenau et al. (2017), RMSE = 1.0 cm/km. The present study also confirms the Altenau et al. (2017) finding that AirSWOT WSE precisions in rivers vary nonlinearly with channel mask width (Figure 3-4c). Because the Altenau et al. (2017) study did not investigate lakes, a comparison of the two studies for non-channelized systems is not possible.

Two additional differences between the present study and Altenau et al. (2017) provide useful insights into AirSWOT precisions. First, Altenau et al. (2017) have a higher data density and significant overlap between AirSWOT flight paths, which permits a data filtering scheme based on magnitude, error, and statistical outliers without direct consideration of incidence angles or SNR. This suggests that the higher data density resulting from the Tanana experiment design helps increase WSE precision, which is consistent with the results we present in Figures 3-4a and 3-4b. However, the improvement is incremental, given the similarity in RMSE between the two studies. Second, the YFB AirSWOT flight lines are oriented perpendicularly to the Yukon River, whereas AirSWOT was flown parallel to the study river in Altenau et al. (2017). This results in data gaps in the downstream profiles presented here (e.g., gaps at ~10, ~65, and ~75 km in Figure 3-2c). This suggests that future AirSWOT campaigns should design

airborne flight experiments that maximize spatial overlap between paths while also orienting flight paths parallel to the overall river course direction.

While AirSWOT WSE precisions in rivers generally meet or exceed SWOT standards, the RMSE = 21 cm found here for lake WSE is less encouraging, particularly from a SWOT validation perspective. However, from an airborne remote sensing perspective, these precisions remain high, especially considering no additional ground calibrations were used in AirSWOT data processing. The AirSWOT InSAR processor applies bundle adjustments to correct for aircraft movement that produces along- and cross-track height anomalies. However, additional calibrations such as height correction using ground-based GPS surveys could be applied to further increase the derived WSE precision.

It is also important to emphasize that despite technological similarities to other airborne SARs, AirSWOT remains an experimental sensor and thus research into sensor calibrations and improvements to the AirSWOT InSAR processor are ongoing (Altenau et al., 2017). Furthermore, environmental conditions such as turbulence and wind speed influence water surface roughness (Moller et al., 2000), increasing radar backscatter and SNR thereby improving the derived WSE measurements. We lack localized measurements of wind speed at the water-air interface during the 15 June 2015 AirSWOT surveys to infer instantaneous wind conditions over the lakes studied here. Wind speeds on 15–16 June 2015 at the Fort Yukon Airport,

which is ~13 km from the western boundary of our study area, were unremarkable: ranging from 0 to 10.3 m/s with a mean of 2.9 m/s (www.ncdc.noaa.gov). River turbulence provides a water surface roughening mechanism that is absent in lakes. Future field studies should consider assessing water surface roughness, especially wind roughening of lakes, as an added factor determining AirSWOT and SWOT WSE precisions.

3.5.2. Scientific Applications of AirSWOT Slope and WSE

Measurements Over Rivers and Lakes

AirSWOT, as a novel remote sensing technology independent of SWOT, offers a range of scientific applications that may advance hydraulic, geochemical, and water management aspects of hydrological research. We present four examples here: (1) detection of WSS and rates of change of WSS at reach-relevant scales, (2) comparison of longitudinal profiles for characterizing catchment geomorphic processes and quantifying river discharge, (3) assessment of permafrost influence on WSE in Yukon Flats lakes, and (4) detecting small changes in lake storage that cannot currently be observed from space.

3.5.2.1. WSS and Rates-of-Change for Investigating River Hydraulics, Reaeration, and Fluvial Geomorphology

River slopes are often calculated by fitting a polynomial between point-based measurements spaced along a reach. This approach is enabled by in situ river gages that monitor WSE continuously, in concert with intermittent satellite altimetry measurements (e.g. Alsdorf et al., 2007; Birkett et al., 2002; Bonnema et al., 2016; Frappart et al., 2006). However, both approaches are limited by sparse measurements, or distant spacing between stream gages and the along track spacing of altimeter footprints. This reduces accuracy of the fitted polynomial and may also miss backwaters, slope breaks, and other real-world hydraulic features present between gaging stations or altimeter tracks. AirSWOT transcends such limitations by mapping WSE at 3.6 m spatial resolution (Figure 3-6), a spatially dense data set (Figures 3-3a–e) from which interesting WSS phenomena are revealed. For example, we find nonmonotonic WSS decays along several reaches of our river GPS surveys, including slopes that are much steeper ~ 5 -km downstream (reach 1, Figure 3-3a) than they are ~ 40 -km downstream (reach 2, Figure 3-3a). The spatially dense quality of AirSWOT thus reveals the true WSS between 0 and 10.07 km downstream to range from 19.98 to 20.10 cm/km for 10 km reaches, followed by a slope range of 7.75 to 16.03 cm/km for 10 km reaches established between 36.17- and 48.69-km downstream distance. In contrast, if only two equally spaced point-based WSEs

were available at the upper and lower ends of these reach (analogous to existing field and altimeter-based techniques), the derived slopes would be 17.21 and 7.94 cm/km, respectively.

Quantifying WSS and spatial rates of change in WSS are also important for water quality modeling and investigating geochemical fluxes in rivers. To that end, Figures 3-3b-e plot the first derivatives or the rate of change between 10 km reach length slopes as a function of downstream distance. To clarify spatial patterns in rates- of-change, these first derivatives (Figures 3-3b-e, blue) are smoothed (Figure 3-3b-e, red) using a Savitzky-Golay or quadratic polynomial filter. These plots emphasize that the rate of change in WSS can be drastic over short downstream distances, for example, flattening by approximately a factor of two over just ~5 km (Figure 3-3e). One particularly relevant application for mapping phenomena like this is mapping reaeration or in-channel oxygen absorption at the water surface (Bennett and Rathburn, 1972). WSS is used to calculate reaeration coefficients (Melching and Flores, 1999; Parker and Gay, 1987), while understanding the rate of change in WSS enables investigation of reaeration across large spatial scales. More generally, it follows that AirSWOT, and eventually SWOT, may assist in calculating more detailed patterns of WSS and rates of change, which are important not only for reaeration but also for spatial variations in flow velocity, turbidity, discharge, sediment transport,

and river planform evolution (Dade and Friend, 1998; LeFavour and Alsdorf, 2005; Leopold, 1953).

3.5.2.2. Longitudinal Profiles, Catchment Geomorphology, and Discharge Retrieval

The longitudinal profile of a river is controlled by discharge and sedimentation (Flint, 1974; Knighton, 1998; Leopold et al., 1964; Mackin, 1948) and is important for investigating basin geomorphology (Knighton, 1998) and tectonic deformation (Allen et al., 2013; Kirby & Whipple, 2012). The AirSWOT WSE measurements reported here indicate a concave profile for Birch Creek-Lower (Figure 3-6e) but a convex profile for Beaver Creek (Figure 3-6f). River profiles generally tend to be concave (Knighton, 1998; Leopold et al., 1964), thus the notable convexity of Birch Creek is interesting. Mechanisms that control profile convexity include channel roughness, sedimentation, tectonic deformation, and/or geologic events (Knighton, 1998). The neighboring Birch and Beaver creek watersheds both drain the White Mountains to the south and meander across the YFB before joining the Yukon River downstream of our study area. Three plausible explanations for the different profiles we observe include increased sediment mobilization to channels, river avulsions, and/or differing tectonics in catchment headwaters. These explanations are speculative and require further investigation. However, Figure 3-6 illustrates the types of

geomorphic hypotheses that can emerge from novel AirSWOT WSE and WSS mappings of the longitudinal profiles of rivers. Finally, if repeated AirSWOT mappings are conducted, temporal variations in WSS may be inverted to estimate river discharge (Durand et al., 2014, 2016; Garambois & Monnier, 2015; Oubanas et al., 2018).

3.5.2.3. Topographic and Permafrost Control on WSE Variability in the YFB

Boreal and Arctic lakes are a significant source and emitter of methane (Wik et al., 2016), while future permafrost thaw may boost methane emissions by $>3.4 \pm 0.08$ petagrams of carbon (PgC) from pan-Arctic lakes by the end of this century (Tan & Zhuang, 2015). Furthermore, near-surface permafrost thaw impacts lake volume change more than thaw depth (Jepsen et al., 2013), therefore YFB lakes are particularly vulnerable to warming subsurface temperatures due to the area's shallow aquifer and discontinuous permafrost (Jepsen et al., 2016). We use AirSWOT to demonstrate the possible impact of permafrost presence on spatial patterns in lake WSE across the YFB. We find that where there is low variability in permafrost state (e.g., mostly permafrost or mostly non-permafrost), d (dissimilarity ratio, see section 3.3.4) tends to be <0 and thus prevailing topography appears to dominate the hydraulic gradient. However, as variability in permafrost presence increases, topography no longer dominates the

hydraulic gradient (Figure 3-7). If true, this raises the exciting possibility that areas of permafrost disturbance may be inferred from spatially dense mapping of WSE. However, we emphasize that the permafrost variability bin in Figure 3-7b with $d > 0$ represents only 15 lakes in one grid cell. As such, this simple analysis is presented as an illustrative demonstration of a potential scientific utility for AirSWOT and SWOT, rather than a definitive study on the impact of permafrost presence on hydraulic gradients across the YFB.

3.5.2.4. Detecting Changes in Lake Volume Not Currently Observable from Space

Recent advances in passive spaceborne remote sensing technologies such as Planet's CubeSat-based optical constellation and other visible/infrared submeter resolution sensor constellations (e.g., GeoEye-1 and WorldView-1/2/3/4) enable near real time mapping of the world. Despite limitations in data quality and solar/cloud conditions, these sensors are useful in hydrological sciences, particularly for mapping open water extents (Cooley et al., 2017). Nonetheless, they are not capable of directly measuring WSE, volume change, or flux.

The current spaceborne solution for estimating volumetric changes in surface water is laser or radar altimetry in combination with optical measurements of lake area. This approach has been used to track flux in

lakes since the early 1990s (Gao et al., 2012). For example, ICESat (Zhang et al., 2011) and the forthcoming ICESat-2 can measure lake WSE. But repeat times are >90 days (<https://icesat-2.gsfc.nasa.gov/science/specs>), which is insufficient for tracking surface water dynamics, especially in seasonally frozen systems across the Arctic and sub-Arctic. Radar altimetry WSE measurements can achieve ~2 cm accuracies (Crétaux et al., 2009), but lakes with minimal topographic interference/acceptable roughness characteristics are required for such fidelity. Additionally, altimeter measurements are nadir pointing and make profile rather than swath measurements, meaning they must be gridded to be used in mapping applications (Crétaux et al., 2016). Another major limitation is that altimeters can only observe large lakes. For example, Crétaux et al. (2016) list altimetric WSE errors and areas for 24 lakes. Errors range from 3 to 85 cm, but the smallest lake measured was 350 km² with an RMSE = 64 cm. Arsen et al. (2015) further demonstrate that altimeters can map WSE in lakes as short as 3.3 km along-track, but with an RMSE range of 12–99 cm.

In contrast, the lakes in our YFB study area vary in size from 55.92 m² to 3.26 km² and thus would not be observable with radar altimeter-based remote sensing. Also, AirSWOT can map lake WSEs with an overall RMSE of 21 cm, which is within the range of accuracies quantified over much larger lakes using radar altimetry. SWOT will observe lakes that are ≥0.0625 km² and potentially as small as 0.01 km². Only ~18% (489 of 2,786) of the lakes

in our study are $\geq 0.0625 \text{ km}^2$ and will be observable by SWOT while only $\sim 51\%$ (1,417 of 2,786) of lakes are $\geq 0.01 \text{ km}^2$ and may be observable by SWOT. Thus, the complex lake-river-wetland dynamics of the YFB (and similar Arctic and Boreal wetlands) occur at scales that are currently only observable by AirSWOT-like active airborne remote sensing technologies.

3.6 Conclusions

We conclude that AirSWOT offers utility as a validation tool for SWOT measurements of WSE and WSS in rivers and as an independent experimental technology for scientific surface water hydrology studies. AirSWOT river WSEs meet or exceed SWOT mission standards, and while lake WSEs remain unsatisfactory, improvements to the InSAR processor, enhanced data calibrations, and modifications to experiment design are likely to improve data quality in the future. Independent of SWOT, we demonstrate that AirSWOT enables investigation of complex lake/wetland hydraulic gradients, remote estimation of river discharge, water quality/geochemical flux, channel sedimentation and geomorphic processes, influence of permafrost on surface water storage, and for mapping volumetric surface water changes and fluxes not detectable by current or planned satellite remote sensing technologies.

3.7 Acknowledgements

This work was supported by NASA Terrestrial Hydrology Program Grant NNX13AD05G managed by Jared Entin, NASA Terrestrial Ecology Program Arctic-Boreal Vulnerability Experiment (ABOVE) Grant NNX17AC60A managed by Hank Margolis, NASA Surface Water and Ocean Topography mission Grant NNX16AH83G managed by Eric Lindstrom, and NASA Earth and Space Sciences Fellowship Program Grant NNX14AP57H managed by Lin Chambers. Arctic DEM was created by the Polar Geospatial Center from DigitalGlobe, Inc., imagery and funded under National Science Foundation awards 1043681, 1559691, and 1542736. The late Alberto Behar designed and engineered the custom GPS equipment used for field surveys. We thank Muriel Bergé-Nguyen at Centre National d'Etudes Spatiales (CNES) for completing the GNSS differential GPS processing, John Arvesen of Cirrus Digital Systems for assistance with color-infrared digital imagery, the JPL AirSWOT processing team for radar data processing, Ariana Nickmeyer and Lin Lu at UCLA for support with preliminary AirSWOT investigations, Alex Shapiro of Alaska Land Exploration LLC for logistical and helicopter support, and Jerry Carrol in Fort Yukon for boat transport on the Yukon River. We thank Heather Bartlett, Joshua Rose, and Mike Hinkes of the Yukon Flats National Wildlife Refuge for their field support. All geospatial data products are available via the Oak Ridge National Laboratory (ORNL) Distributed Active Archive Center (DAAC) at [https:// daac.ornl.gov/](https://daac.ornl.gov/) (Pitcher et al.,

2019). Processed lake GPS surveys and pressure transducer (PT) depth corrections are given in Table 3-2; river GPS data are provided in Data Set S3-1.

3.8 Figures

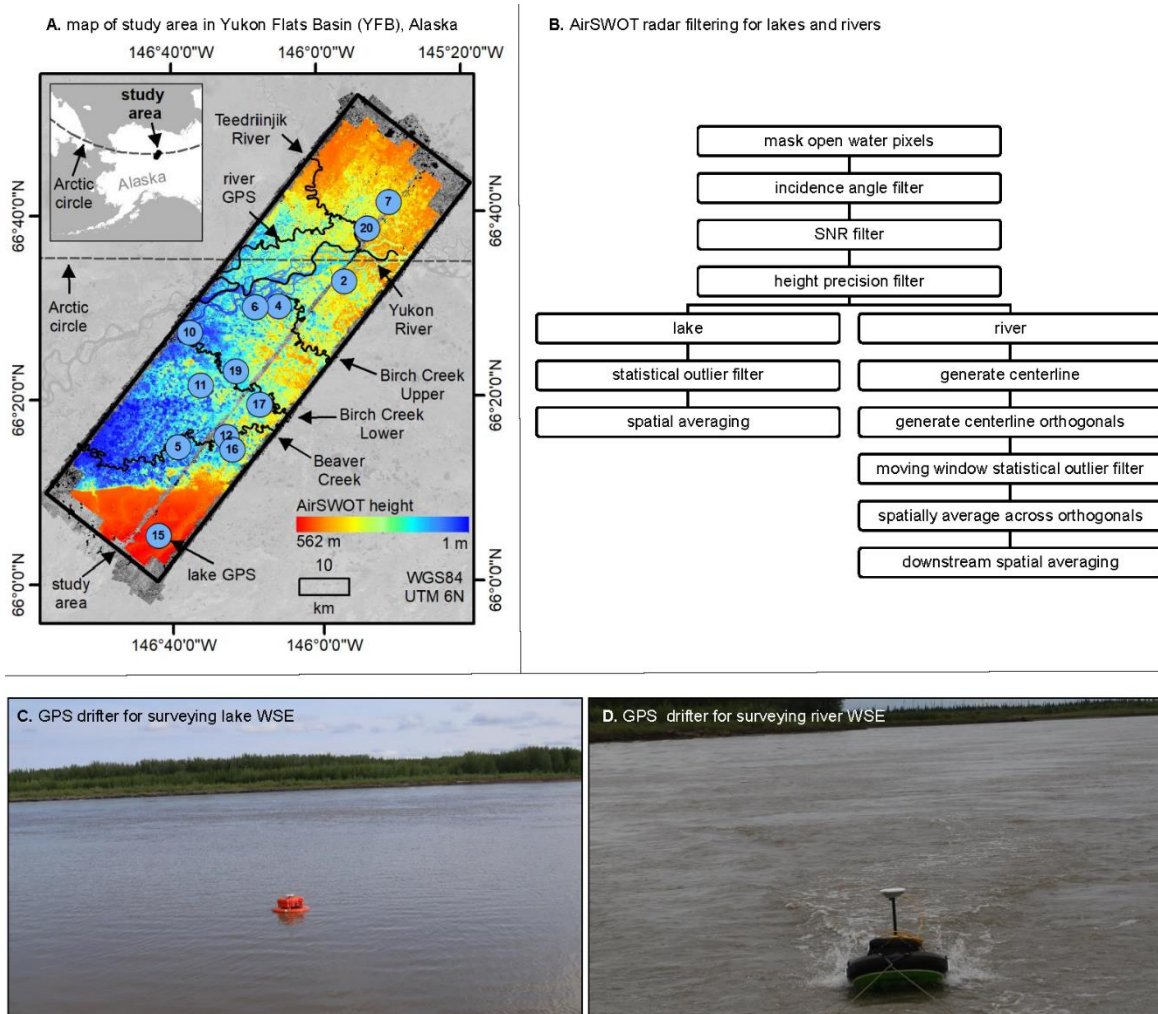


Figure 3-1: AirSOWT mapping extent, data filtering, and field validation. (a) AirSWOT mapping extent (black box) in the YFB, eastern interior Alaska, USA. Underlying image is the AirSWOT DEM overlaid on the near-infrared band from a color-infrared orthomosaic generated using images collected

coincident with AirSWOT radar data (Table 3-1). Background image is a Landsat-8 OLI mosaic. The locations of 13 lakes surveyed in situ are shown (blue circles with numeric identifiers). The Yukon River water surface elevation (WSE) global positioning system (GPS) survey is plotted along with the other river profiles assessed, namely, Yukon River main channel, Birch Creek-Upper, Birch Creek-Lower, Beaver Creek, and the Teedriinjik River. The dashed gray line denotes the Arctic circle boundary, which is $\sim 66.57^{\circ}\text{N}$. The inset shows the location of the study area in eastern interior Alaska. **(b)** AirSWOT data quality filtering and spatial averaging flowchart for lakes (left) and rivers (right). **(c)** The custom GPS system used to survey 13 lakes across the YFB between 27 May 2015 and 12 June 2015. **(d)** The custom GPS system mounted on a SonTek/YSI Hydroboard II that we escort down an ~ 82 -km reach of the Yukon River and a lateral distributary channel towed behind a motorized river boat.

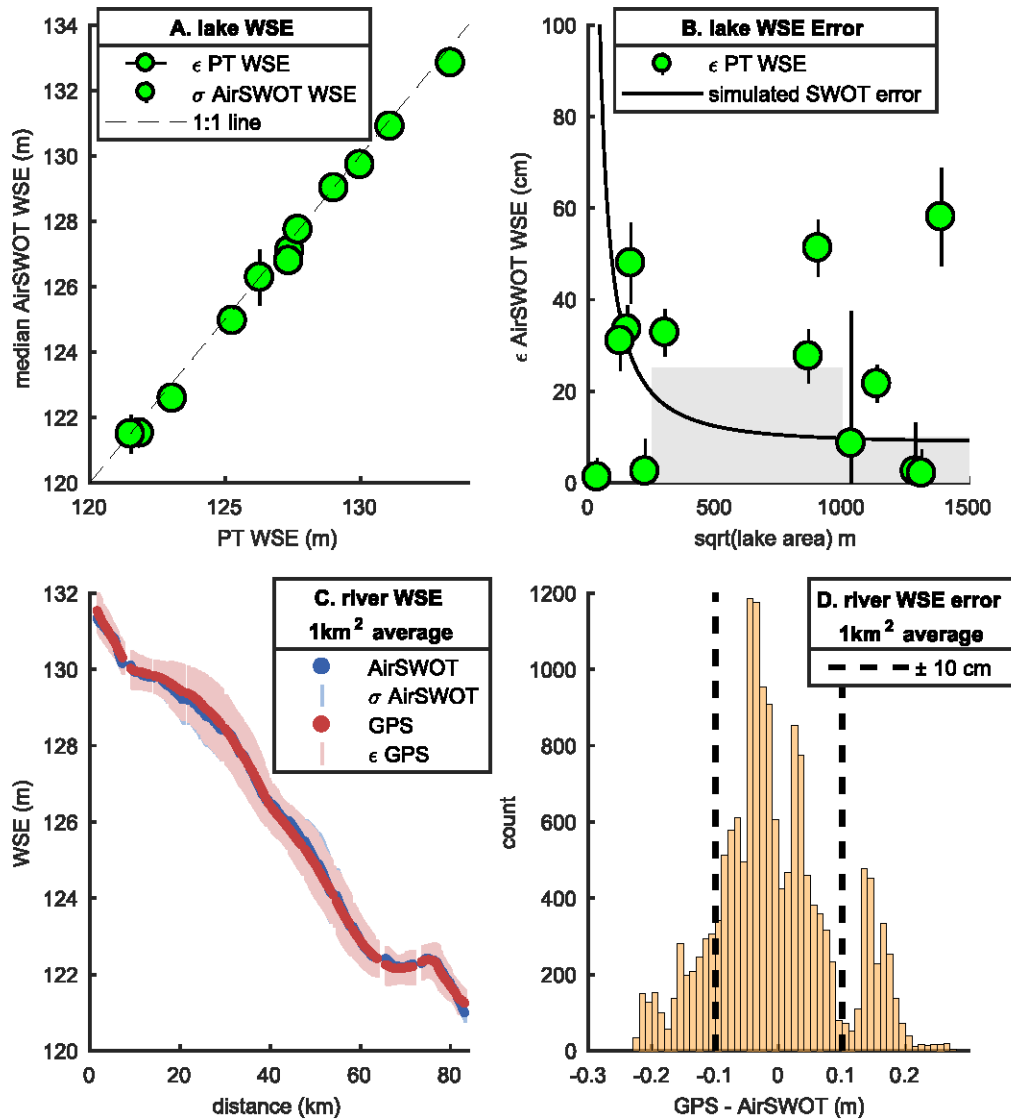


Figure 3-2: comparison of AirSWOT and GPS water surface elevations.

(a, b) Lake water surface elevations (WSEs) calculated from AirSWOT and global positioning system (GPS). (a) AirSWOT WSE is calculated as the median pixel value for each lake, and uncertainty is reported as the standard deviation of pixels. GPS uncertainty is derived from lake pressure transducer and GPS errors; 12 of 13 field lakes are shown; #15 is excluded because it is in the foothills of the White Mountains and has a WSE larger than other

lowland lakes. **(b)** shows the distribution of differences between AirSWOT and GPS for all 13 lakes. Error bars denote uncertainties in field GPS surveys. Gray shading demarcates Surface Water and Ocean Topography (SWOT) mission WSE accuracy requirements. Black line denotes the theoretical SWOT mission error budget (Rodriguez, 2016). **(c, d)** Yukon River WSE measured by AirSWOT is compared with a coincident GPS WSE survey. **(c)** plots AirSWOT (blue) for 1 km² downstream spatial averages compared with GPS data (red). **(d)** plots the difference between AirSWOT and GPS for 1 km² downstream reaches. The SWOT mission accuracy guidelines states that WSE should be accurate to ± 10 cm when spatially averaged over 1 km² open water pixels or ± 25 cm when spatially averaged over 0.0625 km² open water pixels. Spatially averaged AirSWOT reaches achieving these precisions fall within dashed lines. See Figure S3-6 for analogous comparison with 0.0625 km² spatial averages.

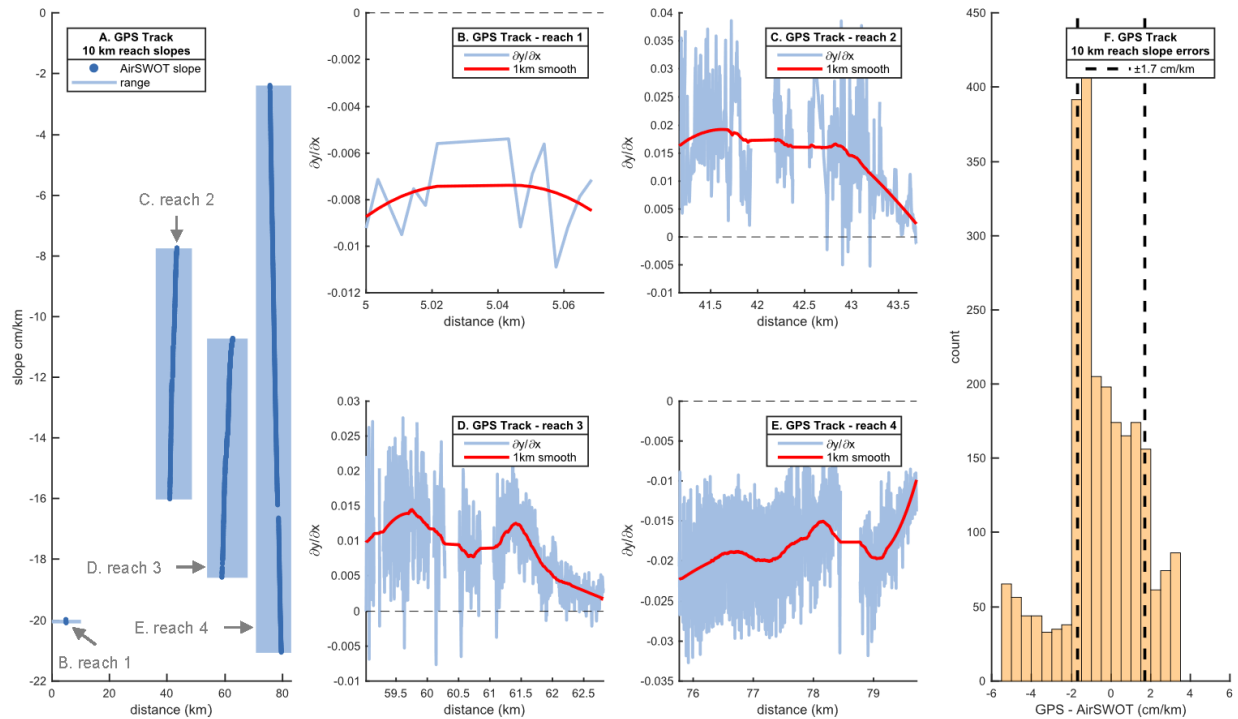


Figure 3-3: Yukon River water surface slopes (WSS).

Comparison of Yukon River water surface slope (WSS) calculated using a linear model for downstream water surface elevation profiles from AirSWOT and global positioning system (GPS) data along 10 km reaches. **(a)** WSS for reaches with channel mask widths of at least 100 m and at least 80% data coverage. **(b–e)** First derivatives or WSS rate of change by reach. Note that ∂x is constant because WSSs are calculated for 10 km reaches. **(f)** Difference between AirSWOT and GPS WSS. Dashed lines demarcate 10 km reaches where AirSWOT WSSs are ± 1.7 -cm/km GPS WSS and thus fall within acceptable SWOT accuracy standards. Removed from this analysis are orthogonal channel cross sections < 100 m wide and 10 km reaches with

<80% AirSWOT data coverage. In general, Yukon River WSS magnitudes spatially vary, and AirSWOT WSS tends to agree with GPS WSS.

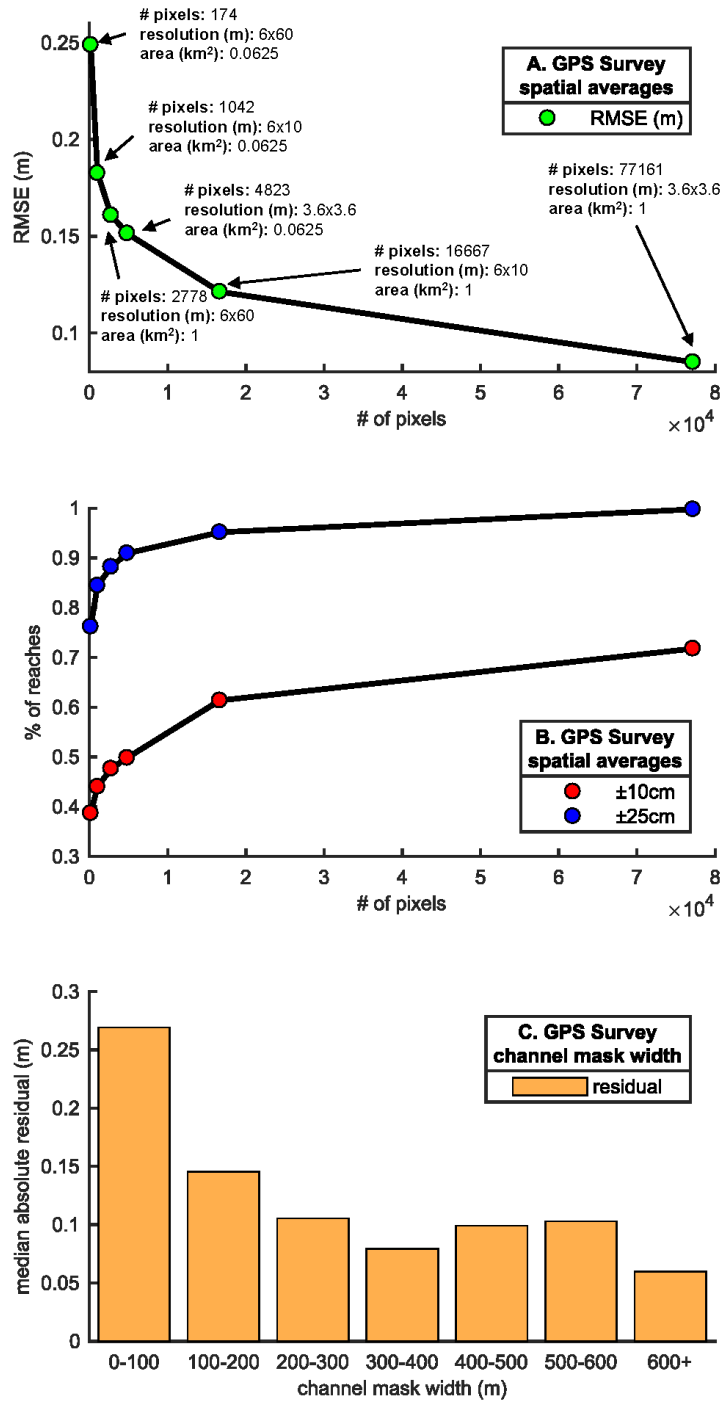


Figure 3-4: AirSWOT WSE, spatial averaging, and channel width.

Comparison of (a) root-mean square error (RMSE) of Yukon River AirSWOT water surface elevation (WSE) and (b) Surface Water and Ocean

Topography (SWOT) mission accuracy standards by the number of pixels used for downstream spatial averaging. Note that **(a)** and **(b)** use the same pixel thresholds (x-axis). **(c)** shows that AirSWOT orthogonal water surface elevation precisions vary with channel mask width.

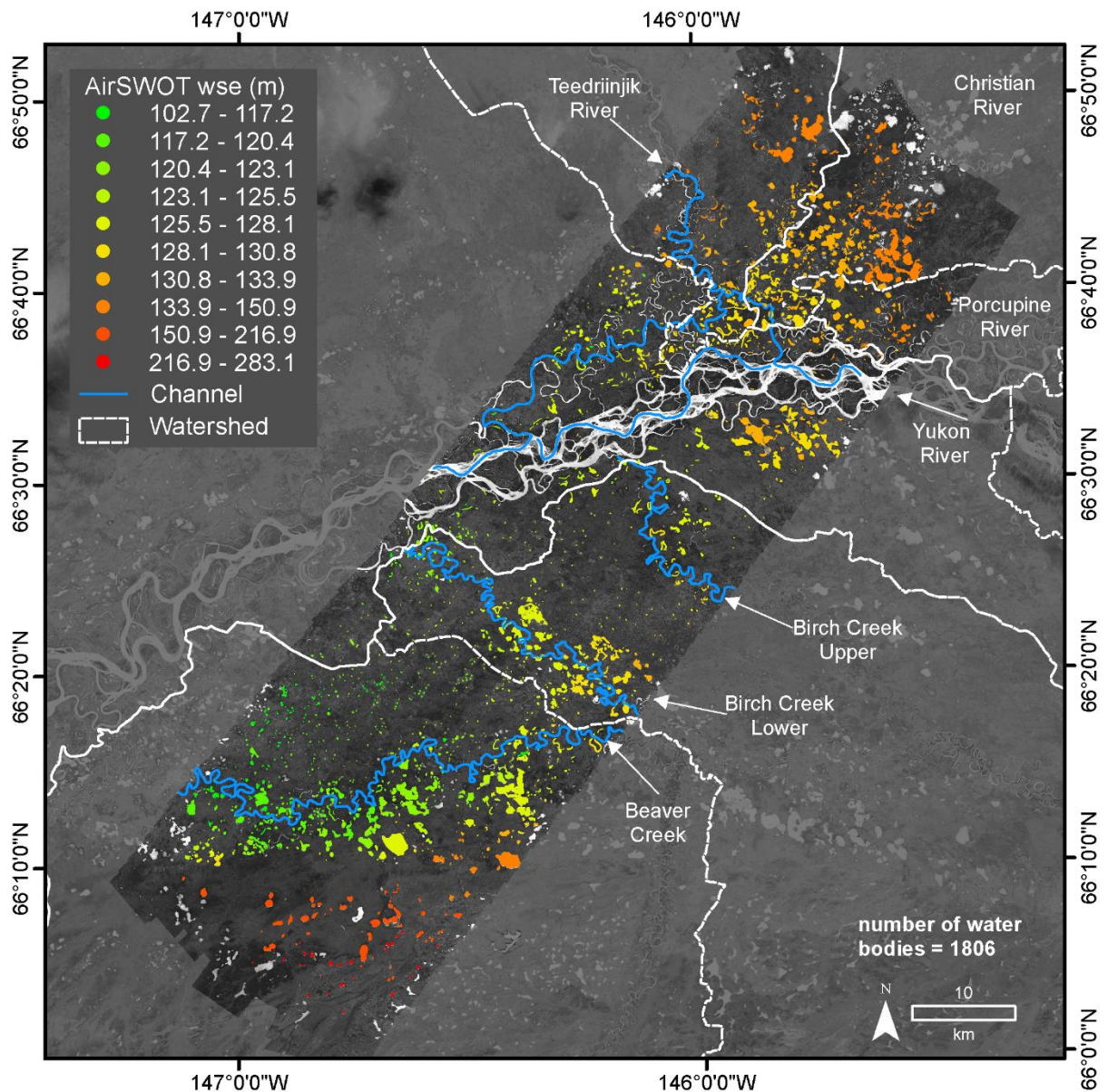


Figure 3-5: Yukon Flats Basin (YFB) lake WSE as mapped by AirSWOT. A map of lake AirSWOT water surface elevations (WSEs). Lakes with AirSWOT WSE standard deviations 1 m or more are removed from analysis. White dashed lines show hydrologic divides from the watershed boundary data set (Table 1).

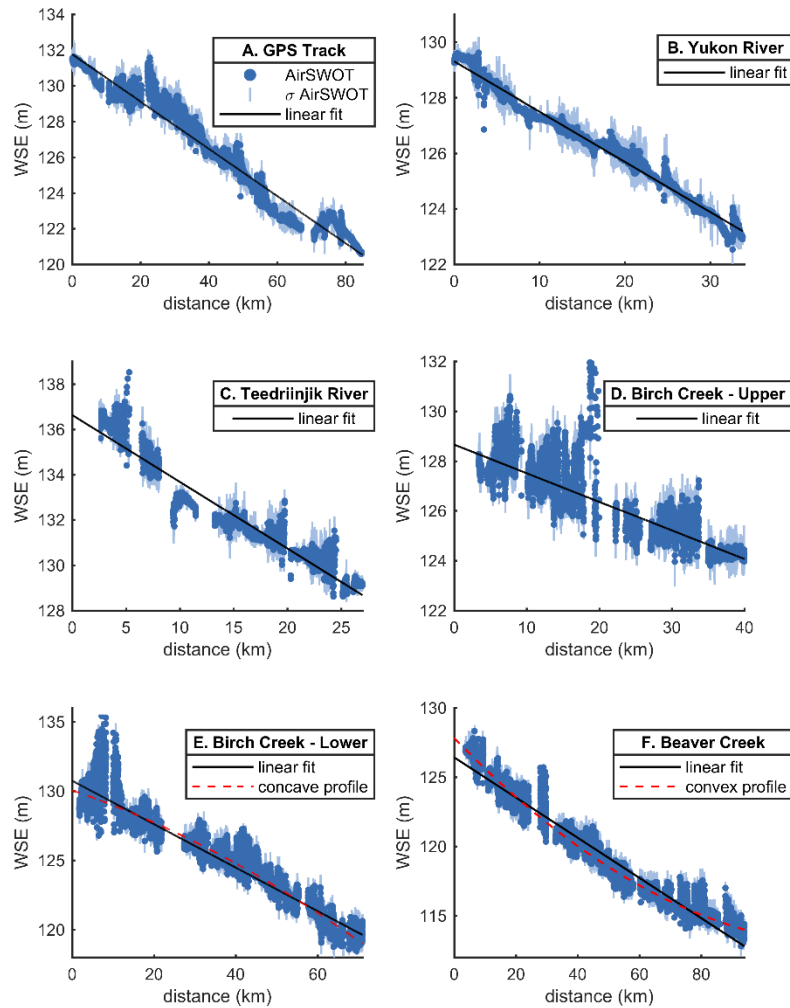


Figure 3-6: AirSWOT longitudinal river mappings.

Downstream water surface elevation (WSE) profile for the (a) global positioning system (GPS) survey track, (b) the main stem of the Yukon River, (c) the Teedriinjik River, (d) Birch Creek-Upper, (e) Birch Creek-Lower, and (f) Beaver Creek. AirSWOT values are orthogonal averages after data quality filters (section 3.3.1) and removal of orthogonals with WSE standard deviations >1 m.

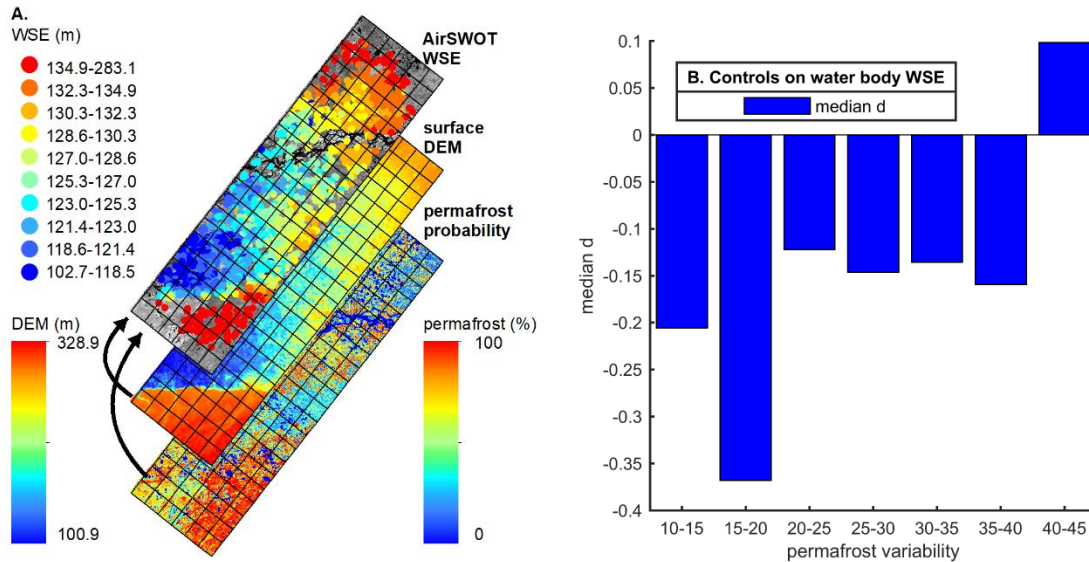


Figure 3-7: controls on water surface elevation (WSE) variability.

Examination of topographic and permafrost control on lake water surface elevation (WSE) variability. The land surface digital elevation model (DEM) is from Yamazaki et al. (2017) and probability of permafrost presence is from Pastick et al. (2013).

3.9 Tables

Category	Name	Code	Info	Use	Source
AirSWOT and satellite optical imagery	Cirrus Digital Systems color-infrared (CIR) multiband imagery	CIR	pixel size: 3.6 m (resampled) bands (or channels): 3 band 1: nir band 2: red band 3: green band 4: data mask units: DN projection: WGS84 UTM6N	generate masks for open water AirSWOT extraction	collected coincident with AirSWOT radar data; data provided by Cirrus Digital Systems
	Landsat OLI	OLI	pixel size: 30 m band 5: nir (only band used) units: DN projection: WGS84 UTM6N	data visualization and mapping	images collected June 15-17, 2015, data acquired from USGS GloVis
AirSWOT interferometric Ka-band radar data (KaSPAR)	Height	WSE	Pixel Size: 3.6 m Units: m relative to WGS84 Projection: WGS84 UTM6N	estimate WSE	Processed AirSWOT radar data provided by NASA/JPL
	Precision (or error)	ϵ	Pixel Size: 3.6 m Units: m Projection: WGS84 UTM6N	AirSWOT data filtering	
	Incidence Angle	\angle	Pixel Size: 3.6 m. Units: degrees ($^{\circ}$) Projection: WGS84 UTM6N * converted original data to $^{\circ}$ from radians		
	Radar backscatter		Pixel Size: 3.6 m. Units: dB Projection: WGS84 UTM6N *converted original data to dB with equation $20*\log_{10}(\text{magnitude})$		
	Noise equivalent radar backscatter		Pixel Size: na Units: dB Projection: na Data provided as netcdf with \angle		
	Signal-to-noise ratio	SNR	Pixel Size: 3.6 m. Units: dB Projection: WGS84 UTM6N *calculated as the difference between backscatter and noise equivalent backscatter		
Digital Elevation Models (DEMs)	ArcticDEM	ArcticDEM	Pixel Size: 5 m Units: m relative to WGS84 Projection: WGS84 UTM6N	AirSWOT radar phase unwrapping, layover simulation	ArcticDEM version 1.0 with data gap interpolation. Data available from the Polar Geospatial Center
	MERIT DEM	MERIT	Pixel Size: 60 m (resampled) Projection: WGS84 UTM6N (reprojected)	hydraulic gradient and permafrost analysis	Yamazaki et al., (2017)
Permafrost	probability of permafrost presence	permafrost probability	Pixel size: 30 m Projection: Albers Conic Equal Area Datum: WGS84	hydraulic gradient and permafrost analysis	Pastick et al., (2013)
Field Data	Yukon Flats water body GPS Surveys	GPS	GPS: Trimble R5700 or R7 Refer to section 3.3 and 3.4 for data processing and precision details	comparison with AirSWOT WSE	see depth corrected WSE in Table 2
	Yukon River GPS Surveys				data set S1

	Yukon Flats water body depths	water body depth	Solinst levellogger and barologgers. See: https://solinst.com//	GPS WSE corrections	depth offsets given in Table 2
Reference .shp files	Watershed Boundary Dataset	WBD	Scale: 1:24,000	separates study area into watersheds	downloaded from USDA Geospatial Data Gateway, also available via USGS

Table 3-1: Summary of data used.

Summary includes: data abbreviation (when given), data resolution, use and data source. Note. DN = digital number; GPS = global positioning system; JPL = Jet Propulsion Laboratory; NASA = National Aeronautics and Space Administration; SWOT = Surface Water and Ocean Topography; WSE = water surface elevation.

Lake #	Lat.	Long.	lake mask area, km ²	AirSWOT WSE, m	# pixels	PT WSE, m	depth offset, cm	GPS survey date	PT WSE - AirSWOT WSE, m
2	66.5448	-145.8871	1.80	130.9±0.2	99876	131.1±0.0	-0.78	06/11/15	0.22
4	66.5012	-146.1861	0.02	121.5±0.2	1801	121.8±0.1	-0.27	06/12/15	0.34
5	66.2483	-146.6431	0.04	122.6±0.2	2159	123.1±0.1	-3.92	06/02/15	0.48
6	66.5004	-146.2901	0.10	125.0±0.2	7048	125.3±0.1	-1.93	06/10/15	0.32
7	66.6868	-145.6761	1.02	132.8±0.2	63271	133.4±0.1	-1.45	06/11/15	0.51
10	66.4553	-146.5879	0.15	121.5±0.6	3869	121.5±0.1	-9.20	06/09/15	0.02
11	66.3592	-146.5396	0.01	126.3±0.9	94	126.3±0.0	-3.65	06/09/15	0.05
12	66.2660	-146.4248	0.03	127.1±0.3	1221	127.4±0.1	-1.48	06/10/15	0.34
15	66.0880	-146.7328	0.86	209.6±0.2	82944	209.5±0.3	-0.24	06/12/15	-0.14
16	66.2431	-146.3996	3.26	127.7±0.2	128472	127.7±0.1	-4.97	06/27/15	-0.02
17	66.3234	-146.2756	1.36	129.0±0.3	133380	129.0±0.1	-1.77	06/09/15	-0.05
19	66.3843	-146.3812	1.98	126.8±0.3	149267	127.4±0.1	-0.65	06/11/15	0.59
20	66.6398	-145.7777	0.84	129.7±0.2	58157	130.0±0.1	-20.56	06/11/15	0.27

Table 3-2: Summary of field surveyed lakes.

Summary includes: Lake Location, Lake Mask Area, AirSWOT WSE, and PT WSE. Note. GPS = global positioning system; PT = pressure transducer; SWOT = Surface Water and Ocean Topography; WSE = water surface elevation. AirSWOT uncertainty is reported as the standard deviation in WSE pixels after data quality filtering. Similarly, number of pixels is the count of remaining pixels in each lake after filtering. Depth offset is the PT measured change in lake level between GPS and AirSWOT surveys.

3.10 References

- Allen, G. H., Barnes, J. B., Pavelsky, T. M., and Kirby, E. (2013). Lithologic and tectonic controls on bedrock channel form at the northwest Himalayan front. *J. Geophys. Res. Earth Surf.* 118, 1806–1825. doi:10.1002/jgrf.20113.
- Alsdorf, D. E., Rodríguez, E., and Lettenmaier, D. P. (2007). Measuring surface water from space. *Rev. Geophys.* 45. doi:10.1029/2006RG000197.
- Altenau, E. H., Pavelsky, T. M., Moller, D., Lion, C., Pitcher, L. ., Allen, G. H., et al. (2017). AirSWOT measurements of river water surface elevation and slope: Tanana River, AK. *Geophys. Res. Lett.* 44, 181–189. doi:10.1002/2016GL071577.
- Arsen, A., Crétaux, J. -f., and del Rio, R. A. (2015). Use of SARAL/AltiKa over Mountainous Lakes, Intercomparison with Envisat Mission. *Mar. Geod.* 38, 534–548. doi:10.1080/01490419.2014.1002590.
- Ascione, A., Cinque, A., Miccadei, E., Villani, F., and Berti, C. (2008). The Plio-Quaternary uplift of the Apennine chain: new data from the analysis of topography and river valleys in Central Italy. *Geomorphology* 102, 105–118. doi:10.1016/j.geomorph.2007.07.022.
- Bennett, J. P., and Rathburn, R. E. (1972). Reaeration in Open-Channel Flow. *Geol. Surv. Prof. Pap.* 737, 86.

- Biancamaria, S., Lettenmaier, D. P., and Pavelsky, T. M. (2016). The SWOT Mission and Its Capabilities for Land Hydrology. *Surv. Geophys.* 37, 307–337. doi:10.1007/s10712-015-9346-y.
- Birkett, C. M., Mertes, L. A. ., Dunne, T., Costa, M. H., and Jasinski, M. J. (2002). Surface water dynamics in the Amazon Basin: Application of satellite radar altimetry. *J. Geophys. Res.* 107. doi:10.1029/2001JD000609.
- Bonnema, M. G., Sikder, S., Hossain, F., Durand, M., Gleason, C. J., and Bjerklie, D. M. (2016). Benchmarking wide swath altimetry-based river discharge estimation algorithms for the Ganges river system. *Water Resour. Res.* 52, 2439–2461. doi:10.1002/2015WR017296.
- Brabets, T. P., Wang, B., and Meade, R. H. (2000). Environmental and Hydrologic Overview of the Yukon River Basin, Alaska and Canada. *Water-Resources Investigations Report 99-4204*. U.S. Geological Survey.
- Cisneros, B. E. J., Oki, T., Arnell, N. W., Benito, G., Cogley, J. G., Döll, P., et al. (2014). Freshwater Resources. doi:10.2134/jeq2008.0015br.
- Cooley, S. W., Smith, L. C., Stepan, L., and Mascaro, J. (2017). Tracking dynamic northern surface water changes with high-frequency planet CubeSat imagery. *Remote Sens.* 9, 1–21. doi:10.3390/rs9121306.
- Crétaux, J. F., Abarca-del-Río, R., Bergé-Nguyen, M., Arsen, A., Drolon, V., Clos, G., et al. (2016). Lake Volume Monitoring from Space. *Surv. Geophys.* 37, 269–305. doi:10.1007/s10712-016-9362-6.

- Crétaux, J. F., Calmant, S., Romanovski, V., Shabunin, A., Lyard, F., Bergé-Nguyen, M., et al. (2009). An absolute calibration site for radar altimeters in the continental domain: Lake Issykkul in Central Asia. *J. Geod.* 83, 723–735. doi:10.1007/s00190-008-0289-7.
- Dade, W. B., and Friend, P. F. (1998). Grain-Size, Sediment-Transport Regime, and Channel Slope in Alluvial Rivers. *J. Geol.* 106, 661–676. doi:https://doi.org/10.1086/516052.
- Durand, M., Gleason, C. J., Garambois, P. A., Bjerklie, D., Smith, L. C., Roux, H., et al. (2016). An intercomparison of remote sensing river discharge estimation algorithms from measurements of river height, width, and slope. *Water Resour. Res.* 52, 4527–4549. doi:10.1002/2015WR018434.
- Durand, M., Neal, J., Rodríguez, E., Andreadis, K. M., Smith, L. C., and Yoon, Y. (2014). Estimating reach-averaged discharge for the River Severn from measurements of river water surface elevation and slope. *J. Hydrol.* 511, 92–104. doi:10.1016/j.jhydrol.2013.12.050.
- Estey, L. H., and Meertens, C. M. (1999). TEQC: The Multi-Purpose Toolkit for GPS/GLONASS Data. *GPS Solut.* 3, 42–49. doi:https://doi.org/10.1007/PL00012778.
- Fisher, G. B., Amos, C. B., Bookhagen, B., Burbank, D. W., and Godard, V. (2012). Channel widths, landslides, faults, and beyond: The new world order of high-spatial resolution Google Earth imagery in the study of

earth surface processes. *Geol. Soc. Am. Spec. Pap.* 2012, 1–22.

doi:10.1130/2012.2492(01).

Fisher, G. B., Bookhagen, B., and Amos, C. B. (2013). Channel planform geometry and slopes from freely available high-spatial resolution imagery and DEM fusion: Implications for channel width scalings, erosion proxies, and fluvial signatures in tectonically active landscapes.

Geomorphology 194, 46–56. doi:10.1016/j.geomorph.2013.04.011.

Flint, J. J. (1974). Stream gradient as a function of order, magnitude, and discharge. *Water Resour. Res.* 10, 969–973.

doi:10.1029/WR010i005p00969.

Fjørtoft, R., Gaudin, J. M., Pourthié, N., Lalaurie, J. C., Mallet, A., Nouvel, J. F., et al. (2014). KaRIn on SWOT: Characteristics of near-nadir Ka-band interferometric SAR imagery. *IEEE Trans. Geosci. Remote Sens.* 52,

2172–2185. doi:10.1109/TGRS.2013.2258402.

Frappart, F., Calmant, S., Cauhopé, M., Seyler, F., and Cazenave, A. (2006). Preliminary results of ENVISAT RA-2-derived water levels validation over the Amazon basin. *Remote Sens. Environ.* 100, 252–264.

doi:10.1016/j.rse.2005.10.027.

Gao, H., Birkett, C., and Lettenmaier, D. P. (2012). Global monitoring of large reservoir storage from satellite remote sensing. *Water Resour. Res.*

48, 1–12. doi:10.1029/2012WR012063.

Garambois, P.-A., and Monnier, J. (2015). *Advances in Water Resources*

- Inference of effective river properties from remotely sensed observations of water surface. *Adv. Water Resour.* 79, 103–120.
doi:10.1016/j.advwatres.2015.02.007.
- Gleason, C. J., Garambois, P.-A., and Durand, M. T. (2017). Tracking river flows from space. *Eos (Washington, DC)*. 98.
doi:https://doi.org/10.1029/2017EO078085.
- Glennie, C. (2018). Arctic high-resolution elevation models: Accuracy in sloped and vegetated terrain. *J. Surv. Eng.* 144, 1–9.
doi:10.1061/(ASCE)SU.1943-5428.0000245.
- Gulbrandsen, M. L., Minsley, B. J., Ball, L. B., and Hansen, T. M. (2016). Semiautomatic mapping of permafrost in the Yukon Flats, Alaska. *Geophys. Res. Lett.* 43, 12,131–12,137. doi:10.1002/2016GL071334.
- Hopkinson, C., Crasto, N., Marsh, P., Forbes, D., and Lesack, L. (2011). Investigating the spatial distribution of water levels in the Mackenzie Delta using airborne LiDAR. *Hydrol. Process.* 25, 2995–3011.
doi:10.1002/hyp.8167.
- Jenson, J. R. (2000). *Remote Sensing of the Environment An Earth Resource Perspective*. Prentice Hall Inc.
- Jepsen, S. M., Voss, C. I., Walvoord, M. A., Minsley, B. J., and Rover, J. (2013). Linkages between lake shrinkage/expansion and sublacustrine permafrost distribution determined from remote sensing of interior Alaska, USA. *Geophys. Res. Lett.* 40, 882–887. doi:10.1002/grl.50187.

- Jepsen, S. M., Walvoord, M. A., Voss, C. I., and Rover, J. (2016). Effect of permafrost thaw on the dynamics of lakes recharged by ice-jam floods: Case study of Yukon Flats, Alaska. *Hydrol. Process.* 30, 1782–1795. doi:10.1002/hyp.10756.
- Kirby, E., and Whipple, K. X. (2012). Expression of active tectonics in erosional landscapes. *J. Struct. Geol.* 44, 54–75. doi:10.1016/j.jsg.2012.07.009.
- Knighton (1998). *Fluvial Forms & Processes: A New Perspective*. Hoder Education.
- LeFavour, G., and Alsdorf, D. (2005). Water slope and discharge in the Amazon River estimated using the shuttle radar topography mission digital elevation model. *Geophys. Res. Lett.* 32. doi:10.1029/2005GL023491.
- Leopold, L. B. (1953). Downstream change of velocity in rivers. *Am. J. Sci.* 251, 606–624. doi:10.2475/ajs.251.8.606.
- Leopold, L. B., Wolman, G. M., and Miller, J. P. (1964). *Fluvial Processes in Geomorphology*. Dover Publications.
- Li, J., and Sheng, Y. (2012). An automated scheme for glacial lake dynamics mapping using Landsat imagery and digital elevation models: A case study in the Himalayas. *Int. J. Remote Sens.* 33, 5194–5213. doi:10.1080/01431161.2012.657370.
- Mackin, J. H. (1948). Concept of the Graded River. *Bull. Geological Soc. Am.*

59, 463–512.

Marty, J. C., Loyer, S., Perosanz, F., Mercier, F., Bracher, G., Legresy, B., et al. (2011). GINS: the CNES/GRGS GNSS scientific software. in *3rd International Colloquium Scientific and Fundamental Aspects of the Galileo Programme, ESA Proceedings WPP326*, 8–10.

Mcfeeters, S. K. (1996). The use of the Normalized Difference Water Index (NDWI) in the delineation of open water features. *Int. J. Remote Sens.* 17, 1425–1432. doi:10.1080/01431169608948714.

Melching, C. S., and Flores, H. E. (1999). Reaeration Equations Derived from U.S. Geological Survey Database. *J. Environ. Eng.* 125, 407–414. doi:https://doi.org/10.1061/(ASCE)0733-9372(1999)125:5(407).

Minsley, B. J., Abraham, J. D., Smith, B. D., Cannia, J. C., Voss, C. I., Jorgenson, M. T., et al. (2012). Airborne electromagnetic imaging of discontinuous permafrost. *Geophys. Res. Lett.* 39, 1–8. doi:10.1029/2011GL050079.

Moller, D. K., Mourad, P. D., and Frasier, S. J. (2000). Field observations of radar backscatter from the ocean surface under low wind speed conditions. *J. Geophys. Res. Ocean.* 105, 24059–24069. doi:10.1029/2000JC900103.

Neeck, S. P., Lindstrom, E. J., Vaze, P. V., and Fu, L.-L. (2012). Surface Water and Ocean Topography (SWOT) mission. in *Sensors, Systems and*

Next-Generation Satellites XVI (Proceedings of SPIE 8533).

doi:10.1117/12.981151.

Otsu, N. (1979). A Threshold Selection Method from Gray-Level Histograms.

Syst. Man Cybern. IEEE Trans. 9, 62–66.

doi:10.1109/TSMC.1979.4310076.

Oubanas, H., Gejadze, I., Malaterre, P. O., and Mercier, F. (2018). River

discharge estimation from synthetic SWOT-type observations using
variational data assimilation and the full Saint-Venant hydraulic model.

J. Hydrol. 559, 638–647. doi:10.1016/j.jhydrol.2018.02.004.

Parker, G. W., and Gay, F. B. (1987). A Procedure for Estimating Reaeration
Coefficients for Massachusetts Streams.

Pastick, N. J., Jorgenson, M. T., Wylie, B. K., Minsley, B. J., Ji, L., Walvoord,

M. A., et al. (2013). Extending airborne electromagnetic surveys for
regional active layer and permafrost mapping with Remote Sensing and
Ancillary Data, Yukon Flats Ecoregion, Central Alaska. *Permafr. Periglac.*

Process. 24, 184–199. doi:10.1002/ppp.1775.

Pavelsky, T. M., and Smith, L. C. (2008). RivWidth: A Software Tool for the
Calculation of River Widths From Remotely Sensed Imagery. *IEEE*

Geosci. Remote Sens. Lett. 5, 70–73. doi:10.1109/LGRS.2007.908305.

Pekel, J.-F., Cottam, A., Gorelick, N., and Belward, A. S. (2016). High-
resolution mapping of global surface water and its long-term changes.

Nature 540, 418–422. doi:10.1038/nature20584.

- Pitcher, L. H., Smith, L. C., Pavelsky, T. M., Fayne, J. V., Cooley, S. W., Altenau, E. H., et al. (2019). ABoVE: AirSWOT Radar, Orthomosaic, and Water Masks, Yukon Flats Basin, Alaska, 2015. doi:10.3334/ORNLDAAC/1655.
- Raymond, P. A., Hartmann, J., Lauerwald, R., Sobek, S., McDonald, C., Hoover, M., et al. (2013). Global carbon dioxide emissions from inland waters. *Nature* 503, 355–359. doi:10.1038/nature12760.
- Rodriguez, E. (2016). Surface Water and Ocean Topography Mission (SWOT) Project: Science Requirements Document (Rev A). Available at: <https://pdms.jpl.nasa.gov>.
- Rosen, P. A., Hensley, S., Joughin, I. R., Li, F., Madsen, S. N., Ernesto, R., et al. (2000). Synthetic aperture radar interferometry. *Proc. IEEE*, 88, 333–382. doi:10.1109/5.838084.
- Smith, L. C., Sheng, Y., and MacDonald, G. M. (2007). A First Pan-Arctic Assessment of the Influence of Glaciation, Permafrost, Topography and Peatlands on Northern Hemisphere Lake Distribution. *Permafr. Periglac. Process.* 18, 201–208. doi:10.1002/ppp.
- Sheng, Y., Song, C., Lettenmaier, D. P., and Ke, L. (2016). Where and in What Quantity Are Lakes Observable by SWOT? in *American Geophysical Union. Fall Meeting.* (San Francisco).
- Tan, Z., and Zhuang, Q. (2015). Methane emissions from pan-Arctic lakes during the 21st century: An analysis with process-based models of lake

evolution and biogeochemistry. *J. Geophys. Res. Biogeosciences* 120, 1–13. doi:10.1002/2015JG003184.Received.

Walvoord, M. A., Voss, C. I., and Wellman, T. P. (2012). Influence of permafrost distribution on groundwater flow in the context of climate-driven permafrost thaw: Example from Yukon Flats Basin, Alaska, United States. *Water Resour. Res.* 48, 1–17. doi:10.1029/2011WR011595.

Wik, M., Varner, R. K., Anthony, K. W., MacIntyre, S., and Bastviken, D. (2016). Climate-sensitive northern lakes and ponds are critical components of methane release. *Nat. Geosci.* 9, 99–105. doi:10.1038/ngeo2578.

Yamazaki, D., Ikeshima, D., Tawatari, R., Yamaguchi, T., O’Loughlin, F., Neal, J. C., et al. (2017). A high-accuracy map of global terrain elevations. *Geophys. Res. Lett.* 44, 5844–5853. doi:10.1002/2017GL072874.

Zhang, G., Xie, H., Kang, S., Yi, D., and Ackley, S. F. (2011). Monitoring lake level changes on the Tibetan Plateau using ICESat altimetry data (2003-2009). *Remote Sens. Environ.* 115, 1733–1742. doi:10.1016/j.rse.2011.03.005.

3.11 Supporting Information

3.11.1 Introduction to supporting information

The supporting information provides information about: AirSWOT radar geolocation error (3.11.2 and Figure S3-1), aircraft movement (Figures S3-2), layover simulation (Figure S3-3), AirSWOT and GPS lake WSEs (Figure S3-4), CIR water mask validation (Figure S3-5), field lake depth corrections (Figure S3-6), river spatial averaging (Figure S3-7 and Table S3-1), river reach lengths and slopes (Table S3-2) and an included data set (Data Set S3-1).

3.11.2 AirSWOT radar geolocation

The geolocation accuracy of AirSWOT radar data is impacted by onboard GPS measurements of aircraft location, noise in radar data, phenomenology, and phase unwrapping errors. Of these, the largest contributor to geolocation errors is phase unwrapping error, which causes imprecise Water Surface Elevations (WSEs) and Water Surface Slopes (WSSs) as well as false pixel locations. However, these errors are sub-image and therefore cannot be quantified without visually inspecting sub-image features, identifying the error, and quantifying the shift. Geolocation errors contributed by noise in the radar data can be quantified by calculating the standard deviation of interferometric phase with the geolocation sensitivity. It is expected that the average geolocation would be accurate to within one pixel. A frequency distribution of the geolocation errors is shown in

Figure S3-1, demonstrating the average frequency of errors greater than 3 meters. The AirSWOT spatial resolution of 3.6 meters was developed to accommodate the approximate geolocation error of 3 meters. Furthermore, after the AirSWOT radar image is produced from the InSAR processor, the data is compared with the original DEM to check for phase unwrapping errors. Because of the radar processing techniques, phase unwrapping errors in the final product are rare. Additionally, the land elevations of co-located lines are compared with each other and corrected for uniformity. Features must have consistent geolocation for the elevation adjustments to be calculated.

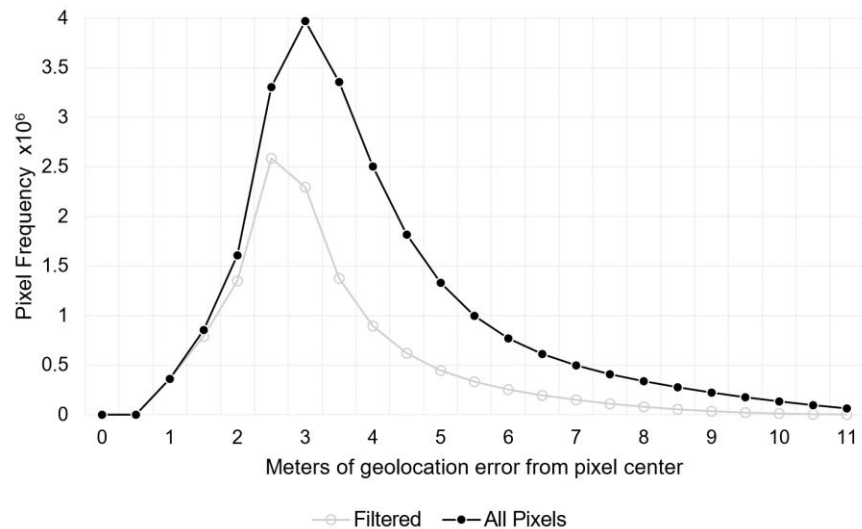


Figure S3-1: AirSWOT geolocation uncertainty.

frequency distribution of AirSWOT radar data geolocation error. The average frequency of errors is ~1 pixel. Black line depicts frequency of geolocation

error for all AirSWOT data, including land pixels. Grey line shows geolocation error for filtered AirSWOT data with data quality filtering methods described in *2.1 AirSWOT Data Collection and Processing* applied, land pixels are also included. This estimate of the frequency of geolocation errors is conservative because it includes land pixels, yet land pixels are removed using an open water mask (see *3.3.2 AirSWOT Open Water Mask*) from Water Surface Elevation (WSE) and Water Surface Slope (WSS) calculations.

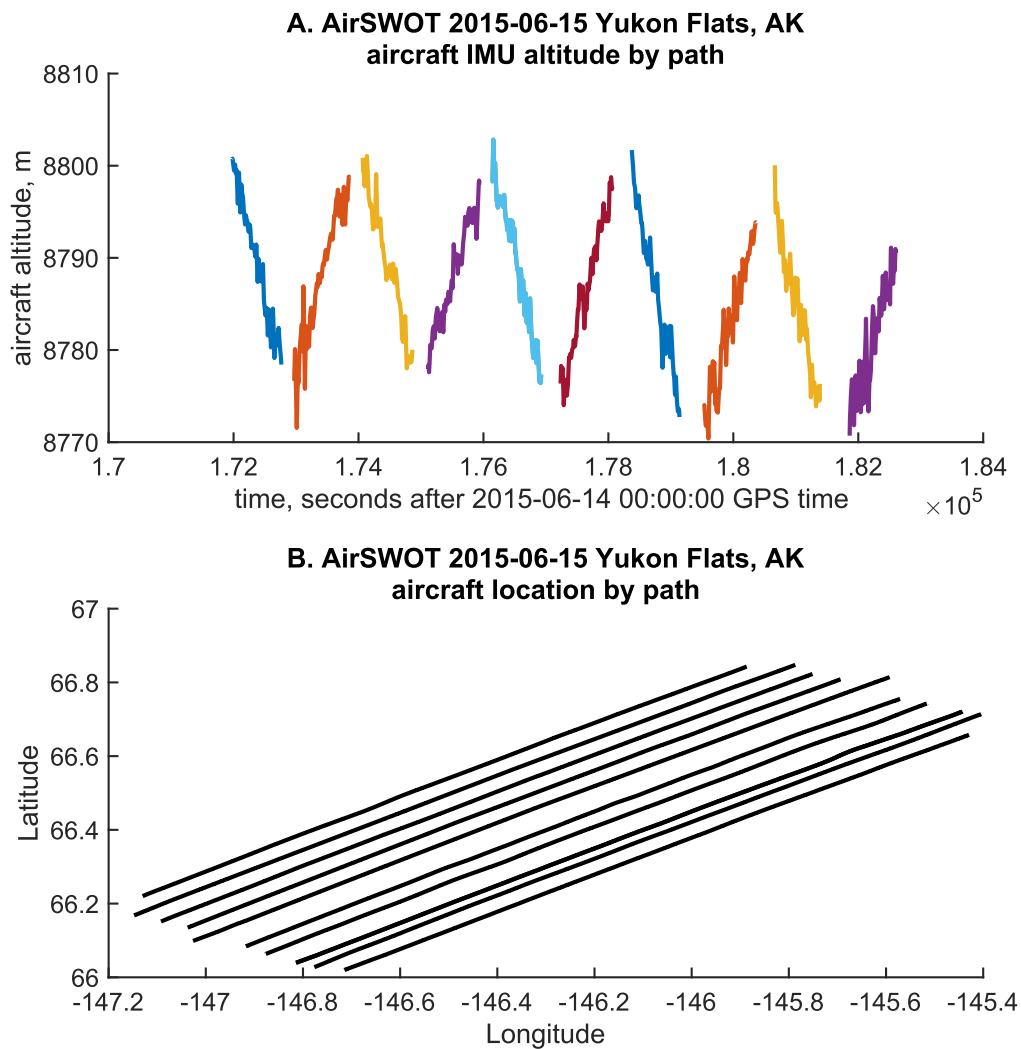


Figure S3-2: AirSWOT aircraft horizontal and vertical locations.

(A) AirSWOT aircraft altitude by time. Altitude is relative to the WGS84 ellipsoid. Each path is displayed as different color. Time is given as GPS time and is formatted as seconds relative to the start of the GPS week – which is equivalent to seconds elapsed since 00:00:00 June 14, 2015. (B) AirSWOT aircraft latitude and longitude by for each path.

3.11.3 AirSWOT layover

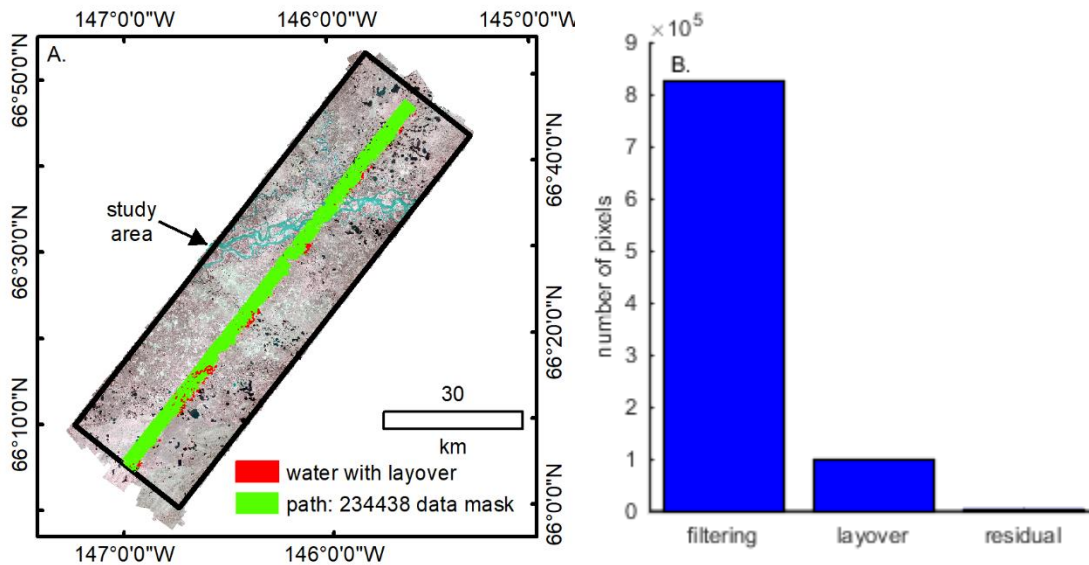


Figure S3-3: AirSWOT layover simulations.

(A) we simulate layover (red) for one path (green) using ArcticDEM as the input surface model. Layover extent is minimal and primarily impacts near range (right side of swath) pixels. (B) data quality filtering (left) removes many more pixels than are potentially impacted by layover (middle) while the residual number of pixels with layover, incidence angles $\geq 5^\circ$, and that are not removed by data quality filtering (right) is small. This residual estimate is conservative because we do not implement the statistical outlier filtering that is applied when spatial averaging to extract WSE and WSS.

3.11.4 Lake water surface elevation (WSE)

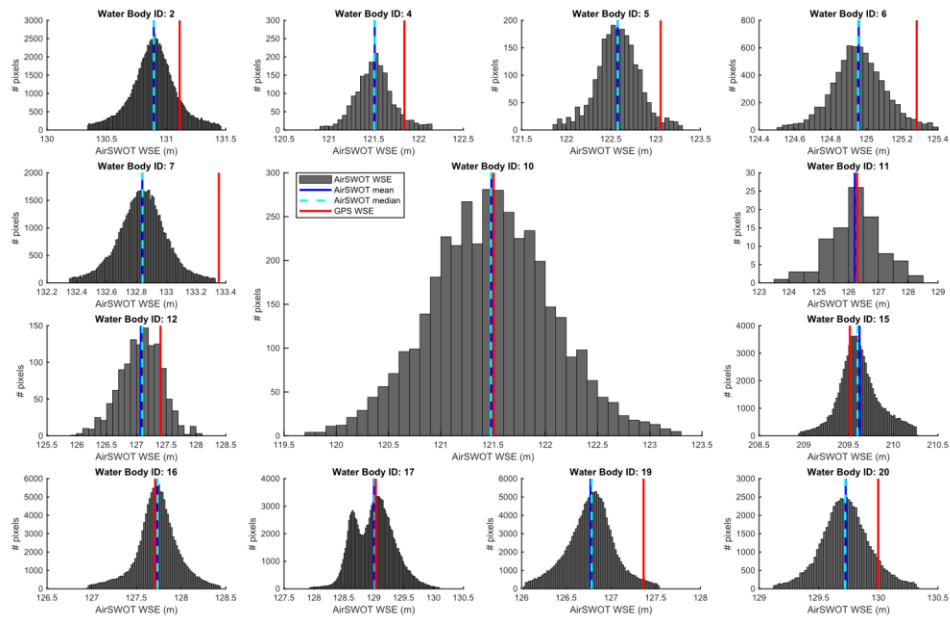


Figure S3-4: Lake water surface elevation (WSE).

Distribution of lake AirSWOT WSE pixels after data quality filtering. Lakes shown are those surveyed in situ (Figure 3-1A).

3.11.5 water mask validation

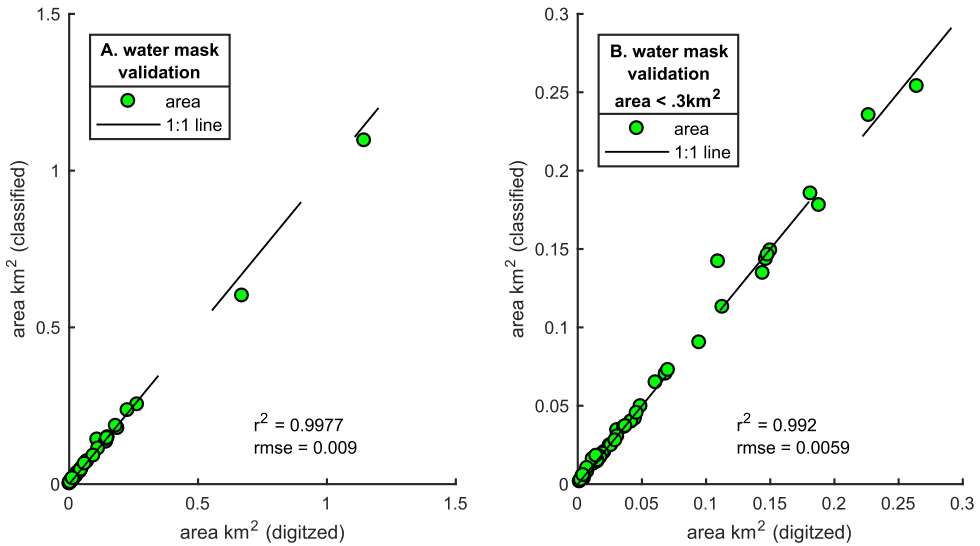


Figure S3-5: CIR water mask validation.

To validate open water masks, 50 lakes are manually digitized using color infrared digital images (CIR) collected coincident with AirSWOT radar data. Areas from manually digitized lakes (y-axis) are compared with areas from auto generated lakes (x-axis). (A) shows all 50 lakes. (B) shows only lakes with areas less than 0.3 km².

3.11.6 manual pressure transducer corrections

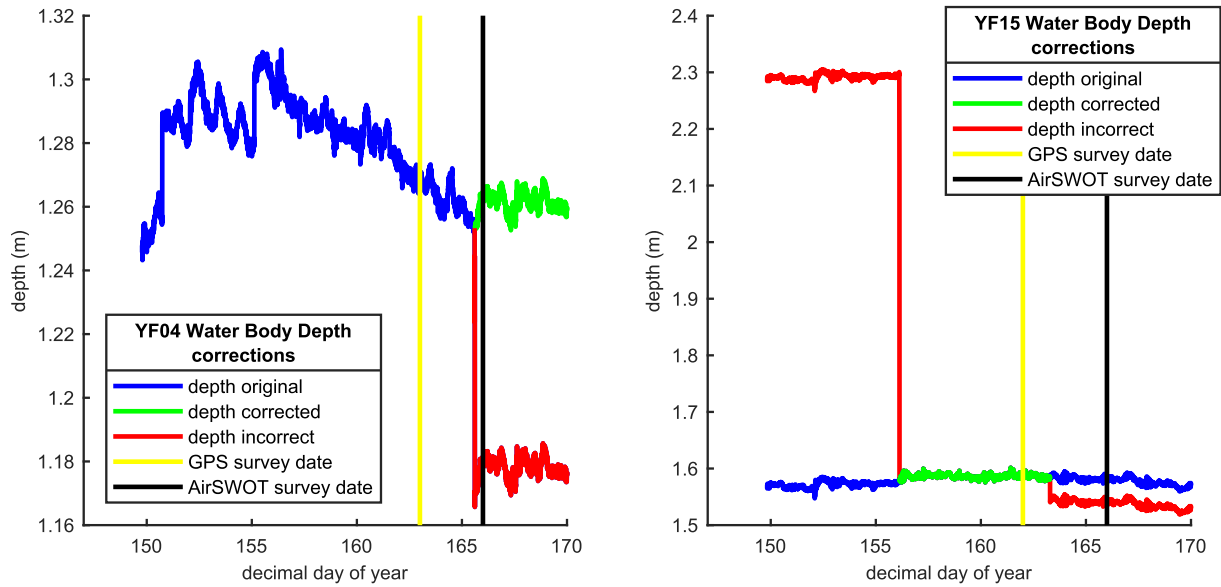


Figure S3-6: manual pressure transducer corrections.

Manual lake depth logger corrections for lake #4 and lake #15 (Figure 3-1A). Manual corrections account for pressure transducer movement between installation, GPS survey date and AirSWOT survey date.

3.11.7 spatial averaging

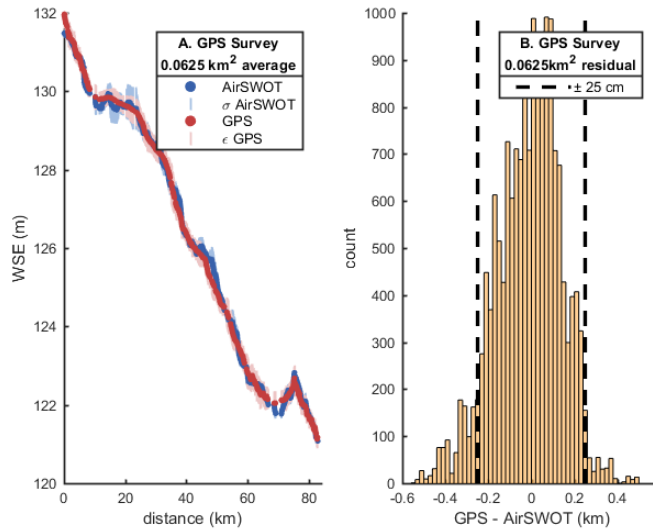


Figure S3-7: downstream spatial averaging in the Yukon River, AK, USA.

Yukon River WSE measured by AirSWOT compared with a GPS WSE survey.

Results are provided for 0.0625 km² spatial averages. This is intended to compliment Figure 3-2C-D.

Sensor	pixel size (m)		# pixels required for SWOT spatial averaging	
	azimuth direction	range direction	0.0625 km ²	1 km ²
SWOT	6	10	1042	16667
	6	60	174	2778
AirSWOT	3.6	3.6	4823	77161

Table S3-1: pixel count to spatial averaging area conversions.

Summary of number of pixels required given variable SWOT resolutions and AirSWOT resolution to establish 1km² and 0.0625 km² open water extents.

3.11.8 Yukon Flats Basins (YFB) channel characteristics

name	channel mask centerline length (km)	WSS (cm/km)	
		mean	median
GPS Track	84.7	-12.9	-13.1
Yukon River	33.8	-17.9	-16.5
Teedriinjik River	24.6	-28.3	-23.0
Birch Creek – Upper	36.6	-11.1	-12.1
Birch Creek – Lower	69.4	-17.5	-17.2
Beaver Creek	90.3	-14.6	-13.5

Table S3-2: Yukon Flats Basins (YFB) channel characteristics

Channel mask length and mean/median 10km reach length water surface slope (WSS) for 6 channels mapped by AirSWOT.

3.11.8 Yukon River GPS water surface elevation (WSE) data

Data Set S3-1.

In situ GPS water surface elevation surveys for the Yukon River and a lateral distributary channel. See section 3.4 for full description

Latitude	Longitude	WSE (m)
66.59264545	-145.6358078	132.4711
66.59321603	-145.6376555	132.4993
66.59378993	-145.6394893	132.3912
66.59431906	-145.6413009	132.3722
66.59485664	-145.643266	132.338
66.59538511	-145.6453133	132.2955
66.59587371	-145.6474517	132.2257
66.59637708	-145.6496089	132.2963
66.59689725	-145.6517513	132.2368
66.59736345	-145.6539367	132.2932
66.59776334	-145.6561962	132.1832
66.59809018	-145.6584988	132.1973
66.59836939	-145.6608477	132.1334
66.59860807	-145.6632336	132.0533
66.59880178	-145.6656913	132.0155
66.59901217	-145.6681963	131.9085
66.59911242	-145.6707291	131.9672
66.59901374	-145.6732533	132.0246
66.59875457	-145.6756946	131.8998
66.59831779	-145.6778949	131.9409
66.59770437	-145.67978	131.8419
66.59696877	-145.6813757	131.9154
66.59613073	-145.6826845	131.8596
66.59523648	-145.6837906	131.8742
66.59431717	-145.6847835	131.8524
66.59337266	-145.6856477	131.8696
66.59239187	-145.6863436	131.8065
66.5914082	-145.6870457	131.8081
66.59043961	-145.6877211	131.7962
66.58947898	-145.6883792	131.7886
66.58851639	-145.6890522	131.7627

66.58758303	-145.6900001	131.8035
66.58670755	-145.6911904	131.6921
66.58584186	-145.6924576	131.5769
66.58501073	-145.6938708	131.6017
66.5842377	-145.6954595	131.5271
66.58357284	-145.6972901	131.5409
66.58304729	-145.6993481	131.4903
66.58260367	-145.7014815	131.4454
66.58225462	-145.7037057	131.4926
66.58204017	-145.7059921	131.5009
66.58197537	-145.7083024	131.503
66.58195317	-145.7106175	131.4471
66.58198346	-145.712936	131.4063
66.58214839	-145.7152231	131.4222
66.58233465	-145.7175047	131.3723
66.58256313	-145.7197794	131.3956
66.58283	-145.7220183	131.4268
66.58313276	-145.724217	131.3572
66.58344109	-145.7264015	131.3204
66.58376779	-145.7285574	131.3263
66.5841086	-145.7307011	131.2565
66.58446341	-145.7328348	131.2297
66.5848578	-145.7349	131.1902
66.58530648	-145.7368946	131.1684
66.58579912	-145.7388314	131.0942
66.58637131	-145.7406511	131.1246
66.58693952	-145.7424604	131.1173
66.58750595	-145.7443283	131.0895
66.58806763	-145.7462446	131.0729
66.58861643	-145.7481514	131.0452
66.58917204	-145.7500502	131.0516
66.58974266	-145.7519268	130.9916

66.59034932	-145.7538019	131.0134
66.59098242	-145.7556025	130.9338
66.59162585	-145.7573993	130.9086
66.5923105	-145.7589496	130.877
66.59300203	-145.7604007	130.9088
66.59369579	-145.7618303	130.7898
66.59439474	-145.763319	130.797
66.59509099	-145.764937	130.753
66.59576769	-145.7666542	130.7703
66.59642009	-145.7684427	130.7454
66.59702389	-145.7703673	130.6798
66.59757407	-145.7723962	130.724
66.59807635	-145.7744938	130.6327
66.59856125	-145.776643	130.6636
66.59901228	-145.7788435	130.6273
66.59942217	-145.7811193	130.5956
66.59978879	-145.7834733	130.5679
66.60003953	-145.7859534	130.5312
66.60022974	-145.7884849	130.5278
66.60032477	-145.7910179	130.5263
66.60042076	-145.7935113	130.529
66.6004359	-145.7960052	130.4881
66.60047479	-145.7985428	130.4783
66.60055836	-145.801121	130.449
66.60063586	-145.8036824	130.4577
66.60071332	-145.8062192	130.4364
66.60081826	-145.8086836	130.4279
66.60089453	-145.8110526	130.437
66.60088992	-145.8134382	130.4158
66.6009202	-145.8157968	130.3973
66.60093321	-145.8181759	130.4048
66.60094715	-145.8205322	130.382
66.60102056	-145.8228876	130.3295
66.60121086	-145.8252131	130.3154
66.6015243	-145.8274107	130.318
66.60202891	-145.8291778	130.3051
66.60271261	-145.8300206	130.2973
66.60321297	-145.8289319	130.3583
66.60366285	-145.8274001	130.3341
66.60421076	-145.8259889	130.328
66.6047636	-145.8246287	130.3179

66.60524599	-145.8232057	130.3246
66.60567233	-145.8217423	130.3224
66.60607216	-145.8202839	130.3342
66.60646872	-145.8188494	130.3234
66.60688283	-145.8174684	130.3262
66.6073044	-145.8161702	130.3224
66.60775207	-145.8149865	130.3239
66.60825675	-145.8139561	130.3144
66.60884289	-145.8130888	130.305
66.60946519	-145.8123384	130.3195
66.61009779	-145.8115925	130.3143
66.61073582	-145.8109461	130.3062
66.61140406	-145.8105682	130.3331
66.61210258	-145.8103272	130.287
66.61282826	-145.810342	130.3375
66.61351018	-145.8109997	130.3617
66.61415995	-145.8117122	130.33
66.6147508	-145.8125931	130.325
66.61530592	-145.8136528	130.3526
66.61587044	-145.8147045	130.3551
66.61645544	-145.8156917	130.3338
66.61703127	-145.8167714	130.3209
66.61762494	-145.8177485	130.3302
66.61816462	-145.8188915	130.3409
66.61866964	-145.8201104	130.3465
66.61918996	-145.8212643	130.3144
66.61971053	-145.8223867	130.3547
66.62021592	-145.8235304	130.3206
66.62072576	-145.8246402	130.3631
66.62124528	-145.8256742	130.3675
66.62180126	-145.8265383	130.3674
66.62240576	-145.8272129	130.3779
66.62303939	-145.8277806	130.3443
66.62370267	-145.8282818	130.3452
66.62439693	-145.8286922	130.3396
66.62509226	-145.8290063	130.4019
66.6258076	-145.829314	130.3482
66.62652297	-145.8297362	130.3431
66.62719702	-145.8303855	130.3608
66.6278406	-145.8310994	130.388
66.62846491	-145.8319139	130.3764

66.62911453	-145.8326411	130.3877
66.62978164	-145.8332935	130.3674
66.63047057	-145.8337398	130.376
66.63116965	-145.8339788	130.3708
66.63184832	-145.8338114	130.417
66.63245421	-145.8332323	130.3924
66.63297625	-145.8323387	130.3995
66.63348949	-145.8312491	130.3741
66.63402205	-145.830087	130.3574
66.63463406	-145.8292447	130.3819
66.63539847	-145.8294687	130.4054
66.63616387	-145.8301317	130.4099
66.63696071	-145.8305708	130.3964
66.63778014	-145.8305116	130.3949
66.63852542	-145.8296781	130.3941
66.63926078	-145.8288134	130.3724
66.64003269	-145.8289168	130.3009
66.64049388	-145.8303611	130.312
66.64067325	-145.8322891	130.3453
66.64099707	-145.8341198	130.3402
66.64167917	-145.8351604	130.3531
66.64249519	-145.8352292	130.3535
66.64331333	-145.8347866	130.3439
66.64406957	-145.8339212	130.3564
66.64478749	-145.8328869	130.3379
66.6455691	-145.83239	130.3195
66.64638025	-145.832614	130.3323
66.64718727	-145.8329809	130.3237
66.64793779	-145.8322758	130.3269
66.64847472	-145.8307126	130.2997
66.64912122	-145.8294675	130.3105
66.64991246	-145.8291432	130.2842
66.6506718	-145.8298171	130.324
66.65131188	-145.831034	130.2797
66.65182319	-145.8325861	130.2429
66.65231611	-145.8341925	130.2596
66.65281096	-145.8357665	130.2742
66.65300143	-145.837604	130.2569
66.65261172	-145.8392024	130.1901
66.65194803	-145.8402725	130.2041
66.65126592	-145.8413289	130.2672

66.65067009	-145.8426591	130.2637
66.65031686	-145.8443889	130.2374
66.65049533	-145.846243	130.2118
66.65109462	-145.8474601	130.2065
66.65180726	-145.8483047	130.205
66.65250545	-145.8492575	130.2471
66.65317796	-145.8503419	130.2319
66.65377614	-145.8516582	130.2192
66.65417793	-145.8532865	130.2197
66.65424764	-145.8551821	130.2103
66.65410253	-145.857109	130.2208
66.65397269	-145.8590624	130.2051
66.65391676	-145.8610411	130.2123
66.65395824	-145.8630395	130.2158
66.65413656	-145.864994	130.2091
66.6544436	-145.86685	130.2348
66.65476679	-145.8686906	130.2004
66.65511267	-145.8704775	130.1685
66.65553145	-145.8721427	130.202
66.65608148	-145.8735525	130.1894
66.6566545	-145.8749374	130.1915
66.65708642	-145.8765295	130.2271
66.65729762	-145.8783785	130.171
66.65740496	-145.8803408	130.1195
66.65772355	-145.8821595	130.1575
66.6584044	-145.8832188	130.1262
66.65901493	-145.8844187	130.1409
66.65918044	-145.8861489	130.1661
66.65908656	-145.8880738	130.1185
66.65939426	-145.8898356	130.0814
66.65980364	-145.891462	130.1233
66.65956017	-145.8931441	130.1165
66.65895771	-145.8942469	130.0718
66.65831409	-145.8953098	130.1146
66.65780074	-145.8968342	130.0576
66.65785194	-145.8987419	130.0929
66.65833653	-145.9003166	130.0445
66.6590409	-145.9012322	130.1157
66.65986126	-145.9010945	130.2632
66.66059283	-145.9001382	130.185
66.66110903	-145.8984997	130.1487

66.66148928	-145.8965677	130.202
66.66190731	-145.8947729	130.1212
66.66263986	-145.8946297	130.1271
66.66317477	-145.8959883	130.1328
66.66338207	-145.8978904	130.1162
66.66341473	-145.8998805	130.1273
66.66337488	-145.9018821	130.1491
66.6635779	-145.9038554	130.0443
66.66405315	-145.9054821	130.1054
66.66456768	-145.9070286	130.1166
66.6650209	-145.9087335	130.091
66.66541315	-145.9105703	130.0727
66.66570223	-145.9125104	130.0739
66.66575924	-145.9145207	130.0836
66.66539793	-145.9160605	130.078
66.66466565	-145.9165135	130.1265
66.66386718	-145.9162839	130.0836
66.66309917	-145.9167726	130.0429
66.66272461	-145.9184642	130.0263
66.66271511	-145.9204327	130.0808
66.66279292	-145.9223442	130.0429
66.66257387	-145.9241735	130.039
66.66190587	-145.924771	130.0306
66.66119892	-145.9255699	130.0765
66.66097108	-145.9273682	129.9783
66.66158255	-145.9284238	129.9483
66.66238362	-145.9289548	130.0203
66.66316664	-145.9297702	130.0564
66.66389273	-145.9308342	129.9751
66.6645889	-145.9320149	129.9709
66.66529171	-145.9331816	129.9108
66.66601662	-145.9342084	129.9045
66.66675296	-145.9352026	129.9101
66.66746118	-145.9363109	129.8992
66.6680006	-145.9378559	129.8752
66.66814235	-145.9397773	129.9035
66.66774512	-145.9412073	129.8966
66.66700716	-145.9405037	129.8424
66.6662856	-145.9392185	129.7974
66.66544381	-145.9385615	129.8295
66.66459828	-145.9387194	129.7363

66.66382628	-145.9396694	129.7653
66.66311493	-145.94087	129.7452
66.66246017	-145.9422633	129.7827
66.66178475	-145.9435801	129.757
66.66108592	-145.9447604	129.6773
66.66032193	-145.9456589	129.7348
66.65950669	-145.9465735	129.6847
66.6586687	-145.9474426	129.7075
66.65783848	-145.9470378	129.6212
66.65722378	-145.9454387	129.514
66.65655847	-145.943953	129.5482
66.65570959	-145.9433289	129.5906
66.65481636	-145.943592	129.5261
66.65416088	-145.9450008	129.4224
66.65353707	-145.946581	129.4757
66.65281441	-145.9479534	129.4492
66.65197181	-145.9487368	129.4154
66.65110994	-145.9484295	129.3926
66.65036131	-145.9473551	129.3658
66.64987049	-145.9456169	129.3681
66.64969887	-145.9435023	129.3518
66.64979792	-145.9413321	129.3459
66.64994286	-145.9390977	129.3669
66.64998762	-145.9367616	129.3493
66.6498601	-145.9344403	129.3426
66.64937686	-145.932701	129.2396
66.64862589	-145.9318972	129.2682
66.6478253	-145.9321749	129.2628
66.64708215	-145.9330923	129.2323
66.64637796	-145.9341794	129.186
66.64587417	-145.9358607	129.2156
66.64540952	-145.9376041	129.2409
66.64498799	-145.939355	129.2605
66.64459013	-145.9411268	129.3025
66.64419234	-145.9428766	129.1994
66.64377207	-145.9446055	129.1874
66.64333551	-145.946356	129.2493
66.64283076	-145.9480749	129.1783
66.64240594	-145.9499635	129.1631
66.64198089	-145.9517608	129.175
66.64160968	-145.9535624	129.1438

66.64138199	-145.9554904	129.2216
66.64120639	-145.9575162	129.138
66.64108776	-145.9596042	129.197
66.64103105	-145.9617261	129.1208
66.64102249	-145.9638196	129.0702
66.64097252	-145.9659019	129.0849
66.64088115	-145.967997	129.1237
66.64070877	-145.9700145	129.0876
66.64048786	-145.9719822	129.0219
66.6401595	-145.9737928	129.0666
66.63967343	-145.9753403	129.0321
66.63907687	-145.9766339	128.9998
66.63833233	-145.9773874	129.1132
66.63751057	-145.9774608	129.002
66.63671582	-145.9768763	128.9177
66.6359726	-145.9759461	129.0287
66.63522895	-145.9749148	129.0374
66.6344584	-145.9739907	129.0376
66.63364455	-145.973366	129.0253
66.63281924	-145.973573	128.9485
66.63209795	-145.9745794	128.9698
66.63155129	-145.9760704	128.9458
66.63119788	-145.9779069	128.9137
66.63104109	-145.9798922	128.9357
66.63100063	-145.9819595	128.9174
66.63103757	-145.9840378	128.9557
66.63122347	-145.9860979	128.9321
66.63158932	-145.9880426	128.9043
66.63212026	-145.9896996	128.9212
66.63275311	-145.9910556	128.9072
66.63345818	-145.9922684	128.9185
66.63422394	-145.9933325	128.878
66.63504281	-145.9941628	128.8821
66.63583384	-145.9950264	128.907
66.63651942	-145.9962966	128.8214
66.63712394	-145.997883	128.8052
66.63767506	-145.999608	128.8667
66.63827731	-146.0012312	128.8028
66.63902556	-146.0024005	128.7366
66.63986232	-146.0029989	128.7572
66.64071988	-146.0032804	128.7897

66.64157651	-146.0036251	128.7728
66.64232517	-146.0045973	128.7826
66.64266088	-146.006419	128.6925
66.64244732	-146.0082924	128.7001
66.64200629	-146.0100251	128.6796
66.64138922	-146.0114803	128.6545
66.64073937	-146.0126846	128.5986
66.64007459	-146.0138346	128.5727
66.6394256	-146.0149629	128.6148
66.63892018	-146.0164245	128.6009
66.63874269	-146.0178299	128.616
66.63862318	-146.0192112	128.5447
66.63812813	-146.0208972	128.4787
66.63773476	-146.0227899	128.4728
66.63792406	-146.0249835	128.4432
66.63790841	-146.0269563	128.4497
66.63745217	-146.0283664	128.4898
66.63667115	-146.028365	128.4118
66.63587743	-146.0277531	128.2981
66.63503922	-146.0271048	128.2348
66.63420725	-146.0263692	128.2988
66.63334267	-146.0260829	128.32
66.63258585	-146.0269512	128.2588
66.63216466	-146.0287119	128.0953
66.63245833	-146.0305649	128.1296
66.63319994	-146.0316363	128.0827
66.63407093	-146.0321273	128.0655
66.63498487	-146.0319502	128.0002
66.63592426	-146.0316715	127.9739
66.63686511	-146.0314417	127.9997
66.63777365	-146.031884	127.9092
66.6384675	-146.0333437	127.8656
66.63894454	-146.0351781	127.8431
66.63926279	-146.0371707	127.81
66.63945344	-146.0391791	127.756
66.63945617	-146.0412606	127.7344
66.63929916	-146.0433533	127.6656
66.63902176	-146.0452964	127.6471
66.63870926	-146.0471728	127.6451
66.63845628	-146.0490922	127.7627
66.6381377	-146.0510058	127.6287

66.63798898	-146.0530642	127.5229
66.63789037	-146.0551089	127.5603
66.63785997	-146.057219	127.4499
66.6377314	-146.0593237	127.5436
66.63734757	-146.0611687	127.567
66.63675261	-146.06234	127.5754
66.63606071	-146.0632058	127.5213
66.63533625	-146.0641268	127.5164
66.63472434	-146.0654838	127.5189
66.63425255	-146.0671699	127.4765
66.63404037	-146.0691911	127.3963
66.63405607	-146.0713615	127.3554
66.63421476	-146.07348	127.3698
66.6344375	-146.0755579	127.3951
66.63474627	-146.0775924	127.3136
66.63500769	-146.0796552	127.2788
66.63532938	-146.0815189	127.2843
66.63582581	-146.0830286	127.2416
66.63643504	-146.0843258	127.1797
66.63710661	-146.0854077	127.1182
66.637815	-146.086255	127.0052
66.63850873	-146.0871077	127.0362
66.63915982	-146.0880078	127.0378
66.63978926	-146.089072	127.045
66.64036199	-146.0903249	126.9758
66.64090142	-146.0917649	127.021
66.64136215	-146.093446	127.0262
66.64165403	-146.0953388	127.0058
66.64174536	-146.0973749	127.0114
66.64166799	-146.0993824	127.0208
66.64146046	-146.1013235	126.9487
66.64111445	-146.1031053	126.9742
66.6406306	-146.1046487	127.0151
66.63998857	-146.1058009	126.9651
66.63929668	-146.106772	126.9124
66.63855897	-146.1074367	126.9025
66.63781171	-146.1081629	126.9156
66.63707555	-146.1089272	126.919
66.63634146	-146.1096521	126.8092
66.63560475	-146.1104097	126.8642
66.63485784	-146.1112738	126.8509

66.63407131	-146.1123755	126.8374
66.63324676	-146.1133693	126.7913
66.63238498	-146.1140264	126.7669
66.63150697	-146.1144915	126.7393
66.63059016	-146.1147249	126.7689
66.62963066	-146.1146167	126.7726
66.62867594	-146.1142724	126.6919
66.62771154	-146.1138785	126.6815
66.62675047	-146.11335	126.6536
66.62578994	-146.1128612	126.6554
66.62484839	-146.1124526	126.6639
66.62393382	-146.1121098	126.6682
66.6230293	-146.1120246	126.6305
66.6221258	-146.1121992	126.6225
66.62128665	-146.1128919	126.5972
66.62055795	-146.1140216	126.5122
66.62003981	-146.1157098	126.5678
66.61977847	-146.1177521	126.592
66.61967019	-146.119864	126.5475
66.61963461	-146.1219939	126.5898
66.61973406	-146.1241171	126.5402
66.62002277	-146.1261149	126.4938
66.62040154	-146.1280566	126.5561
66.6208285	-146.1299759	126.5534
66.62128537	-146.1317789	126.514
66.62164242	-146.1336703	126.4865
66.62180971	-146.1356991	126.4885
66.62177709	-146.1378699	126.4723
66.62166551	-146.1400708	126.409
66.62144082	-146.1422157	126.5022
66.6211191	-146.1442324	126.4303
66.62075843	-146.1461894	126.4538
66.62036775	-146.1481215	126.3227
66.62008975	-146.1498805	126.5345
66.61991361	-146.151497	126.3799
66.61982755	-146.1531079	126.3284
66.61978304	-146.1547806	126.4481
66.61971389	-146.1564624	126.4556
66.61967476	-146.1582281	126.4782
66.61967811	-146.1600485	126.5017
66.61957522	-146.1616761	126.4294

66.61915876	-146.163001	126.468
66.61866404	-146.1640325	126.39
66.61823236	-146.1654927	126.4175
66.61799651	-146.167445	126.3802
66.61806833	-146.1695284	126.4019
66.61849045	-146.1713163	126.3157
66.61893799	-146.1730327	126.2956
66.6194509	-146.1745933	126.3032
66.6199351	-146.1761992	126.2671
66.62046171	-146.1777027	126.2943
66.62109571	-146.1788974	126.305
66.62177609	-146.1799931	126.2833
66.62251464	-146.1807443	126.3202
66.62329342	-146.1811676	126.2952
66.62408506	-146.181489	126.3181
66.62487137	-146.1818497	126.2812
66.62563324	-146.1823626	126.2393
66.62637492	-146.1831084	126.2844
66.62702024	-146.1841784	126.2821
66.6275097	-146.1856951	126.2393
66.62771407	-146.1875698	126.2301
66.62752614	-146.1894222	126.239
66.62701058	-146.1908142	126.2577
66.62625216	-146.1911816	126.2094
66.62538172	-146.1912731	126.0994
66.62447136	-146.1916235	126.0682
66.62356855	-146.1915257	126.0713
66.6226578	-146.1913143	126.0457
66.62175703	-146.1909318	125.9576
66.62086656	-146.1904927	125.9645
66.61996822	-146.190308	125.8889
66.61910079	-146.1904107	125.8864
66.61827484	-146.1907747	125.8009
66.61745127	-146.191339	125.8376
66.61662509	-146.1917503	125.8683
66.61577041	-146.1917962	125.7904
66.61493701	-146.1913906	125.8144
66.61412537	-146.1907649	125.7895
66.61335894	-146.1898548	125.7033
66.61263952	-146.1886192	125.7222
66.61196797	-146.1872133	125.7639

66.61133416	-146.1856665	125.7427
66.61072188	-146.1840455	125.7272
66.61010022	-146.1825227	125.7356
66.60944864	-146.1811728	125.6854
66.60869589	-146.1802234	125.6964
66.60787458	-146.1801566	125.6301
66.60713541	-146.1810476	125.6438
66.60661438	-146.1826122	125.5983
66.60645063	-146.1845928	125.6321
66.60658866	-146.1865924	125.5979
66.60683613	-146.1885384	125.5607
66.6072491	-146.1903527	125.5186
66.6079046	-146.1917026	125.5343
66.60859906	-146.1930504	125.4334
66.60918925	-146.1948091	125.4159
66.60967393	-146.1967712	125.4289
66.61003042	-146.1988899	125.4162
66.61036923	-146.2010087	125.4192
66.61064415	-146.2031631	125.4065
66.61092258	-146.2052975	125.3933
66.61120861	-146.2074247	125.4213
66.61150229	-146.2095337	125.3545
66.61171634	-146.2117097	125.3076
66.61190602	-146.2138768	125.3298
66.61206395	-146.2160585	125.3032
66.61217957	-146.2182552	125.301
66.61223222	-146.2203973	125.2912
66.6121064	-146.2224989	125.2107
66.61186289	-146.2245815	125.2035
66.61148105	-146.2265436	125.1653
66.61098615	-146.2283458	125.1437
66.61042737	-146.2300754	125.1118
66.60978644	-146.2316015	125.104
66.60904078	-146.2328526	125.0572
66.6082326	-146.2338779	125.0982
66.60741017	-146.2348022	125.1192
66.60664618	-146.2359972	125.0727
66.60595386	-146.237419	125.0527
66.60532819	-146.2390038	125.089
66.60502731	-146.2411707	125.0931
66.60500821	-146.2434885	125.0206

66.60526958	-146.245668	124.9995
66.6056522	-146.2477158	125.0512
66.60613189	-146.249602	125.0453
66.60670915	-146.2512933	125.0225
66.60735424	-146.2528252	125.0166
66.60802707	-146.2542957	125.0205
66.6087462	-146.2556011	125.0442
66.60954572	-146.2565919	124.9931
66.61042447	-146.2573034	124.9554
66.6113291	-146.2579082	124.9511
66.61226421	-146.2582005	124.9663
66.61320639	-146.2581379	124.871
66.61410639	-146.2575963	124.884
66.61494334	-146.2567574	124.8589
66.61577234	-146.2558069	124.7848
66.61659134	-146.2546752	124.7857
66.61743865	-146.253592	124.7892
66.61830187	-146.2527905	124.7623
66.61918027	-146.2525673	124.7215
66.62002312	-146.2532452	124.6961
66.62066971	-146.2547037	124.7161
66.62103728	-146.256639	124.6571
66.62112786	-146.2587633	124.6292
66.62088007	-146.2607515	124.5963
66.62031843	-146.2621554	124.5697
66.6194587	-146.2616862	124.5126
66.61852442	-146.2609384	124.4273
66.61761106	-146.2605561	124.4598
66.61671205	-146.2608583	124.4315
66.61591693	-146.2620029	124.3858
66.61531733	-146.2637877	124.3703
66.61494766	-146.2659274	124.3221
66.61458994	-146.2680404	124.2609
66.61422746	-146.2700833	124.2629
66.61380553	-146.2719155	124.2585
66.61330749	-146.2738224	124.2273
66.61266671	-146.2754204	124.1409
66.61190623	-146.2766616	124.1804
66.61106231	-146.2774519	124.1818
66.61018324	-146.2777543	124.136
66.60931657	-146.278235	124.1135

66.60848746	-146.2790186	124.1595
66.60770415	-146.2801098	124.2258
66.60698909	-146.2814614	124.1451
66.60637325	-146.2830212	124.0797
66.60588314	-146.2848494	124.054
66.60561302	-146.2869411	124.0603
66.60550538	-146.2891187	124.0272
66.60555082	-146.2913291	124.0633
66.605764	-146.2935273	124.015
66.60603499	-146.295726	123.9561
66.60639876	-146.2978444	123.9565
66.60679389	-146.2999348	123.9781
66.60725391	-146.3019831	123.9485
66.60774895	-146.3039902	123.934
66.60835425	-146.3058211	123.8802
66.60903813	-146.3074081	123.9417
66.60974022	-146.3087209	123.8536
66.61035996	-146.3102	123.7867
66.6108974	-146.3118972	123.8525
66.61122775	-146.3139053	123.7759
66.61145752	-146.3160298	123.7989
66.61162489	-146.3181839	123.8037
66.61173604	-146.3203273	123.7863
66.61181258	-146.3224778	123.7934
66.61175825	-146.3247881	123.685
66.61183915	-146.3270969	123.6357
66.61190919	-146.3293468	123.6327
66.61173953	-146.3314182	123.661
66.61142864	-146.3334235	123.5821
66.61107889	-146.3353418	123.5654
66.61072611	-146.3372504	123.5125
66.61036629	-146.3391479	123.5821
66.60996669	-146.3410806	123.5252
66.60951319	-146.3430417	123.4475
66.60905008	-146.3449516	123.4591
66.6085924	-146.3468721	123.5179
66.60806836	-146.3487052	123.4046
66.60743164	-146.3503884	123.3718
66.6066839	-146.3517707	123.2692
66.60591716	-146.3528341	123.277
66.60530804	-146.353431	123.3142

66.60464606	-146.353977	123.2682
66.60395506	-146.3544729	123.3086
66.6032756	-146.3550374	123.4039
66.60260924	-146.3556435	123.247
66.60200802	-146.3561753	123.3241
66.60141228	-146.3566479	123.252
66.60081869	-146.3572021	123.2616
66.60022602	-146.3578295	123.1815
66.59966044	-146.3584366	123.2092
66.59909948	-146.359017	123.2102
66.59851643	-146.3595098	123.0352
66.59791994	-146.359841	123.1666
66.59731592	-146.3600443	123.2058
66.59671592	-146.3601436	123.2123
66.59610476	-146.3602165	123.1957
66.59550616	-146.3601445	123.2197
66.59491901	-146.3599129	123.3718
66.59434742	-146.3596046	123.3144
66.59378659	-146.3593006	123.3091
66.59323143	-146.3589813	123.2347
66.59269542	-146.3586389	123.2407
66.59215308	-146.3583424	123.2062
66.59160108	-146.3580459	123.1674
66.59103339	-146.3577556	123.2241
66.59043207	-146.3575179	123.2425
66.58981781	-146.3572153	123.1247
66.58920614	-146.3569185	123.207
66.58859369	-146.3566205	123.0971
66.58797742	-146.3563705	123.1839
66.58729461	-146.3561931	123.1676
66.58656167	-146.3560407	123.0905
66.58582675	-146.3559432	123.105
66.58507267	-146.3558669	122.9746
66.58431212	-146.3557279	123.1053
66.58357693	-146.3556065	123.0431
66.58280782	-146.3554769	123.1129
66.58207286	-146.3554542	123.1633
66.58129934	-146.3554595	123.059
66.58046447	-146.3555546	122.9826
66.57962531	-146.3561287	122.8579
66.57878714	-146.3566875	123.0071

66.57796916	-146.3571802	122.9401
66.57716661	-146.3577398	122.9014
66.5763686	-146.3583338	122.9685
66.57562118	-146.3589266	122.831
66.57496405	-146.3594856	122.8412
66.57445279	-146.3599781	123.0378
66.57399523	-146.3604515	122.8316
66.57353747	-146.3609353	122.8739
66.57313404	-146.3615236	122.8713
66.57266799	-146.3621764	122.9109
66.57211734	-146.3629189	122.8455
66.57167062	-146.363709	122.7925
66.57126421	-146.3647922	122.841
66.57090012	-146.3659986	122.5972
66.57058283	-146.3673188	122.8053
66.57038547	-146.3688175	122.8696
66.57021213	-146.3703572	122.8057
66.57007476	-146.3719249	122.8553
66.56998945	-146.3735046	122.8396
66.56993382	-146.3750848	122.7943
66.56991574	-146.3766599	122.8203
66.56992134	-146.3782384	122.7954
66.56993834	-146.3798152	122.8229
66.56995621	-146.3815305	122.8082
66.57000084	-146.3835518	122.8049
66.57007978	-146.3856545	122.9051
66.5700608	-146.3877329	122.7932
66.56985501	-146.3897257	122.7851
66.56959152	-146.391609	122.7061
66.56923052	-146.3933348	122.7134
66.56887193	-146.3950083	122.7355
66.568513	-146.3966422	122.7792
66.56816189	-146.3981816	122.6816
66.56785921	-146.3997723	122.6156
66.56755706	-146.4011513	122.7494
66.56732238	-146.4024092	122.7252
66.56710402	-146.4036472	122.6209
66.56688363	-146.4049429	122.7447
66.56663496	-146.40621	122.7599
66.56638882	-146.4074627	122.7518
66.56615278	-146.4087261	122.7519

66.56593994	-146.4100301	122.7243
66.5657295	-146.4113435	122.7636
66.56556022	-146.4126516	122.661
66.56542448	-146.4139753	122.6486
66.56532707	-146.4153157	122.6935
66.56518091	-146.4167227	122.6454
66.56497978	-146.4180824	122.7172
66.56482648	-146.4194429	122.6536
66.56470381	-146.4208093	122.7239
66.56468131	-146.4222628	122.7236
66.5646981	-146.423784	122.6141
66.56471263	-146.4252766	122.6433
66.56477591	-146.4269051	122.7132
66.5648637	-146.4287756	122.6927
66.56502432	-146.4308989	122.5858
66.56518373	-146.433178	122.6371
66.56534978	-146.4354402	122.6105
66.56550285	-146.4376756	122.6152
66.5656604	-146.4399079	122.6311
66.56577063	-146.4419658	122.6363
66.56583028	-146.4438652	122.5607
66.56576565	-146.4458772	122.5743
66.56563958	-146.4475418	122.5585
66.56550446	-146.4489276	122.6105
66.56532307	-146.4503007	122.6124
66.56509864	-146.4516308	122.5376
66.56500538	-146.4527755	122.463
66.56511334	-146.4535577	122.4896
66.56527502	-146.4539355	122.5963
66.5653597	-146.4541066	122.5833
66.56539478	-146.4542572	122.4949
66.5654151	-146.4543746	122.6151
66.56543112	-146.4544363	122.5964
66.56544317	-146.4544596	122.6
66.56545369	-146.4544788	122.5771
66.56545763	-146.4544852	122.636
66.56546097	-146.454485	122.5692
66.56547089	-146.4544745	122.5437
66.56550856	-146.4542925	122.5376
66.56542855	-146.4540607	122.63
66.56519832	-146.4541922	122.5156

66.56492547	-146.4549624	122.4355
66.56459891	-146.4558974	122.5608
66.56424335	-146.4567898	122.5987
66.56391017	-146.4575309	122.4187
66.56357729	-146.4582457	122.4729
66.56323589	-146.4589308	122.612
66.56288634	-146.4595691	122.6751
66.56252469	-146.4601752	122.493
66.56214682	-146.4607576	122.572
66.56179732	-146.4612425	122.4731
66.56146467	-146.461735	122.5131
66.56113079	-146.4622383	122.5285
66.56075557	-146.4627742	122.6216
66.5604083	-146.4632713	122.5042
66.5600477	-146.4636946	122.451
66.55966008	-146.4640701	122.5265
66.55920807	-146.464418	122.5295
66.55870884	-146.4647153	122.5756
66.55818942	-146.4650366	122.6187
66.55764568	-146.4652867	122.6103
66.55706243	-146.4655174	122.5431
66.55645567	-146.46564	122.4834
66.55584586	-146.465676	122.4859
66.5552474	-146.4656324	122.4642
66.55464213	-146.4654874	122.534
66.55400027	-146.4652609	122.6179
66.55332483	-146.465061	122.5769
66.5526502	-146.4647802	122.5256
66.55195199	-146.4643889	122.56
66.55130231	-146.4639578	122.5421
66.55077932	-146.4634321	122.5679
66.55071867	-146.4621271	122.5222
66.55120633	-146.4611021	122.5881
66.55169256	-146.4602995	122.5897
66.55210901	-146.4592837	122.5501
66.55241399	-146.4586639	122.4974
66.55278974	-146.4579983	122.6261
66.5531992	-146.4570646	122.5972
66.55363413	-146.4558073	122.5745
66.55402201	-146.4542747	122.5828
66.55428277	-146.4526758	122.6891

66.55456354	-146.4511762	122.6916
66.55484299	-146.4497081	122.5744
66.55510792	-146.4482489	122.6645
66.55530525	-146.4466793	122.6187
66.55537847	-146.4450783	122.6679
66.55533157	-146.4434907	122.6815
66.55517106	-146.44193	122.65
66.55496721	-146.4403904	122.6193
66.55470149	-146.4389279	122.5964
66.55441002	-146.4374847	122.6716
66.55411194	-146.4358992	122.6982
66.55387308	-146.4342069	122.6027
66.55359442	-146.4325894	122.6264
66.55328531	-146.4310243	122.6655
66.55296333	-146.4295023	122.6623
66.55259693	-146.4280449	122.6691
66.5521832	-146.426688	122.6986
66.55175599	-146.425382	122.6512
66.55133521	-146.4240679	122.6704
66.55091933	-146.4227746	122.6795
66.5504995	-146.421458	122.7433
66.55003985	-146.4201666	122.6793
66.54959302	-146.4188228	122.5942
66.54923417	-146.4173624	122.6979
66.5488306	-146.4160195	122.6427
66.54838925	-146.4148208	122.724
66.54800491	-146.413527	122.81
66.5476407	-146.4122428	122.6951
66.5472936	-146.4109331	122.7609
66.5469165	-146.4097066	122.7355
66.54653432	-146.4084966	122.7304
66.54614392	-146.4072918	122.7128
66.54577563	-146.4060238	122.7735
66.54536817	-146.4047784	122.7435
66.5449676	-146.4034594	122.8199
66.54461635	-146.4020946	122.7656
66.54428174	-146.4007124	122.7978
66.54401359	-146.3992749	122.8193
66.5437951	-146.3978015	122.8628
66.5436264	-146.3962737	122.8055
66.54349309	-146.3947271	122.8041

66.54338645	-146.3931411	122.8433
66.54333427	-146.3915561	122.8341
66.54333938	-146.3899769	122.8416
66.54341205	-146.3884059	122.9295
66.54355244	-146.386881	122.7993
66.54380795	-146.3854775	122.8269
66.54403295	-146.3840473	122.9103
66.54423927	-146.3826048	122.9039
66.54441339	-146.3811314	122.9131
66.54461299	-146.3796457	122.9209
66.54485246	-146.3781708	122.9953
66.54498205	-146.3766542	122.9761
66.5450179	-146.3751625	122.9551
66.54500872	-146.3736859	122.9571
66.54496056	-146.3722174	122.9463
66.54491181	-146.3707674	122.9342
66.54484478	-146.3693298	123.011
66.54472595	-146.3679087	123.0367
66.54470721	-146.3664905	123.0293
66.54467342	-146.3651173	123.0427
66.54453246	-146.3638295	123.1212
66.54432357	-146.3625515	123.0871
66.54405047	-146.3612426	123.1364
66.54361684	-146.3602431	123.2429
66.54303147	-146.3605009	123.1398
66.54236985	-146.3616449	123.2579
66.54160378	-146.3631216	123.2702
66.5408229	-146.3646611	123.1474
66.5400097	-146.3661639	123.0127
66.53916344	-146.3675435	123.0804
66.5382877	-146.3688981	123.0448
66.53741209	-146.3702746	122.983
66.53653148	-146.3717076	122.9362
66.53565768	-146.3732083	122.9601
66.53483598	-146.3748734	122.8889
66.53408632	-146.3766931	122.9043
66.5334056	-146.3786091	122.7928
66.53279814	-146.3806477	122.8655
66.53227374	-146.3827761	122.8389
66.53182688	-146.3849668	122.8118
66.53142365	-146.3872368	122.7227

66.53110899	-146.3895895	122.6613
66.53084385	-146.391947	122.652
66.53064537	-146.3942712	122.6237
66.53046628	-146.3965564	122.6967
66.53030889	-146.3988756	122.5678
66.53016474	-146.4013024	122.536
66.53009676	-146.4037736	122.5473
66.5300493	-146.4063041	122.5362
66.52994476	-146.4089012	122.5666
66.52990091	-146.4114874	122.5011
66.52987148	-146.4140311	122.4887
66.52983774	-146.4165489	122.5474
66.5297711	-146.4190102	122.5259
66.52970274	-146.421411	122.4897
66.52965551	-146.4237946	122.5463
66.529622	-146.4261976	122.5176
66.52960693	-146.4286134	122.394
66.52957873	-146.4309787	122.4604
66.52952706	-146.4333517	122.4274
66.52944811	-146.4357522	122.317
66.52936504	-146.4381412	122.2817
66.52919763	-146.4404769	122.2686
66.52890623	-146.4427293	122.2617
66.52861975	-146.4449783	122.2799
66.52832755	-146.4472229	122.2496
66.52799956	-146.4494236	122.2259
66.52761185	-146.4515434	122.2225

66.52718991	-146.453616	122.1572
66.52671738	-146.4556151	122.2067
66.52623196	-146.4576124	122.1956
66.52569216	-146.4595084	122.1874
66.52509746	-146.4613006	122.1329
66.52450519	-146.4631018	122.1446
66.52386401	-146.4648588	122.1299
66.52318783	-146.4665979	122.1571
66.52249501	-146.4683014	122.0569
66.52173104	-146.469879	122.0606
66.52095572	-146.4714952	122.0432
66.52017434	-146.4730691	122.0044
66.5194016	-146.4746665	122.0185
66.51865562	-146.4762747	121.9775
66.51797245	-146.4779877	121.9057
66.51732342	-146.4797711	121.8848
66.51667479	-146.4815874	121.9365
66.51604443	-146.4834434	121.9537
66.51541327	-146.4853073	121.8906
66.51476255	-146.4871296	121.8526
66.51411265	-146.4889711	121.8069
66.51345366	-146.4907862	121.8049
66.5127922	-146.4925918	121.7233
66.51223294	-146.4945613	121.6731
66.51176838	-146.4961723	121.6446
66.51134258	-146.4976876	121.7031

CHAPTER 4

Advancing field-based GNSS surveying for validation of remotely sensed water surface elevation products

4.1 Abstract

Surface water resources are vital for biological, physical, and socioeconomic processes on the Earth's surface, yet knowledge of storage and flux across broad spatial scales is lacking. To help address this knowledge gap, new remote sensing technologies such as the forthcoming Surface Water and Ocean Topography (SWOT) satellite (launch 2021) and its experimental airborne prototype AirSWOT are being developed to map water surface elevation (WSE) and slope (WSS) of the world's rivers, lakes, and reservoirs. However, the vertical accuracies of these novel technologies are largely unverified thus standard and repeatable field procedures to validate remotely sensed WSE and WSS are needed. To that end, we designed, engineered and operationalized a Water Surface Profiler (WaSP) system that efficiently and accurately surveys WSE and WSS in a variety of surface water environments using Global Navigation Satellite Systems (GNSS) time-averaged measurements with Precise Point Positioning (PPP) corrections. Here, we present WaSP construction, deployment, and a data processing workflow. We demonstrate WaSP data collections from repeat field

deployments in the North Saskatchewan River and three prairie pothole lakes near Saskatoon, Saskatchewan, Canada. We find that WaSP reproducibly measures WSE and WSS with vertical accuracies similar to standard field survey methods (WSE RMSD \sim 8 cm, WSS RMSD \sim 1.3 cm/km), and that repeat WaSP deployments accurately quantify water level changes (RMSD \sim 3 cm). Collectively, these results suggest that WaSP is a low cost, easily-deployed, self-contained system with sufficient accuracy for validating the decimeter level expected accuracies of SWOT and AirSWOT. We conclude by discussing the utility of WaSP for validating airborne and spaceborne WSE mappings, present 63 WaSP in-situ lake WSE measurements collected for NASA's Arctic Boreal and Vulnerability Experiment (ABOVE).

4.2 Introduction

Freshwater resources in rivers, lakes, wetlands, and reservoirs are vital for biological, physical, and socioeconomic processes on the earth's surface (Margulis, 2017). To enhance understanding of such resources, remote sensing technologies have been developed and deployed to quantify volumetric change in terrestrial inland waters via simultaneous mappings of inundation extent, water surface elevation (WSE), and water surface slope (WSS) (Altenau et al., 2019; Bates et al., 2006; Crétaux et al., 2016; Kiel et al., 2006; Lee et al., 2010; LeFavour and Alsdorf, 2005; Papa et al., 2010;

Smith, 1997; Tuozzolo et al., 2019). Despite such efforts, knowledge of freshwater storage and flux outside of gauged river basins and at large spatial scales is lacking (Alsdorf et al., 2007; Alsdorf and Lettenmaier, 2003).

To help address the need for better observation of Earth's surface waters, the forthcoming Surface Water and Ocean Topography (SWOT) satellite mission (launch 2021) will repeatedly map WSE and WSS in terrestrial inland waters at sub-monthly repeat intervals using Ka-band radar interferometry (Biancamaria et al., 2016; Durand et al., 2010; see: <https://swot.jpl.nasa.gov/>). In preparation for SWOT, NASA developed AirSWOT as an airborne validation instrument that also uses Ka-band radar interferometry to map WSE and WSS (Altenau et al., 2017, 2019; Pitcher et al., 2019; Tuozzolo et al., 2019). Key science requirements for SWOT include mapping WSE to at least 10 cm accuracy (all accuracies 1σ) for open water areas >1 km², 25 cm or better for open water areas 0.0625 to 1 km², and mapping WSS to at least 1.7 cm/km accuracy for 10 km river reaches 100 m wide or wider (Rodriguez, 2016). However, the ability of SWOT to meet these accuracies remains theoretical, so a standard and repeatable field method that surveys WSE and WSS with accuracies sufficient to validate both AirSWOT and SWOT is needed. To that end, we developed, tested, and operationalized a Water Surface Profiler (WaSP) system that uses ruggedized Global Navigation Satellite Systems (GNSS)

time-averages measurements with Precise Point Positioning (PPP) corrections to accurately map WSE and WSS.

WaSP also helps overcome certain shortcomings associated with traditional field-based methods for measuring WSE and WSS. For example, traditional in situ measurements obtain WSE at a single location (i.e. at a gauging station), typically in a stable, single-thread river channel cross-section for the purpose of establishing an empirical rating curve relating WSE (i.e. river stage from a permanent water level recorder) to discharge (Q). Broad-scale estimates of river WSS, in turn, are commonly calculated by interpolating WSE between gauging stations, or estimated from static topographic maps (e.g. Durand et al., 2014; Yamazaki et al., 2017). A limitation of this approach is that it requires installation of costly permanent equipment and provides spatially limited data at a small number of point locations.

Such point-based measurement approaches often fail to capture the range of WSE and WSS complexity, for example riffle-pool sequences (e.g. Jowett, 1993; Montgomery et al., 1999), WSE super-elevation around channel meander bends (e.g. Dietrich et al., 1979), or varying WSE and WSS through anabranching rivers and complex river/lake/wetland systems. Single-point WSE measurements in lakes do not capture hydrologic events like seiches, which are important for lake productivity (Ostrovsky et al., 1996) and regulating tributary flows (e.g. Prowse et al., 2006).

Furthermore, at a global scale, lakes are sparsely instrumented, particularly in comparison to the total number of lakes on the earth's surface. Spatially dense mappings from airborne and spaceborne remote sensing technologies hold promise to overcome these and other limitations of point-based WSE measurements (Alsdorf et al., 2003, 2007).

From a remote sensing validation perspective, point-based measurements of WSE can be equally problematic. First, the sparseness of point measurements limits the size of validation datasets. In rivers, non-contact stage gauges are commonly mounted beneath bridges, while pressure-based stage gauges are often hidden beneath foliage along channel shorelines. Such locations are not always imaged, especially by radar systems like AirSWOT and SWOT that are vulnerable to topographic and vegetation induced layover. Deployed arrays of static, near-shore surveys require considerable effort, cost, and trained field technicians, and still only provides WSE data at a handful of fixed points.

To address these shortcomings, we propose WaSP as both a stand-alone scientific instrument to aid hydraulic understanding of rivers, lakes, and wetlands, and to serve as an operational new technology for validating airborne and spaceborne mappings of WSE and WSS. In the following sections, we first describe the WaSP system, including its construction, development, deployment techniques and a potential data processing workflow. Next, we present first results from multiple WaSP deployments in

the North Saskatchewan River and three nearby prairie pothole ponds near Saskatoon, Saskatchewan, Canada, coincident with three AirSWOT overflights on July 8, 2017, August 16, 2017 and August 17, 2017 as part of the NASA Arctic-Boreal Vulnerability Experiment (ABoVE; Miller et al., 2019). Also presented are a collection of WaSP in situ lake WSEs acquired in support of AirSWOT and other ABoVE flight assets. We conclude with a general discussion of WaSP applications for surface water studies, ABoVE research, and citizen science.

4.3 Methods

4.3.1 WaSP Description

The WaSP system (Figure 4-1) is deployed on the free water surface and is designed to accurately quantify absolute WSE relative to a known vertical datum and WSS along a defined river reach. The WaSP hardware includes 4 primary components: a GPS/GNSS receiver/antenna, a power system (Figure 4-2), a ruggedized enclosure, and a float (Figure 4-3). To survey a fixed location in a lake or pond, WaSP can be temporarily anchored in place. To longitudinally map WSE and WSS, WaSP can be towed along a transect.

4.3.1.1 GNSS receiver and antenna

WaSPs can integrate most GNSS receiver and antenna combinations, as long as the form factor of the receiver (length to width ratio) is appropriate for the waterproof case enclosure. The 2017 WaSP field surveys presented here were deployed using Trimble 5700 and R7 GPS receivers and Zephyr Geodetic antennas. WaSP has also been deployed using Septentrio PolaRX-5 GNSS receivers and Septentrio PolaNt-x MF antennas. While the form factor of these receivers is similar, the port configurations are different. The 5700/R7 has antenna and power ports on the same short end of the receiver, while the PolaRX-5 has these ports on opposite short ends. Therefore, the internal antenna cable for the PolaRX-5 is an 18-24" RG-58 with a right angle TNC connector on the receiver end, while the 5700 and R7 use a 12" RG-58 cable with straight male TNC connectors on both ends. Both Zephyr Geodetic and PolaNt-x MD antennas have TNC cable connections, so no additional modifications are required for the external antenna cable. We deployed RG-58 TNC(m)-TNC(m), 12-24" cables, with the internal and external antenna cables both connected to a female-female TNC bulkhead mounted to the pelican case enclosure.

Antennas are mounted at the highest point on WaSP to ensure maximum sky view and limit multipath interference from other components. The antenna mast is secured to the float using slit PVC pipe tensioned with a hose clamp. When possible, we recommend using small profile antennas to

limit system weight and awkwardness during deployment and to maintain a low wind profile. The standard mount for most GPS antennas is a 5/8 x 11 threaded rod or bolt. We recommend using a stopper (such as a nut) to prevent the mount from bottoming out against the antenna casing. A lock washer may also be used in high vibration environments to prevent the antenna from working loose on the mount.

4.3.1.2 Power system

WaSP power requirements depend on receiver type, receiver configuration, and temperature. For single day use with either a Trimble 5700/R7 or Septentrio PolaRX-5 receiver in Arctic and sub-Arctic environments, we recommend a 7 Ah AGM battery. In ideal conditions at peak battery health, a 7 Ah battery should run a Trimble 5700/R7 for ~22.7 h, and the Septentrio PolaRX-5 for ~26.3 to 38.2 h. The UNAVCO Polar group assumes up to 50% battery capacity reduction due to extreme cold temperatures (tested to -40 °C). Therefore, the 7 Ah battery should power the system for a full workday deployment in most conditions.

Power consumption calculations with various receiver configurations for Septentrio PolaRX-5 can be found at:

<http://kb.unavco.org/kb/article/septentrio-polarx5-power-consumption-841.html>.

For this project, with logging rates of 1 Hz and no external communications, power draw was 2.2 to 3.2 W, depending on constellation

tracking. Power consumption for the Trimble 5700/R7 was approximately 3.7 W (<http://kb.unavco.org/kb/article/trimble-r7-5700-resource-page-472.html>). The 5700/R7 can be powered either by internal Li-ion rechargeable batteries or an external power source. UNAVCO Polar experience suggests that the Li-ion batteries are unreliable in cold conditions.

The power cable was adapted for use with the battery selected. The cable was shortened, and the bare ends were terminated with tab connectors to fit the battery terminals. A 3A fuse was added in line to the positive lead as protection for the receiver from short circuits or power surges.

4.3.1.3 Enclosure

The receiver, battery, and internal cabling are housed in a Pelican 1450 case. The case is mounted on the float (Figure 4-3a) using prusik knots tied through holes drilled into plastic ribbing on the external front and back of the Pelican case (Figure 4-3b). The case is then secured using cam strap fasteners that run through the prusik and tie point handles on the float (Figure 4-3c). This fastening system enables access to the case during deployment (Figure 4-3g). Due to the sensitivity of the GNSS equipment contained within the case, good waterproofing is required, both on the seal around the lid and the holes drilled for the antenna bulkhead. This can be

accomplished with either rubber gaskets or marine-grade silicone sealant. In initial waterproofing tests, the modified case was filled with batteries and completely submerged for 5 minutes. No water intrusion was detected. It is recommended that seals be checked before deployment and replaced as needed.

Given that the WaSP system is deployed on water, it is important to ensure that weight is evenly distributed so that the system stays horizontal and the antenna remains level. The battery is the heaviest component of the system, and thus the final layout of the receiver and battery within the enclosure should be chosen to be as close to level as possible along the long axis (Figure 4-3g). This may be tested by balancing the closed Pelican case (with components) on a thin wooden rod centered along the length of the case. Any changes to either receiver or battery size should be accompanied by a new leveling test.

Components inside the case were separated and protected using Pick 'n' Pluck foam provided by Pelican. This component securing system is easily adaptable and inexpensive.

4.3.1.4 WaSP float

The WaSP float is constructed using a durable, expanded polyethylene foam float that repels water. The float is hand cut, glued, and shaped using routers with custom constructed molds. The shape includes a nose rocker,

which reduces the likelihood of the system submerging and is particularly important for towed deployments. The deck contains slanted grooves, which help drain water from the surface and results in float thicknesses varying between ~ 11 cm and ~ 13 cm. The nose is protected by a polyurethane bumper. The float widens to ~ 46 cm at ~ 23 cm from the nose. A width of ~ 46 to ~ 47 cm is maintained throughout the float before pulling into a wide swallow tail with ~ 7.5 cm tail blocks, and a ~ 30.5 cm wide and ~ 18 cm deep swallow. The float has hard rails, resulting in a step-deck with aggressive angles between the deck and the vertical side rail. The bottom is flat and has a slick-skin hot air welded finish for ruggedness and durability.

A recessed compartment for the Pelican Case 1450 is hand routed into the deck and four handles are secured through the float surrounding the corners of the Pelican Case recess (Figure 4-3a). These handles provide tie-points for securing the case to the float (Figure 4-3c) and enable easy transport. A ~ 4 cm outer-diameter slit PCV pipe is routed through the deck at both the front and rear of the Pelican Case (Figure 4-3a-b). These provide attachment points for the antenna mast (Figure 4-3d-e), anchors if deployed in lakes/ponds, or tether points if deployed in rivers (Figure 4-3f). There are also optional side-stabilizer arms with polyethylene water-wings that mount into two PVC T-brackets both secured into the foam (Figure 4-3e). We find that these stabilizers can induce an additional drag which results in increased system drift, especially in windy lake/pond surveys. Furthermore,

given the sufficiently high data precision attained without side-stabilizers, we do not recommend deploying side-stabilizers.

4.3.2 WaSP Deployment

An important consideration for WaSP accuracy is site selection. If deploying in a pond/lake, it is important that WaSP is located near the middle of the water body and away from metal docks, boats, or other obstructions (cliffs, trees, etc.). If there is a depth logger in the lake, WaSP should be placed near the instrument with the maximal clear sky view for optimal satellite trilateration.

Prior to deploying a WaSP unit in the field, it is important to enable at least one logging session on the GPS receiver and make sure that batteries are fully charged. After this, field set-up can be completed at each site in ten minutes or less. First, insert the Pelican Case into the recess in the center of the float (Figure 4-3a-b) and secure it to the float by routing each prusik through its neighboring handle and tethering prusiks on the same side of the float with a cam-strap (Figure 4-3c). Next, carefully insert the antenna mount into the PVC through-hole on the back of the float and mount the antenna to the mast (Figure 4-3d). Attach a coaxial cable to the antenna and TNC bulkhead on the Pelican Case (Figure 4-3d), then attach a drogue and/or anchor system to the float using the webbing at the back of the board and PVC-lined hole at the front of the board (Figure 4-3f).

The optimal anchor/drogue configuration is site dependent. For example, in large lakes with rough water, a Danforth-style fluke anchor may be most appropriate. In small, calm ponds a lightweight, folding Grapnel-style anchor may suffice. When towing a WaSP with a boat, a drogue is recommended for added stability.

To record GPS data, open the Pelican Case, connect the antenna cable to both the interior TNC bulkhead and the receiver, and connect the power cable first to the battery and then the receiver (Figure 4-3g). It is important to cover exposed battery terminals to prevent cable movement and/or accidental shorting. GPS receivers have model dependent protocols to initiate logging. But, ensure that the GPS receiver is powered on, observing satellites, and recording data. Then, carefully tuck cables into the box and close/secure the lid.

Lastly, place the WaSP system in the water, fix the antenna mast height and tighten it in place. Next, use a folding ruler or survey rod to measure the vertical offset between the antenna and the water surface (Figure 4-3h). We recommend measuring the vertical offset from at least three locations on the antenna and re-measuring offsets upon WaSP recovery to make sure that the offset remained constant during the survey. Note that antenna offsets can be measured relative to the antenna measurement point (AMP) or the antenna reference point (ARP), given that appropriate, antenna specific offsets are applied in data processing. Finally, we recommend taking

photos of the field site and making note of environmental conditions such as calm versus rough water as this may assist in data processing.

4.3.3 WaSP Data Processing

The first step in calculating WSE for WaSP surveys using Trimble or Septentrio receivers is to convert native GPS data to the Receiver Independent Exchange Format (RINEX) file type, a commonly used ASCII file format that can be opened with most text readers. GPS surveys recorded by Trimble 5700/R7 receivers are stored as .tXX Trimble data files, whereas surveys recorded by Septentrio receivers are stored as .SBF Septentrio Binary Format data files. With Trimble files, we use Trimble's Convert To RINEX – TBC utility Version 3.0.5.0. For Septentrio receivers, we use SBF Converter, which is part of the Septentrio RxTools software package. When a GPS survey is recorded as multiple files, we use TEQC software freely available from UNAVCO to splice files together. Pseudo syntax for executing a splicing operation in TEQC is:

[eq 1] ***teqc InputFile00.obs InputFileN.obs > OutputFile.obs***

where *InputFile00.obs* through *InputFileN.obs* is a list of input files to be spliced and *OutputFile.obs* denotes the name of the output file after splicing.

Next, the spliced RINEX file is submitted for post processing using PPP software. For the WaSP demonstration in the North Saskatchewan river and

three prairie pothole ponds presented here, the Canadian Spatial Reference System (CSRS-PPP) web application (link: <https://webapp.geod.nrcan.gc.ca/geod/tools-outils/ppp.php>) is used. Specifically, the ellipsoidal height data contained within the .pos output file, relative to the International Terrestrial Reference Frames (ITRF, as defined by the International GNSS Service at the epoch for the specific orbit ephemerides), is used. For the 63 lake surveys spanning $\sim 17^\circ$ latitude and ~ 476 m vertical elevation collected during 2017 NASA ABoVE airborne sorties, PPP solutions are calculated using GINS software (developed by the Groupe de Recherche en Géodésie Spatiale (GRGS); Marty et al., 2011) and the International GPS Service (IGS) precise GPS orbit and clock products. Resultant WSEs are given relative to the WGS84 ellipsoid. Note that the ITRF and WGS84 reference frames are quite similar, yet there are centimetric level absolute differences that spatially and temporally vary. For AirSWOT versus WaSP WSE comparisons, we do not apply a correction for the ellipsoid differences because the expected decimeter scale AirSWOT WSE uncertainty (Altenau et al., 2017; Pitcher et al., 2019) is much larger than the centimetric scale uncertainty associated with the different ellipsoids.

For the North Saskatchewan river data, we also convert from ellipsoidal heights (h) to orthometric heights (H), as:

$$[\text{eq 2}] \quad \mathbf{H} \approx \mathbf{h} - \mathbf{n}$$

where n is the height of the EGM96 geoid. Conversion from ellipsoidal to orthometric heights is particularly important for calculating WSS from longitudinal river surveys and in large, low-gradient lakes.

For lakes and ponds, the latitude, longitude (Figure 4-4a), and height (Figure 4-4b) data series from PPP results are analyzed, the field measured offset between the antenna and the water surface is applied and the data series is manually subset to a period in which WaSP is in the water and relatively stable (orange circles, Figure 4-4a-b). Pseudo syntax for clipping or time windowing in TEQC is:

[eq 3] *teqc + st YYMMDDHHMMSS.ssss + dh * "InputFile.obs" >*
OutputFile.obs

where +st denotes the desired survey start time, YY is the last two digits of the start year and MM, DD, HH, MM, SS are the start month, day, hour, minute, and second, respectively. +dh refers to the duration in hours from start time and * denotes the number of hours. Finally, "InputFile.obs" refers to the input RINEX file to be windowed and OutputFile.obs is the name of the output file after the time windowing operation. After time windowing, prairie pothole pond survey times ranged from 1 to 4 hours whereas NASA ABoVE survey times varied from 0.9 to 10.4 hours.

Next, we use a Hampel filter in MATLAB with a 600-point window (10 minutes with 1Hz logging interval) and 1.5 sigma threshold to remove

outliers from the data series. A Hampel filter defines the median of a moving window and replaces outliers with the median value. The mean latitude, longitude (Figure 4-4c) and height (Figure 4-4d) of the windowed and filtered GPS time series are calculated as the final vertical and horizontal coordinates. Measurement uncertainty for a lake/pond survey is then calculated as

$$[\text{eq 4}] \quad \mathbf{WaSP\ lake\ uncertainty} = \mathbf{SDHGT} + \mathbf{SDANT} + \mathbf{0.01\ m}$$

where *SDHGT* is the standard deviation of 1 Hz heights from WaSP PPP solutions, *SDANT* is the standard deviation of antenna offset measurements and the additional 0.01 m is intended to account for antenna offset measurement error. Note that the mean horizontal coordinates are representative, not an exact survey location because the WaSP systems move even during anchored lake/pond surveys.

For rivers, initial PPP results are converted to a .shp file and overlaid on nearly coincident satellite or airborne imagery in GIS software. The .shp file is visually inspected and locations in the data series when WaSP is not in the water and moving are manually removed (red circles, Figure 4-5).

Uncertainty in river WSE measurements is then calculated as:

$$[\text{eq 5}] \quad \mathbf{WaSP\ river\ uncertainty} = \sqrt{(\mathbf{SDHGT} + \mathbf{r})^2}$$

where SDHGT is the standard deviation of the estimated vertical positions from the NRCAN PPP output, and r is range in antenna offset measurements. Next, a centerline for the study reach is defined. For North Saskatchewan River results presented here, we use the Global River Widths from Landsat (GRWL) database (Allen and Pavelsky, 2018) and remove right angles from the centerline (Pitcher et al., 2019) (Figure 4-5 and Figure 4-8). Channel orthogonals are then established at right angles to the centerline at 25 cm downstream intervals (Ferreira, 2014) (Figure 4-5 and Figure 4-8). Lastly, 1 Hz GPS solutions from filtered PPP .shp file outputs are assigned a downstream distance by joining each point with its nearest neighbor channel orthogonal.

4.3.4 AirSWOT radar processing

AirSWOT is an airborne ka-band radar that uses interferometry to produce swath-based maps of WSE (Altenau et al., 2017, 2019; Pitcher et al., 2019; Tuozzolo et al., 2019). Here, we use AirSWOT data collected over the North Saskatchewan River on July 8, 2017, August 16, 2017 and August 17, 2017 to demonstrate how WaSP can be used to validate AirSWOT-like mappings of WSE. These data were collected as part of the 2017 NASA Arctic Boreal and Vulnerability Experiment (ABOVE) airborne campaign and are freely available via the Oak Ridge National Laboratory (ORNL) Distributed Active Archive Center (DAAC) at: <https://doi.org/10.3334/ORNLDAAC/1646>

(Fayne et al., 2019). Each swath of AirSWOT radar data is delivered as a 6 band geotiff with 3.6 m x 3.6 m pixel size. Band 1 contains interferometrically derived heights, in meters, relative to the WGS84 ellipsoid. Bands 2 through 6 are the radar incidence angle (radians), magnitude (which can be converted to dB using $20 \cdot \log_{10}(\text{mag})$), correlation (dimensionless), height sensitivity (meter/radian) and height uncertainty (as 'error' in meters). See Fayne et. al., (in review) for discussion of specific limitations of these data.

To aid interpretation of radar data, AirSWOT also integrates a color-infrared (CIR) digital camera. The images collected by the CIR system were used to produce 1 m resolution orthomosaics using Agisoft's PhotoScan photogrammetry software (Kyzivat et al., 2018). A derivative high-resolution open water mask was also created from the orthomosaics (Kyzivat et al., 2019a, 2019b) (Figure 4-5). Here, we use the open water mask created from August 17, 2017 CIR data over the North Saskatchewan River to systematically remove non-open-water pixels from both July and August radar data. Note that of the three days surveyed by AirSWOT in 2017, North Saskatchewan River water levels were lowest on August 17, 2017 (Figure S4-1). Therefore, we contend that the use of only the water mask from August 17, 2017 conservatively eliminates non-open-water pixels for all three sorties.

Raw AirSWOT radar data requires data quality filtering to eliminate pixels with anomalous WSE retrievals (Altenau et al., 2017; Pitcher et al., 2019). The filtering applied to radar data here includes first removing non-open-water pixels using the open-water mask (Kyzivat et al., 2019a, 2019b). Second, the global MERIT DEM (Yamazaki et al., 2017) is used to filter out pixels with WSE values greater or less than 5 m from MERIT (Fayne et al., in review). Note that original MERIT DEM pixel heights are given relative to the EGM96 geoid. For comparison with AirSWOT, the EGM96 geoid is subtracted such that heights are relative to the WGS84 ellipsoid. Lastly, AirSWOT pixel values with random height error >1 m are removed (Pitcher et al., 2019). After filtering, remaining AirSWOT WSE pixels are joined to their nearest-neighbor centerline orthogonal. When an orthogonal has >1 nearest neighbor AirSWOT pixels, these pixel WSEs are averaged. Lastly, all pixels are assigned a downstream distance (in streamwise km from the Petrofka Bridge), enabling direct comparison with WaSP WSE surveys.

4.3.5 North Saskatchewan River motorboat GNSS surveys

Accompanying July 7, 2017 and August 16, 2017 WaSP deployments on the North Saskatchewan River presented here, a GNSS receiver and antenna were affixed to a vertical mast on a motorboat and driven along the same reach. While this motorboat mounted survey technique is a standard field

measurement protocol for surveying WSE in rivers (e.g. Altenau et al., 2017), the motorboat data collection pattern was not optimized for longitudinal WSE and WSS surveys. That is, the primary objective of the motorboat team was to collect hydrographic surveys of water depth and velocity at downstream cross sections. Therefore, the motorboat made more turns and frequently approached the shore, likely leading to multipath errors and loss of geometry compared to WaSP surveys. Therefore, we present the motorboat data as validation of WaSP and refrain from commenting on the comparative accuracies of motorboat and WaSP WSE and WSS mappings.

4.3.6 North Saskatchewan River in situ water level sensor arrays

In addition to the WaSP and motorboat surveys, the Water Survey of Canada (WSC), a branch of Environment and Climate Change Canada (ECCC), installed and surveyed in an array of nine temporary pressure transducers (PTs) in the North Saskatchewan River study reach (Figure 4-7, Table S4-1). These PT's were programmed to measure WSE at 5-minute intervals and all nine PTs were operational during July 2017 WaSP, motorboat and AirSWOT surveys. This array is used as an independent validation of WaSP WSE (Figure 4-10a) and WSS (Figure 4-11a).

Unfortunately, data from only one of the nine PTs was recovered for the August 2017 surveys. The PT recovered was located 0.37 km from the start of the study reach, near Petrofka Bridge (Figure 4-7). The raw pressure data

series from this PT was manually converted to water depth using a barometric pressure logger located near the end of the study reach (close to Wingard Ferry). Notable jumps in the data series suggest that the PT location shifted between installation and recovery. To rectify this, jumps in the data series were manually identified and a constant offset calculated as the difference between neighboring high-quality measurements was applied to subsequent data readings. After manual adjustment, outlier readings from the 5-minute data series were removed using a hampel filter with a 288-point (or one-day given a 5-minute logging interval) window. Finally, the daily average was computed (Figure S4-1 and Table S4-2) and is used here to determine the total water level drawdown between July and August 2017 (Figure 4-10b).

4.5 Results

4.5.1 WaSP and near-shore static surveys in Prairie Pothole ponds

WaSP units were deployed in three ponds separated by <2 km, all located ~65 km northwest of Saskatoon, Saskatchewan, Canada (Figure 4-6a-c). Deployments were conducted on July 4, 2017, August 17, 2017 and June 16, 2018 on Pond 1, and July 4, 2017 and August 17, 2017 on Pond #2 and Pond #3. In all three ponds, water levels fell between July and August

2017. In Pond #1, WSE dropped from 506.55 m to 506.35 m, a net drawdown of 20 cm (Figure 4-6d,g). WSE in Pond #2 and Pond #3 fell from 509.21 m to 508.96 m and 498.87 m to 498.71 m, net drawdowns of 25 cm and 16 cm respectively (Figure 4-6e-f,g-i). WSE uncertainty (eq 4) across the seven WaSP surveys in all three ponds ranged from ~3 cm to ~5 cm.

These drawdowns also correlate with pond shoreline area, as manually mapped in situ using a handheld Garmin eTrex GPS and hand digitized in nearly coincident Planet 3.125 m resolution satellite imagery (Planet Team, 2019; see Figure 4-6a-c). The WaSP measures WSE drawdowns between July and August 2017, which are accompanied by a reduction in both mapped and digitized shoreline areas (Table S4-3). Near-shore static WSE surveys conducted the following spring find that water levels increased in all ponds between August 2017 and June 2018. These WSE increases were similarly accompanied by an increase in outer shoreline area in all three ponds (Figure 4-6g-i; Table S4-3). These results suggest that WaSP can detect cm scale changes in WSE.

On June 16, 2018 Pond #1 was surveyed using both WaSP and a near-shore static survey (Figure 4-1c), using identical Septentrio GNSS receivers, antenna combinations, and logging protocols. For the near-shore survey, a monument was pounded into the pond bottom, a tripod was levelled over the monument using a tribrach with an optical plummet, and offsets between the water surface, the top of the monument and the antenna phase

center were measured. The absolute WSE difference between the near-shore static and WaSP surveys was <1 cm, suggesting that WaSP lake surveys are reproducible and closely match other, common survey methods.

4.5.2 North Saskatchewan River

On July 7, 2017 and August 16, 2017, WaSP units were tethered to canoes and towed down a ~45 km reach of the North Saskatchewan River to measure longitudinal WSE and WSS between Petrofka Bridge and Wingard Ferry (Figure 4-7). To determine reproducibility of results, surveys on both days were conducted using two WaSP units, each outfitted with identical Trimble R7 receiver/Zephyr geodetic antenna combinations, loaded with the same 1 Hz logging sessions, and escorted downstream by two canoes and two field teams. The median absolute WSE difference between these WaSP systems was ~3 cm on July 7, 2017 and ~2 cm on August 16, 2017 (Table 4-1a). These differences are less than the median ~6 cm to ~7 cm measurement uncertainty (eq 5) associated with each survey (Table 4-1b), affirming that the WaSP platform yields reproducible results.

WaSP WSEs on July 7, 2017 are also similar to nine ECCC PTs surveyed in along our study reach (Figure 4-8). The absolute differences of the median WaSP WSE for 20 m reaches centered on each PT compared to an accompanying PT WSE ranges from 5 cm to 14 cm, with a median overall difference of 8 cm. The median WaSP WSE is also +/- 10 cm PT WSE for 8

out of the 9 PTs (Figure 4-10a), suggesting that longitudinal WaSP surveys measure WSE with accuracies exceeding SWOT requirements for 1 km² open water areas with 20 m or less downstream spatial averaging. See Figure S4-2 for analogous comparisons between PT, motorboat and AirSWOT.

To further validate WaSP, longitudinal WSE profiles are compared with those mapped by the motorboat mounted GNSS. Overall, the two longitudinal profiles (Figure 4-8) and resultant WSEs (Figure 4-9) are similar, but there are notable differences. First, given that the motorboat made several transects orthogonal to flow direction for hydrographic depth and velocity surveys, the WSE data had to be carefully inspected and manually filtered, resulting in data gaps (e.g. ~21.7 km downstream; Figure 4-8a). Second, the angle of the antenna on the motorboat would tilt when weight on the boat was redistributed due to people or equipment moving. Third, the motorboat was unable to survey shallow reaches of the river. This was particularly problematic for the August 16, 2017 motorboat survey when the antenna height changed three times to accommodate shallow water conditions. This resulted in three unique vertical offset corrections that were applied to the final data series. Shallow water is not a problem for WaSP because the platform has low draft. Therefore, WaSP is equally capable of surveying WSE in shallow and deep water and is insensitive to weight redistribution due to people moving on the towboat. Such flexibility is notable in complex braided rivers and/or floodplains where shallow water

conditions are common and WSE cannot be easily measured with point-based survey techniques.

The primary motivation for WaSP development is to validate AirSWOT and forthcoming SWOT mappings of WSE and WSS. To test WaSP's suitability for this task, we compared WaSP WSE surveys on the North Saskatchewan River collected on July 7, 2017 and August 16, 2017 with nearly coincident AirSWOT mappings of the same reach collected on July 8, 2017, August 16, 2017 and August 17, 2017. Unfortunately, ~84%, ~87% and ~45% of the study reach water surface area on these dates was not mapped by AirSWOT due to poor radar reflectivity as the radar signal scatters away from the sensor at higher incidence angles (commonly referred to a "dark water"). Because of the lack of available data, the downstream spatial averaging of open water pixels required to test SWOT accuracy requirements (Rodriguez, 2016) was not possible in this analysis. Despite this limitation, a pixel based AirSWOT WSE and WSS to WaSP comparison was conducted.

Figure 4-8a shows downstream WaSP WSE (yellow circles) compared with PT WSE (black diamonds), motorboat WSE (orange circles) and AirSWOT WSE (blue circles) on July 7-8, 2017, and Figure 4-8b compares WaSP WSE (green circles) with motorboat WSE (orange circles) and AirSWOT pixels (blue circles) on August 16-17, 2017. These subplots show similar longitudinal profiles for both AirSWOT and WaSP. That is, the WSS

calculated as the linear fit between WSE and downstream distance for the full study reach from WaSP is -16 cm/km on both July 7, 2017 and August 16, 2017, respectively. Slopes from AirSWOT are -14 cm/km and -15 cm/km on July 8, 2017 and August 16-17, 2017, respectively. While the longitudinal profiles are similar, the absolute WSE difference between WaSP and AirSWOT are inconsistent (Figure 4-9b,d). The median difference between AirSWOT and WaSP was -20 cm and -78 cm on July 7-8, 2017 and August 16-17, 2017, respectively. AirSWOT is biased (lower) during both surveys, with an inconsistent absolute bias as August mappings are nearly three times lower than July. Again, it is important to emphasize that in order to meet accuracy requirements, AirSWOT and SWOT data require downstream spatial averaging. Due to lack of data density, such spatial averaging is not performed and thus the accuracy of 2017 AirSWOT mappings in terms of SWOT mission requirements is not assessed. Despite this limitation, these results confirm that WaSP is a standard, repeatable and flexible solution for validating remotely sensed estimates of WSE from platforms like AirSWOT.

Figure 4-11a compares WSS measured by WaSP with PT, motorboat and AirSWOT for the reach lengths ranging from 2.44 km to 7.23 km established between downstream PTs (Table 4-2a). For PTs, slope is calculated as the dividend between the change in WSE and downstream distance (i.e. rise/run). For WaSP, motorboat, and AirSWOT WSS is the slope of the linear fit between WSE and downstream distance. The root-

mean-squared-difference (RMSD; Table 4-2b) between WaSP and PT WSS on July 7, 2017 is 1.35 cm/km. The RMSD between WaSP and motorboat is also small, whereas the RMSD between WaSP and AirSWOT is >15 cm/km (Table 4-2b). This confirms that when compared to traditional PT based WSS, WaSP WSS accuracies over reaches as small as 2.44 km exceed the SWOT mission requirement of ± 1.7 cm/km for 10 km reaches at least 100 m wide (Rodriguez, 2016), suggesting that WaSP is a capable tool for AirSWOT and SWOT WSS validation.

Figure 4-11b,c compare WSS for 10 km reaches measured by WaSP (blue and green lines), motorboat (orange lines), and AirSWOT (grey and black lines) in July (Figure 4-11b) and August 2017 (Figure 4-11c). WSS is calculated as the slope of the linear fit between WSE and distance for 10 km reaches established every 1 km downstream. In July and August, the absolute median difference in WSS from WaSP surveys was <1 cm/km, emphasizing the repeatability of WaSP WSS. When comparing WaSP WSS with motorboat WSS, median absolute differences are also <1 cm/km. Therefore, motorboat and WaSP WSS comparisons for 10 km reaches both meet SWOT requirements, again suggesting utility for future SWOT and AirSWOT validation. On August 17, 2017, the absolute median WSS difference between AirSWOT and WaSP was <1.4 cm/km. On July 8, 2017 and August 16, 2017, the resultant absolute median WSS difference compared to WaSP was <5.6 cm/km. Collectively, these results emphasize

that for 10 km reaches, WaSP correctly and consistently maps WSS with sufficient accuracy to validate AirSWOT and SWOT.

The power of multitemporal mappings of WSE is the ability to quantify water level changes and volumetric flux. To demonstrate this, Figure 4-10b compares median orthogonal WSE changes between July and August, 2017 for WaSP (green bars), AirSWOT (blue bars) and motorboat gnss data (orange bar) with in situ ECCC PT data (grey bars). The WaSP, AirSWOT, motorboat and ECCC PT data all measure a net drawdown between the July and August 2017. However, the drawdown measured by these independent technologies differs. On average, WaSP measures a ~ 39 cm drawdown compared to a ~ 43 cm decrease measured by ECCC PT, a difference of ~ 4 cm. In contrast, the difference between motorboat and ECCC PT data is ~ 22 cm, while the difference between AirSWOT and ECCC is 42 cm to 54 cm for August 16 and August 17, 2017 surveys, respectively. These results suggest that repeat WaSP WSE surveys yield accurate water level changes that closely match standard field measurement methods.

4.6 Discussion

4.6.1 Overall WaSP performance

These pond and river results yield important insights about WaSP overall performance. First, the sub-centimeter difference between a WaSP

and a near-shore-static survey in Pond #1 (Figure 4-6d), the minimal difference between nearly coincident WaSP river surveys (Table 4-1), and the close agreement with ECCC PT data (Figure 4-10a) suggest that WaSP yields reproducible data. Second, the comparisons between WaSP and AirSWOT suggest that WaSP is a standard and repeatable solution for validating remotely sensed estimates of WSE (Figure 4-9) and WSS (Figure 4-11). The strong agreement between shoreline areas and pond levels (Figure 4-6g-i), as well as the small absolute difference between WaSP drawdowns and ECCC PT data (Figure 4-10b) reveals that multitemporal WaSP surveys accurately reproduce water level drawdowns. Finally, the WaSP and PT WSE and WSS comparisons suggest that WaSP data accuracy is comparable to standard methods for surveying WSE and WSS. WaSP also has the added benefit of working equally well in shallow or deep water and is immune to the suite of shoreline conditions required for near-shore surveys.

4.6.2 WaSP for NASA SWOT validation

To determine if, after launch, SWOT meets or exceeds key WSE and WSS accuracy requirements (Rodriguez, 2016), a standard and reproducible field validation instrument is needed. For at least three reasons, we propose WaSP as a standardized instrument that can readily serve this purpose. First, when compared to PTs, WaSP WSE RMSD is ~8 cm without any downstream spatial averaging (which, akin to SWOT and AirSWOT data

processing, will reduce WSE uncertainty). This suggests that raw WaSP WSE data accuracy is appropriate for SWOT validation in rivers and lakes. Second, median WaSP WSS differences for 10 km reaches is <1 cm/km when compared with motorboat GNSS surveys and WSS RMSD is 1.3 cm/km when compared to PTs along reaches <10 km, which is higher than that required by SWOT for 10 km reaches. Third, WaSP survey results are standard and repeatable, and the system is flexible, easy to deploy and can be operated by experts and non-experts alike. This is ideal for a global satellite mission such as SWOT, because it allows for reliable and precise measurement validation on global scales simply by loaning WaSP hardware to university, government, and citizen science partners around the world.

4.6.3 WaSP lake surveys for the NASA Arctic Boreal Vulnerability

Experiment (ABOVE)

The NASA Arctic-Boreal Vulnerability Experiment (ABOVE) is a decadal project that aims to enhance understanding of ecological and social consequences of environmental change across Alaska and Canada (Miller et al., 2019; see <https://above.nasa.gov>). In 2017, as a part of ABOVE, NASA deployed AirSWOT to map multitemporal WSE in rivers, lakes, and wetlands across Arctic and Boreal regions of Canada and Alaska. To validate AirSWOT WSE retrievals, dispersed field teams equipped with WaSP units were deployed to targeted locations under various AirSWOT overflights across the

ABOVE study domain. The result is the largest known collection of airborne and field WSE measurements (Figure 4-12). WaSP units were distributed to government field technicians and university partners, without prior field training. All surveys were successfully executed, which demonstrates the ease-of-use of WaSP. Furthermore, WaSP deployments were conducted on foot, by pack-raft, canoe, motorized boat, helicopter, and float plane. This highlights the flexibility of the system given different logistical conditions. In total, 63 WaSP WSE surveys were executed, spanning $\sim 17^\circ$ latitude. All GPS data has been successfully processed using GINS PPP (Marty et al., 2011) software and resultant WSEs (Table 4-3) are being used to validate AirSWOT ABOVE mappings (Fayne et al., in review).

4.6.4 Future WaSP improvements

The data presented here are from WaSP version 1. However, targeted deployments in support of NASA ABOVE and pre-planning for NASA SWOT validation have illuminated system improvements that should be considered in future builds. First, a known source of uncertainty in WaSP surveys is the current necessity of making manual antenna offset measurements. Future builds should consider either fixed-height antennas and/or permanent metric markings so that a user can quickly and accurately determine the offset between the water surface and the antenna without need for additional field measurements. Second, the antenna mount can work loose in the foam over

multiple deployments. This can be rectified by securing the antenna to both the float and the Pelican Case. Third, more rocker, higher attachment points, and an asymmetrical boat-tethering system should be added to the float to minimize the risk of the nose pearling during tethered longitudinal surveys. Fourth, stronger attachment points for anchors used during lake/pond surveys should be considered, such as short webbing with locking carabiners secured to the deck. Fifth, the deck T-connectors and side stabilizer should be removed from the system. This will reduce WaSP costs and system weight/volume, which is particularly important during float plane and helicopter deployments. Sixth, the internal Pelican Case Pick 'n' Pluck foam could be upgraded to custom cut, closed-cell, polyethylene foam which would limit water absorption and be more durable through multiple years of deployments. Finally, the WaSP float has sufficient buoyancy that additional instruments could be integrated with the GPS. For example, a low cost and lightweight inertial measurement unit (IMU) could be integrated with WaSP and used in data processing to improve kinematic solutions. Similarly, integration of a high-frequency sonic roughness sensor and/or an optical sensor should be considered, specifically to improve AirSWOT/SWOT models of radar backscatter versus water surface roughness. Water quality sensors and bathymetric sonars could also be integrated with WaSP to broaden the scientific scope of the platform.

There are also field deployment and data processing techniques that could be improved. An initialization or a single-phase ambiguity resolution period consisting of a static survey with a duration of at least 15 minutes and up to an hour should be recorded prior to deploying WaSP in the water. Then the kinematic survey should begin continuously from the static collection. This static position can later be used in data processing to resolve atmospheric and positioning errors. The beginning of a kinematic survey can also be manually removed from both final positional averages and error compilations to minimize the impact of an initialization period.

4.7 Conclusions

Operational repeat mappings of WSE and WSS from the SWOT mission and its experimental validation instrument AirSWOT, have the potential to transcend current limitations in monitoring global surface water resources. However, prior to forthcoming SWOT data being operationally adopted, direct field validation is needed. Such validation should be conducted in an accurate, efficient, standard and repeatable manor. We thus propose the Water Surface Profiler (WaSP) system as an operational tool for validating forthcoming SWOT data and as a standalone instrument for mapping large-scale hydraulics in lakes, wetlands and rivers. WaSP has been successfully deployed in Arctic and Boreal regions of Alaska and Canada as part of the NASA ABoVE project and is operationally used as part of the Lake

Observation by Citizen Scientists and Satellites (LOCSS) project. WaSP is a rugged and flexible platform that can be deployed in a wide range of environments with minimal training by both experts and non-experts alike. This ease-of-use and system flexibility is essential for a global satellite mission like SWOT, because it allows for standard, repeatable, reliable and accurate measurement validation on global scales simply via collaboration with interested partners around the world.

4.8 Acknowledgements

This work was supported by NASA Terrestrial Hydrology Program Grant NNX13AD05G managed by Jared Entin, NASA Terrestrial Ecology Program Arctic-Boreal Vulnerability Experiment (ABoVE) Grant NNX17AC60A managed by Hank Margolis, NASA Surface Water and Ocean Topography mission Grant NNX16AH83G managed by Eric Lindstrom, and NASA Earth and Space Sciences Fellowship Program Grant NNX14AP57H managed by Lin Chambers. The processed AirSWOT radar data collected as part of 2017 NASA ABoVE campaign are available at: <https://doi.org/10.3334/ORNLDAAAC/1646> (Fayne et al., 2019). The AirSWOT color-infrared orthomosaics collected as part of 2017 NASA ABoVE are available at: <https://doi.org/10.3334/ORNLDAAAC/1643> (Kyzivat et al., 2018). The North Saskatchewan River water mask derived from AirSWOT color-infrared data collected as part of 2017 NASA ABoVE are available at:

<https://doi.org/10.3334/ORNLDAAAC/1707> (Kyzivat et al., 2019). Additional thanks to John Arvesen of Cirrus Digital Systems for assistance with color-infrared digital imagery; the NASA/JPL AirSWOT processing team for processing the radar data; Alex Shapiro of Alaska Land Exploration LLC for logistical and helicopter support out of Fairbanks, AK, USA; Jerry Carrol in Fort Yukon, AK, USA for boat transport on the Yukon River; Heather Bartlett and Mark Bertram of the Yukon Flats National Wildlife Refuge for field support; Dave Olesen of Hoarfrost River Huskies Ltd. for logistics and aircraft support out of Yellowknife, NWT, Canada; Bruce Hanna of the Government of the Northwest Territories Environment and Natural Resource Division for assistance in collecting lake level records out of Yellowknife, NWT, Canada.

4.9 Figures



Figure 4-1: the Water Surface Profiler (WaSP) system

Example of **(a)** readying a Water Surface Profiler (WaSP) system for deployments, **(b)** a WaSP survey using optional side-stabilizers, and **(c)** a comparison between a WaSP kinematic survey and a near-shore static survey. The WaSP system integrates a GPS receiver and a power system within a ruggedized, waterproof case mounted atop a custom shaped, high-

density foam float with an external antenna mount and fastening locations for tow-lines, anchors and drogues.

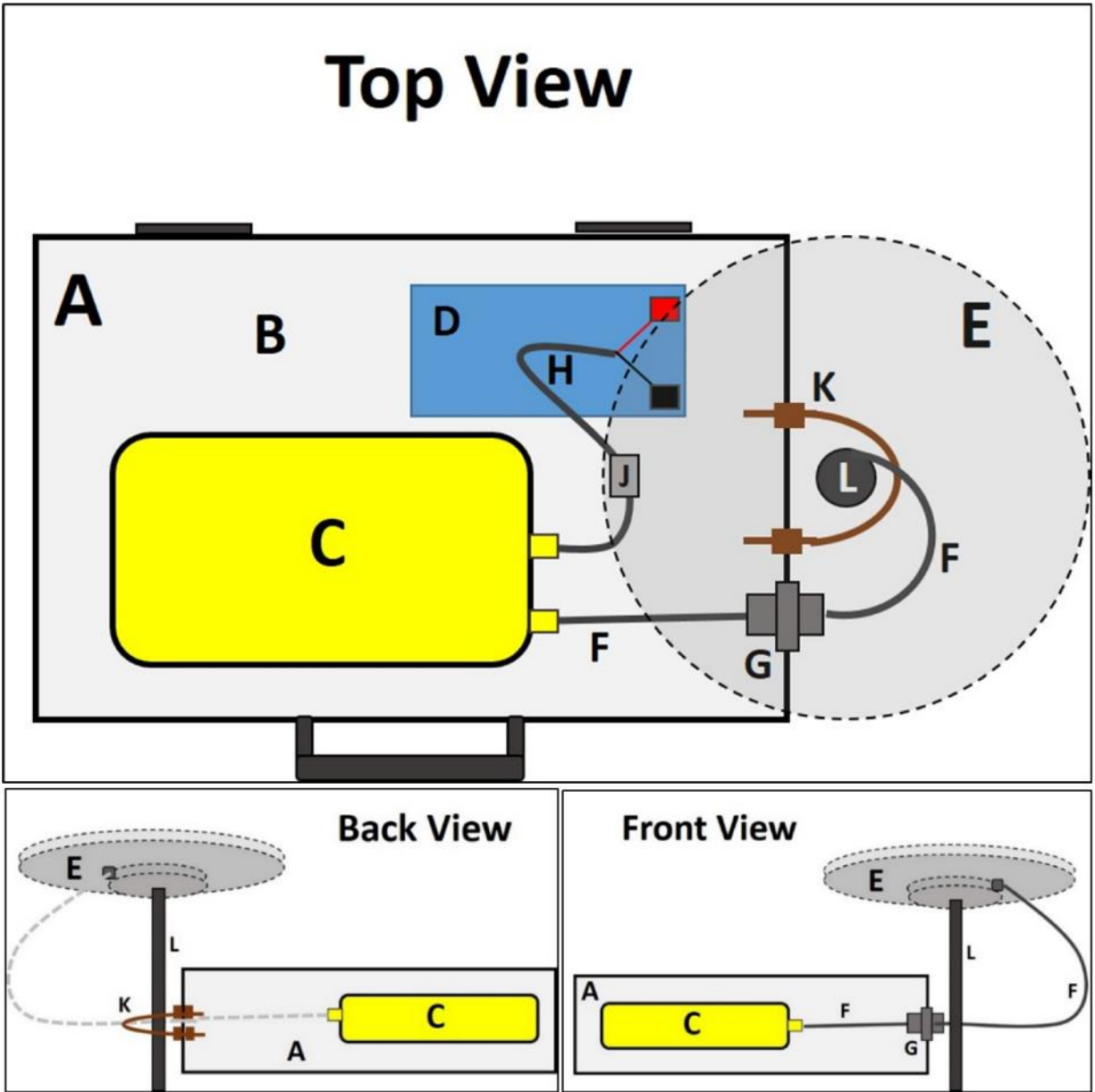


Figure 4-2: illustration of WaSP components

Schematic of WaSP GPS receiver/antenna and power system from top view, back view, and front view. WaSP components shown include: **(A)** Pelican Case 1450; **(B)** Pelican Pick 'n' Pluck foam; **(C)** GPS receiver; **(D)** 12v 7Ah sealed lead-acid battery; **(E)** GPS antenna; **(F)** RG-58 coaxial antenna cable with male TNC connectors; **(G)** TNC bulkhead, female-female, with

watertight gasket; **(H)** GPS receiver power cable; **(J)** 3A automotive fuse; and **(L)** antenna mount with 5/8-11 threads. Illustration courtesy of Annie Zaino (UNAVCO).

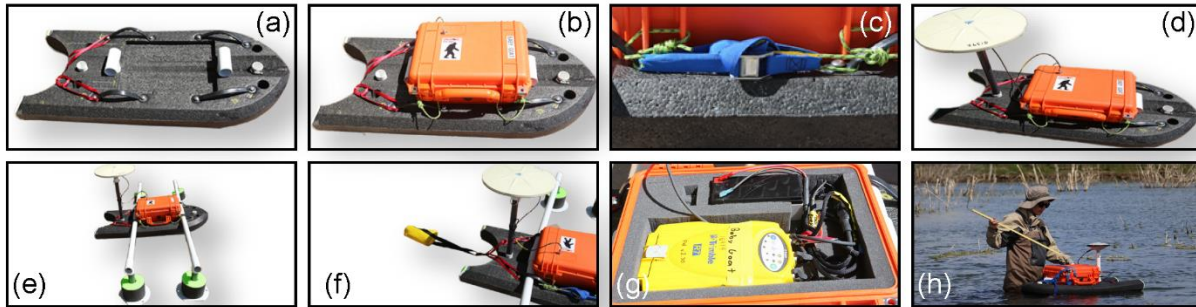


Figure 4-3: WaSP set up steps

WaSP is deployed using an **(a)** custom shaped and designed high-density foam float. The case **(b)** containing the **(g)** power system and GPS receiver is **(c)** secured to the float using prusiks knots, cam straps, and side handles. The **(d)** GNSS antenna is placed atop a mast, affixed to the float and connected to the TNC bulkhead on the case. There are **(e)** optional side stabilizers that can be used in still water conditions. A **(f)** drogue and/or anchor system can be used for river or lake/pond surveys. To begin a survey, the **(g)** GPS receiver needs to be powered on and connected to the antenna via the TNC bulkhead on the inside of the case. The **(h)** offset between the water surface and the antenna must also be manually measured and a location with a clear sky view should be selected.

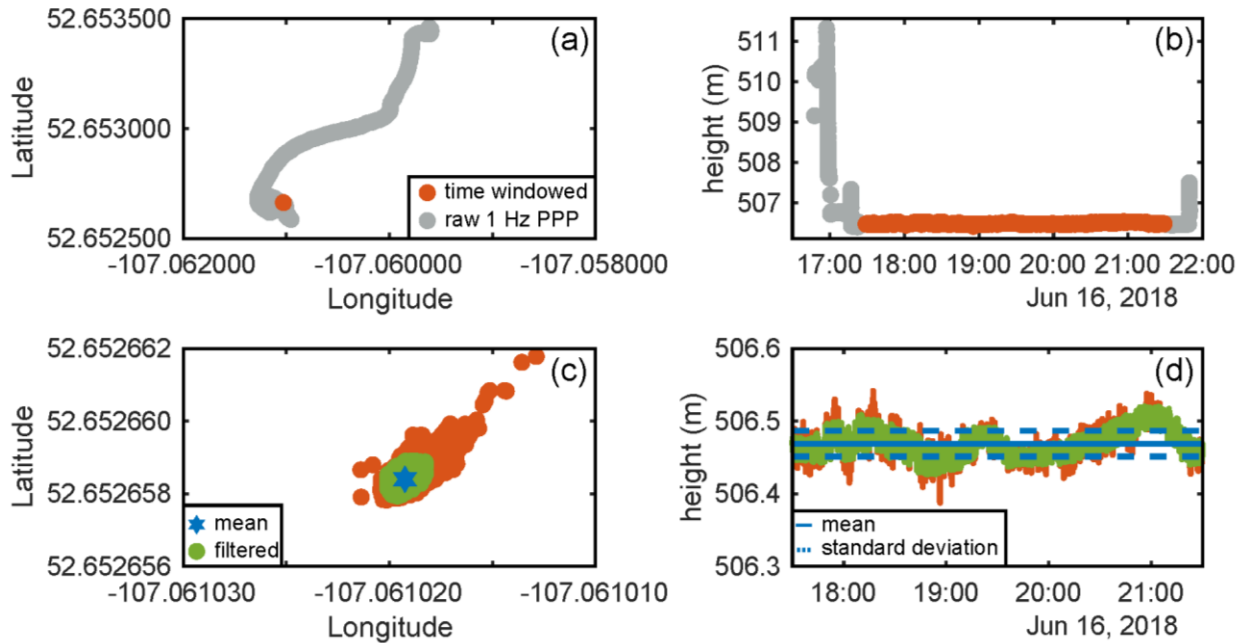
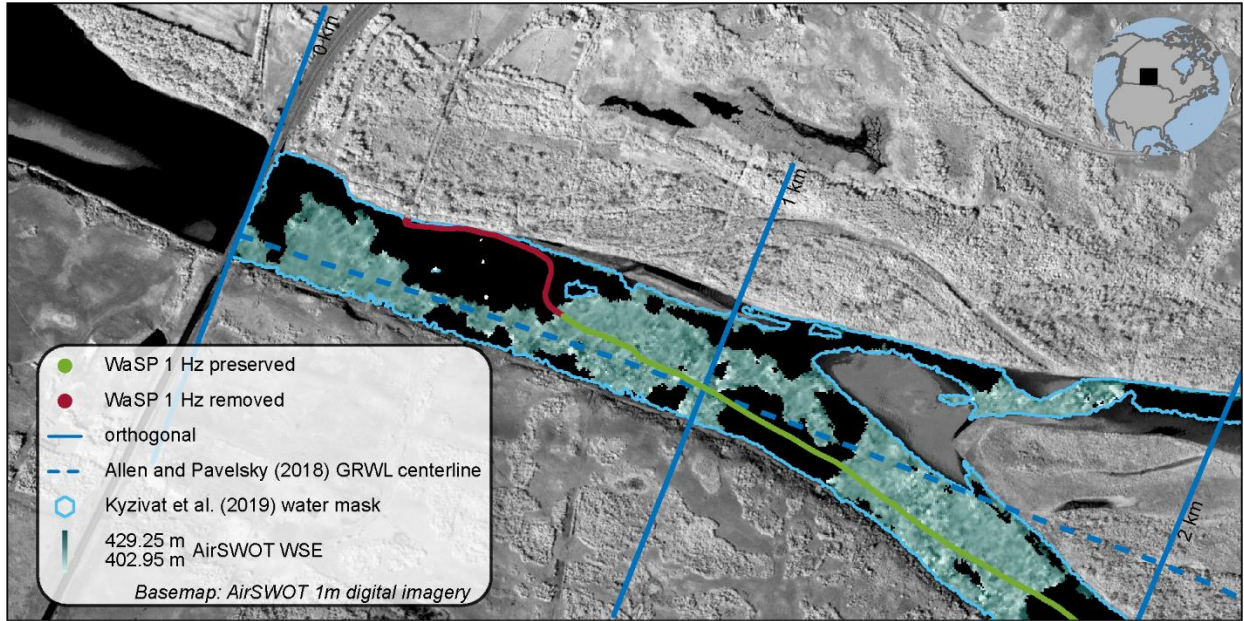
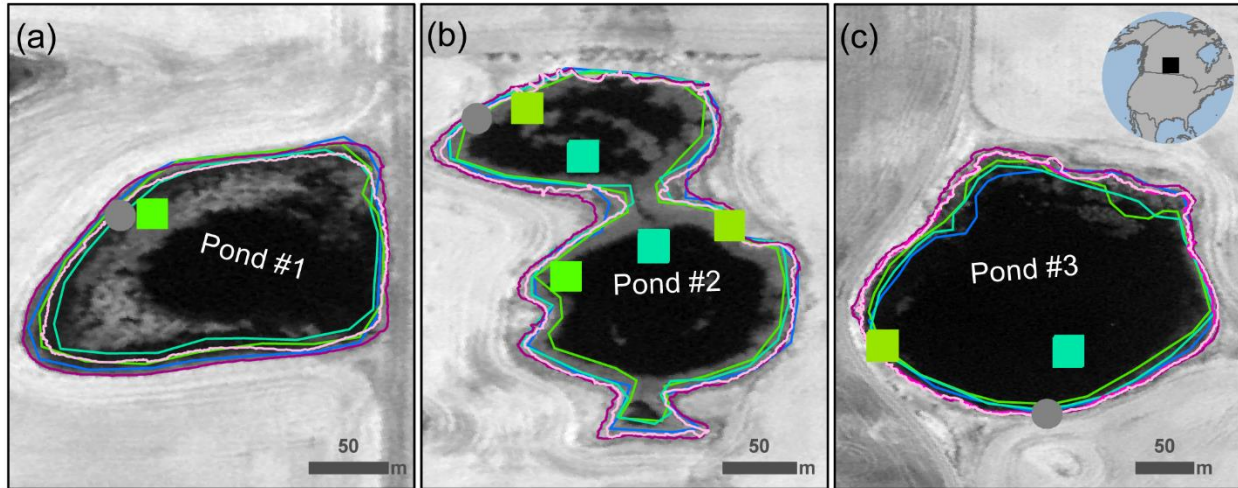


Figure 4-4: WaSP lake/pond data processing

WaSP data processing for lake/pond surveys requires first analyzing the original latitude, longitude (a) and height (b) data series (grey circles) and clipping the survey to times when the system is in the water and there is minimal vertical and horizontal drift (orange circle). An outlier filter is then applied to the latitude, longitude (c) and height (d) data (green circles) and the average values are preserved latitude, longitude (blue star in (c) and blue solid line in (d)).





⬭ GPS area 07/2017 ⬭ Planet area 07/2017 ■ WaSP 07/2017 ■ WaSP 06/2018
⬭ GPS area 08/2017 ⬭ Planet area 08/2017 ■ WaSP 08/2017 ● static 06/2018
⬭ GPS area 06/2018 ⬭ Planet area 06/2018

AirSWOT 1 m resolution digital imagery, August 17, 2017

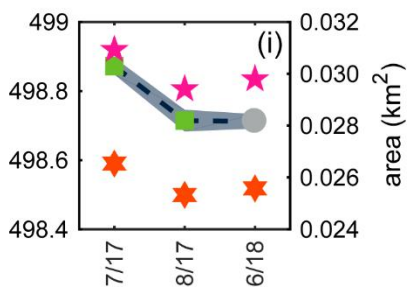
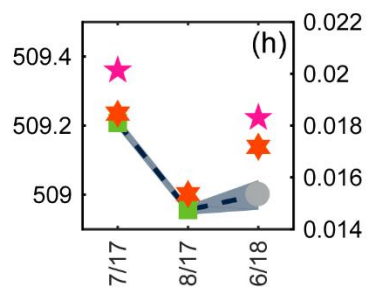
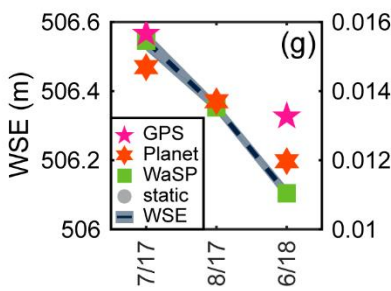
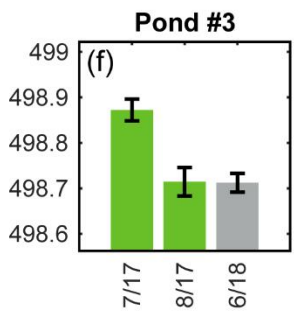
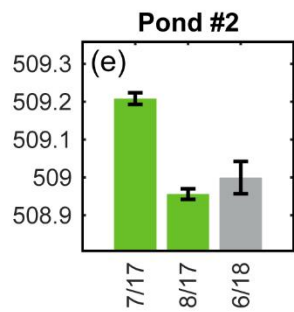
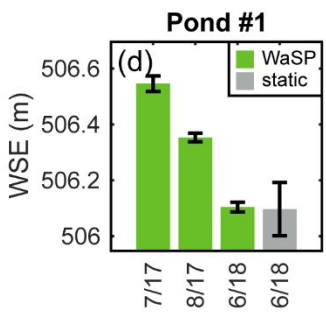


Figure 4-6: prairie pothole ponds, Saskatchewan, Canada

Three Prairie Pothole ponds near Saskatoon, Saskatchewan, Canada (**a-c**) were surveyed in July and August 2017, and June 2018 using WaSP (green squares) and near-shore static tripod surveys (grey circles). Outer shorelines were manually mapped in situ using handheld Garmin eTrex GPS's (pink vector lines) and also hand digitized ignoring floating and/or inundated vegetation within the pond using Planet 3.125 m resolution satellite imagery (Planet Team, 2019) collected on July 4, 2017, August 18, 2017, and June 16, 2018 (green and blue vector lines). The base map is a 1 m resolution digital orthomosaic collected by AirSWOT on August 17, 2017 as part of the NASA Arctic Boreal Vulnerability Experiment (ABOVE). **d-f** shows resultant WaSP water surface elevation (WSE) surveys (green bars). Pond #1 (**d**) was surveyed in July and August 2017 and again in June 2018 using both a WaSP and a near shore static survey (grey bar). Pond #2 (**e**) and Pond #3 (**f**) were surveyed using WaSP's in July and August 2017 and again in June 2018 using only a near shore static survey. The (**g-i**) WSE changes in all three ponds co-vary with changes in outer shoreline area, which independently validates that WaSP data is both accurate and reproducible. Note that the WSE values shown are ellipsoidal heights.

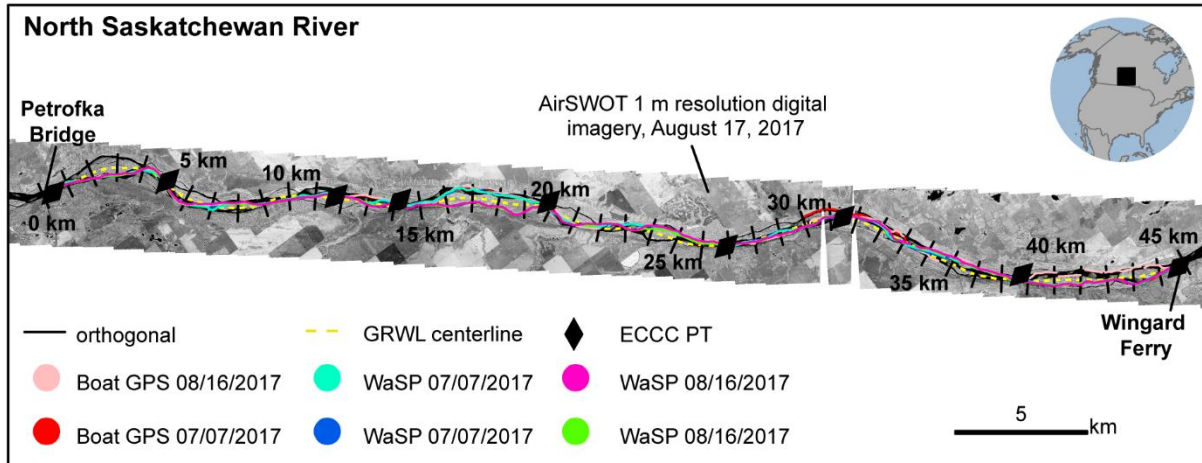


Figure 4-7: map of North Saskatchewan River study reach

On July 7, 2017 (blue circles) and August 16, 2017 (green and magenta circles) WaSP systems were escorted down a ~45 km reach of the North Saskatchewan River. For comparison with WaSP, a motorboat-mounted GPS system was also used to survey WSE in this reach (red circles). The river centerline (dashed black line) and channel orthogonals (solid black lines, created every ~25 cm along the channel centerline, but shown at 5 km spacing) were used to establish the streamwise coordinates of WaSP and motorboat survey points. The base map is a 1 m resolution color-infrared orthomosaic collected by AirSWOT on August 17, 2017 as part of the NASA Arctic Boreal and Vulnerability Experiment (ABOVE).

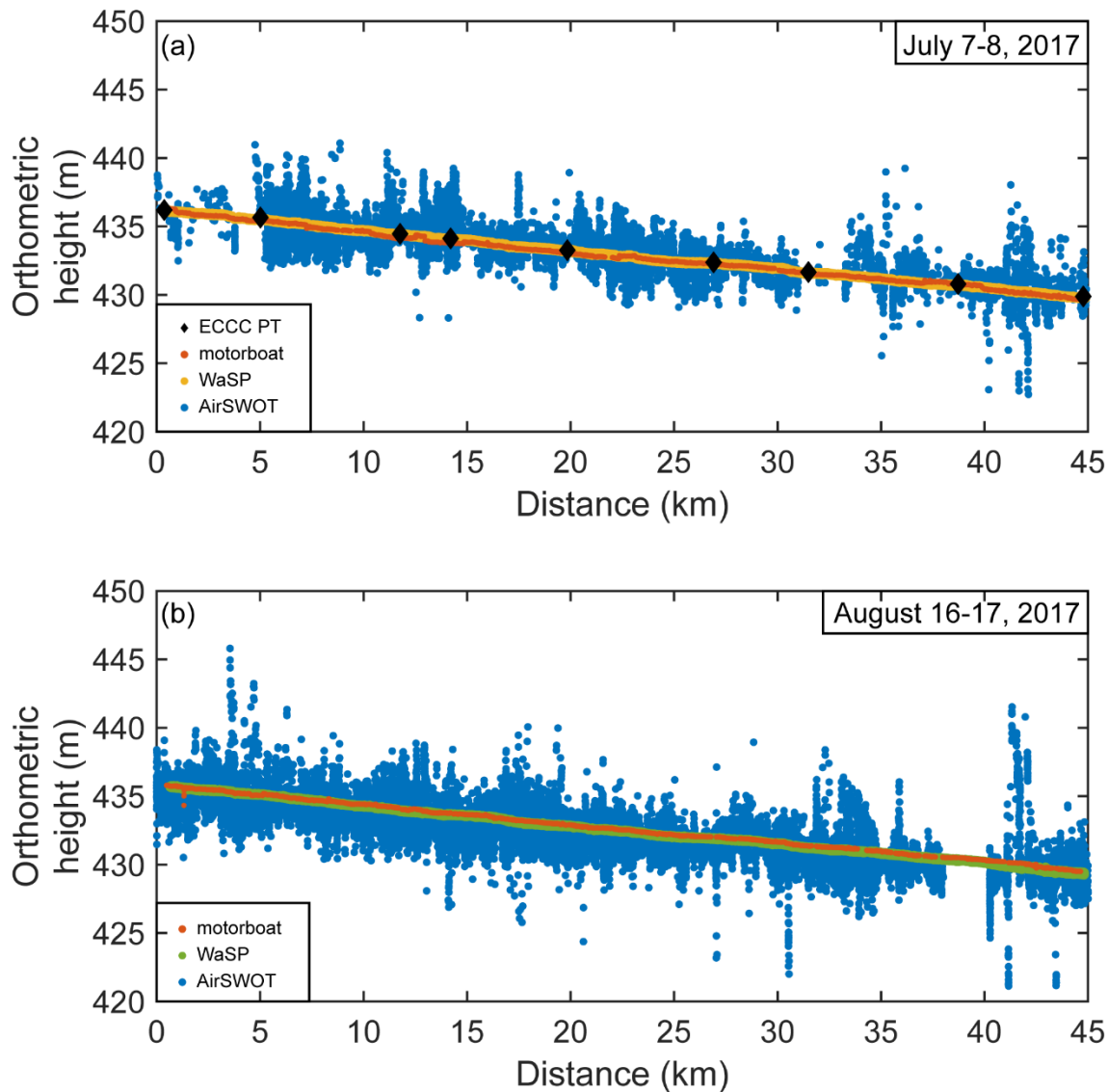


Figure 4-8: North Saskatchewan River study reach WSE

WaSP is designed to be a standard and repeatable validation instrument for remotely sensed mappings of WSE. As a demonstration of this, **(a-b)** compares WaSP longitudinal profiles (yellow and green circles) along a ~45 km reach of the North Saskatchewan River with, nine pressure transducer (PT; black diamonds) water level loggers, a motorboat mounted GNSS

survey, and AirSWOT mappings (blue circles) along the same reach on both (a) July 7-8, 2017 and (b) August 16-17, 2017. Note that the WSE values shown are orthometric heights. Outlier AirSWOT WSE values >450 m and <420 m are not shown.

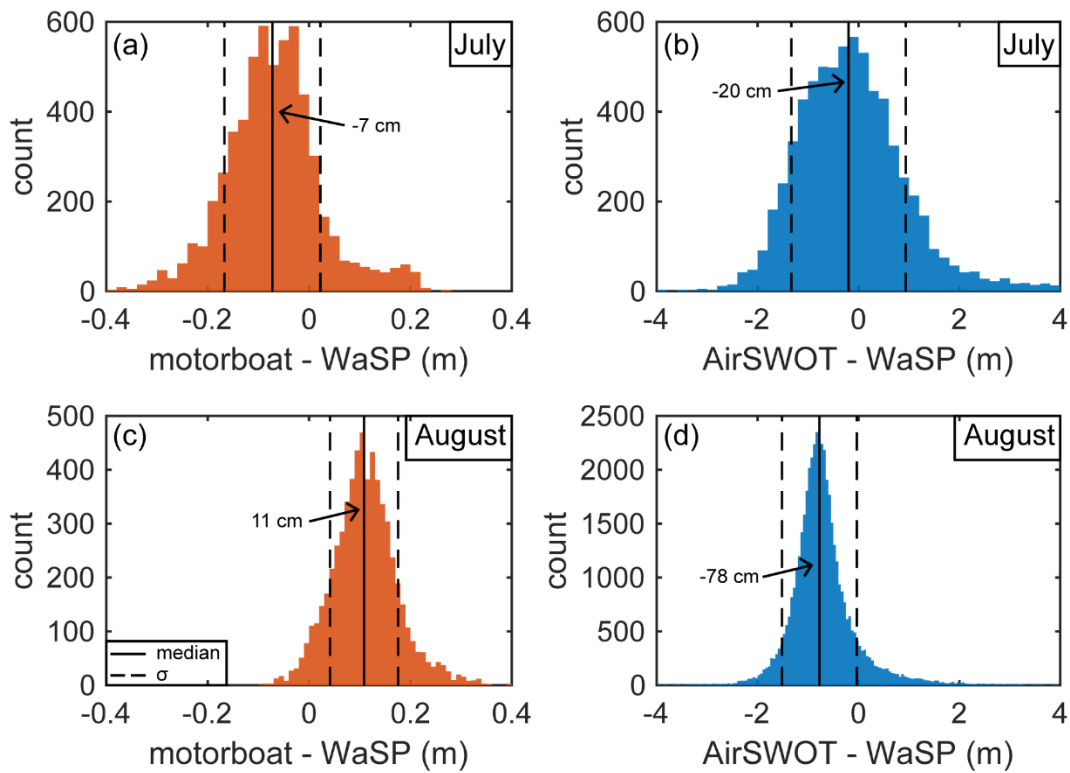


Figure 4-9: WaSP versus AirSWOT in the North Saskatchewan River

The WSE differences between motorboat (**a,c**), AirSWOT (**b,d**) and WaSP in July (**a-b**) and August, 2017 (**c-d**). Median differences (solid black line) and 1 standard deviation of the distribution of differences (σ ; dashed black line) are plotted. Note that outlier differences falling outside of x-axis bounds are not shown.

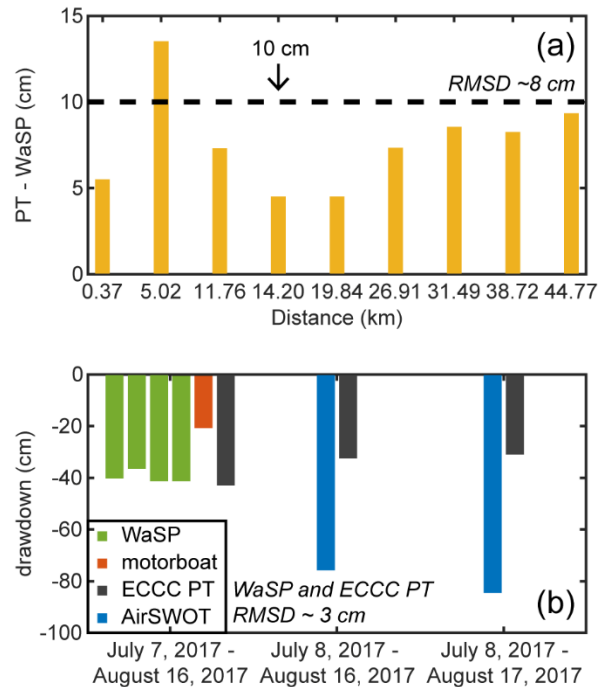


Figure 4-10: water level drawdown

On July 7, 2017 the absolute WSE difference between (a) Environment and Climate Change Canada (ECCC) pressure transducer (PT) water level loggers and WaSP averaged along 20 m reaches centered on each PT was <10 cm (dashed black line) for 8 of 9 PTs. (b) shows the WSE drawdown between July and August measured by WaSP (green bars), motorboat (orange bar), AirSWOT (blue bars) and an ECCC PT located near the Petrofka Bridge at the upstream end of our study reach. Drawdowns from WaSP closely match ECCC PT, suggesting that repeat WaSP surveys accurately quantify water level changes.

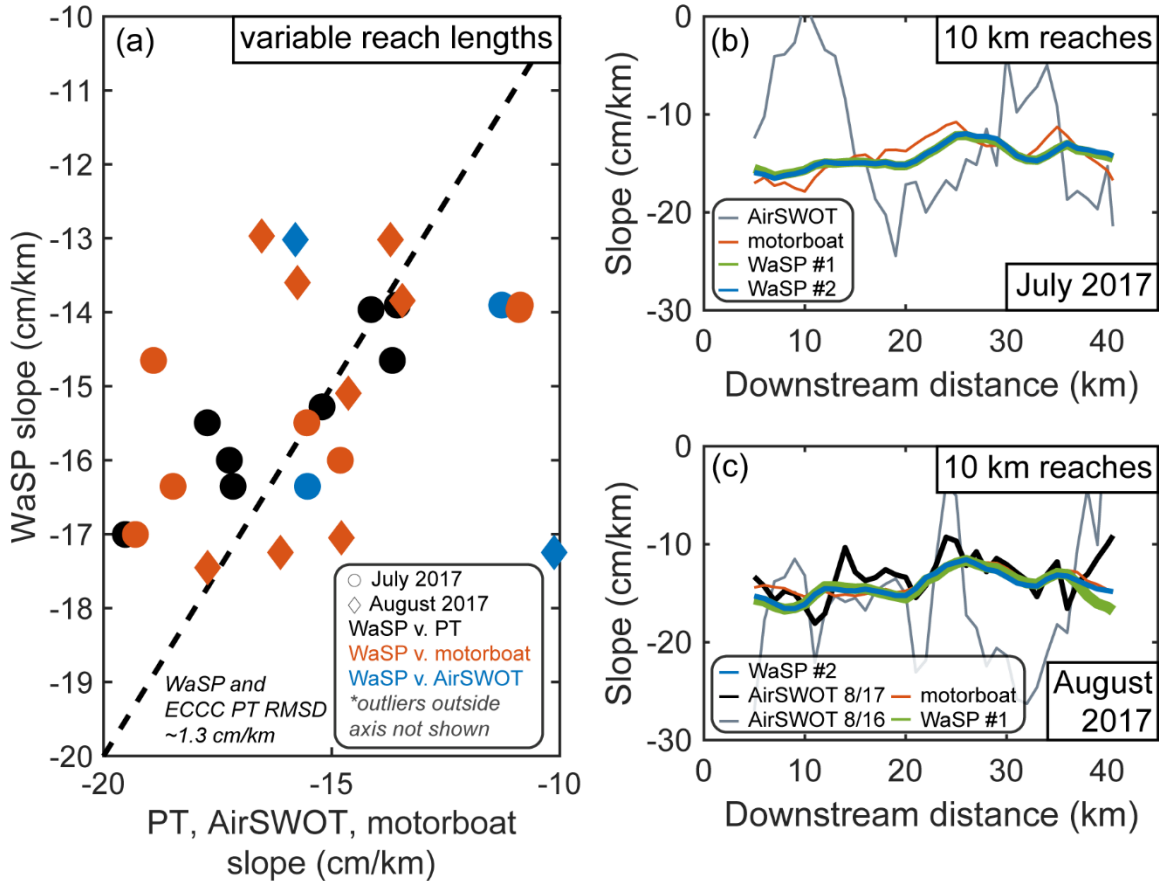


Figure 4-11: water surface slope

Comparison of (a) water surface slope (WSS) from WaSP (y-axis) and motorboat (orange; x-axis), AirSWOT (blue; x-axis) and Environment and Climate Change Canada (ECCC) pressure transducer (PT; black; x-axis) water level loggers in July (circles) and August (diamonds) 2017. Reach lengths vary from ~2.4 to ~7.2 km and are defined by the downstream spacing between ECCC PTs. Note that PT data is not available in August 2017. Outliers WSS > -10 cm/km and < -20 cm/km are not shown. (b-c) plots WSS for 10 km reaches established every 1 km downstream along the North Saskatchewan River. WSS was surveyed by two WaSPs (green and

blue lines), AirSWOT (grey and black lines) and a motorboat in **(b)** July 2017 and **(c)** August 2017.

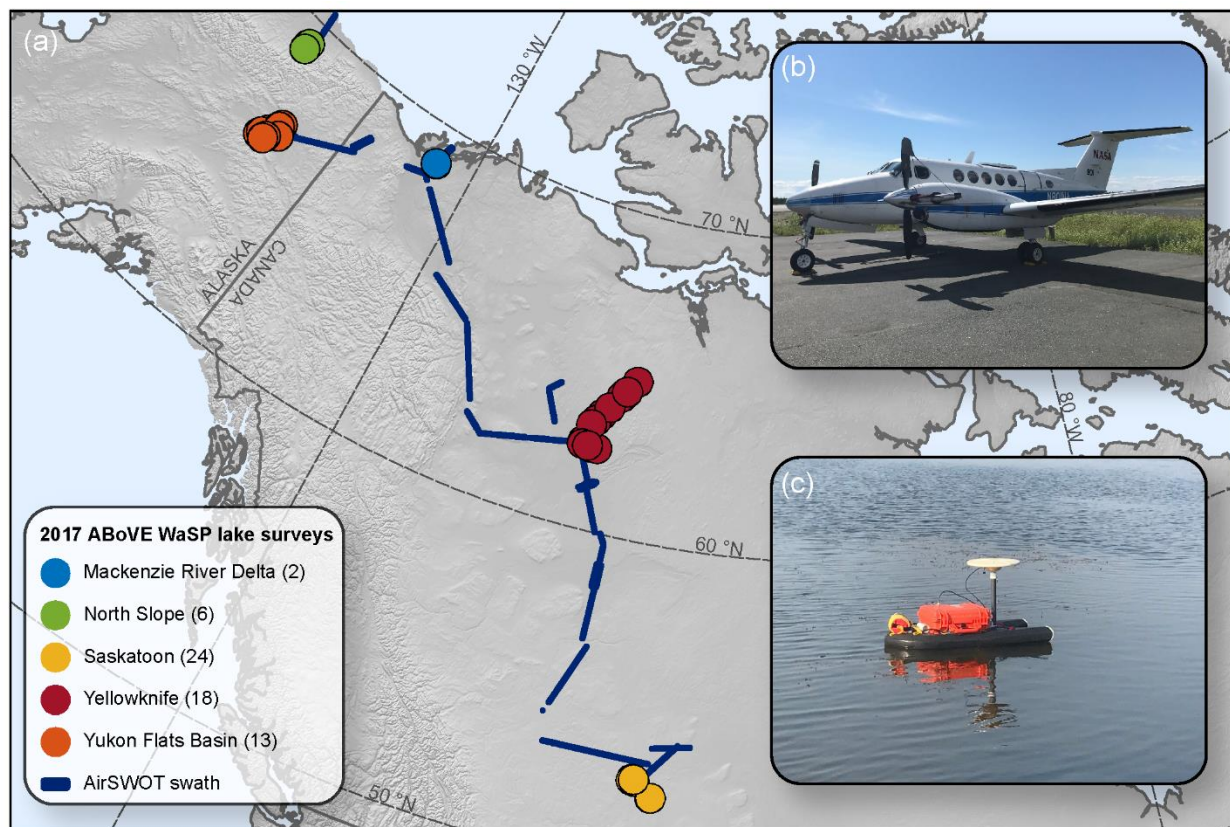


Figure 4-12: 2017 WaSP lake deployments in support of NASA ABoVE

In 2017, WaSP was (a) deployed to remote regions of Canada and Alaska to validate (b) AirSWOT mappings of WSE that were commissioned by NASA Arctic Boreal and Vulnerability Experiment (ABoVE). In total 63 WaSP (c) lake/pond surveys were executed, spanning $\sim 17^\circ$ of Latitude and ~ 476 m of vertical elevation. Notably, WaSP surveys were successfully conducted by government scientists, academic partners and field engineers alike and were deployed on foot, by kayak, by truck, by motorboat, floatplane and helicopter. This highlights the flexibility of the WaSP system, which is particularly valuable for standard and repeatable validation of forthcoming

global Surface Water and Ocean Topography (SWOT) satellite-based mappings of WSE and WSS.

4.10 Tables

TABLE 4-1				
(a) mean and median absolute water surface elevation (WSE) difference between WaSP surveys collected on the same day in the North Saskatchewan River, Canada.				
	July 7, 2017		August 16, 2017	
Mean WSE absolute difference (cm)	3.38		2.72	
Median WSE absolute difference (cm)	3.30		2.12	
(b) mean and median WaSP water surface elevation (WSE) uncertainty for surveys collected on the same day in the North Saskatchewan River, Canada.				
	July 7, 2017		August 16, 2017	
WaSP unit identifier	WaSP #1	WaSP #2	WaSP #1	WaSP #2
Mean WSE uncertainty (cm)	6.67	7.31	6.85	6.50
Median WSE uncertainty (cm)	6.60	7.22	6.71	6.40

Table 4-1: WaSP uncertainty

Table 4-2									
(a) summary of slopes for variable reach length									
Reach info			slope (cm/km)						
start (km)	end (km)	length (km)	Jul-17			Aug-17			
			WaSP	AirSWOT	motorboat	PT	WaSP	AirSWOT	motorboat
0.37	5.02	4.65	-14.65	40.73	-18.90	-13.67	-13.60	-24.29	-15.75
5.02	11.76	6.75	-17.00	-3.32	-19.30	-19.52	-17.05	-20.93	-14.79
11.76	14.20	2.44	-15.28	10.81	-23.55	-15.21	-12.97	-38.59	-16.53
14.20	19.84	5.64	-16.00	-32.61	-14.81	-17.24	-17.25	-10.12	-16.12
19.84	26.91	7.07	-13.96	-25.02	-10.90	-14.14	-13.84	-26.04	-13.45
26.91	31.49	4.58	-15.49	-36.36	-15.54	-17.73	-15.09	-41.28	-14.63
31.49	38.72	7.23	-13.90	-11.27	-10.86	-13.56	-13.02	-15.80	-13.71
38.72	44.77	6.05	-16.35	-15.53	-18.48	-17.16	-17.45	-4.55	-17.72
(b) slope root mean square difference (RMSD*) compared to WaSP									
month	technology	RMSD (cm/km)							
July 2017	PT	1.35							
	motorboat	3.81							
	AirSWOT	24.43							
August 2017	motorboat	1.75							
	AirSWOT	15.19							
* root mean square difference (RMSD) is calculated as:									
$RMSD = \sqrt{\frac{\sum_{n=1}^n (WSS_{WaSP} - WSS_{p,m,a})^2}{n}}$									
where WSS_{WaSP} is the WSS from WaSP, $WSS_{p,m,a}$ is the WSS from PT, motorboat or AirSWOT, and n is the number of observations									

Table 4-2: summary of water surface slope

TABLE 4-3

Resultant water surface elevation (WSE) surveys from WaSP surveys in Canada and Alaska collected to validate 2017 NASA Arctic Boreal Vulnerability Experiment (ABoVE) AirSWOT sorties

Region	Longitude	Latitude	WSE (m)	WSE error (m)	Survey Date	Day of Year
Mackenzie River Delta	-133.5222	68.7426	53.4483	0.0418	17-Jul-17	198
	-133.5288	68.7526	79.6726	0.0417	17-Jul-17	198
North Slope	-148.8288	69.1852	302.2120	0.0321	23-Jul-17	204
	-148.8473	69.0370	387.2296	0.0796	23-Jul-17	204
	-148.8585	69.1669	323.5982	0.0454	23-Jul-17	204
	-148.8177	69.0061	353.9454	0.0468	23-Jul-17	204
	-148.8298	69.1844	301.7595	0.0447	23-Jul-17	204
	-148.8286	68.9820	364.2325	0.0501	23-Jul-17	204
Saskatoon	-106.1058	52.2066	527.5217	0.1064	17-Aug-17	229
	-106.0923	52.2027	523.8466	0.0298	5-Jul-17	186
	-107.2051	52.7135	482.9965	0.0505	6-Jul-17	187
	-107.1066	52.6974	483.0490	0.0390	8-Jul-17	189
	-107.2168	52.6684	483.0950	0.0386	8-Jul-17	189
	-106.0920	52.2026	523.7553	0.0332	17-Aug-17	229
	-106.0879	52.2149	529.0673	0.0251	17-Aug-17	229
	-106.0854	52.2133	527.4918	0.0747	5-Jul-17	186
	-107.2058	52.7135	483.0227	0.0388	16-Aug-17	228
	-107.0601	52.6529	506.3182	0.0363	17-Aug-17	229
	-107.2117	52.6758	483.0603	0.0304	16-Aug-17	228
	-107.0575	52.6529	508.9351	0.0488	17-Aug-17	229
	-107.1119	52.6962	482.9667	0.0558	16-Aug-17	228
	-107.0840	52.6606	498.6402	0.0357	17-Aug-17	229
	-106.1006	52.2109	529.4029	0.0434	17-Aug-17	229
	-107.0826	52.6606	498.8452	0.0583	4-Jul-17	185
	-106.0897	52.2132	527.8228	0.0922	5-Jul-17	186
	-106.0898	52.2134	527.6945	0.0474	17-Aug-17	229
	-106.0878	52.2149	529.2325	0.0415	5-Jul-17	186
	-107.0572	52.6526	509.0371	0.0360	4-Jul-17	185
	-106.1057	52.2058	527.5958	0.0674	5-Jul-17	186
	-107.0605	52.6528	506.4899	0.0513	4-Jul-17	185
	-106.0849	52.2130	527.3977	0.0561	17-Aug-17	229
	-107.1065	52.6974	483.0763	0.0632	6-Jul-17	187
Yellowknife	-112.4099	64.3709	424.9593	0.0389	9-Jul-17	190
	-112.5715	64.2623	405.6145	0.0350	10-Jul-17	191
	-114.4418	62.6623	204.7298	0.0317	11-Jul-17	192
	-113.8379	62.5258	178.6840	0.0266	8-Jul-17	189
	-113.6085	63.6059	335.5635	0.0384	10-Jul-17	191
	-113.9566	62.5477	184.7538	0.0445	11-Jul-17	192
	-113.9997	62.5544	181.9594	0.0486	12-Jul-17	193
	-111.6683	64.8351	391.1230	0.0452	9-Jul-17	190
	-113.8953	63.4020	330.2163	0.0541	10-Jul-17	191
	-113.9345	62.5481	178.5824	0.0433	11-Jul-17	192
	-113.7356	62.5200	141.2626	0.0317	8-Jul-17	189
	-113.2135	63.8692	340.4361	0.0841	9-Jul-17	190
	-112.2515	64.4628	440.6832	0.0398	10-Jul-17	191
	-114.1187	62.5384	157.8755	0.0340	12-Jul-17	193
	-113.3797	62.5257	198.4356	0.0230	8-Jul-17	189
	-114.1571	63.2189	256.5165	0.0429	10-Jul-17	191
	-114.4073	62.5618	175.4881	0.0393	11-Jul-17	192
	-114.0444	62.5489	173.0687	0.0318	12-Jul-17	193
Yukon Flats Basin	-145.7919	66.7859	133.7659	0.0528	15-Jul-17	196
	-146.3791	66.2258	127.5550	0.0392	15-Jul-17	196
	-146.7334	66.0915	209.4129	0.1111	16-Jul-17	197
	-145.5504	66.4561	137.2486	0.0606	15-Jul-17	196
	-146.3889	66.2458	127.4344	0.0476	15-Jul-17	196
	-145.8406	66.6660	129.2561	0.0473	19-Jul-17	200
-146.3533	66.3836	126.8725	0.0341	15-Jul-17	196	

	-146.4181	66.1739	134.3166	0.0781	15-Jul-17	196
	-146.6518	66.1831	126.1839	0.1163	16-Jul-17	197
	-145.8415	66.6778	129.4319	0.0610	19-Jul-17	200
	-145.4340	66.4324	139.0149	0.0599	15-Jul-17	196
	-146.1487	66.1762	147.8695	0.0357	15-Jul-17	196
	-146.2748	66.0755	234.5194	0.0590	16-Jul-17	197

Table 4-3: 2017 WaSP lake surveys during NASA ABoVE campaign.

4.11 References

- Allen, G. J., and Pavelsky, T. M. (2018). Global extent of rivers and streams. *Science (80-.)*, 585–588. doi:10.5268/IW-2.4.502.
- Alsdorf, D. E., and Lettenmaier, D. P. (2003). Tracking Fresh Water from Space. *Science (80-.)*. 301, 1491–1494. doi:10.1126/science.1089802.
- Alsdorf, D. E., Lettenmaier, D. P., and Vörösmarty, C. J. (2003). The need for global, satellite-based observations of terrestrial surface waters. *EOS, Trans. Am. Geophys. Union Trans. Am. Geophys. Union* 84, 269–276. doi:10.1029/2003EO290001.
- Alsdorf, D. E., Rodríguez, E., and Lettenmaier, D. P. (2007). Measuring surface water from space. *Rev. Geophys.* 45. doi:10.1029/2006RG000197.
- Altenau, E. H., Pavelsky, T. M., Moller, D., Lion, C., Pitcher, L. ., Allen, G. H., et al. (2017). AirSWOT measurements of river water surface elevation and slope: Tanana River, AK. *Geophys. Res. Lett.* 44, 181–189. doi:10.1002/2016GL071577.
- Altenau, E. H., Pavelsky, T. M., Moller, D., Pitcher, L. H., Bates, P. D., Durand, M. T., et al. (2019). Temporal variations in river water surface elevation and slope captured by AirSWOT. *Remote Sens. Environ.* 224, 304–316. doi:10.1016/j.rse.2019.02.002.
- Bates, P. D., Wilson, M. D., Horritt, M. S., Mason, D. C., Holden, N., and Currie, A. (2006). Reach scale floodplain inundation dynamics observed

- using airborne synthetic aperture radar imagery: Data analysis and modelling. *J. Hydrol.* 328, 306–318. doi:10.1016/j.jhydrol.2005.12.028.
- Biancamaria, S., Lettenmaier, D. P., and Pavelsky, T. M. (2016). The SWOT Mission and Its Capabilities for Land Hydrology. *Surv. Geophys.* 37, 307–337. doi:10.1007/s10712-015-9346-y.
- Crétaux, J. F., Abarca-del-Río, R., Bergé-Nguyen, M., Arsen, A., Drolon, V., Clos, G., et al. (2016). Lake Volume Monitoring from Space. *Surv. Geophys.* 37, 269–305. doi:10.1007/s10712-016-9362-6.
- Dietrich, W. E., Smith, J. D., and Dunne, T. (1979). Flow and Sediment Transport in a Sand Bedded Meander. *J. Geol.* 87, 305–315. Available at: <https://www.jstor.org/stable/30060821>%0D.
- Durand, M., Lee-Lueng, F., Lettenmaier, D. P., Alsdord, D. E., Rodriguez, E., and Esteban-Fernandez, D. (2010). The surface water and ocean topography mission: Observing terrestrial surface water and oceanic submesoscale eddies. *Proc. IEEE* 98, 766–779. doi:10.1109/JPROC.2010.2043031.
- Durand, M., Neal, J., Rodríguez, E., Andreadis, K. M., Smith, L. C., and Yoon, Y. (2014). Estimating reach-averaged discharge for the River Severn from measurements of river water surface elevation and slope. *J. Hydrol.* 511, 92–104. doi:10.1016/j.jhydrol.2013.12.050.
- Fayne, J. V., Smith, L. C., Pitcher, L. H., Kyzivat, E. D., Cooley, S. W., Cooper, M. G., et al. Airborne Observations of Arctic-Boreal Water

Surface Elevation from AirSWOT Ka-Band InSAR and LVIS LiDAR.

Fayne, J. V., Smith, L. C., Pitcher, L. H., and Pavelsky, T. M. (2019). ABoVE: AirSWOT Ka-band Radar over Surface Waters of Alaska and Canada, 2017. *ORNL DAAC, Oak Ridge, Tennessee, USA*. doi:<https://doi.org/10.3334/ORNLDAAC/1646>.

Ferreira, M. (2014). Perpendicular Transects. Available at: <http://gis4geomorphology.com/stream-transects-partial/>.

Jowett, I. G. (1993). A method for objectively identifying pool, run, and riffle habitats from physical measurements. *New Zeal. J. Mar. Freshw. Res.* 27, 241–248. doi:10.1080/00288330.1993.9516563.

Kiel, B., Alsdorf, D., and LeFavour, G. (2006). Capability of SRTM C- and X-band DEM Data to Measure Water Elevations in Ohio and the Amazon. *Photogramm. Eng. Remote Sens.* 72, 313–320. doi:10.14358/PERS.72.3.313.

Kyzivat, E. D., Smith, L. C., Cooley, S. W., Pitcher, L. H., and Horvat, C. (2019a). High-resolution water mask from NASA ABoVE AirSWOT flight campaign reveals variable size distributions of Arctic-Boreal lakes. *Remote Sens.* 11, 1–28. doi:<https://doi.org/10.3390/rs11182163>.

Kyzivat, E. D., Smith, L. C., Pitcher, L. H., Fayne, J. V., Cooley, S. W., Cooper, M. G., et al. (2019b). ABoVE: AirSWOT Water Masks from Color-Infrared Imagery over Alaska and Canada, 2017. *ORNL DAAC, Oak Ridge, Tennessee, USA*. doi:<https://doi.org/10.3334/ORNLDAAC/1707>.

- Kyzivat, E. D., Smith, L. C., Pitcher, L. H., J., A., Pavelsky, T. M., Cooley, S. W., et al. (2018). ABoVE: AirSWOT Color-Infrared Imagery Over Alaska and Canada, 2017. *ORNL DAAC, Oak Ridge, Tennessee, USA*. doi:<https://doi.org/10.3334/ORNLDAAC/1643>.
- Lee, H., Durand, M., Jung, H. C., Alsdorf, D., Shum, C. K., and Sheng, Y. (2010). Characterization of surface water storage changes in Arctic lakes using simulated SWOT measurements. *Int. J. Remote Sens.* 31, 3931–3953. doi:[10.1080/01431161.2010.483494](https://doi.org/10.1080/01431161.2010.483494).
- LeFavour, G., and Alsdorf, D. (2005). Water slope and discharge in the Amazon River estimated using the shuttle radar topography mission digital elevation model. *Geophys. Res. Lett.* 32. doi:[10.1029/2005GL023491](https://doi.org/10.1029/2005GL023491).
- Margulis, S. A. (2017). *Introduction to Hydrology*. doi:[10.5021/ad.2012.24.4.438](https://doi.org/10.5021/ad.2012.24.4.438).
- Marty, J. C., Loyer, S., Perosanz, F., Mercier, F., Bracher, G., Legresy, B., et al. (2011). GINS: the CNES/GRGS GNSS scientific software. in *3rd International Colloquium Scientific and Fundamental Aspects of the Galileo Programme, ESA Proceedings WPP326*, 8–10.
- Miller, C. E., Griffith, P. C., Goetz, S. J., Hoy, E. E., Pinto, N., McCubbin, I. B., et al. (2019). An overview of ABoVE airborne campaign data acquisitions and science opportunities. *Environ. Res. Lett.* 14, 080201. doi:[10.1088/1748-9326/ab0d44](https://doi.org/10.1088/1748-9326/ab0d44).

- Montgomery, D. R., Beamer, E. M., Pess, G. R., and Quinn, T. P. (1999). Channel type and salmonid spawning distribution and abundance. *Can. J. Fish. Aquat. Sci.* 56, 377–387. doi:10.1139/f98-181.
- Ostrovsky, I., Yacobi, Y. Z., Walline, P., and Kalikhman, I. (1996). Seiche-induced mixing: Its impact on lake productivity. *Limnol. Oceanogr.* 41, 323–332. doi:10.4319/lo.1996.41.2.0323.
- Papa, F., Durand, F., Rossow, W. B., Rahman, A., and Bala, S. K. (2010). Satellite altimeter-derived monthly discharge of the Ganga-Brahmaputra River and its seasonal to interannual variations from 1993 to 2008. *J. Geophys. Res. Ocean.* 115, C12013. doi:10.1029/2009JC006075.
- Pavelsky, T. M., Ghafoor, S., Hossain, F., Parkins, G. M., Yelton, S. K., Little, S. B., et al. (2019). Monitoring the World's Lakes: Progress from Citizen Science and Remote Sensing. *Mag. Environ. Manag.*
- Pitcher, L. H., Pavelsky, T. M., Smith, L. C., Moller, D. K., Altenau, E. H., Allen, G. H., et al. (2019). AirSWOT InSAR mapping of surface water elevations and hydraulic gradients across the Yukon Flats Basin, Alaska. *Water Resour. Res.* doi:https://doi.org/10.1029/2018WR023274.
- Planet-Team (2019). Planet Application Program Interface: In Space For Life On Earth. Available at: <https://api.planet.com>.
- Prowse, T. D., Beltaos, S., Gardner, J. T., Gibson, J. J., Granger, R. J., Leconte, R., et al. (2006). Climate change, flow regulation and land-use effects on the hydrology of the Peace-Athabasca-Slave system; Findings

from the Northern Rivers Ecosystem Initiative. *Environ. Monit. Assess.* 113, 167–197. doi:10.1007/s10661-005-9080-x.

Rodriguez, E. (2016). Surface Water and Ocean Topography Mission (SWOT) Project: Science Requirements Document (Rev A). Available at: <https://pdms.jpl.nasa.gov>.

Smith, L. C. (1997). Satellite remote sensing of river inundation area, stage, and discharge: a review. *Hydrol. Process.* 11, 1427–1439. doi:10.1002/(SICI)1099-1085(199708)11:10<1427::AID-HYP473>3.0.CO;2-S.

Tuozzolo, S., Lind, G., Overstreet, B., Mangano, J., Fonstad, M., Hagemann, M., et al. (2019). Estimating River Discharge With Swath Altimetry: A Proof of Concept Using AirSWOT Observations. *Geophys. Res. Lett.* 46, 1459–1466. doi:10.1029/2018GL080771.

Yamazaki, D., Ikeshima, D., Tawatari, R., Yamaguchi, T., O’Loughlin, F., Neal, J. C., et al. (2017). A high-accuracy map of global terrain elevations. *Geophys. Res. Lett.* 44, 5844–5853. doi:10.1002/2017GL072874.

4.12 Supporting Information

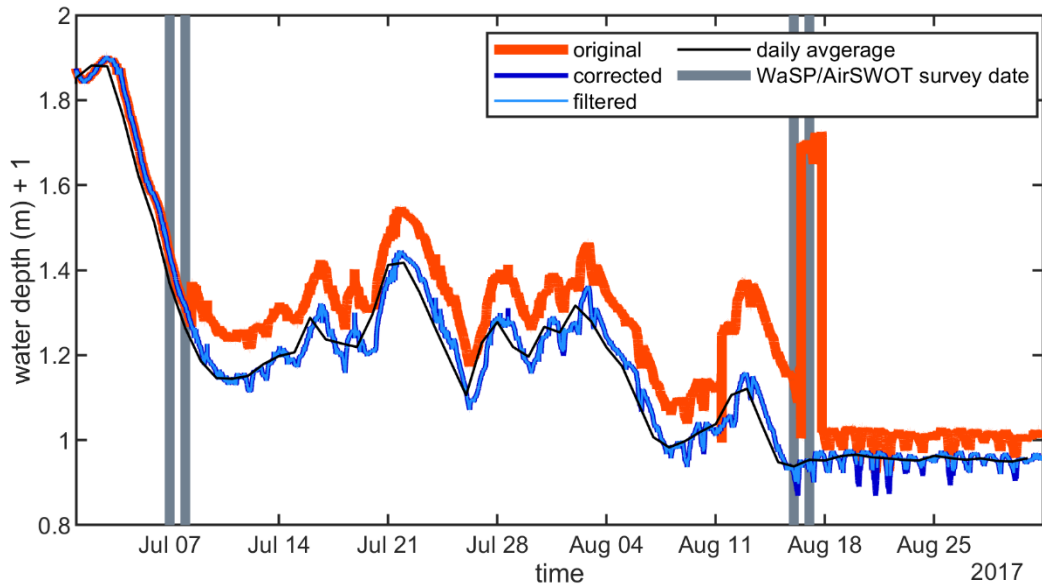


Figure S4-1: ECCC pressure transducer record

Environment and Climate Change Canada (ECCC) pressure transducer (PT) water level record for one PT located 0.37 km from the start of our study reach. The original pressure data series (5-minute logging interval) was manually converted to water depth using a barometric pressure logger located near Wingard Ferry at the end of the study reach (orange line). Notable jumps in the data series suggest that the PT location shifted between installation and recovery. To rectify this, jumps in the data series were manually identified and a constant offset, calculated as the difference between high-quality neighboring measurements was applied to subsequent data readings (dark blue line). Vertical grey bars denote WaSP and AirSWOT survey days.

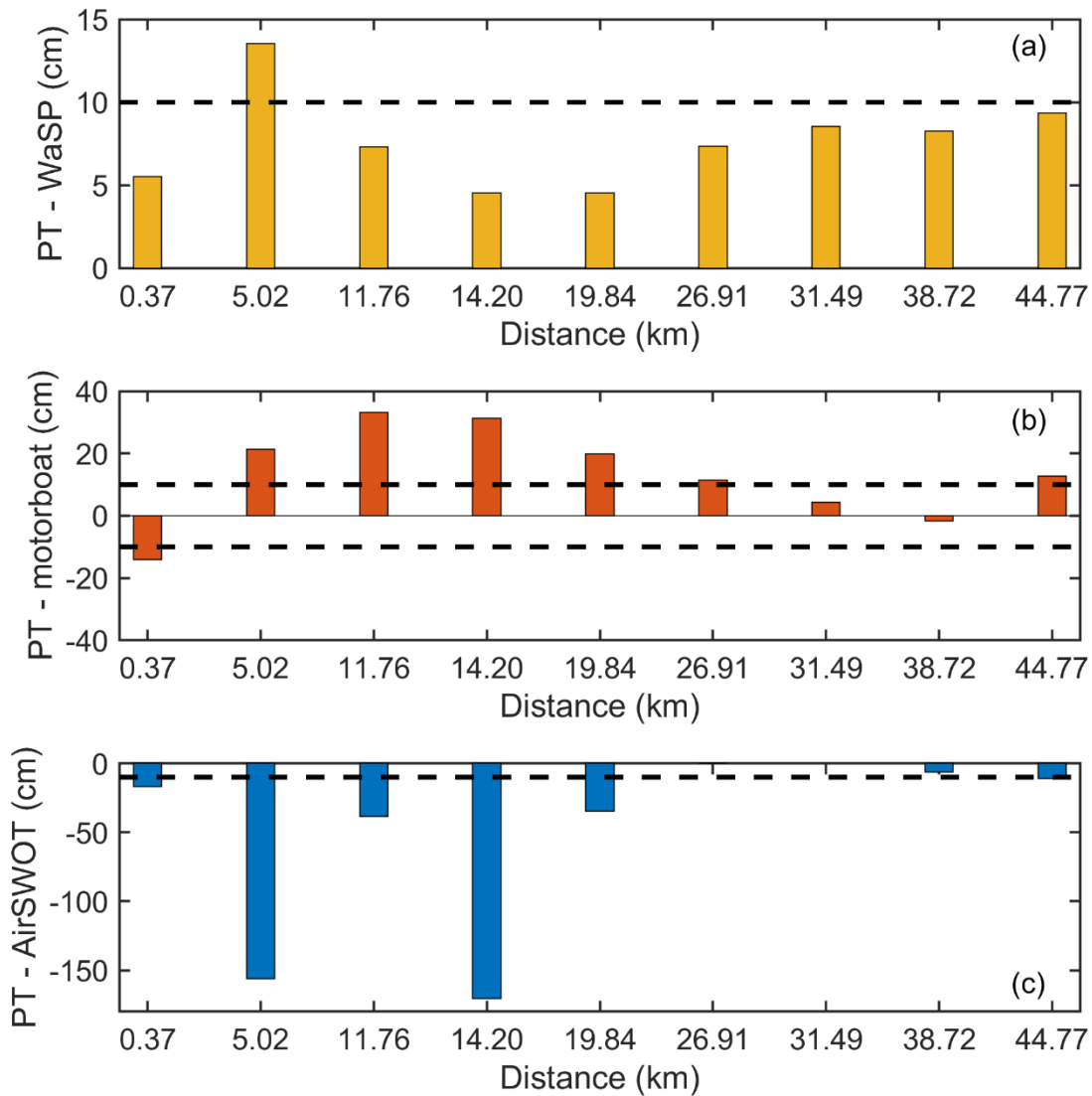


Figure S4-2: PT WSE difference

The water surface elevation (WSE) difference between Environment and Climate Change Canada (ECCC) pressure transducer (PT) water level loggers and (a) WaSP, (b) motorboat, and (c) AirSWOT for 20 m reaches centered on each PT. Differences of ± 10 cm are noted by dashed black line.

Comparison is for surveys conducted on July 7-8, 2017 only. Analogous PT data is not available for August 2017 surveys.

Table S4-1.								
PT	Lat.	Lon.	distance (km)	Ellipsoidal height (h)		EGM96 geoid correction (n)	Orthometric height (H)	
				July 7, 2017	July 8, 2018		July 7, 2017	July 8, 2018
05GEX01	52.649	-106.84	0.37	413.67	413.56	-22.53	436.20	436.09
05GEX02	52.683	-106.81	5.02	413.03	412.84	-22.62	435.65	435.46
05GEX03	52.726	-106.75	11.76	411.72	411.58	-22.74	434.46	434.32
05GEX04	52.743	-106.72	14.20	411.35	411.22	-22.78	434.13	434.00
05GEX05	52.784	-106.67	19.84	410.37	410.26	-22.89	433.26	433.15
05GEX06	52.824	-106.59	26.91	409.37	409.26	-23.00	432.37	432.26
05GEX07	52.861	-106.57	31.49	408.56	408.46	-23.10	431.66	431.56
05GEX08	52.899	-106.48	38.72	407.58	407.48	-23.21	430.79	430.69
05GEX09	52.944	-106.43	44.77	406.54	406.44	-23.34	429.88	429.78

Table S4-1: pressure transducer locations

Location, ellipsoidal (h) and orthometric (H) water surface elevations (WSE) on July 7-8, 2017 from a temporary array of nine pressure transducers (PTs) surveyed in along the North Saskatchewan River by the Water Survey of Canada (WSC), a branch of Environment and Climate Change Canada (ECCC) during spring/summer 2017. The distance (km) field refers to downstream distance along our study reach, which runs from Petrofka Bridge to Wingard Ferry. $H \approx h - n$, where H is the orthometric height, h is the ellipsoidal height, and n is the height of the EGM96 geoid.




Table S4-2.					
July 2017			August 2017		
Date	Day of year	Average depth (m) + 1 (m)	Date	Day of year	Average depth (m) + 1 (m)
1-Jul-17	182	1.85	1-Aug-17	213	1.25
2-Jul-17	183	1.88	2-Aug-17	214	1.32
3-Jul-17	184	1.88	3-Aug-17	215	1.28
4-Jul-17	185	1.76	4-Aug-17	216	1.22
5-Jul-17	186	1.62	5-Aug-17	217	1.17
6-Jul-17	187	1.51	6-Aug-17	218	1.09
7-Jul-17	188	1.37	7-Aug-17	219	1.01
8-Jul-17	189	1.26	8-Aug-17	220	0.98
9-Jul-17	190	1.19	9-Aug-17	221	1.00
10-Jul-17	191	1.15	10-Aug-17	222	1.02
11-Jul-17	192	1.14	11-Aug-17	223	1.04
12-Jul-17	193	1.15	12-Aug-17	224	1.11
13-Jul-17	194	1.18	13-Aug-17	225	1.12
14-Jul-17	195	1.20	14-Aug-17	226	1.03
15-Jul-17	196	1.21	15-Aug-17	227	0.95
16-Jul-17	197	1.29	16-Aug-17	228	0.94
17-Jul-17	198	1.24	17-Aug-17	229	0.95
18-Jul-17	199	1.23	18-Aug-17	230	0.95
19-Jul-17	200	1.22	19-Aug-17	231	0.96
20-Jul-17	201	1.30	20-Aug-17	232	0.97
21-Jul-17	202	1.41	21-Aug-17	233	0.96
22-Jul-17	203	1.42	22-Aug-17	234	0.96
23-Jul-17	204	1.35	23-Aug-17	235	0.95
24-Jul-17	205	1.27	24-Aug-17	236	0.95
25-Jul-17	206	1.18	25-Aug-17	237	0.96
26-Jul-17	207	1.11	26-Aug-17	238	0.96
27-Jul-17	208	1.23	27-Aug-17	239	0.95
28-Jul-17	209	1.28	28-Aug-17	240	0.96
29-Jul-17	210	1.22	29-Aug-17	241	0.95
30-Jul-17	211	1.20	30-Aug-17	242	0.95
31-Jul-17	212	1.27	31-Aug-17	243	0.96
Legend		WaSP and motorboat surveys			
		AirSWOT survey only			
		WaSP, motorboat and AirSWOT surveys			
* data from PT 05GEX01 (see Table s1)					

Table S4-2: corrected pressure transducer data

Manually corrected, outlier removed, daily mean water level (+ 1 m) from one pressure transducer (PT) located near the Petrofka Bridge in the North Saskatchewan River. Cell shading denotes accompanying WaSP, AirSWOT and motorboat surveys.

Table S3.		
Date	Planet area (m²)	GPS area (m²)
Pond #1		
4-Jul-17	14691.46	15665.67
18-Aug-17	13702.76	NA
16-Jun-18	11970.84	13272.35
Pond #2		
4-Jul-17	18458.63	20134.70
18-Aug-17	15356.06	NA
16-Jun-18	17184.79	18304.89
Pond #3		
4-Jul-17	26531.98	30927.92
18-Aug-17	25325.65	29409.88
16-Jun-18	25574.53	29794.04

Table S4-3: pond shoreline areas

Pond shoreline areas (m²) as manually digitized using Planet satellite imagery (Planet Team, 2019) and mapped in situ using handheld Garmin eTrex GPSs.